Toward a Measurement of the Neutrino Mass with Tritium: Ion Studies for the KATRIN and TRIMS Experiments

By
Ana Paula Vizcaya Hernández

A dissertation
submitted in partial fulfilment of the
requirements for the degree of

Doctor of Philosophy

Carnegie Mellon University
Department of Physics
Pittsburgh, Pennsylvania

November 2021

Advisor:
Professor Diana Parno
Thesis committee:
Professor Curtis Meyer
Professor Manfred Paulini
Professor Walter Pettus

In memory of Marquitos

Carnegie Mellon University

Abstract

Toward a Measurement of the Neutrino Mass with Tritium: Ion Studies for the KATRIN and TRIMS Experiments

Ana Paula Vizcaya Hernández

Chair of the Supervisory Committee:
Assistant Professor Diana Parno
Department of Physics

The KATRIN (KArlsruhe TRItium Neutrino) experiment aims to measure the effective neutrino mass with an unprecedented design sensitivity of 0.2 eV at the 90% confidence level by measuring the energy spectrum of electrons produced in tritium β-decay. Magnetic fields guide charged particles through the energy-analyzing retarding spectrometers towards the main detector. In this process, ions produced from the decay and from scattering processes, act as a background source as they further ionize residual gas and produce secondary electrons. Ion-blocking mechanisms are implemented in the transport section for which we found preferred settings and neutralization times. We monitor the small ion flux in the spectrometers by the current that they make by striking electrodes along the beamline and by electron generation by ion-impact in the spectrometer. We calibrated the monitoring devices and present their performance during the first neutrino mass campaigns. We demonstrated that it was safe to run the experiment without ion contamination at the high tritium concentration used during neutrino mass measurements.

The molecular final-state theory, used to calculate the β-energy spectrum for the KATRIN experiment, is validated by the TRIMS (Tritium Recoil-Ion Mass Spectrometer) experiment. The goal of the TRIMS experiment is to measure the molecular tritium β-decay branching ratio to the bound state $^3HeT^+$ and resolve discrepancies between theory and experimental results. In this thesis we will discuss selected analysis projects done for the TRIMS experiment, including characterization of the ion detector to correct for energy-loss effects, and investigations of the β-decay daughter ion energy spectrum.

ACKNOWLEDGMENTS

I would like to thank my advisor Diana Parno, for her guidance and assistance during my PhD. Her physics insight, willingness to always meet, and her numerous comments played a key role in my development as a physicist. Thanks for showing us that having a beautiful family and being successful in academia is possible.

I thank my thesis committee: Curtis Meyer, Manfred Paulini and Walter Pettus.

I thank the Physics Department and the Medium Energy Group at CMU for all their support. I'm especially grateful to Gregg Franklin, for his support as a second advisor and for recommending me to talk to Diana even before she got to CMU.

I would like to thank the Ion Lion Team: Fabian Friedel, Ferenc Glück, Manuel Klein, and Magnus Schlösser. I was really fortunate to be part of such an amazing group. Thanks for all the physics discussions, suggestions, corrections and great teamwork. I learned a lot from all of you. Thanks for all the laughs after long hours in the control room, and for always waiting for me to finish my food at the canteen.

I would like to thank my colleagues and friends in the KATRIN collaboration. I don't want to write names for fear I will forget someone. Nevertheless I want to give special thanks to Woo-Jeong for becoming a true friend, Florian for the warm welcome and advice, and Alexey and Rudi for all the talks.

I would like to thank the TRIMS team: Hamish for all your brilliant ideas and your willingness to explain things, Ting for answering emails long after you left UW, Byron for your help with the simulations, Eris, and Matt.

Thanks to the best office mates I could have asked for. Larisa, thanks for being there for us and for becoming such a good friend. Juan Carlos, thanks for all the talks in Spanish, coding advice, and for your friendship. Thanks to Hao and Feynman.

Thanks to the CMU Parno group, it has been a great source of support, special thanks to Becca and Aishwarya.

I would like to thank my CMU cohort (2016): Danny and Maddy, thanks for all the avatar sessions. Sayan, thanks for the morning tea. KW, thanks for introducing me to bubble tea. Husni, thanks for all the travelling advice. And thanks to Yizhou, Andrew, Fet, Olga and Ying.

I would like to thank my oldest friends and chosen sisters: Marimar, Pauthi, Rebe and Sofi. Thanks for always being there for me. Popos para siempre. Thanks to all my Frisbee friends, playing with you helped me forget about physics for a while. Jorge, thanks for you friendship bestia. Thanks to my undergrad friends Erika, Luis, Aramis, and Papaqui. Thanks to my math friends: David, Mihir, Wony, Michael, Likhit, Aditya, Ananya, and Junichi. I enjoyed winning on board games.

Thanks to my very big family. To my grandparents for their inspiration. My aunts, uncles, and cousins, for all their love. I want to thank the Mazari family for welcoming me and always making me feel like one of them.

I would like to thank my father Fernando for all his love and support, thanks for sharing with me your love for astronomy and physics, and for encouraging me to follow my dreams. And my mother Gloria for always taking care of me. Thank to my siblings: Andrea, Fer and Guillermo, you will always be my best friends.

Finally, I want to thank my family, Marcos, Marquitos and Ana Sofia for bringing me so much happiness. Ana Sofia, thanks for all the non-planned but very much needed distractions while writing my thesis. Marcos, thanks for everything, for your neverending love, support, and encouragement, because together we make it possible.

Gracias Dios por todas las bendiciones.

TABLE OF CONTENTS

LIST OF FIGURES

LIST OF TABLES

ACRONYMS

BAO baryon acoustic oscillation. 9

CMB cosmic microwave background. 8, 9

CPS Cryogenic Pumping Section. 27, 28, 38, 51, 57, 85, 88, 99, 118, 160

DE1 Dipole Electrode 1. xv, xvi, xix, 71, 75–80, 82, 85, 89, 97–100, 115–117

DE2 Dipole Electrode 2. xv, 72, 75, 97–99, 116

DE3 Dipole Electrode 3. xv, 52, 72, 75, 76, 97–99

DE4 Dipole Electrode 4. 51, 52, 63, 71, 72, 81, 89, 107, 110

DPS Differential Pumping Section. xiv, xv, xviii, 26, 27, 40, 43, 50, 51, 53–55, 62, 70, 72–74, 76, 85, 86, 88, 90, 92, 96, 104, 115–117

FPD Focal Plane Detector. xv, xvi, xix, 21, 30, 33, 38, 39, 50, 54, 57, 58, 66, 70, 74–76, 80–82, 84–93, 95, 103, 105, 107, 109–114, 116–118, 160, 161

FT First Tritium. 44

FT-ICR Fourier Transform Ion Cyclotron Resonance. 70

FV fiducial volume. 141

ICE Ion Conversion to Electron. xv, xvi, xviii, xix, 54, 57–59, 66–68, 74, 76, 80–84, 88–90, 96, 101, 103–105, 109–111, 118, 161

KATRIN KArlsruhe TRItium Neutrino experiment. xiii, xiv, 16, 19–22, 28, 32–34, 36–38, 41, 42, 45, 49–54, 59, 69, 70, 94, 95, 105, 117, 158, 160

KNM KATRIN Neutrino Mass measurements. 63

KNM1 KATRIN Neutrino Mass measurement 1. xiv, xv, xix, 28, 36, 37, 44, 63, 77, 80, 84, 94–104, 107, 108, 118, 119, 161

KNM2 KATRIN Neutrino Mass measurement 2. xv, xviii, xix, 28, 36, 44, 52, 63, 77, 84, 94–97, 99–101, 103, 104, 106, 108, 114, 115, 118, 119, 161

MAC-E Magnetic Adiabatic Collimation with Electrostatic. xiii, 20–23, 28, 160

MoS Monitor Spectrometer. 28

MS Main Spectrometer. ix, 22, 28–30, 38, 39, 50, 58, 66, 67, 70, 71, 81–84, 116

PAE Post Acceleration Electrode. 30

PS Pre-Spectrometer. x, xiv, xviii, xix, 27–29, 38, 39, 54, 56–59, 62–65, 67, 76–79, 84–86, 88, 96, 99, 101, 103, 104, 118, 160

PS-DCE Pre Spectrometer Downstream-Cone Electrode. xv, xviii, xix, 54, 56, 58, 63, 64, 66, 76–79, 87, 88, 100–104, 118, 160, 161

PS1 PreSpectrometer magnet 1. 63, 66, 103, 111

RCF Raw Count Function. xvi, xvii, 150, 151, 153–156

RE-DPSa Ring Electrode DPS a. xv, xvi, xix, 51, 72–74, 85, 86, 88–93, 105–107, 110–115

RE-PS1 PreSpectrometer magnet 1. xv, xvi, xix, 51, 88–90, 105–108, 110, 113–115

RW Rear Wall. 22–24, 50, 53, 74, 79, 81, 82, 85, 91, 97, 99, 100

SDS Spectrometers and Detector Section. ix, xiii, 27–30, 38–40, 50–54, 56–59, 62, 66, 70, 73, 74, 76–84, 87, 88, 90, 94, 95, 97, 100, 101, 103–105, 111, 118, 160, 161

SRIM Stopping and Range of Ions in Matter. 137, 139–143, 146, 158, 159

STS Source and Transport Section. 23, 73, 90

STS-IIIa STS Commissioning Phase IIIa. 69, 74, 76, 79, 85, 88, 160

TLK Tritium Laboratory Karlsruhe. 23

TMP Turbo Molecular Pump. 27, 28, 30

TRIMS Tritium Recoil Ion Mass Spectrometer. 12, 42, 120, 122–124, 130, 131, 133, 136, 137, 139, 145–147, 149–151, 158, 159

UV ultraviolet. 24

V2 Valve 2. 97, 99, 100, 118

VFT Very First Tritium. 71, 84, 85, 88, 92

WGTS Windowless Gaseous Tritium Source. ix, xiii–xv, 24–26, 33, 34, 38–45, 49–51, 53, 70, 72–74, 76, 79, 80, 84, 85, 88, 91, 92, 96, 97, 99, 100, 105–111, 115, 117

XML Extensible Markup Language. 59, 60, 62

CHAPTER 1
INTRODUCTION TO NEUTRINO PHYSICS

1.1 Physics motivation for a new particle: the neutrino

As with a lot of great discoveries in physics, the idea of the neutrino was proposed after some experimental measurements could not be explained with the particle theory used at the time.

Although it was not known back then, the first evidence of the neutrino was seen in the measured energy spectrum of the beta electrons after a β-decay. During the 1920's it was believed that all matter was formed by protons and electrons [1]. It was thought that β-decay was described by a final state with two particles: the daughter ion and an electron. The daughter ion had one extra proton ($Z+1$) compared to the parent atom, and both had atomic mass A:

$$ {}^{A}_{Z}X \rightarrow {}^{A}_{Z+1}X' + \beta^{-}. \tag{1.1} $$

If that were the case, because of energy conservation, the energy spectrum of the beta should have a narrow distribution around a single value, just like in α- radiation. However James Chadwick measured a continuous beta energy spectrum [2] which could not be explained by a two-particle final state.

In 1930 Wolfgang Pauli proposed the existence of a new particle, difficult to detect, that he called the "neutron" [1], which explained the conservation of energy and momentum in beta decay. If this particle was also emitted in the decay, the released energy could be shared between three particles allowing a continuous beta energy spectrum.

It wasn't until 1934 that Enrico Fermi called this new particle a *neutrino* in his description of β-decay [3] where he stated "... each transition of a neutron to a proton is associated with the creation of an electron and a neutrino":

$$ n \rightarrow p^{+} + e^{-} + \overline{\nu}_{e}. \tag{1.2} $$

Neutrinos were first detected in 1956 by Cowan and Reines, in their experiment an anti-neutrino interacted with a proton to produce a neutron and a positron [4]. This process is

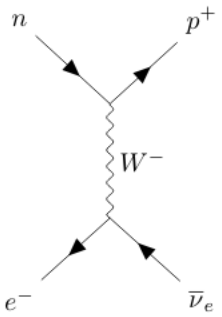

Figure 1.1: Feynman diagram of a beta decay where the neutron decays into a proton, an electron and a electron anti-neutrino. The diagram was done using TikZ-Feynman [6].

known as Inverse Beta Decay (IBD):

$$\overline{\nu}_e + p^+ \rightarrow n + e^+. \tag{1.3}$$

The detection mechanism consisted of a coincidence of gamma rays produced by electron-positron annihilation and gamma rays produced by neutron capture.

1.2 Neutrinos in the Standard Model

There are three different types of neutrino flavours associated with the charged leptons: electron (e), muon (μ), and tau (τ). They are conveniently called: the electron neutrino (ν_e) which was the first to be detected; the muon neutrino (ν_μ) detected a few years latter; and the tau neutrino (ν_τ) which was detected decades after the other two. Neutrinos are classified in the Standard Model as leptons giving a total of 6 lepton particles. They have half-integer spin (1/2). They only interact via the weak force and very weakly with the gravitational force due to their extremely small mass.

A weak interaction occurs when two particles exchange a weak boson (W^+, W^-, or Z). It is called weak because of its small field strength. Its effective range is less than the diameter of a proton [5]. One common weak decay is the β-decay which is illustrated as a Feynman diagram in Fig. 1.1.

Fermion antiparticles have the same properties of the fermions but with opposite charge conjugation. Since neutrinos do not have charge it is not known if they are their own antiparticles (Majorana particles) or not (Dirac particles).

The first detection of the ν_e by Cowan and Reines [4] was in fact a detection of an electron anti-neutrino ($\overline{\nu}_e$) which is an antiparticle because of assumed lepton number conservation; the positron in the inverse β-decay has lepton number -1 and the rest of the particles in the decay have lepton number 0, so the neutrino has to have lepton number -1

making it an anti-particle. Reines went on to win the Nobel Prize in Physics (1995) for the detection of the neutrino [7].

The muon neutrino was detected years later, in 1962 by Lederman, Schwartz, Steinberger, *et al.*, at the Brookhaven National Laboratory [8]. In their experiment, pions decayed into muons and ν_μ, and the particles detected were products of further ν_μ interactions with neutrons and protons. Lederman, Schwartz, and Steinberger went on to win the Nobel Prize in Physics (1988) for the neutrino beam method and the demonstration of the doublet structure of the leptons through the discovery of the muon neutrino [9].

The existence of the tau neutrino was not suspected until the mid-1970s, after the tau lepton was discovered. This can be attested by the text from Feynman's general physics book from 1963, handed to me by my grandfather:

"There is a lepton which is neutral, called a neutrino, and this particle has zero mass. In fact, it is known that there are two different kinds of neutrinos, one related to electrons and the other related to muons." [10]

The tau neutrino was finally detected in 2001 by the DONuT experiment at Fermilab [11].

The quote also states that neutrinos do not have mass. In the Standard Model particles have mass by interacting with the Higgs boson. To understand this interaction we have to talk about handedness. A particle is right-handed when the direction of its spin is the same as the direction of its motion, and it is left-handed if they are opposites. When particles interact with the Higgs boson they exchange their handedness [12].

The helicity (or handedness) of the neutrinos was measured in 1958 by Goldhaber, Grodzins, and Sunyar. They found that the neutrinos are left-handed and anti-neutrinos are right-handed [13]. The neutrinos cannot interact with the Higgs boson because there are no right-handed neutrinos and so they cannot get mass via the Higgs mechanism. So, why do we think that neutrinos have mass?

1.3 Neutrino flavor oscillations

The discovery of a new neutrino process, called neutrino oscillation, challenged the idea of massless neutrinos and required an extension of the Standard Model to explain it.

1.3.1 The solar neutrino mystery

Every second, around a trillion neutrinos pass through our body, and most of them come from fusion reactions in the sun's core [12]. So it was just natural for scientists to study this abundant source of neutrinos.

The primary initial reaction in the sun's core is the fusion of two protons with the emission of a neutrino (the pp-neutrino), a positron, and a deuteron [14]:

$$p + p \rightarrow {}^{2}\mathrm{H} + e^{+} + \nu_e. \tag{1.4}$$

Neutrinos are also produced at other stages of the proton-proton chain, but all created neutrinos are ν_e. The solar neutrino flux was calculated by J. N. Bahcall *et al.* [15], and it was measured starting in 1968 with the Homestake experiment, where ν_e were measured with the inverse β-decay reaction:

$$\nu_e + {}^{37}\mathrm{Cl} \rightarrow {}^{37}\mathrm{Ar} + e^{-}. \tag{1.5}$$

Their results showed that only one third of the predicted solar neutrino flux was detected [16]. The deficit of two thirds of the flux was referred to as the solar neutrino mystery. A year later, in 1969, Pontecorvo proposed a solution; namely that neutrinos were massive particles and that they could change flavor (oscillate) while they were propagating [17]. Since the Homestake experiment was only sensitive to ν_e then the rest could have oscillated to ν_μ and ν_τ.

1.3.2 Neutrino oscillation theory

As we previously mentioned, there are three neutrino flavor eigenstates $\{\nu_e, \nu_\mu, \nu_\tau\}$, where the flavors describe the neutrino interaction with the weak force. Neutrino oscillation occurs when a neutrino with an initial flavor eigenstate i is later measured in a different flavor eigenstate j with probability amplitude P_{ij}. It happens because neutrinos are created and measured in weak interactions in flavor eigenstates but they are propagated in mass eigenstates $\{\nu_1, \nu_2, \nu_3\}$. The flavor eigenstates can be written as superpositions of the mass eigenstates using the mixing matrix, the Pontecorvo-Maki-Nakagawa-Sakata (PMNS) matrix [18]:

$$\begin{pmatrix} \nu_e \\ \nu_\mu \\ \nu_\tau \end{pmatrix} = \begin{pmatrix} U_{e1} & U_{e2} & U_{e3} \\ U_{\mu 1} & U_{\mu 2} & U_{\mu 3} \\ U_{\tau 1} & U_{\tau 2} & U_{\tau 3} \end{pmatrix} \begin{pmatrix} \nu_1 \\ \nu_2 \\ \nu_3 \end{pmatrix}. \tag{1.6}$$

The PMNS matrix can be parametrized as the product of three rotations with angles θ_{12}, θ_{13}, and θ_{23} and a CP-violation phase δ_{CP}:

$$U = \begin{pmatrix} 1 & 0 & 0 \\ 0 & c_{23} & s_{23} \\ 0 & -s_{23} & c_{23} \end{pmatrix} \begin{pmatrix} c_{13} & 0 & s_{13}e^{-i\delta_{\mathrm{CP}}} \\ 0 & 1 & 0 \\ -s_{13}e^{i\delta_{\mathrm{CP}}} & 0 & c_{13} \end{pmatrix} \begin{pmatrix} c_{12} & s_{12} & 0 \\ -s_{12} & c_{12} & 0 \\ 0 & 0 & 1 \end{pmatrix} P', \tag{1.7}$$

where $c_{lm} \equiv \cos\theta_{lm}$, $s_{lm} \equiv \sin\theta_{lm}$ and P' is the identity matrix in the Dirac case. In the Majorana case P' is:

$$P'_{\text{Majorana}} = \begin{pmatrix} 1 & 0 & 0 \\ 0 & e^{i\phi_2} & 0 \\ 0 & 0 & e^{i(\phi_3+\delta_{\text{CP}})} \end{pmatrix} \tag{1.8}$$

with two additional CP-violating phases ϕ_2 and ϕ_3.

Additional parameters that influence neutrino oscillations are the squared-mass differences $\Delta m^2_{kk'} = m^2_k - m^2_{k'}$ where m_k is the mass of the kth neutrino mass eigenstate. They come into play when calculating the probability amplitude P_{ij}. The case of a two-neutrino states will be described for convenience.

Two-neutrino case

Taking $\{\nu_e, \nu_\mu\}$ as the two neutrino-flavor eigenstates and $\{\nu_1, \nu_2\}$ as the mass eigenstates, we can write the flavor eigenstates as linear combinations of the mass eigenstates:

$$\begin{pmatrix} \nu_e \\ \nu_\mu \end{pmatrix} = \begin{pmatrix} \cos\theta & \sin\theta \\ -\sin\theta & \cos\theta \end{pmatrix} \begin{pmatrix} \nu_1 \\ \nu_2 \end{pmatrix}. \tag{1.9}$$

The propagation of a mass eigenstate (i) with energy (E_i) and momentum (p_i) can be described by:

$$|\nu_i(t)\rangle = e^{-i(E_i t - \vec{p}_i \cdot \vec{x})} |\nu_i(0)\rangle . \tag{1.10}$$

Then, the probability of finding a ν_μ at a time t after the creation of a ν_e is:

$$P_{\nu_e \to \nu_\mu} = \sin^2 2\theta \sin^2 \left(\frac{(E_2 - E_1)t}{2} \right). \tag{1.11}$$

Assuming the mass to be very small we can approximate the relativistic dispersion relation as $E_i^2 = p_i^2 + m_i^2 \approx p_i^2$. Also, each mass state has approximately the same energy ($E_i \approx E$). So we can write:

$$E_i = p_i \sqrt{1 + \frac{m_i^2}{p_i^2}} \approx E \sqrt{1 + \frac{m_i^2}{E^2}} \approx E + \frac{m_i^2}{2E}. \tag{1.12}$$

The distance travelled by the neutrino is $L = ct$ and with natural units $L = t$. Then the probability is:

$$P_{\nu_e \to \nu_\mu} = \sin^2 2\theta \sin^2 \left(\frac{(\Delta m^2_{21} L)}{4E} \right), \tag{1.13}$$

where we see that the probability is dependent on the mass splitting. This is why, by

Parameter	Best fit	$\pm 3\sigma$ range
$\sin^2\theta_{12}$	0.297	$0.250 - 0.354$
$\sin^2\theta_{23}$	0.437	$0.379 - 0.616$
$\sin^2\theta_{13}$	0.0214	$0.0185 - 0.0246$
δ/π	1.35	$0.92 - 1.99$
Δm^2_{21}	7.37×10^{-5} eV^2	$(6.93 - 7.97) \times 10^{-5}$ eV^2
$m^2_3 - (m^2_2 + m^2_1)/2$	2.50×10^{-3} eV^2	$(2.37 - 2.63) \times 10^{-3}$ eV^2

Table 1.1: Values of observed oscillation parameters of neutrino mass eigenstates with the normal hierarchy. The table was adapted from [20].

measuring this probability and the mixing angles, neutrino oscillation experiments can infer the neutrino mass splittings. Which means, that there must be at least three distinct neutrino mass values, two of which must be non-zero. The mixing angles have been measured over the years by neutrino oscillation experiments.

1.3.3 Observed parameters and neutrino oscillation experiments

The parameters of neutrino oscillations have been measured with various experiments. One of the main differences between the experiments is the creation mechanism of the neutrinos, which includes: atmospheric neutrinos, solar neutrinos, reactor neutrinos, and beam neutrinos.

Muon neutrinos are produced in the atmosphere and experiments such as Super-Kamiokande [19] measure their oscillation to electron neutrinos. The dominant atmospheric ν_μ oscillation parameters are Δm^2_{31} and θ_{23} and sometimes they are called atmospheric neutrino oscillation parameters [20].

Solar neutrinos were described in Sec. 1.3.1. The neutrino mass difference and the mixing angle primarily responsible for the solar oscillations of ν_e are Δm^2_{21} and θ_{12}, so they are called the solar mixing parameters [20].

Electron antineutrinos are produced at nuclear reactors, and at first no oscillations were found. It wasn't until the detectors were placed far away from the reactors, around 2 km apart, that oscillations were measured.

Beam neutrinos come from particle accelerator experiments. In the long-baseline experiments, neutrinos are produced when a high-energy proton beam hits a target creating pions that decay primarily into ν_μ [21].

The measured oscillation parameters include mixing angles and mass splittings. Table 1.1 contains a list of these parameters as well as their current best fit values using neutrino mass eigenstates with the normal hierarchy, which will be explained in the following section.

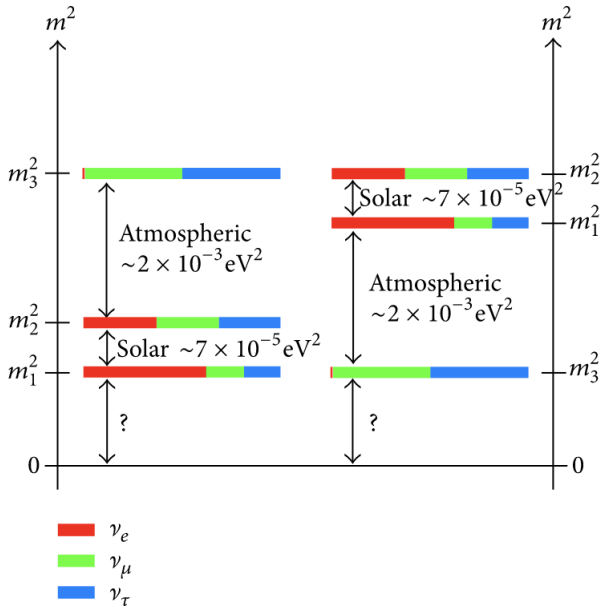

Figure 1.2: Normal (left) versus inverted (right) hierarchy of neutrino mass eigenstates. An approximation of the current best values of the mass splittings is given. The question marks refer to the offset of the smallest neutrino mass from zero, or the neutrino-mass scale. The plot comes from [23].

1.3.4 Neutrino mass splittings and ordering

Oscillation experiments give information on the mass splittings as shown in table 1.1, but the mass ordering is still unknown. Which is the heaviest mass eigenstate? Which one is the lightest? In other words, are the mass eigenstates related like $m_1 < m_2 < m_3$ (normal hierarchy) or $m_3 < m_1 < m_2$ (inverted hierarchy)? Both mass orderings are represented in Fig. 1.2 and although various experiments are currently investigating it, the neutrino ordering remains a mystery.

The relationship between m_1 and m_2 is already known from solar neutrino observations. The constraint comes from observations of matter effects in the sun, which constrain $\Delta m^2_{21} \cos 2\theta_{12} > 0$, fixing $\Delta m^2_{21} > 0$ [22].

Another neutrino parameter that is currently under investigation, represented in Fig. 1.2 by a question mark, is the offset of the smallest neutrino mass eigenstate from zero. This parameter is the neutrino mass scale.

1.4 Neutrino mass scale

The neutrino mass splitting is studied with neutrino oscillation experiments, but to study its mass scale, or the offset of the smallest neutrino mass from zero, requires separate

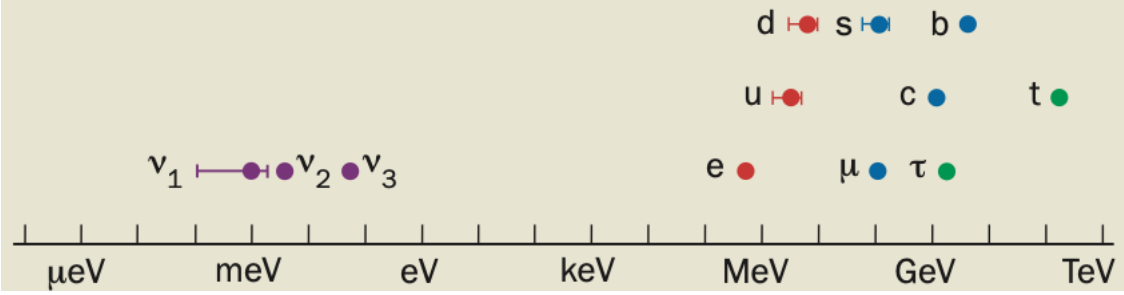

Figure 1.3: Fermion masses with their uncertainties. The mass splitting on the neutrino masses comes from oscillation experiments and it assumes normal hierarchy. The upper limit comes from other dedicated experiments. The figure was taken from [12].

methodology.

Although there is no consensus on how neutrinos get their mass, there are a lot of theories that try to explain it. And similarly, there are various experiments with the goal of measuring the neutrino masses. More details can be found in a recent review of direct measurements of neutrino mass [24].

It is not surprising that it has taken a long time and really precise experiments to study the neutrino masses since they are really small compared to the masses of the rest of the fermions as seen in Fig. 1.3. The electron, which is the fermion that is closest in mass to the neutrino, is around six orders of magnitude heavier than the neutrino.

One thing to point out about Figure 1.3 is that the neutrino mass eigenstates are represented in a hierarchical scenario, where the neutrino mass scale is extremely small and the neutrino mass splittings are significant. There is another scenario, the quasi-degenerate scenario, where the neutrino mass scale is not that small and so the three neutrino mass eigenvalues are of similar size. Both scenarios are represented in Fig. 1.4.

Some of the main methods with which neutrino mass is being studied will be discussed below.

1.4.1 Cosmological models

Cosmological observables can be modified by massive neutrinos. For example, neutrinos affect the anisotropies of the cosmic microwave background (CMB), which is electromagnetic radiation from the early universe, because they affect the distribution of large-scale structure in the universe [26]. These observables can be measured and used to improve the constraints on the sum of the neutrino masses $\sum m_\nu$. Some tools currently used to measure them are: CMB lensing, galaxy clustering, optical lensing, and Galaxy-Lensing Cross-Correlation [27].

The current best upper limit on the sum of the neutrino masses comes from data from the

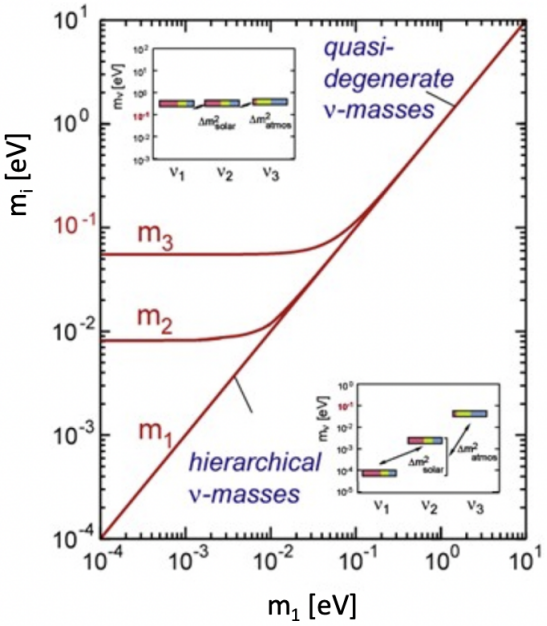

Figure 1.4: Normal hierarchical neutrino mass eigenstate scenario, where m_1 eigenvalue is small and so the atmospheric and solar splittings are significant (bottom). Quasi-degenerate neutrino mass eigenstate scenario where all mass eigenstates have similar values and the atmospheric and solar splittings are small in comparison (top). The figure was taken from [25].

Planck satellite [28]. They studied CMB anisotropies from temperature and polarization maps, combined them with baryon acoustic oscillation (BAO) measurements, and found that the sum of the neutrino masses is constrained to:

$$\sum m_\nu < 0.12\,\mathrm{eV}\,\mathrm{at}\,95\,\%\,\mathrm{CL}. \tag{1.14}$$

We have to be careful when using these results because as they state [28] the sum of the neutrino masses is partly degenerate with other parameters coming from the framework of the Lambda cold dark matter (ΛCDM) model. One such parameter is the dark energy equation-of-state parameter w. Allowing these ingredients in the Standard Model of cosmology loosens the upper bound on the sum of the neutrino masses by about a factor of three [24]. Recent analysis from cosmic surveys give similar results, but bounds obtained before Planck-18 data were weaker, for a more detailed discussion see [24]. New neutrino properties also impact the sensitivity to the sum of its mass, for example if they are unstable but very long lived, it can relaxed it one order of magnitude [24]. Since the neutrino masses are treated as a fit parameter, and there are not many cosmological parameters susceptible to laboratory measurements, getting the mass via experiments would allow better

determination of the other cosmological parameters.

1.4.2 Supernovae

Another method to extract the neutrino mass is by observing supernova neutrinos. A supernova is an explosion that occurs when a star with sufficient mass, at least five times the mass of the sun, starts collapsing after the nuclear reactions that used to counteract the force of gravity are no longer energetic enough. This happens because the fusion processes in the star produce heavier nuclei each time, and generally fusion releases less energy the heavier the nuclei. This proceeds up to iron which has the highest nuclear binding energy per nucleon [29]. The core density increases, the core heats up, and electrons and protons merge via inverse beta decay which produces neutrons and neutrinos.

The total time that it takes a neutrino of mass m_ν and energy E created in the supernova to reach earth is [30]:

$$t_{obs} - t_i = t_0(1 + \frac{m_\nu^2}{2E^2}) \tag{1.15}$$

where t_{obs} is the time at observation, t_i is the time at emission and t_0 is the time it takes light to travel from the supernova to Earth. Since the equation is energy dependent there is a time spread between neutrino arrival ($\Delta t = t_{obs2} - t_{obs1}$) for neutrinos at different energies E_1 and E_2:

$$\Delta t = \frac{t_0 m_\nu^2}{2}(\frac{1}{E_2^2} - \frac{1}{E_1^2}) \tag{1.16}$$

The current best limit for the effective electron anti-neutrino rest mass coming from observed supernova SN 1987A neutrinos was found to be less than 5.7 eV with 95 $\%$ confidence [31]. Further improvement will need new observations of a neighbourhood supernova, since the sensitivity worsens as the distance increases, where the larger time spread of the neutrinos is compensated by the loss of statistics as the distance increases. For a more detailed discussion see [24]. The JUNO experiment, currently under construction, will be sensitive to $m > 1$ eV if the supernova explosion happens in a distance of around 20 kpc [32]. The DUNE experiment, in planning phase, also estimated similar sensitivity of $m > 0.5$ eV [33].

1.4.3 Neutrinoless double beta decay

A $\beta\beta$-decay refers to the rare process in which a nucleus undergoes two simultaneous β-decays. The most common $\beta\beta$-decay occurs when two neutrons in the nucleus are converted to protons and the emitted particles are two electrons and two $\overline{\nu}_e$ ($2\nu\beta\beta$). It is a rare process, but it has been observed in numerous nuclei, a review together with the nuclei

half-life can be found in [34] . Some of the experiments that have observed it are: NEMO-3 [35], GERDA [36], and EXO-200 [37], etc.

If neutrinos are their own antiparticles (Majorana particles) then a neutrinoless $\beta\beta$-decay ($0\nu\beta\beta$-decay) would be allowed. In this case, one emitted neutrino would be absorbed by the other decaying nucleon (light neutrino exchange) and all the energy of the decay would go to the pair of electrons. The manifestation of the $0\nu\beta\beta$-decay would be a spike of events at the endpoint of the $\beta\beta$-decay energy spectrum.

It is possible to get the neutrino mass from the $0\nu\beta\beta$-decay because the observable rate ($\Gamma^{0\nu}_{\beta\beta}$) is proportional to the effective Majorana mass $\langle m_{\beta\beta}\rangle^2 = |\sum_i U^2_{ei} m_{\nu_i}|^2$ [20]:

$$\Gamma^{0\nu}_{\beta\beta} = (T^{0\nu}_{1/2})^{-1} = G^{0\nu} \cdot |M^{0\nu}|^2 \cdot \langle m_{\beta\beta}\rangle^2, \tag{1.17}$$

where $T^{0\nu}_{1/2}$ is the half life, $G^{0\nu}$ is the phase space and $M^{0\nu}$ is the nuclear matrix element.

$0\nu\beta\beta$-decay has not been observed but numerous experiments are currently looking for it. There are also some next-generation experiments in the planning and design phase, such as LEGEND [38] and nEXO [39]. The current best limit on $\langle m_{\beta\beta}\rangle^2$ is in the range of 61 - 165 meV at 90 $\%$ CL, and it comes from the KamLAND-Zen experiment studying ^{136}Xe [40]. The big range in the result comes from uncertainties in the nuclear matrix element, so even if $0\nu\beta\beta$-decay is detected it will still be difficult to extract an accurate neutrino mass.

1.4.4 Direct beta-decay kinematic methods

One direct kinematic method that can be used to study neutrino mass consists of studying the β-electron produced in β-decay. The neutrino mass can be extracted by fitting the end point region of the β-energy spectrum and leaving the neutrino mass as a free parameter. This is shown for a tritium β-energy spectrum in figure 1.5.

A few nuclei have been used to study neutrino mass via β-decay. Currently, the most popular one is tritium (^{3}H) because:

- It has a relatively low Q-value $\approx$ 18.6 keV (total kinetic energy released in the decay). This is desirable because the effect of the neutrino mass is most clearly seen near the end point of the β energy spectrum, and a low Q-value means that a larger fraction of these events fall within this sensitive region.

- The decay daughter atom ^{3}He has relatively simple molecular excitation energies, which can be predicted by theory as will be discussed in section 1.5

- It has a half life of 12.3 years [42] allowing high-activity sources to be constructed. This contrasts with other isotopes like ^{187}Re with a half-life of around 4.1×10^{20}

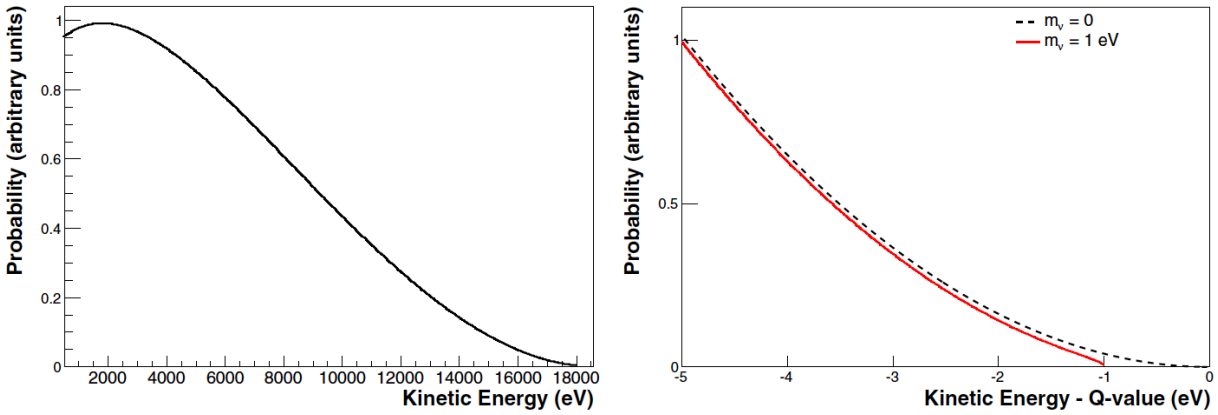

Figure 1.5: Beta spectrum of tritium decay with the effective electron anti-neutrino mass of $m_\nu = 1$ eV for the full spectrum (left) and the last 5 eV before the end point (right). The dotted line represents the spectrum for the $m_\nu = 0$ eV case. The figure was taken from [41].

years [23], and ^{163}Ho where electron capture half-life is of around 4570 years [43].

One technique used to study the β-energy spectrum is the MAC-E filter technique. Since this thesis relies heavily on the study of the effective neutrino mass from molecular tritium (TT) β-decay via the MAC-E filter technique, a dedicated section (Sec. 1.5) explains the decay theory with more detail and gives a time line of the experiments that measure the β-energy spectrum using the MAC-E filter. Besides that, Sec. 4.1 explains the working principle of a MAC-E filter.

Most experiments use TT molecules to study the neutrino mass because T atoms interact and form bonds. It becomes difficult to have a source of lone T atoms. Nevertheless Project8 [44] is developing an atomic tritium source, to get the β energy spectrum via cyclotron radiation. An electron with kinetic energy K in a magnetic field B will have a cyclotron frequency (f) of:

$$f = \frac{1}{2\pi} \frac{eB}{m_e + K} \tag{1.18}$$

where m_e is the electron mass and e its charge. Hence by measuring the frequency of the electron, its energy can be determined.

Another technique used to study the β-energy spectrum consists of using micro-calorimeters [23]. In modern experiments, the type of β-decay that occurs in the calorimeters is electron-capture decay[1]. The energy is reconstructed by measuring the change in temperature inside a calorimeter. A small quantity of β-decay isotope is set in the micro-calorimeter to

[1] An electron-capture decay is a process where a nuclear proton absorbs an inner atomic electron. This changes the nuclear proton to a neutron and an electron neutrino is emitted.

avoid pile-up and to achieve a good energy resolution. Large numbers of small microcalorimeters are necessary to have enough statistics. Two experiments that use this technique are ECHo [45] and HOLMES [46], and they use ^{163}Ho as the decay isotope.

1.5 TT beta decay theory

TT beta decay is a T decay in which the decaying nucleus is bound in a TT molecule. In this section we present a theoretical calculation of the β-energy spectrum (Sec. 1.5.1). We describe the molecular final state distribution in detail since, to first order, an error in the final state distribution variance will shift the extracted squared neutrino mass with a factor of 2 penalty (Sec. 1.5.2). We evaluate the validity of the used theory to calculate the final state distributions (Sec. 1.5.3) and we present the Tritium Recoil Ion Mass Spectrometer (TRIMS) experiment whose results are used to corroborate the theory (Sec. 1.5.4).

1.5.1 Theoretical β-decay spectrum

The β-decay rate to a final state f can be calculated using Fermi's Golden rule by summing and integrating over the discrete and continuous final states f:

$$N = 2\pi \sum \int |T_f(E)|^2 df, \tag{1.19}$$

where natural units are used ($c = \hbar = 1$), and $|T_f(E)|^2$ is the transition matrix to the final state f. In TT β-decay, there are three particles in the final state, the daughter molecule, the β-electron, and the neutrino.

The decay rate to a fixed final state f of the daughter molecule ^{3}HeT$^+$ at a given β-electron energy E is calculated by integrating over the neutrino final states and the electron directions [47, 48]:

$$\begin{aligned} N_f(E) = \frac{|T_f(E)|^2}{2\pi^3}(E + m_e)\sqrt{(E + m_e)^2 - m_e^2} \\ \times \varepsilon_f(E)\sqrt{\varepsilon_f(E)^2 - m_\nu^2} \cdot \Theta(\varepsilon_f(E) - m_\nu), \end{aligned} \tag{1.20}$$

where m_e is the β-electron mass, and m_ν is the neutrino mass. The energy of the neutrino ($\varepsilon_f(E)$) has energy conservation enforced by the Heaviside function $\Theta(\varepsilon_f(E) - m_\nu)$.

The transition matrix $|T_f(E)|^2$ can be factorized in the sudden approximation, the validity of which is demonstrated in [49], as [47]:

$$|T_f|^2 = |T_f^{\text{weak}}|^2 |T_f^{\text{lep}}|^2 |T_f^{\text{mol}}|^2, \tag{1.21}$$

and the factors are explained in the following paragraphs. The weak part $|T_f^{\text{weak}}|^2$ does not depend on the electron energy for the superallowed T β-decay.

The leptonic part $|T_f^{\text{lep}}|^2$ partially incorporates the Coulomb interactions between the electron and the daughter nucleus charge Z':

$$|M_f^{\text{lep}}|^2 \propto F(E, Z' = 2), \tag{1.22}$$

where $F(E, Z' = 2)$ is the Fermi function.

The molecular part, $|T_f^{\text{mol}}(E)|^2$, accounts for the probability P_f of the daughter molecule $^3\text{HeT}^+$ to be in a molecular, electronic, vibrational and rotational final state f with energy V_f. Calculating the probability P_f to the final state distribution is rather challenging and will be further discussed in section 1.5.2 .

After calculating $|T_f(E)|^2$ by summing over the allowed nuclear states and the included molecular states, we can derive from equation 1.20:

$$\begin{aligned} N(E) = C|M_{\text{nuc}}|^2 F(E, Z' = 2)(E + m_e)\sqrt{(E + m_e)^2 - m_e^2} \\ \times \sum_{f \in \text{mol}} P_f \varepsilon_f(E) \sqrt{\varepsilon_f(E)^2 - m_\nu^2} \cdot \Theta(\varepsilon_f(E) - m_\nu), \end{aligned} \tag{1.23}$$

where $|M_{\text{nuc}}|^2$ is the nuclear matrix element for the transition, and:

$$C = \frac{G_F^2 \cos^2 \theta_c}{2\pi^3}, \tag{1.24}$$

where G_F is the Fermi constant, and θ_c is the Cabibbo angle.

The neutrino energy $\varepsilon_f(E)$ is modified by the molecular excitation energies (V_f) of the daughter molecule as:

$$\varepsilon_f(E) = E_0 - V_f - E, \tag{1.25}$$

where the reduced end point (E_0) is the maximum electron kinetic energy in the case of a massless neutrino.

Equation 1.23 is plotted in Fig. 1.5. In the right plot of Fig. 1.5 it can be seen that the shape of the β-spectrum is especially affected by the effective electron anti-neutrino mass near the end point. In reality, the spectrum is distorted by the three neutrino mass eigenstates. However, if the mass splittings are not experimentally resolvable, then the neutrino squared mass (m_ν^2) observable is the incoherent sum of the squared mass eigenstates:

$$m_\nu^2 = m(\overline{\nu}_e)^2 = \sum_{i=1}^{3} |U_{ei}|^2 m_{\nu_i}. \tag{1.26}$$

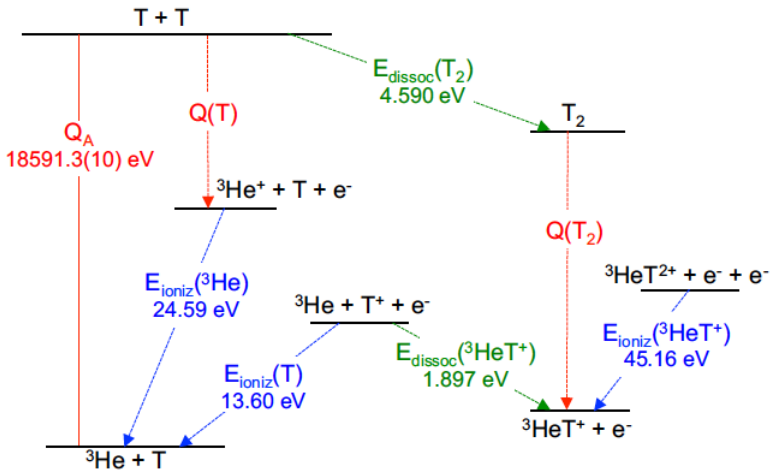

Figure 1.6: Energy levels of the decay of molecular and atomic tritium [41]. The values of the binding energies can be found in [41].

As a first order approximation Eq. 1.23 is correct, but for high precision, higher order corrections are needed [50]. One such correction comes into play because the calculation is done in a center-of-mass framework which is almost, but not the same, as the framework centered on the decaying molecule. In a molecule the atoms are moving, which causes Doppler broadening. The Doppler corrections can be treated by using a relativistic framework for a three body system. A calculation of the lepton phase-space density with such considerations was performed in [51] and in [52, 53]. The binding energies are also needed for this calculation, which refers to the energy released in removing a particle from a system of particles. A compendium of the relevant binding energies is shown in Fig. 1.6.

Corrections to the inputs of Eq. 1.23 are also done. For example, while deriving the electron-neutrino phase space, the mass of the nucleus is considered to be infinite. The energy used for the electronic excitations is unavailable for the outgoing leptons, the modification of the lepton phase space is captured in the V_f terms that come into play while calculating the electron energy. However, the calculation of the rotational and vibrational excitations becomes limited by the approximation of the recoil mass.

Modern theoretical calculations of the β-decay use the geminal-basis method. It was developed by Kolos and Wolniewicz, who described a hydrogen molecule with a basis set of correlated two-electron wave functions [54].

1.5.2 Final-state distribution

A TT molecular state is defined by electronic (n), rotational (J), vibrational (v), and azimuthal (M) quantum numbers. Another challenge that we face when using Eq. 1.23 is to

calculate the probability P_{if} of transitioning from the initial molecular state $i \equiv n, J, v, M$ to the final state $f \equiv n_f, J_f, v_f, M_f$:

$$P_{if} = |T_f^{\rm mol}(E)|^2 = |\left\langle \Psi_f^{^3{\rm HeT}^+} \right| e^{i\vec{K}\cdot\vec{R}} \left| \Psi_i^{\rm TT} \right\rangle|^2, \tag{1.27}$$

where $\Psi_f^{^3{\rm HeT}^+}$ and $\Psi_i^{\rm TT}$ are the wave functions of the daughter ($^3{\rm HeT}^+$) and the parent (TT) molecules, $\vec{K}$ is the recoil momentum and $\vec{R}$ is the nuclear separation.

The Schrödinger equation has to be solved to calculate the states of the initial and final molecular systems. For this calculation, the reduced mass[2] of the daughter molecule is needed. Coxon and Hajigeorgiu obtained the best reduced mass by comparing predicted energy levels with spectroscopic measurements [55]. Doss *et al.* used this result in their calculation of the final state distribution [56].

The spectrum of final state molecular excitations can be theoretically calculated. Figure 1.7 shows this spectrum calculated by Saenz *et al* (in 2000) [57] compared to the one calculated by Fackler *et al* (1985) [58]. The large peak centered at 0.2 eV binding energy is the electronic ground state and it is broadened by rotational and vibrational excitations. The continuum spectrum below ≈ -15 eV corresponds to the electronic exited states modified by rotational and vibrational excitations. There have been great improvements in the newest results, especially below -45 eV binding energy. KATRIN uses a combination of Saenz [57], Doss [56], and small recent corrections [47].

Since the molecular excitations of the final-state molecule of TT β-decay play a role in the calculation of the β-energy spectrum (Eq. 1.23), it is important to validate the theory that is used to calculate them. It is of special importance for neutrino mass experiments since the final-state distributions have a big impact on the neutrino mass. As an example consider the following historical case. Two neutrino-mass experiments LANL [59] and LLNL [60] originally reported a negative m_ν^2 using the final state distribution theory of Fackler *et al.* Robertson and Knapp had previously demonstrated that the extracted neutrino-mass squared is modified by the neglected contributions to the variance of the FSD ($\Delta\sigma^2_{\rm FSD}$) as [61]:

$$\Delta m_\nu^2 \simeq -2\Delta\sigma^2_{\rm FSD}. \tag{1.28}$$

Applying this rule to estimate the effect of using the later Saenz *et al.* theory, gives m_ν^2 closer or consistent with zero [41].

[2]The reduced mass is the effective mass in the two body problem, which allows us to treat it as a one-body problem.

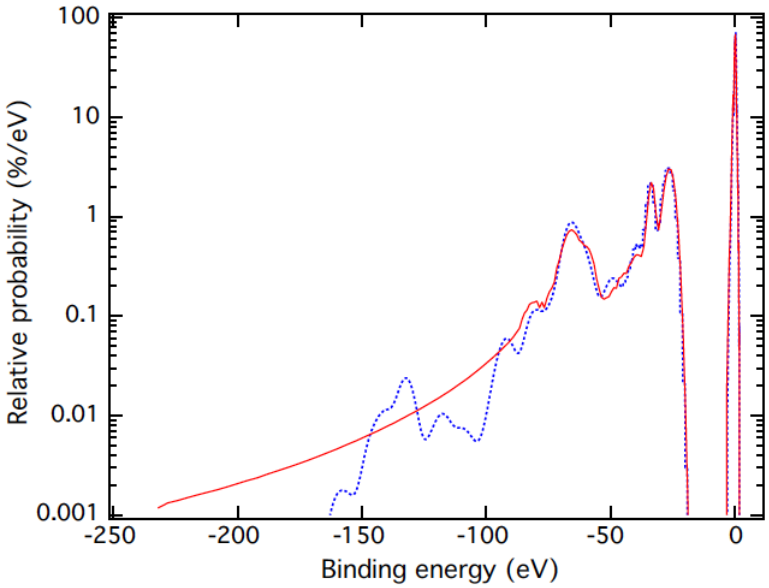

Figure 1.7: Spectrum of the final state molecular excitation of TT β-decay as calculated by Saenz *et al* (red solid line) [57] and by Fackler *et al* (dotted blue line) [58]. For displaying purposes, a Gaussian profile with a standard deviation of 3 eV was given to the discrete states of the spectrum calculated by Fackler *et al*. The figure was taken from [41].

1.5.3 Validity of the theory and disagreements with experimental results

It is not feasible to directly measure the rotational and vibrational excitations of the daughter molecule after β-decay because they are often in the sub-eV energy range, and because the time scale for further evolution is not known [41]. That is why other observables, calculated with the same theory, are used for tests. For example, the rotational and vibrational level transitions of both parent and daughter molecules, which can be measured with high precision spectroscopy, agree quite well with the theory, for example see: [62, 63, 64, 65].

Another observable is the branching ratio to the various possible molecular and atomic species. TT can β-decay in different channels as listed in table 1.2. The decay channels have different probabilities that can be calculated with theory or measured with experiments.

In the 1950s two experiments measured the branching ratio to the bound-state daughter molecule of HT β-decay ($^3HeH^+$) [66, 67], and of TT β-decay [67] ($^3HeT^+$). Using the same theory as Saenz *et al.*, theoretical calculations were carried out by Jonsell *et al.* [68], giving results that strongly disagree with the experimental results. These results are compared in table 1.3. The big range on the theoretical results comes from the bounds on the dissociation of the quasi-bound final state molecule. In other words, it comes from the fact we don't know whether quasi-bound states dissociate within the time-scale of the

i	Decay channel
No electron	
1.	^{3}He + T
One electrons	
2.	^{3}HeT$^+$ + e^-_β
3.	^{3}He$^+$ + T + e^-_β
4.	^{3}He + T$^+$ + e^-_β
5.	^{3}He^{++} + T$^-$ + e^-_β
Two electrons	
6.	^{3}He$^+$ + T$^+$ + e^-_β + e^-_{so}
7.	^{3}He^{++} + T + e^-_β + e^-_{so}
Three electrons	
8.	^{3}He^{++} + T$^+$ + e^-_β + 2e^-_{so}

Table 1.2: Possible final states of TT molecule β-decay excluding the neutrino; e^-_β refers to the β-electron and e^-_{so} refers to shakeoff electrons [69].

Molecule	Theory [68]	Snell *et al.* [66]	Wexler *et al.* [67]
HT	0.55 - 0.57	0.932(19)	0.895(11)
TT	0.39 - 0.57	-	0.945(6)

Table 1.3: Comparison of branching ratios to the bound molecular state from theory and experiments. Table inspired by [41].

measurement.

To reconcile the experimental data with the theory calculations a new experiment was needed.

1.5.4 The TRIMS experiment

The goal of the TRIMS (Tritium Recoil Mass Spectrometer) experiment is to measure the branching ratio to the bound molecular state of HT and TT β-decay, utilizing a different method from the previous experiments, to resolve this discrepancy.

The experimental set-ups of Snell *et al.* and Wexler *et al.* experiments each consisted of a mass spectrometer with a ring electrode to focus ions into a magnetic analyser followed by an electron multiplier [70]. The experimental set-up of the TRIMS experiment consists of a decay chamber with electric and magnetic fields to accelerate and guide the charged particles toward an electron and an ion detector at opposite ends. A dedicated chapter explains this in more detail (Chapter 2).

1.6 TT neutrino mass experiments

There is a long list of experiments that have used tritium β-decay to measure the effective neutrino mass [24]. In this section I will mention a few highlights. Bergkvist [71] measured $m_\nu < 55$ eV in the 1970s, and was the first to note that a good understanding of the excitations of the daughter nucleus was necessary to improve the results.

Los Alamos National Laboratory then constructed a TT gas source and improved the limit to $m_\nu < 9.3$ eV at the 90% confidence level [59, 72] based on a negative central value of m_ν^2. Another experiment at Lawrence Livermore National Laboratory (LLNL) also reported a negative central value with better statistical uncertainty [60]. Other experiments had similar results, that is electron-neutrino mass consistent with zero but a negative best-fit squared mass [73, 74]. Motivated by these results, new calculations of the final excitation states of the TT β-decay were calculated by Saenz [57] as mentioned in Sec. 1.5.

The next improvement on the electron neutrino mass came from a pair of experiments in the late 1990s and the early 2000s using a new kind of spectrometer: the Magnetic Adiabatic Collimation with Electrostatic (MAC-E) filter, which filters high-energy electrons with an unprecedented precision (Sec. 4.1). The Mainz experiment had a condensed TT source where solid state effects came into play. They published a final result of $m_\nu < 2.3$ eV at the 95% confidence level [75]. The Troitsk experiment used a gaseous TT source and published $m_\nu < 2.05$ eV at the 95% confidence level [76].

1.6.1 The KATRIN experiment

The current best limit on the effective electron neutrino mass comes from the KATRIN experiment at $m_\nu < 0.8$ eV at the 90% confidence level, based on the first two measurement campaigns [77]. The desired sensitivity is $m_\nu < 0.2$ eV at the 90% confidence level and they expect to achieve it after five calendar years.

The experiment has a gaseous TT source and it uses the MAC-E filter method previously mentioned. Most of the results that this thesis will cover come from data taken by the KATRIN experiment, and a more in-depth explanation of how the experiment works is given in chapter 4.

CHAPTER 2
THE TRIMS EXPERIMENT

TT β-decay is used in various neutrino experiments to measure the effective $\overline{\nu}_e$ mass. A precise knowledge of the β-energy spectrum (Eq. 1.23) is necessary to fit the experimental data and extract the mass. Electronic, vibrational and rotational final-state excitations modify the β-energy spectrum (Sec. 1.5). The excitations cannot be measured but they can be calculated with theory. Hence, to test the validity of the theory, other predicted quantities are measured (Sec. 1.5.3).

The main objective of the Tritium Recoil Ion Mass Spectrometer (TRIMS) experiment is to measure one of these quantities, which has a significant disagreement between its theoretically predicted value and previous experimental results. The aforementioned quantity is the branching ratio of HT and TT β-decay to the bound molecular final states $^3HeH^+$ and $^3HeT^+$ respectively. In this chapter we will discuss the TRIMS apparatus (Sec. 2.1) and the main analysis technique (Sec. 2.2) developed primarily by Ying-Ting Lin [78]; my own contributions to the analysis will be discuss in detail in chapter 3. A first result on the HT branching ratio to $^3HeH^+$ of 56.5(6)% is in accordance with the theory and disagrees with the previous experimental results [79].

2.1 The TRIMS apparatus

The TRIMS experiment is a time-of-flight mass spectrometer that consists of a decay chamber where the source β-decays (Sec. 2.1.1). A sketch of the experiment is shown in Fig. 2.1. Magnetic fields guide the charged particles towards the ion- and electron- detectors (Sec. 2.1.2), while electric fields accelerate them. The source has two main operational modes with sources consisting of different mixtures of HT and TT gas (Sec. 2.1.3). A more in-depth description of the apparatus can be found in [78].

2.1.1 The decay chamber

Gaseous TT and HT β-decay in a cylindrical chamber of length L = 0.235 m and diameter D = 0.102 m known as the decay chamber or the acceleration chamber. It consists of an acceleration column built by the National Electrostatics Corporation (NEC). It is made up by alternating conducting Kovar alloy rings with insulating alumina rings. There is a

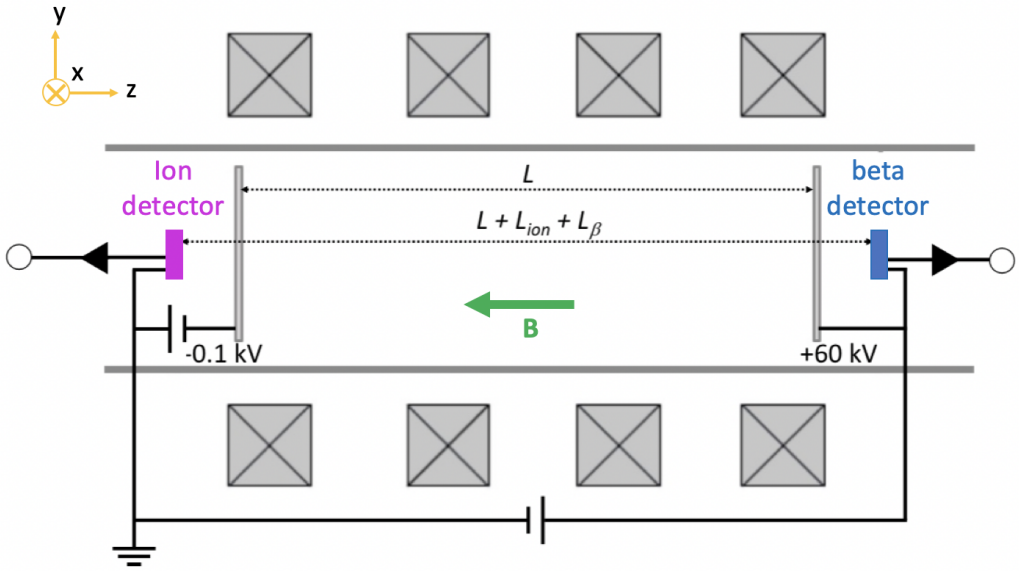

Figure 2.1: Sketch of the TRIMS experimental apparatus. The source β-decays inside the decay chamber, and charged particles are accelerated towards the ion detector (positive particles) and the beta detector (negative particles). They are guided by the magnetic field of approximately 0.2 T and accelerated by the electric potential of 60 kV. The triangles represent the pre-amplification stages. The sketch is based on a figure from [69]

.

uniform voltage gradient between the two electrodes positioned at each end of the chamber. The potential difference is 60 kV and the voltage is applied at the anode (beta) side while the cathode (ion) side is grounded. A magnetic field of 0.236 T is produced by four external magnet coils that surround the decay chamber. The side view sketch of the experiment shown on Fig. 2.1 indicates the general coordinate reference used throughout the analysis via the vectors at the upper left corner: $\vec{x}$, $\vec{y}$, and $\vec{z}$.

The detectors are positioned behind the electrodes. The β detector sits behind a gold-plated stainless-steel disk with an opening in the center through which the detector can view the decay chamber. The ion detector sits behind a stainless-steel mesh which lets through around 85 % of the ions. The mesh also serves the purpose of blocking secondary electrons coming from the ion detector, because it is electrically isolated from the rest of the experiment and it is set to -100 V. In Fig. 2.2 we can see a model of the acceleration chamber, the detectors, the electrodes and the magnets.

The decay chamber is in ultra-high vacuum, and the base pressure is 3.5×10^{-9} Torr.

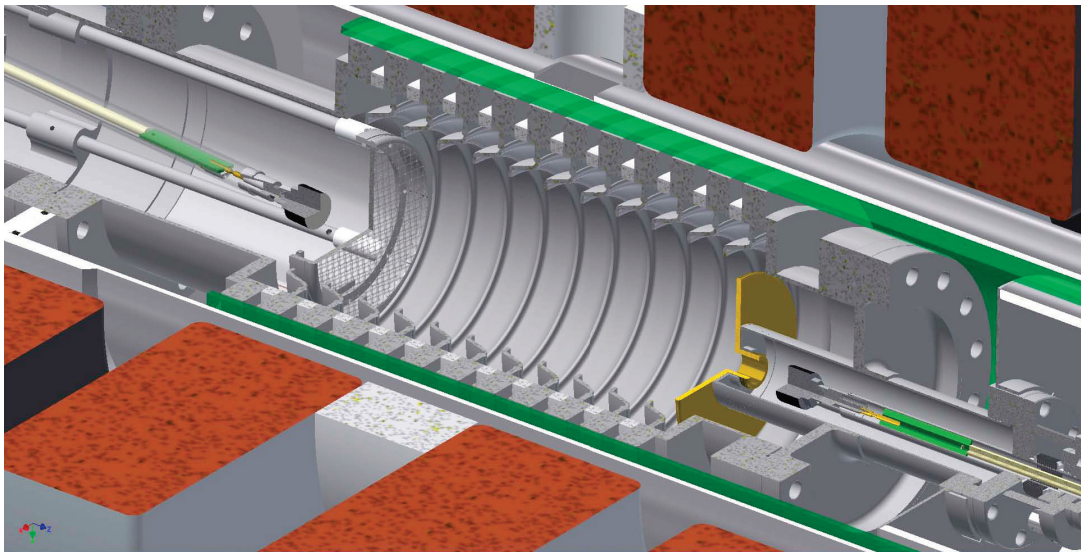

Figure 2.2: Cross-section view of the decay chamber with the electrodes and detectors on each end. The ion detector is depicted on the left behind the mesh, and the β detector is depicted on the right, behind the gold-plated disk. The decay chamber is surrounded by an insulating silica tube, an aluminium tube and the magnetic coils. Figure from [79]

2.1.2 The silicon detectors and scan motion

The two silicon detectors were made by Canberra (type PD50-11-500AM). They have an active area of 50 mm^2 and a thickness of 0.5 mm. Their dead layer is specified to be 50 nm, which means that the energy deposited by the particles in the first 50 nm is not recovered by the pre-amplifier.

Each detector is mounted on a re-entrant tube with a custom preamp directly on the feedthrough pin. Waveforms for both ion- and β- detector channels are recorded in a digitizer on each singles trigger. Both detectors can be displaced; the motion is achieved because each detector is positioned at the end of a bellows. Although the β-detector can be moved, it was always stationary during the measurements, and it was positioned behind the hole at the center of the gold-plated disk. Both detectors and their mounts can be seen in Fig. 2.2.

The ion-detector Y-position is changed by adjusting the translation stage up and down. The X-position is adjusted by a micrometer attached to a bellows that moves the whole translation stage left and right.

In TRIMS, the data was taken by performing scans with the ion detector moving in the X-direction. The scan was performed in the following manner:

- The ion detector started at the home-position (X_0), determined to be at 80 mm in the micrometer.

- For a right-scan, the detector was moved ten steps of 1.1 mm each, until it reached scan position X_{10} located 11 mm to the right.
- For a left-scan, the the detector was moved to the left in a similar manner until scan position X_{-10} was reached.
- At each scan position, a run was taken. In the TRIMS context, a run is a continuous data-taking period of 300 s, where the recorded data comes from the ion- and β-detectors.
- A complete scan consisted of 21 positions (X_i with $i \in$ [-10, 10]) of the ion detector where a run was taken.

2.1.3 The HT and TT sources

There were two main source modes during data-taking in the TRIMS experiment. Both source modes contained a combination of HT and TT gas, in the "high-TT " mode TT gas predominated, and in the "high-HT" mode HT gas predominated. The decay chamber operated at a pressure of order 10^{-8} mbar which corresponds to a count rate of approximately 200 cps in our detectors.

The TT gas came from a commercially filled cylinder via a leak valve that was closed once the desired pressure was reached. The HT gas came in a more convoluted way. It was created by TT reactions with the HH outgasing from the walls and it was catalyzed by platinum group metals which are present in the experiment in auxiliary gauge filaments. The TT conversion to HT was completed in around 10 minutes, and the valve to the auxiliary gauges was closed when a "high-TT" mode was desired.

2.2 Main analysis technique

The TRIMS main analysis was carried out for two main data sets: high-HT data and high-TT data. First a data quality check was done to all the raw-data (Chapter 3). The data was displayed in a ion time-of-flight versus ion energy plot where it was possible to distinguish the decay channels (Sec. 2.2.1). Then, the ion charge and mass were reconstructed and plotted (Sec. 2.2.2). From these plots it was possible to separate the events of each decay channel; nevertheless contamination between channels occurred, and it was corrected in the analysis (Sec. 2.2.3).

2.2.1 Ion energy and time of flight

The ion time of flight ($T_{\rm ion}$), or the time that it takes an ion to travel from the decay position to the ion detector, was reconstructed as follows:

$$T_{\rm ion} = t_{\rm ion} - (t_\beta - \overline{T}_\beta) - \Delta t_0 \tag{2.1}$$

where $t_{\rm ion}$ is the time at which the ion signal was detected; t_β is the time of the β signal; and the rest are correction parameters. $\overline{T}_\beta \approx 2.3$ ns is the mean β time of flight from simulation, and Δt_0 is the electronic offset between ion and electron signals.

The energy scale of each detector was calibrated with four different sources all giving consistent results. Corrections for the dead layer, the backscattered ions and the transmitted ions were taken into account as will be shown in chapter 3.

The high-HT data and the high-TT data were plotted in a ion energy versus ion time-of-flight plot shown in Fig. 2.3. It is possible to distinguish the different decay channels by looking at the bands. Other data structures come from interactions of the ions and electrons with the apparatus and a more detailed explanation is shown in table 2.3.

Tables 2.1 and 2.2 relate the labels of Fig. 2.3 with the decay channels that they correspond to from high-HT data and high-TT data respectively. The neutrally charged decay branches can't be detected with the TRIMS experiment but they correspond to a low percentage of the total decays; Bahcall estimated the rate, for a bare tritium nucleus, to be around 0.69% [80]. Some branches have more than one detection channel since there are different particle combinations that can be detected and still produce an event; an event corresponds to a coincidence signal in both the ion- and the β- detectors. The detection channel column can be read as follows: it starts with the decay molecule (HT or TT), then the particles that are detected are written between the parentheses, and finally the particles from the decay that are not detected are on the right of the parentheses; $e^-_{\rm so}$ refers to the shake-off electrons. Since neutrinos are never detected they are omitted. As we see in Tables 2.1 and 2.2 there are some overlapping band structures like a2 since both beta decays (HT and TT) have a final state with a mass-3 ion, while band a1 is unique to HT because of the mass-1 ion final state and band a4 is unique of TT decay because of the mass-6 ion final state.

2.2.2 Charge and mass reconstruction

To better separate the decay populations, the ion charge and mass were reconstructed as follows.

In TRIMS the effective charge ($Q_{\rm ie}$) is defined as the number of free electrons in the

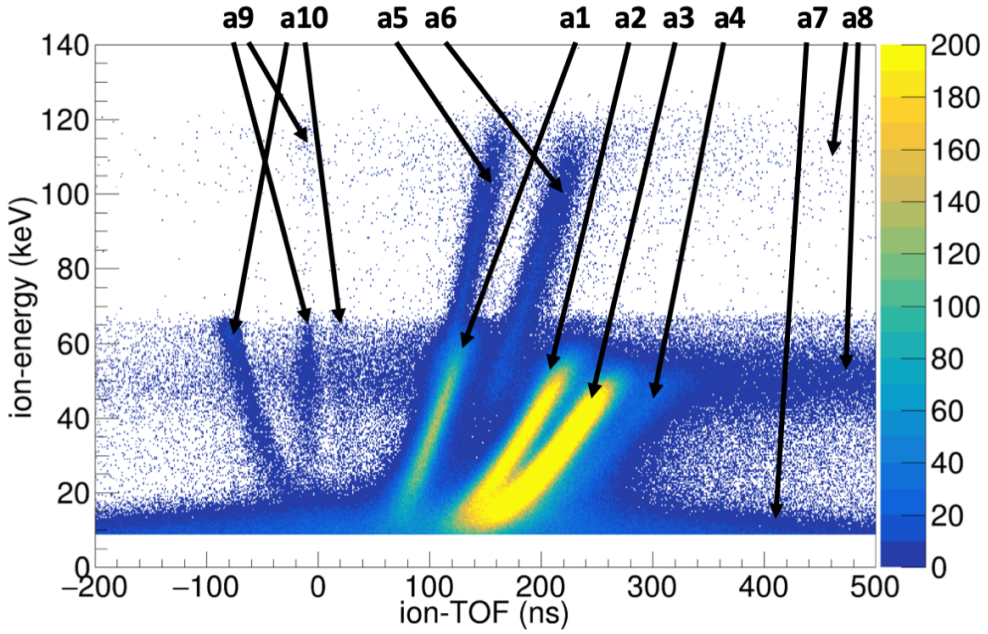

(a) High-HT data set

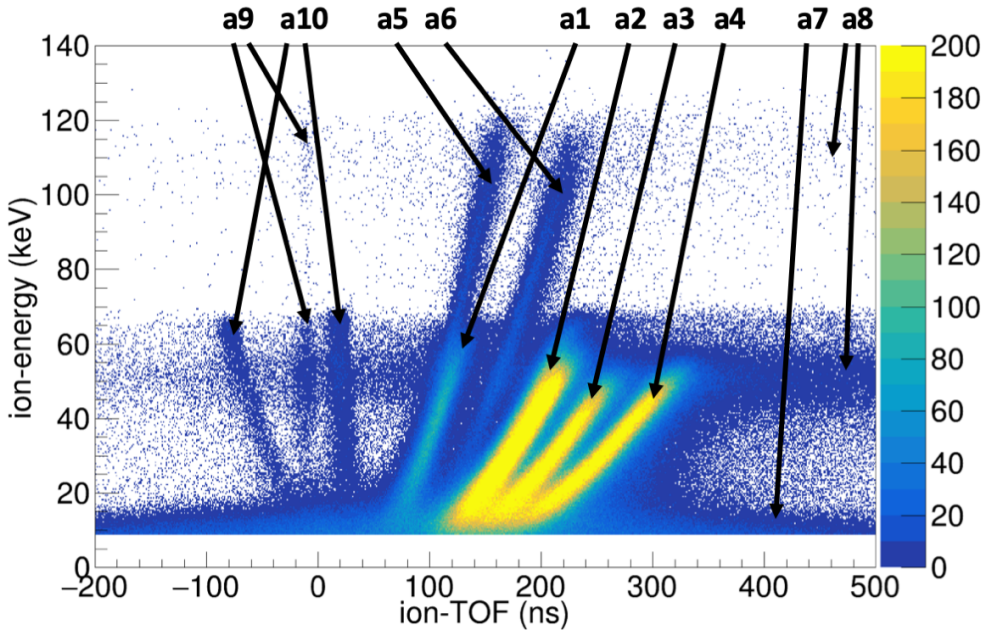

(b) High-TT data set

Figure 2.3: Histograms of ion energy versus ion time of flight of the high-HT data set (a), and the high-TT data set (b). The labels on top refer to the decay channel or the detection channel of each band, and their explanations can be found in tables 2.1, 2.2 and 2.3. Plots from [78].

Figure label	Decay Branch	Detection Channel
–	$\mathrm{He} + \mathrm{H}$	–
a3	$\mathrm{HeH}^+ + \beta^-$	HT($\mathrm{HeH}^+ + \beta^-$)
a2	$\mathrm{He}^+ + \mathrm{H} + \beta^-$	HT($\mathrm{He}^+ + \beta^-$)H
a1	$\mathrm{He} + \mathrm{H}^+ + \beta^-$	HT($\mathrm{H}^+ + \beta^-$)He
a6	$\mathrm{He}^+ + \mathrm{H}^+ + \beta^- + e^-_{so}$	HT($\mathrm{He}^+ + \mathrm{H}^+ + \beta^- + e^-_{so}$)
a6		HT($\mathrm{He}^+ + \mathrm{H}^+ + \beta^-$)$e^-_{so}$
a2		HT($\mathrm{He}^+ + \beta^- + e^-_{so}$)$\mathrm{H}^+$
a1		HT($\mathrm{H}^+ + \beta^- + e^-_{so}$)$\mathrm{He}^+$
a2		HT($\mathrm{He}^+ + \beta^-$)$\mathrm{H}^+ + e^-_{so}$
a1		HT($\mathrm{H}^+ + \beta^-$)$\mathrm{He}^+ + e^-_{so}$
a5	$\mathrm{He}^{++} + \mathrm{H} + \beta^- + e^-_{so}$	HT($\mathrm{He}^{++} + \beta^- + e^-_{so}$)H
a5		HT($\mathrm{He}^{++} + \beta^-$)H $+e^-_{so}$
a5	$\mathrm{He}^{++} + \mathrm{H}^- + \beta^-$	HT($\mathrm{He}^{++} + \mathrm{H}^- + \beta^-$)
a5		HT($\mathrm{He}^{++} + \beta^-$)$\mathrm{H}^-$
–	$\mathrm{He}^{++} + \mathrm{H}^+ + \beta^- + 2e^-_{so}$	HT($\mathrm{He}^{++} + \mathrm{H}^+ + \beta^- + 2e^-_{so}$)
–		HT($\mathrm{He}^{++} + \mathrm{H}^+ + \beta^- + e^-_{so}$)$e^-_{so}$
–		HT($\mathrm{He}^{++} + \mathrm{H}^+ + \beta^-$)$e^-_{so}$
–		etc, but small

Table 2.1: Decay branch and detection channels for HT decay in TRIMS. Some channels can be related by the figure labels to the bands in figure 2.3a. Table adapted from [79].

Figure label	Decay Branch	Detection Channel
–	$\mathrm{He} + \mathrm{T}$	–
a4	$\mathrm{HeT}^{+} + \beta^{-}$	TT($\mathrm{HeT}^{+} + \beta^{-}$)
a2	$\mathrm{He}^{+} + \mathrm{T} + \beta^{-}$	TT($\mathrm{He}^{+} + \beta^{-}$)T
a2	$\mathrm{He} + \mathrm{T}^{+} + \beta^{-}$	TT($\mathrm{T}^{+} + \beta^{-}$)He
a6	$\mathrm{He}^{+} + \mathrm{T}^{+} + \beta^{-} + e^{-}_{so}$	TT($\mathrm{He}^{+} + \mathrm{T}^{+} + \beta^{-} + e^{-}_{so}$)
a6		TT($\mathrm{He}^{+} + \mathrm{T}^{+} + \beta^{-}$)$e^{-}_{so}$
a2		TT($\mathrm{He}^{+} + \beta^{-} + e^{-}_{so}$)$\mathrm{T}^{+}$
a2		TT($\mathrm{T}^{+} + \beta^{-} + e^{-}_{so}$)$\mathrm{He}^{+}$
a2		TT($\mathrm{He}^{+} + \beta^{-}$)$\mathrm{T}^{+} + e^{-}_{so}$
a2		TT($\mathrm{T}^{+} + \beta^{-}$)$\mathrm{He}^{+} + e^{-}_{so}$
a5	$\mathrm{He}^{++} + \mathrm{T} + \beta^{-} + e^{-}_{so}$	TT($\mathrm{He}^{++} + \beta^{-} + e^{-}_{so}$)T
a5		TT($\mathrm{He}^{++} + \beta^{-}$)T $+e^{-}_{so}$
a5	$\mathrm{He}^{++} + \mathrm{T}^{-} + \beta^{-}$	TT($\mathrm{He}^{++} + \mathrm{T}^{-} + \beta^{-}$)
a5		TT($\mathrm{He}^{++} + \beta^{-}$)$\mathrm{T}^{-}$
–	$\mathrm{He}^{++} + \mathrm{T}^{+} + \beta^{-} + 2e^{-}_{so}$	TT($\mathrm{He}^{++} + \mathrm{T}^{+} + \beta^{-} + 2e^{-}_{so}$)
–		TT($\mathrm{He}^{++} + \mathrm{T}^{+} + \beta^{-} + e^{-}_{so}$)$e^{-}_{so}$
–		TT($\mathrm{He}^{++} + \mathrm{T}^{+} + \beta^{-}$)$e^{-}_{so}$
–		etc, but small

Table 2.2: Decay branch and detection channels for TT decay in TRIMS. Some channels can be related by the figure labels to the bands in figure 2.3b. Table adapted from [79].

Figure label	Description
a7	Low-ion-energy events mostly coming from decays near the ion detector
a8	Low-beta-energy events mostly coming from decays near the beta detector
a9	Events where the pulse in the beta detector comes from a secondary electron from an ion hitting the ion detector instead of the β
a10	Events where the pulse in the beta detector comes from a secondary electron from an ion hitting the ion electrode. Two ions are required, one to be detected in the ion detector and the other to hit the mesh.

Table 2.3: Population of events of Fig. 2.3 coming from an ion or a β interacting with the TRIMS apparatus.

final state in a decay, i.e. 0, 1, 2, or 3. Hence we write it as:

$$Q_{\mathrm{e}} \;=\; \frac{K_{\mathrm{ion}} + K_{\beta} - K_{\beta}^{0}}{q_e \cdot V}, \tag{2.2}$$

where K_{β} is the energy detected in the beta detector, K_{ion} is the energy detected in the ion detector, K_{β}^{0} is the unknown initial beta kinetic energy (fixed at 3 keV for sorting events), $q_e = -1.6 \times 10^{-10}$ C is the electrons charge, and V is 60 kV corresponding to our HV potential.

In this context, the mass (m_{ion}) refers to the ion mass after the decay. It is reconstructed, for each event, using the ions' kinetic information. In order to do so the following assumptions come into play: the ions are non-relativistic; the mesh voltage is small compared to the 60 kV HV; and the initial kinetic energy of the ions is negligible because the recoil energy is in the tens-of-eV range. With these assumptions the mass can be written as:

$$m_{\mathrm{ion}} = 2K_{\mathrm{ion}} \left(\frac{T_{\mathrm{ion}}}{\frac{2K_{\mathrm{ion}}}{q_{\mathrm{ion}}V} L + L_{\mathrm{ion}}} \right)^{2}, \tag{2.3}$$

where L is the decay chamber length, L_{ion} is the distance between the ion-detector and the ion-mesh, and q_{ion} is the ion charge. Throughout this thesis, most of the plots containing the mass parameter will be plotted against the square root of the mass so that all the data peaks have about the same width.

The charge versus mass histograms shown in Fig. 2.4 are created with the reconstructed quantities. The plane is partitioned into eight regions or boxes, each of which is heavily dominated by a decay branch or a limited number of detection channels of TT and HT decay. There are three charge-regions c1, c2, and c3, each of which contains mostly one event topology: an ion of charge one and one electron, an ion of charge one and two electrons, and an ion of charge two and two electrons. There are four mass regions, each of which mostly encloses one of the main decay branches. By comparing the number of counts in each box it is possible to get the ratios to the different decay branches. Nevertheless, there is cross-contamination between adjacent regions that needs to be accounted for.

2.2.3 Cross Contamination

Here, we describe the cross contamination analysis chain very briefly. A full description may be found in [78, 79].

There are three main types of cross-contamination (CC) in the data from figure 2.4: source-CC, charge-CC, and mass-CC.

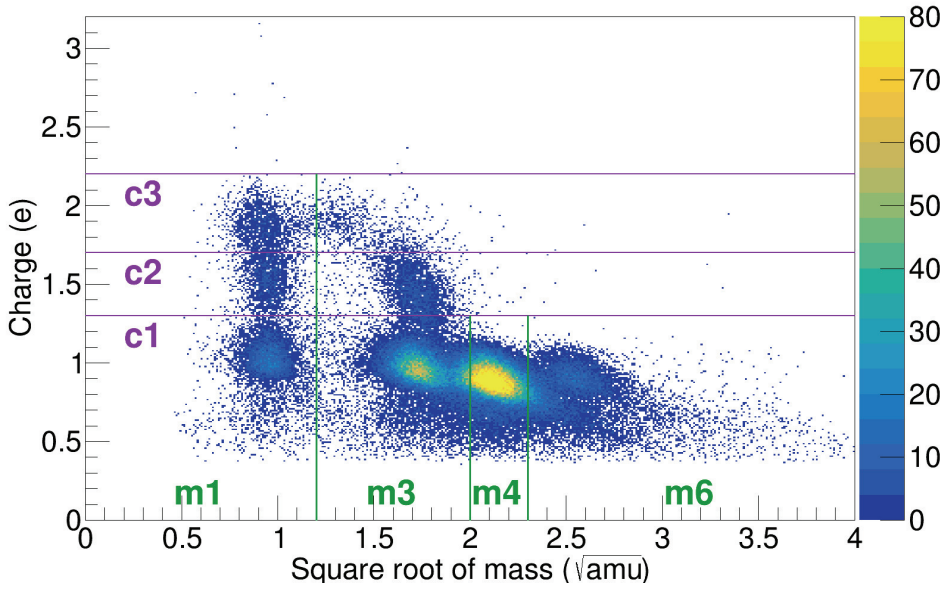

(a) High-HT data set

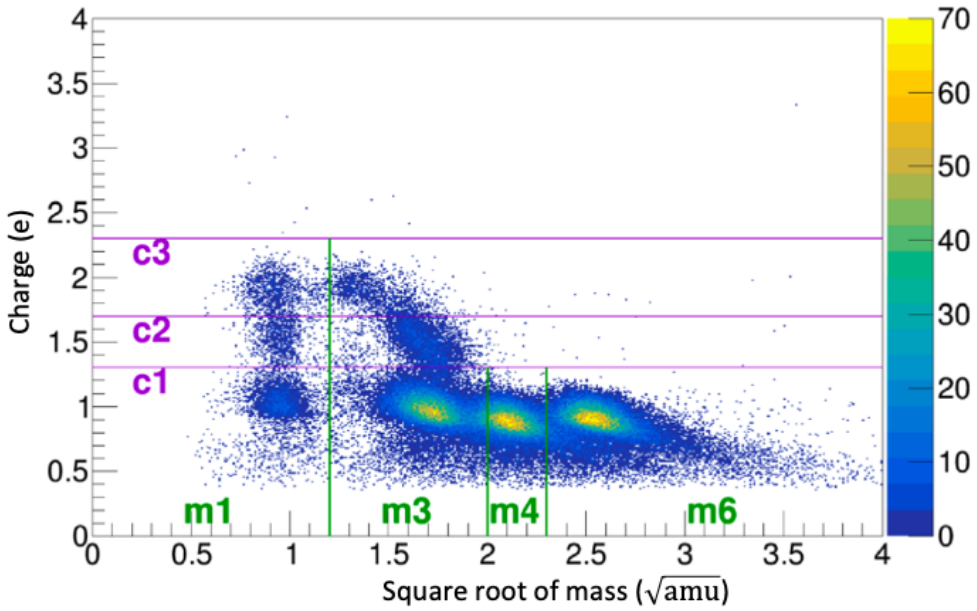

(b) High-TT data set

Figure 2.4: Histograms of charge versus ion square root of mass of the high-HT data set (a) and the high-TT data set (b). The purple lines are the charge cuts and the green lines are the mass cuts used to divide the data, or the plot, into segments with one dominant branch each. Plots from [78].

Source-CC was produced because the TRIMS source was not pure, with a combination of HT and TT gas in both run configurations. Two source-CC ratios were produced to quantify how much TT gas was in the high-HT data set and vice versa.

Charge-CC refers to the leakage of the dominant bands to other regions along the Y-axis of Fig. 2.4. All of the charge 1 events reside in the c1 region, so the contamination comes from channels in the c2 and c3 regions. The charge-CC ratios were calculated, for each detection channel with charge bigger than 1, using simulation data.

Mass-CC refers to the leakage of the dominant bands to other regions along the X-axis of Fig. 2.4. Mass ratios were calculated by grouping event populations with the same reconstructed mass, fitting it with a Gaussian and counting how much of the distribution fell on each mass region.

The ratios were used, in each data set, to account for the contamination. A deconvolution procedure was applied to account for finite detector size using data from different scan positions. And finally, the branching ratios where extracted from the data.

2.3 Branching ratios

Branching ratios of HT β-decay were published by the TRIMS collaboration in 2020 [79]. A first result of the TT β-decay branching ratios was presented in Ying-Ting Lin thesis in December, 2019 [78]. We are currently writing a longer paper [69] with more in-depth explanations of: the experimental setup, the analysis chain, and TT branching ratios, taking into account results from this thesis. Both branching ratios agree with the theoretically calculated values and disagree with the previous experimental values.

The branching ratios of HT β-decay can be seen in table 2.4, and the ones of TT β-decay can be found in table 2.5.

2.4 Re-assessment of old experimental results

Our results, on the branching ratios to the bound state molecule, greatly differ with the results by Snell *et al.* [66], and Wexler [67]. We believe that the reason behind this disagreement comes from the unknown acceptance of the mass spectrometers, as Wexler himself said. We can correct for the acceptance of the mass spectrometers using: the Liouville's theorem, predictions of the initial ion energies from Bodine *et al.* [41], the leptons averaged energy, and our branching results.

A mass spectrometer accelerates ions through an acceleration section. The ions are then detected with an ion detector after passing through a slit. According to Liouville's theorem,

i	Decay Branch	
	Daughter particles	(%)
No electron		
1.	$He + H$	-
One electron		
2.	HeH^+	56.51(55)
3.	$He^+ + H$	24.98(41)
4.	$He + H^+$	5.64(45)
5.	$He^{++} + H^-$	< 0.021
Two electrons		
6.	$He^+ + H^+$	10.72(49)
7.	$He^{++} + H$	2.16(21)
Three electrons		
8.	$He^{++} + H^+$	< 0.045

Table 2.4: HT β-decay branching ratios and their uncertainties [69].

i	Decay Branch	
	Daughter particles	(%)
No electron		
1.	$He + T$	-
One electron		
2.	HeT^+	50.3(15)
3., 4.	$He^+ + T$ or $He + T^+$	33.2(18)
5.	$He^{++} + T^-$	< 0.018
Two electrons		
6.	$He^+ + T^+$	14.8(11)
7.	$He^{++} + T$	1.8(19)
Three electrons		
8.	$He^{++} + T^+$	< 0.015

Table 2.5: TT β-decay branching ratios and their uncertainties [69]. The branches 3. and 4. appear together since they can't be distinguished in the TRIMS experiment since the ions have the same charge and mass.

a volume in phase space is given by

$$\phi \;=\; \Delta p_x \Delta p_y \Delta p_z \Delta x \Delta y \Delta z. \tag{2.4}$$

The total number of particles in this phase space remains constant as it passes the accelerator chamber. Considering a volume of tritium source gas $\Delta x \Delta y \Delta z$, the ion momentum values are $(2 m_i E_i)^{3/2}$, where m_i and E_i are the mass and energy, respectively, of recoil ion i. The ratio of phase space volume occupied by two kinds of ions i and j is [69].

$$\frac{\phi_i}{\phi_j} \;=\; \left(\frac{m_i E_i}{m_j E_j} \right)^{3/2}. \tag{2.5}$$

As explained in [69], it was found that the phase volume for mass-3 ions was 9.2 times that for mass-4 ions. This meant that the acceptance was 9.2 times smaller. The 37% ratio to the mass-3 ions (from table 2.4) drops to about 4%. And considering the phase-space of all ions, the ratio to the bound state molecule $^3HeH^+$ goes from about 56% to about 85%. This is not exactly what Wexler had measured (94%) but it comes closer to their result.

CHAPTER 3
SELECTED TRIMS ANALYSIS PROJECTS

In this chapter we present a selection of the analysis projects that I have done for the Tritium Recoil Ion Mass Spectrometer (TRIMS) experiment.

The first of these projects consisted on a data quality check where the method used to look for runs with digitizer glitches was automated, and the defective data was removed (Sec. 3.1). Next is the characterization of the ion detector, to account for systematics that depend on the ion incident energy and the ion type; these systematics include backscattering of ions, and dead layer effects (Sec. 3.2). Finally, I present calculations and simulations done to extract the proton energy of the charge-2 HT β-decay branch $\{\mathrm{H}^+ + \mathrm{He}^+ + \beta^- + e^-_{so}\}$ (Sec. 3.3).

3.1 Data quality checks

In TRIMS, the TT and HT raw data were divided in runs (Sec. 2.1.2). A run consisted of 300 s of stored data coming from the ion and β detectors. During a run, the ion detector was stationary at a specific scan position. There are almost 500 runs of raw data.

Defective runs, or runs with problematic data, were manually found (Sec. 3.1.1) by Lin [78]. So, an automatic method was implemented to look for some of these type of runs (Sec. 3.1.2). Finally, after the defective runs were found with the automatic method, they were treated accordingly (Sec. 3.1.3).

3.1.1 Defining the defective runs

Defective runs were manually found in the run database. These runs were categorized as follows:

- **Excess runs**. They have substantially more total count of events than runs (from other scans) taken at the same scan location, or the same ion-detector position. This excess was specific to the run at the scan location and did not affect the rest of the runs from the scan. The data of these runs was found to be of otherwise good quality. These runs were found by comparing the data of all the scans at each scan location. There are 21 positions in total, so just 21 plots had to be checked. As an example, Fig. 3.1 shows the total count of events in each of the runs taken at scan position

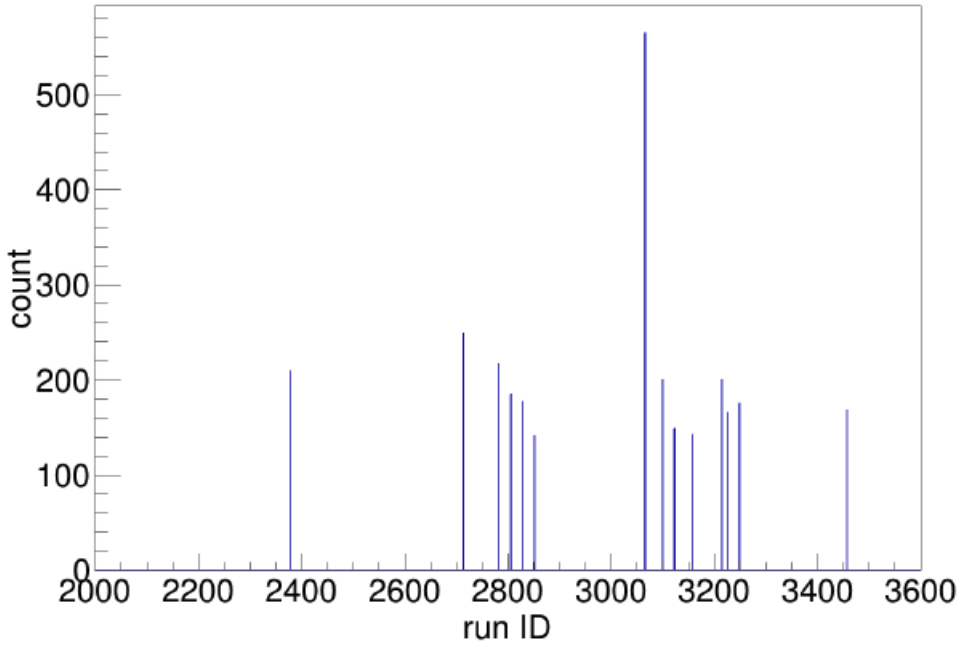

Figure 3.1: The total count of events in each of the runs taken at scan position x_{-7}. There is an excess run with double the count of the rest of the runs.

x_{-7}. There is one excess run with almost double the count as the rest of the runs. 5 excess runs were found with more than double of the expected data. They were not removed from the analysis since, as stated, the rest of the data was found to be good quality by comparing the rest of the parameters with the parameters from runs taken at that scan position. More information on this runs can be found in [78].

- **Fuzzy runs**. In these runs the waveforms of the data from the detectors had digitizer glitches. Hence, the ion-energy versus ion-TOF histogram did not contain the band structure observed in the rest of the data. The lack of structure was used to clearly pick out these runs from the rest. This type of run is rare (around 20 runs were found) and so they were taken out entirely from the analysis, together with their run scan, without greatly affecting the statistics since most of them corresponded to the same scans.

- **Deficit runs**. In these runs, the rate of events decreased suddenly for a brief period of time and then returned to normal. The rate decrement could happen at any point of the 300 s of data-taking. A normal run should have a constant rate through the 300 s. The data of these runs was found to be of otherwise good quality. These runs were found by inspection of the plots of the event rate over time of all the runs. Figure 3.2 shows the histograms of a good run, and of two deficit runs. The histograms of the

deficit runs are Fig. 3.2b and Fig. 3.2c, they differ in the position of the rate deficit as well as the width. These deficits were also found to be due to digitizer glitches.

As stated, the defective runs were initially found manually. The fuzzy runs and the deficit runs were not hard to find because of the clear signatures. On the other hand, the deficit runs required looking for a wide variety of signatures (as shown in Fig. 3.2) in a lot of plots. So, to reduce the human error, an automatic tool that could find these runs was programmed.

3.1.2 Method to automatize deficit-run search

The method implemented to find the deficit runs was the following:

1. Find the mean (μ_{T}) and the standard deviation (σ) of the event rate of a run
2. Bin the data in 3 second intervals and get the event-rate mean $\mu_{3\mathrm{s},i}$ of each bin
3. Compare the means and classify as a deficit run if:

$$|\mu_{3\mathrm{s},i} - \mu_{\mathrm{T}}| > 3.0\sigma \tag{3.1}$$

4. Repeat the process with 1 s bins and the lower bound of the condition set to 3.5σ
5. Repeat the process with 10 s bins and the lower bound of the condition set to 1σ
6. Look at the event rate of the runs that were classified as deficit runs

All the manually found deficit runs were successfully flagged using this method. Moreover, deficit runs that had not been previously marked were found. This method also flagged runs that had spikes or an excess in the event-rate. Only two runs of this type were found and they were treated as deficit runs.

3.1.3 Deficit-run correction

After successfully finding all the deficit runs using the automatic method, and finding that the deficit was due to digitizer glitches, it was decided to remove these data from the TRIMS analysis. Since a lot of runs were found to be deficit runs (around 8%), removing them from the analysis would have impacted the statistics. The following procedure was implemented to take out just the affected data of the deficit runs:

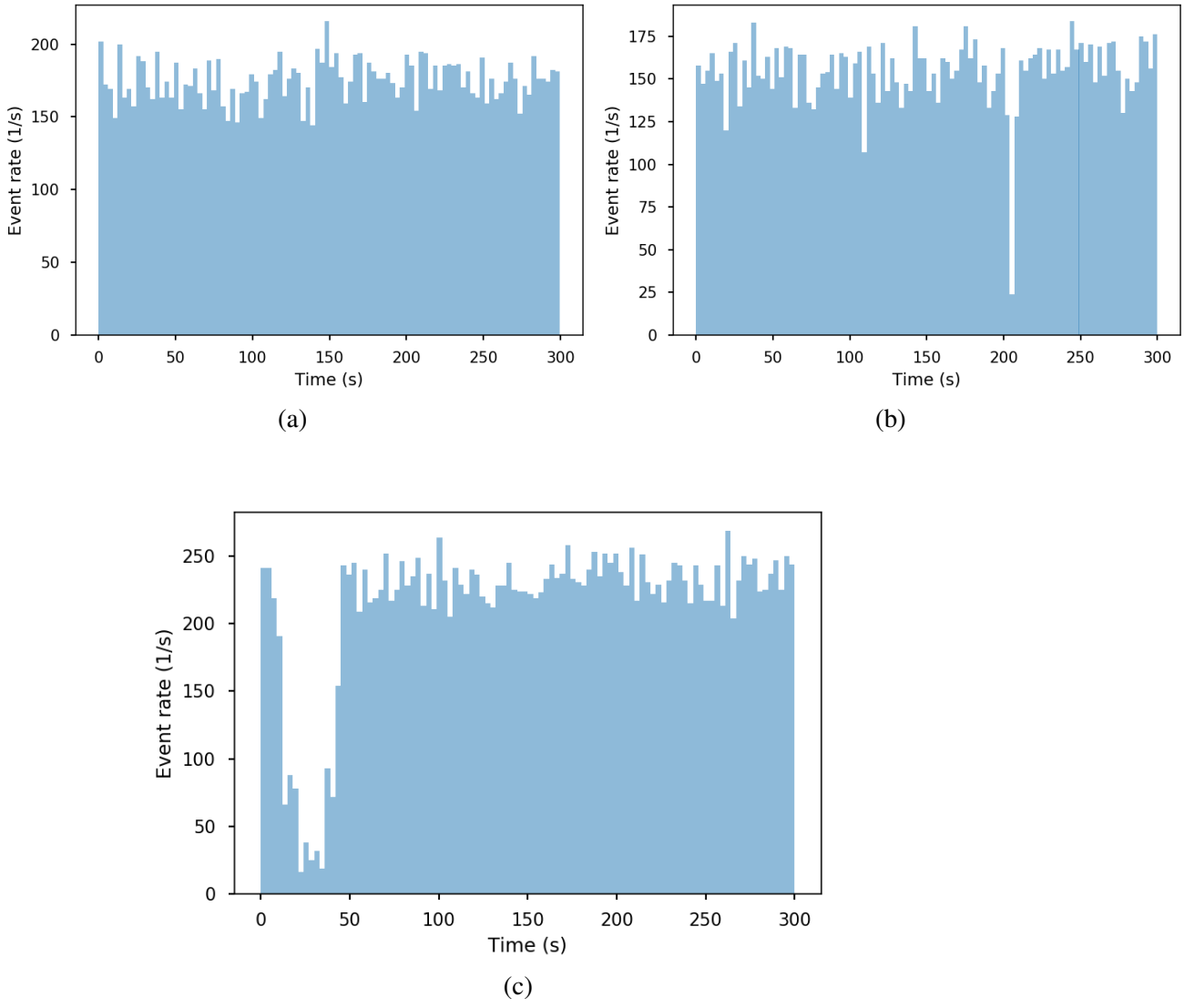

Figure 3.2: Example histograms of the event rate of: (a) run 2732 which is a good run; (b) and (c) runs 2259 and 2732 respectively which are deficit runs. The plots have different mean rates because they correspond to runs taken at different scan positions. We expect more events when the ion detector is in the center of the decay chamber and fewer events when the ion detector is moved away from the center. Plots (b) and (c) differ in that they present deficits of different sizes and at different times within the run. The dark blue line in b) is a plotting artefact.

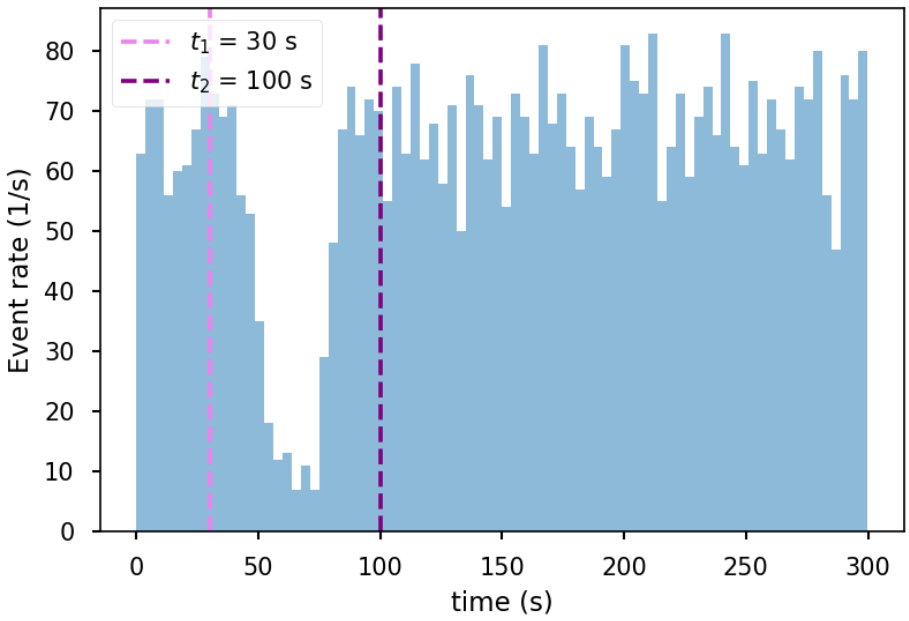

Figure 3.3: Example of a deficit-run correction process. The two vertical lines represent the timestamps at which the data is cut to exclude data from the deficit interval.

1. Manually select the time interval in which the deficit takes place (t_1, t_2). As an example, Fig. 3.3 shows the event rate histogram, and the times $t_1 = 30$ s, and $t_2 = 100$ s. The intervals are taken conservatively to contain all the deficit data. t_1 and t_2 are not set finer than 5 s.

2. Cut the data, in this time interval, from the run. In the example, the data are cut from $(30, 100)$ s

3. To compensate for the cut data, we normalise the total count by multiplying it with the following term:

$$\frac{300}{300 - (t_2 - t_1)}. \tag{3.2}$$

A list of all the deficit runs and their corresponding time interval cuts is given in table 3.1.

3.2 Ion detector characterization

To understand the TRIMS ion-energy reconstruction and compute correct branching ratios, we modelled interactions of ions with the ion detector using the software SRIM. In this section, we start by introducing the Stopping and Range of Ions in Matter (SRIM) software

Deficit run	t_1 (s)	t_2 (s)	Final run time (s)
2259	195	215	280
2266	40	60	280
2381	20	40	280
2697	0	70	230
2698	0	50	250
2699	80	100	280
2700	0	30	270
2721	0	30	270
2723	0	20	280
2724	30	50	280
2725	30	100	230
2835	10	25	285
2838	0	25	275
2850	30	55	275
2853	30	50	280
2854	0	110	190
2860	50	70	280
2870	30	60	270
2887	20	40	280
2888	0	30	270
2890	30	70	260
2963	45	65	280
2965	0	50	250
2969	60	85	275
2979	40	60	280
3001	0	50	250
3003	0	20	280
3004	0	25	275
3010	0	45	255
3050	0	40	260
3051	0	20	280
3055	40	65	275
3057	20	50	270
3064	0	80	220
3066	90	130	260
3068	35	105	230
3069	150	170	280
3267	50	75	275
3268	0	30	270
3353	40	70	270
3354	0	60	240
3355	30	50	280
3373	35	65	270

Table 3.1: List of deficit-runs found with the automated method. t_1, and t_2 give the time interval chosen for the cut. The final run time is the time of the run after the cut.

(Sec. 3.2.1). The TRIMS ion detector is a silicon PIPS Canberra detector (Sec. 2.1.2). Simulations of ions interacting with a silicon layer were carried out (Sec. 3.2.2). Interactions that depend on ion incident energy and on ion type were investigated. The branching ratios were corrected for: ion backscattering in the ion detector (Sec. 3.2.3), dead layer effects (Sec. 3.2.4), and the pulse-height defect (Sec. 3.2.5).

3.2.1 SRIM software

SRIM is a software that simulates the collision, stopping, and range of ions in matter [81, 82]. It can simulate low energy ions, of 1 eV/amu, up to high energy ones, of 2 GeV/amu. It treats the collisions between the ion and the target atoms using quantum mechanics. And, it uses statistical algorithms that allow the ion to make "jumps" between each collision, and then averages the collision result in the jump interval. A full description of the ion-target interaction treatment can be found in [82].

In SRIM it is possible to choose the material of the target, ranging from a simple one-layer target made of a single atom type, to an eight-layer target made of compound materials. It calculates the final distribution and kinematics of the ions, producing information on: target damage, sputtering, ionization, backscattering, phonon production, and electron and nuclear stopping. All these interactions are associated with the energy loss of the ion [82].

3.2.2 SRIM simulations of the ion detector

Amongst other things, the TRIMS analysis relies on: the correct reconstruction of the ion energies from the voltage signal of the ion detector (Sec. 2.2.1), and on simulations, as close as possible, to the experimental settings (Sec. 2.2.3).

There are some interactions between the ions and the silicon detector in which the ion loses energy which is not collected in the detector's signal. These interactions were studied with SRIM simulations. Then, they were incorporated in the TRIMS analysis using one or more of the following strategies: include them in the TRIMS experiment Geant4 simulations, include them in the reconstruction of the ion energy from the data, or directly correct the final branching ratios.

The TRIMS electric field accelerates the ions towards the silicon detector. Most of the ions reach the detector and interact with it, but a small fraction are backscattered, losing energy in the process. Another factor that affects the detected energy is the detector dead layer, which is specified by Canberra as 50 nm. The energy deposited in the dead layer is not completely recovered in the voltage signal. In the simulations we will use a half dead

layer, with 50% charge collection, of 100 nm as recommended in [83].

Simulations of the ion detector were done as follows:

1. A silicon layer of 100 nm was simulated with SRIM.

2. 1 million events were simulated per ion incident energy E_{inc}, where the incident energy is the energy of the ion when it reaches the ion detector. This energy mainly depends on the location of the β-decay, which dictates acceleration by the electric field.

3. 1 million events were simulated per ion type. A list of the possible daughter ions after HT and TT β-decay can be seen in tables 2.1 and 2.2 respectively. In SRIM it is not possible to simulate molecules. Instead of a molecule, we simulated the dissociated ions, since its highly probable that the molecule will dissociate on impact. For example, instead of a 40 keV $^3HeH^+$ ion, we simulated a 30 keV H^+ ion and a 10 keV $^3He^+$ ion, where energy and momentum conservation have been enforced.

4. The interactions that resulted in ion energy loss were investigated.

In the following sections we will present the results obtained from said simulations.

3.2.3 Backscattered ions

Backscattered ions lose energy in the process of backscattering. If the ion is backscattered it will return to the ion detector, due to the electric field, but it will have a smaller incident energy.

Unlike electron backscattering, ion backscattering is not implemented in the TRIMS Geant4 simulation and so it is not accounted for in the charge-CC ratios (Sec. 2.2.3). SRIM simulations were carried out, following the previously outlined method, to obtain the percentage of backscattered ions. This number depends on ion type and on ion energy. The correction for backscattered ions was done directly on the calculated branch intensities, as will be further explained.

Results

Figure 3.4 shows the backscattering probability of ions in a silicon layer, with incident energies in the range of 10 keV to 100 keV. The probability of backscattering greatly decreases for high-energy ions. We also observe that the probability is similar for one-proton ions (H^+ and T^+) while $^3He^+$ is slightly different. Nevertheless, the probability of backscattering between (20, 40) keV, which is the fiducial volume cut, is less than 2% in all cases.

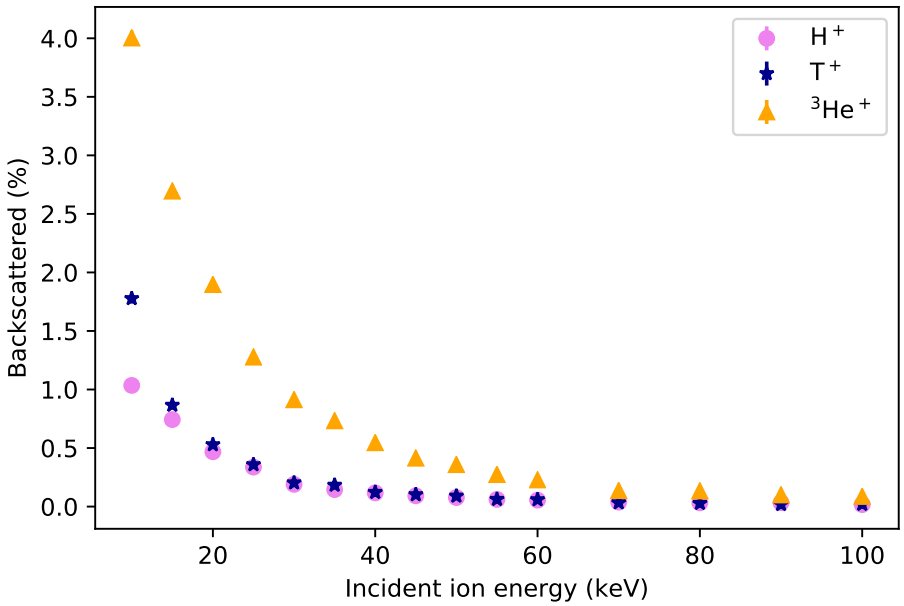

Figure 3.4: Backscattering probability of: He (orange triangles), T (dark blue stars), and H (pink circles) ions in a silicon layer obtained from SRIM simulated data. The error $\sqrt{N}$ is too small to be noticeable.

Table 3.2 gives the average ion-backscattering probability of each ion type within the main fiducial-volume energy range cut. The molecules are treated as dissociating ions with energies K_1 and K_2, and their energy range is limited by energy and momentum conservation:

$$K_1 = \frac{m_2}{m_1} K_2, \tag{3.3}$$

where m_1 and m_2 are the masses of ions 1 and 2 respectively.

Ion	Dissociated ion	Backscattering (%)	Energy range (keV)
He^+ or He^{++}	-	1.07 ± 0.01	[20,40]
	HT β-decay		
H^+	-	0.25 ± 0.01	[20, 40]
HeH^+	H^+	0.43 ± 0.01	[15, 30]
	He^+	4.00 ± 0.06	[5, 10]
	TT β-decay		
T^+	-	0.28 ± 0.01	[20,40]
HeT^+	T^+	1.06 ± 0.02	[10,20]
	He^+	2.86 ± 0.02	[10,20]

Table 3.2: Average ion backscattering probability for each ion type in main fiducial volume.

i	Decay Branch		$B(\%)$
	Daughter particles	$I_i(\%)$	
No electron			
1.	He + H	-	-
One electron			
2.	HeH^+	56.51(55)	4.43 ± 0.06
3.	He^+ + H	24.98(41)	1.07 ± 0.01
4.	He + H^+	5.64(45)	0.25 ± 0.01
5.	He^{++} + H^-	< 0.021	1.07 ± 0.01
Two electrons			
6.	He^+ + H^+	10.72(49)	1.32 ± 0.03
7.	He^{++} + H	2.16(21)	1.07 ± 0.01
No electrons			
8.	He^{++} + H^+	< 0.045	1.32 ± 0.01

Table 3.3: Backscattering probability of each HT β-decay branch, together with the branch intensities where the backscattered probability has already been accounted for [69].

Corrections to the branch intensities

The main fiducial volume (FV) cut was applied directly to the data. Any ion backscattering with energies in the FV energy regime is removed from the main FV because of their energy loss in the process. Moreover, the probability of the case that a high-energy ion ends up inside the main-FV energy range after backscattering is negligible (Fig. 3.4). Therefore we treat the backscattered ion as lost.

The backscattered ion corrections were carried out directly on the branch intensities, I_i(TT) or I_i(HT) calculated as discussed in Sec. 2.2, as follows:

$$I_i(\mathrm{TT}) = I_i^b(\mathrm{TT})\frac{100}{100 - B_i}. \tag{3.4}$$

where I_i^b are the intensities before the backscattering correction, I_i are the final intensities found in tables 3.3 and 3.4, and B_i is the backscatter probability of the branch.

B_i is calculated for each branch as follows. In the case of a one-ion branch, B_i is equal to the backscattering probability of the ion in table 3.2. In the case of a molecule or the two-ion branches, B_i is the sum of the backscattering probabilities of the two corresponding ions. The B_i values for each branch can be found in tables 3.3 and 3.4.

As an example, take branch $i = 3$ (table 2.4) where He^+ is the daughter ion. For this correction its branch intensity was multiplied by: $100/(100 - 1.07) \approx 1.011$.

i	Decay Branch		$B(\%)$
	Daughter particles	$I_i(\%)$	
No electron			
1.	He + T	-	
One electron			
2.	HeT^+	50.3(15)	3.92± 0.03
3., 4.	He^+ + T or He + T^+	33.2(18)	1.07 ± 0.01
5.	He^{++} + T^-	< 0.018	1.07± 0.01
Two electrons			
6.	He^+ + T^+	14.8(11)	1.10± 0.03
7.	He^{++} + T	1.8(19)	1.07± 0.01
No electrons			
8.	He^{++} + T^+	< 0.015	1.10± 0.01

Table 3.4: Backscattering probability of each TT β-decay branch, together with the branch intensities where the backscattered probability has already been accounted for [69].

3.2.4 Dead layer effects

As previously explained, a 100 nm half-dead layer was simulated with SRIM to calculate the energy ($E_{\rm dead}$) which is deposited in the dead layer of the ion detector because half of it is not recovered in the voltage signal.

The incident energy ($E_{\rm inc}$), or the total kinetic energy with which the ion arrives at the detector is:

$$E_{\rm inc} = E_{\rm det} + \frac{1}{2}E_{\rm dead}, \tag{3.5}$$

where $E_{\rm det}$ is the energy reconstructed from the voltage signal. It is possible to reconstruct the incident energy from the detected energy if we know the energy lost in the dead layer, which depends on ion type and on incident energy.

The energy lost in a 100 nm half-dead layer was simulated for $E_{\rm inc}$ in the range of 10 keV to 60 keV in 10 keV steps. Figure 3.5 shows the detected energy, calculated using equation 3.5 where the distribution of $E_{\rm dead}$ comes from the energy deposited in the dead-layer of the SRIM simulations. Each detected energy distribution was fitted with a Gaussian function.

The data points in Fig. 3.6 are the mean and the standard deviation of each distribution from Fig. 3.5. The data points of each ion type (H^+, T^+, and $^3He^+$) were fitted with a second degree polynomial. The results of the fits are shown in table 3.5.

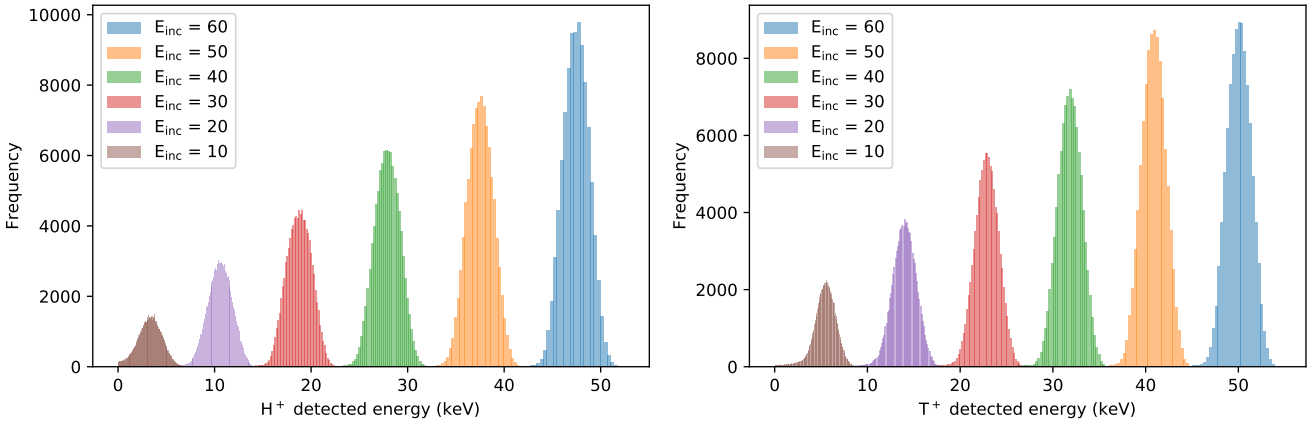

(a) (b)

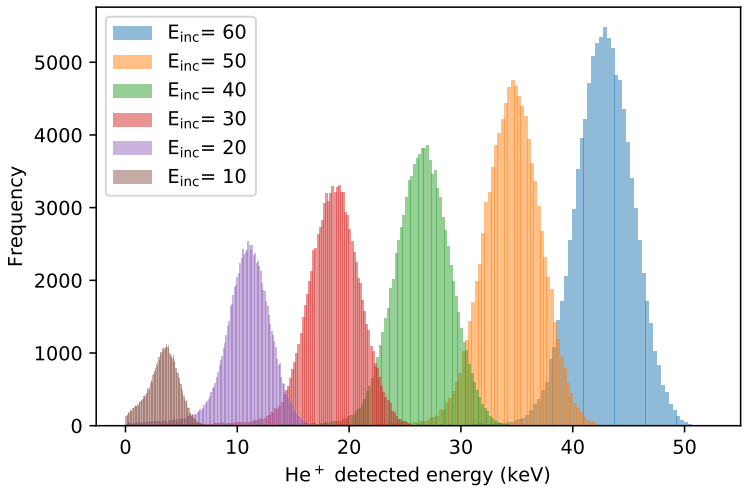

(c)

Figure 3.5: Histograms of the detected energy after the ions lose energy in a half-dead layer of 100 nm. Six incident energies were simulated for each ion type (a) H^+, (b) T^+, and (c) $^3He^+$. The incident energies are in the range [10, 60] keV.

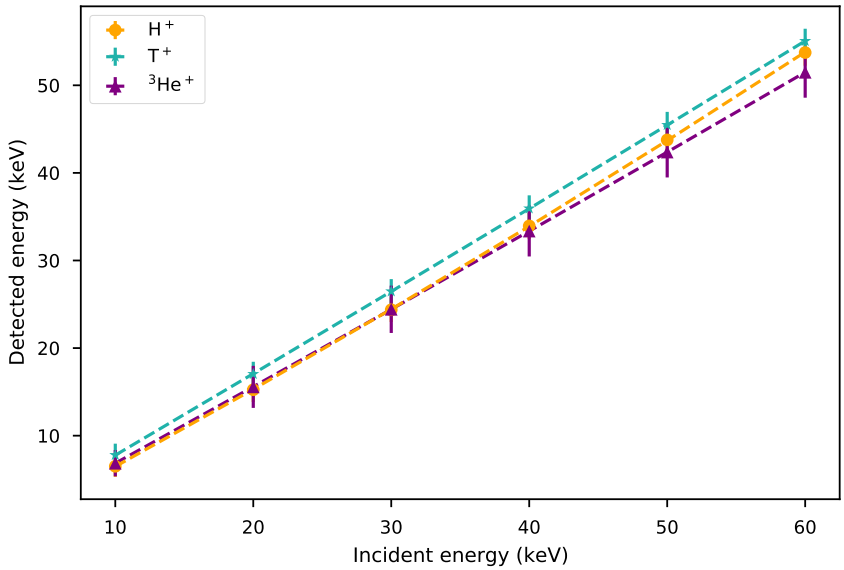

Figure 3.6: Detected energy versus incident energy of: H^+ (orange circle), T^+ (blue stars), and $^3He^+$ (purple triangle), where the ions lose energy in a half-dead layer of 100 nm. The data and errors come from Gaussian fits to the data of figure 3.5. The data points are fitted with a second degree polynomial.

	Fit parameters		
	Constant (keV)	Linear (1)	Quadratic (keV^{-1})
H^+	-2.0 ± 2.3	0.83 ± 0.16	$(1.6 \pm 2.3) \times 10^{-3}$
$^3He^+$	-1.8 ± 3.3	0.86 ± 0.26	$(0.3 \pm 3.9) \times 10^{-3}$
T^+	1.5 ± 2.4	0.91 ± 0.16	$(0.4 \pm 2.2) \times 10^{-3}$

Table 3.5: Quadratic polynomial fit parameters to convert the incident-energy into detected-energy of H^+, T^+, and $^3He^+$ ions. The valid incident-energy range is from 10 keV to 60 keV. The fits were carried out on the data of Fig. 3.6.

TRIMS experimental simulations were carried out with Geant4, which is better suited to simulate high-energy physics, where the dead-layer effect is insignificant. That is why the results shown in table 3.5 were incorporated in our TRIMS simulations. Geant4 provided the incident ion energy while SRIM results (along with a Gaussian broadening) were used to obtain the simulated detector signal [78].

In the case of molecular ions ($^3HeH^+$, and $^3HeT^+$), the dead-layer effect correction was done directly in the Geant4 code using the previously calculated corrections for atomic

ions, because the molecules dissociate and ionize on impact. By energy conservation the incident energy ($E_{\rm inc}^{\rm HeH}$) of $^3HeH^+$ was distributed as follows:

$$E_{\rm inc}^{\rm HeH} = \frac{1}{4}E_{\rm inc}^{\rm He} + \frac{3}{4}E_{\rm inc}^{\rm H}. \tag{3.6}$$

And in the case of $^3HeT^+$:

$$E_{\rm inc}^{\rm HeT} = \frac{1}{2}E_{\rm inc}^{\rm He} + \frac{1}{2}E_{\rm inc}^{\rm T}. \tag{3.7}$$

3.2.5 Pulse-height-defect correction of the data

Besides the energy lost in the dead layer, there is another way in which the ion can lose energy in the silicon detector that is not recovered in the voltage signal. This is the nuclear stopping power ($E_{\rm nuc}$), or the nuclear recoil, that causes the so-called pulse-height defect. Only the electronic stopping power ($E_{\rm ele}$), in the active layer, contributes to the detected voltage signal ($E_{\rm det}$) from that layer. Thus, the detected energy from equation 3.5 is modified:

$$E_{\rm inc} = E_{\rm det} + E_{\rm nuc}^{\rm active} + \frac{1}{2}E_{\rm dead}, \tag{3.8}$$

where $E_{\rm nuc}^{\rm active}$ is the energy lost to nuclear recoil in the detector's active layer.

Using SRIM simulations, it is possible to get the total stopping power of an ion in a silicon layer, separated into the nuclear and the electronic components. The ratio of the nuclear versus the electronic stopping powers of the ions H^+, T^+, and $^3He^+$ in a silicon layer is shown in Fig. 3.7. The pulse-height deficit of the incident energy of the ion in the TRIMS data was corrected using equation 3.8.

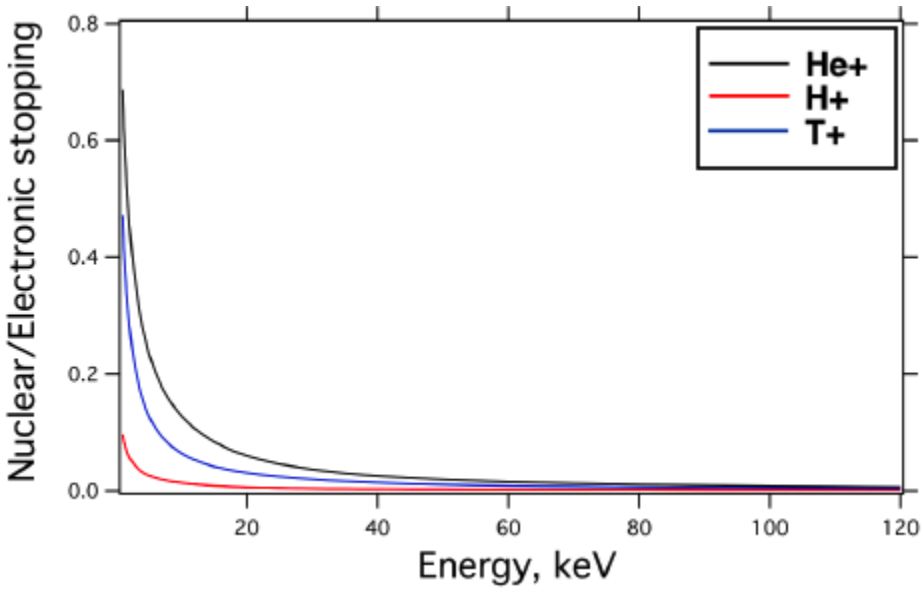

Figure 3.7: Ratio of the nuclear versus the electronic stopping power of the ions H^+, T^+, and $^3He^+$ in a silicon layer from SRIM simulations [78]. The energy refers to the in-flight energy of the ion while moving in the silicon layer.

3.3 Proton energy of HT decay branch H^+ + He^+

In this section, the initial proton energy of the HT decay branch $He^+ + H^+ + \beta^- + e^-_{so}$ is sought. We start by motivating this measurement (Sec. 3.3.1). Then, a theoretical calculation is carried out (Sec. 3.3.2). The data measured with the TRIMS experiment is introduced (Sec. 3.3.3) and a comparison between data and simulation is done (Sec. 3.3.4).

3.3.1 Motivation

As was explained in Sec. 2.4, a calculation was carried out to investigate why the experiments from Snell *et al.* [66] and Wexler [67] gave apparent branching ratios to the bound molecular state that differ so greatly with the theory (table 1.3). The calculations do not exactly match what the old experiments measured, but the large measured ratio to the bound state becomes understandable based on the differing phase space volumes for the various ion species.

Furthermore, we investigated the possibility of having a higher mean proton energy than the 9.7 eV estimated by Bodine *et al.* [41] since most of the ionized protons come from molecular dissociation from states above an excitation threshold of 45 eV. Raising the proton energy to 25 eV, and using it in the phase space ratio calculation (equation 2.5), results in apparent branching ratios in better accordance to the ones measured by the old experiments.

As will be explained, two paths were followed to obtain the proton energy, namely a theory calculation and a comparison between data and simulations using different proton energies.

3.3.2 Theoretical calculation

The final state of a molecule, after β-decay, depends on the electronic, rotational, vibrational and azimuthal quantum numbers. There is an energy threshold above which the final state will be electronically excited. It is also possible to have a doubly ionized state, albeit it is less probable and its energy threshold is higher. As explained in Sec. 5.2.3 there can be high-energy ions from molecular dissociation. And as shown in Fig. 5.3, the higher the excited state, the more energy that the ion can have.

The charge-2 branches in the HT β-decay are:

$$\mathrm{HT} \rightarrow \mathrm{H}^+ + \mathrm{He}^+ + \beta^- + e^-_{so} - 45.16\ \mathrm{eV} \tag{3.9}$$

$$\rightarrow \mathrm{H} + \mathrm{He}^{++} + \beta^- + e^-_{so} - 86\ \mathrm{eV}. \tag{3.10}$$

The given energies are threshold energies relative to the ground state of HeH^+, which is bound by 1.897 eV. Here we will focus on the two-ion final state. The threshold energy was calculated by Kolos *et al.* [84]. They calculated a "vertical" transition, in the Franck-Condon sense (Sec. 5.2.3), at an internuclear separation of 1.4 a_0.

It is theoretically difficult to deal with continuum states of ionized molecules, as attested by the fact that those were the major source of uncertainties of the HT and TT final state calculations available in the 1980s and 1990s [41]. The work of Saenz *et al.* has greatly improved this (Sec. 1.5.2). In [69] the continuum spectrum of the shakeoff electron is derived, and it is displayed in Fig. 3.8. The shakeoff electron is emitted together with the β-electron in the charge-2 final states.

For the scope of this thesis, a lower limit of the proton energy of the two-ion charge-2 branch will be calculated, and not the energy spectrum.

The total available energy (E_{Total}) for the ions is the threshold energy minus the binding energy previously mentioned:

$$E_{\mathrm{Total}} = 45.16\,\mathrm{eV} - 1.897\,\mathrm{eV} = 43.263\,\mathrm{eV}. \tag{3.11}$$

This energy is divided between the kinetic energies (E_{H} and E_{He}) of the two ions H^+

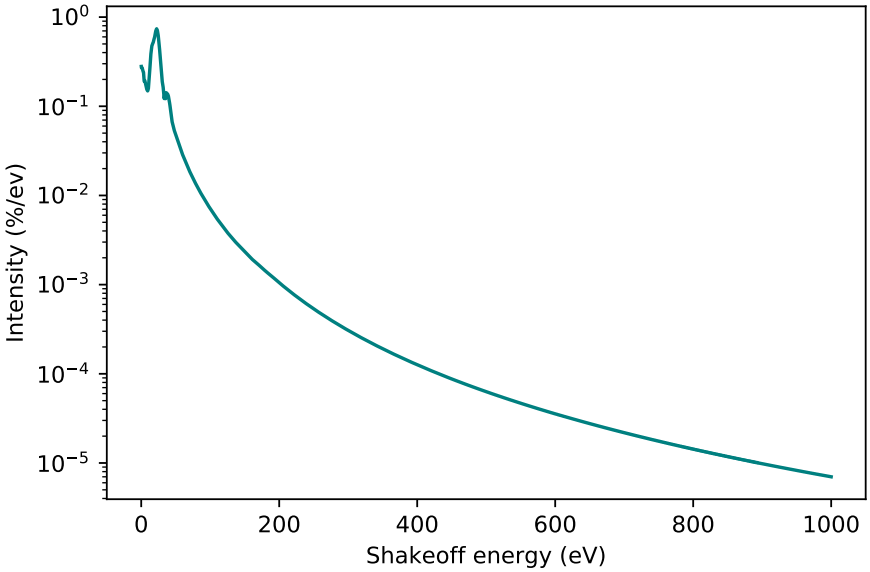

Figure 3.8: Spectrum of shakeoff electrons in β-decay of molecular tritium [69, 85]. The peak in the spectrum is located around 22 eV and the tail was calculated up until 1 keV energies due to its receding intensity.

and He^+ after molecular dissociation:

$$E_{\text{Total}} = E_{\text{H}} + E_{\text{He}}, \tag{3.12}$$

We can obtain their respective energies from momentum conservation:

$$m_{\text{H}}\vec{v}_{\text{H}} = m_{\text{He}}\vec{v}_{\text{He}} = 3m_{\text{H}}\vec{v}_{\text{He}}, \tag{3.13}$$

where m_{H}, $\vec{v}_{\text{H}}$ and m_{He}, $\vec{v}_{\text{He}}$ are the mass and velocity of the ions H^+ and He^+ respectively. And as a reminder, we write He^+ for convenience instead of $^3He^+$, so the masses relate as $3m_{\text{H}} = m_{\text{He}}$. The kinetic energy of each ion is:

$$E_{\text{ion}} = \frac{1}{2}m_{\text{ion}}|\vec{v}_{\text{ion}}|^2. \tag{3.14}$$

From equations 3.13 and 3.14, and from their mass relation, we get:

$$E_{\text{H}} = 3E_{\text{He}}. \tag{3.15}$$

Using the total available energy from equation 3.12 we thus obtain the minimum kinetic

energy of the ions:

$$E_{\mathrm{H}} \geq 32.45\,\mathrm{eV},$$
$$E_{\mathrm{He}} \geq 10.81\,\mathrm{eV}. \tag{3.16}$$

3.3.3 TRIMS data of the proton charge-2 detection channel

The possible final state branches of HT β-decay are shown in table 2.1. With TRIMS we can detect and differentiate most of them. The possible detection channels of each branch are also shown in table 2.1. For some branches, there is more than one detection channel. For example, the two-ion charge-2 branch

$$\mathrm{HT} \rightarrow \mathrm{He}^{+} + \mathrm{H}^{+} + \beta^{-} + e^{-}_{so}, \tag{3.17}$$

has six distinct detection channels. This means that there are six data structures that correspond to this decay branch, and in order to get the branch intensity we have to sum up the counts of all its detection channels.

By studying the TRIMS data for a specific channel, we can gain information on the detected ion.

There are two channels of the $\{\mathrm{He}^{+} + \mathrm{H}^{+} + \beta^{-} + e^{-}_{so}\}$ decay branch that can give us information on the proton energy spectrum of the two-ion charge-2 branch. These channels are:

$$\mathrm{HT} \rightarrow (\mathrm{H}^{+} + \beta^{-} + e^{-}_{so})\mathrm{He}^{+},$$
$$\mathrm{HT} \rightarrow (\mathrm{H}^{+} + \beta^{-})\mathrm{He}^{+} + e^{-}_{so}, \tag{3.18}$$

where the final state particles inside the parentheses are detected by the TRIMS detectors while the rest are not detected. The expectation is that the proton energy will be relatively high.

The main characteristic of the two detection channels shown in equation 3.18 is that the He^{+} ion is not detected in the ion detector while the H^{+} ion, or the proton, is detected. There are two detection channels because we can either detect one or two electrons. The He^{+} ion misses the ion detector via one of two mechanisms:

1. It can hit the mesh electrode, located in front of the ion detector (Fig. 2.2), where it is neutralized and lost.

2. It can miss the ion detector because of its cyclotron motion, or its creation position.

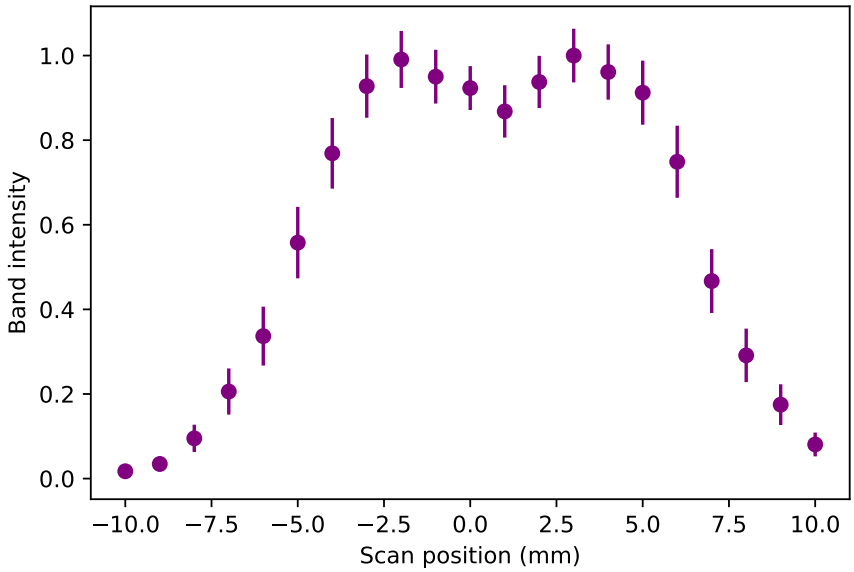

Figure 3.9: RCF of the detection channels shown in equation 3.18 that correspond to the two-ion charge-2 HT decay branch. These channels detect the proton but not the He^+. We observe a double peak structure.

The raw data collected with TRIMS using the high-HT source is displayed in figure 2.3a. The different β-decay branches and TRIMS detection channels can be distinguished by the data structures. Table 2.1 relates the data structures with the decay branches and detection channels. The two detection channels from which it is possible to extract information about the proton energy of this decay branch (Eq. 3.18) are labelled as (a1) in Fig. 2.3a.

As explained in section 2.1.2 the ion detector takes data in 21 scan-positions. With the data of each scan position it is possible to produce a plot similar to Fig. 2.3a. The data from each detection channel was segregated (more details on this process can be found in [78]) and a raw-count number was obtained for each one. The raw count is the number of counts that corresponds to that particular detection channel. For each detection channel, a raw count was obtained at each scan position, and the collection of all the raw counts is the raw count function (Raw Count Function (RCF)).

The RCF of the proton detection channels shown in equation 3.18 is plotted in Fig. 3.9, where the data have been normalized to the maximum value of the RCF. We observe a double peak structure. This structure is unique to the proton detection channel of the charge-2 branch.

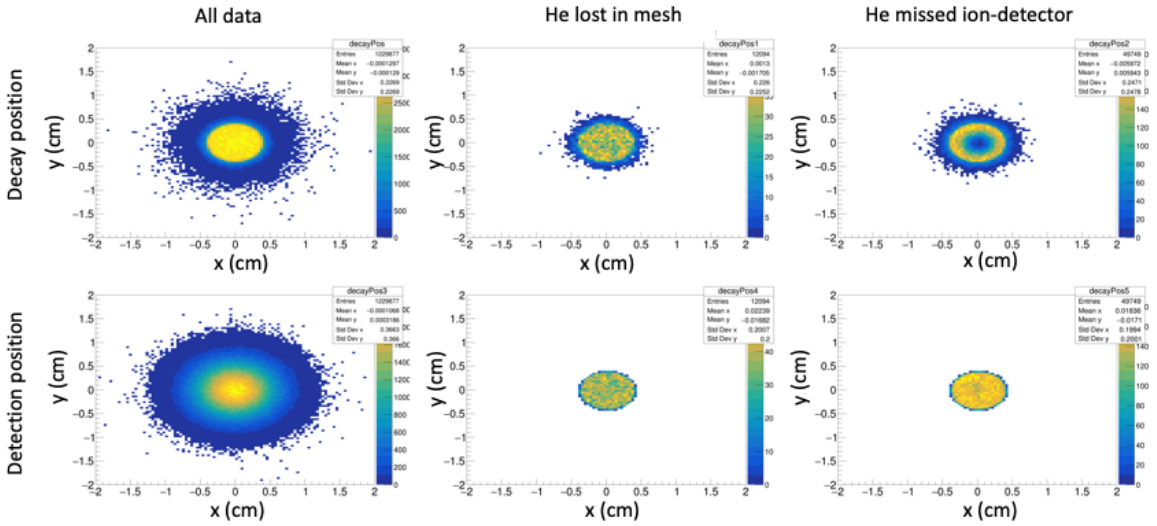

(a)

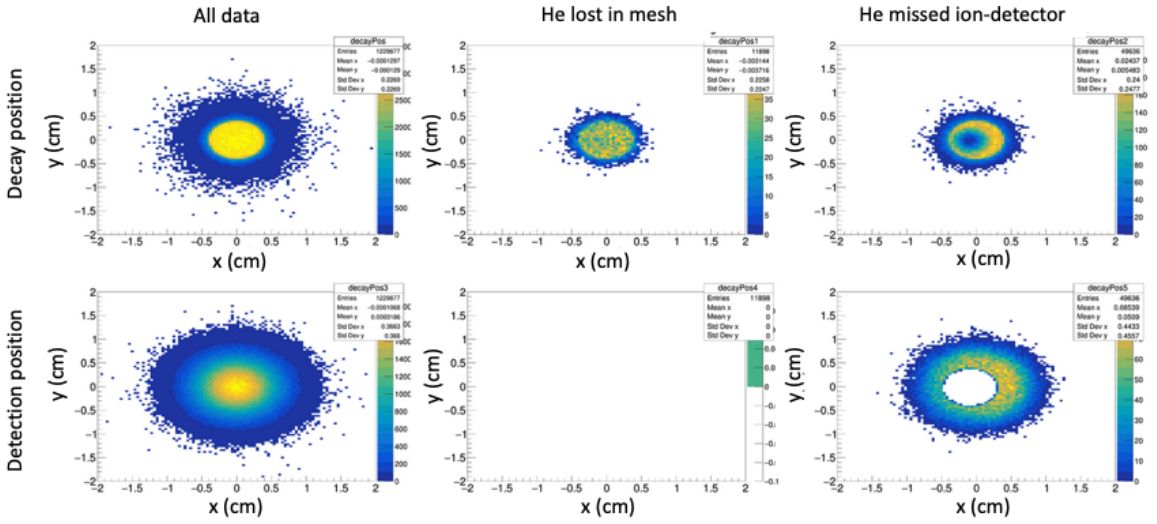

(b)

Figure 3.10: Simulation data of the HT β-decay position and the detected position of: (a) H^+ ion with the ion detector in the center position, and (b) He^+ ion with the ion detector in the $x = -1$ position, of the $\{H^+ + He^+\}$ decay branch. The detected position refers to a detection in a large simulated detector of radius 2 cm that covers all the scan positions of the ion detector. The left column contains all the data, without cuts; the middle column displays the case where He^+ hits the mesh and is lost while the proton is detected in the ion detector; and the right column displays the case where the He^+ misses the ion detector but the proton is detected.

3.3.4 Comparison of simulations and experimental data

Simulations of HT and TT β-decay in the TRIMS experiment were programmed by Lin [78], using the Geant4 software framework, and run by Byron Daniel for a variety of initial ion energies. The simulations' main purpose was to correct for the charge-CC (Sec. 2.2.3), but other studies were also carried out with them.

One of said projects was to try to reproduce the double peak structure observed in the RCF of the proton detection channels (Fig. 3.9). The goal was to obtain the proton energy of this double electronic excited final state by comparing experimental data with simulations. The following procedure was used:

- Run TRIMS simulations of the HT β-decay to the two-ion charge-2 branch ($H^+ + He^+ + \beta^- + e^-_{so}$), where the proton energy was uniformly distributed between [20, 100] eV, and the He^+ energy followed equation 3.15. Energy and momentum conservation was ensured.

- Cut the simulation data with the same base cuts used for the experimental data [78]. For example, use the main fiducial volume cut which restricts the decay position to occur in a volume at the center of the decay chamber.

- Select the data from the two-ion detection channels of the charge-2 branch (equation 3.18).

- Study the data from this branch by plotting the decay position and detected position of both ions.

- Bin the simulation data in proton energy and compare to experimental data. Three different energy bin sizes were tried, namely 1 eV, 2 eV, and 3 eV energy bins.

- Segregate the simulation data according to the mechanism by which the He^+ ion is lost, and compare to data.

- Segregate the simulation data according to the number of detected electrons, and compare to data.

- Weight each proton energy bin using the shakeoff electron spectrum

The HT β-decay position and ion-detection position, of the proton and the He^+, are displayed in Fig. 3.10. The structure of the data depends on the mechanism of how the He^+ is lost. The HT β-decay position is displayed in the top row. We get a homogeneous decay position for the case where He^+ is lost in the mesh because the mesh covers the whole

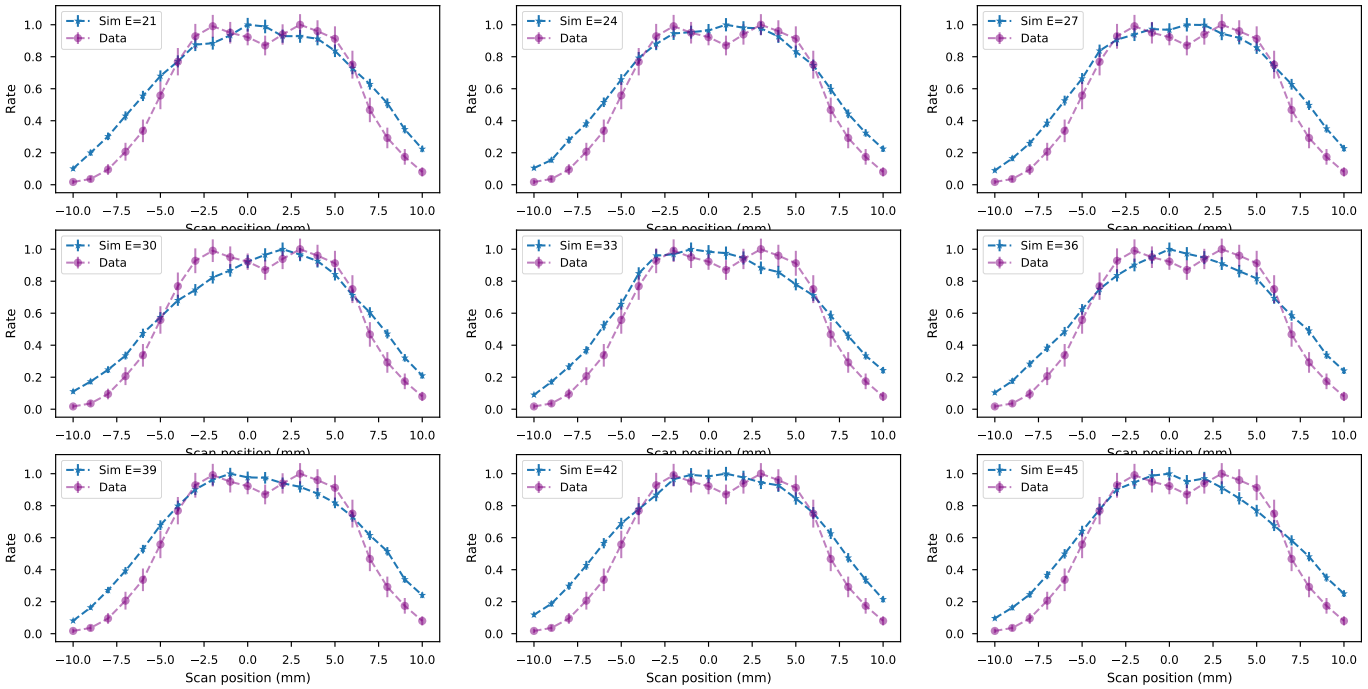

(a)

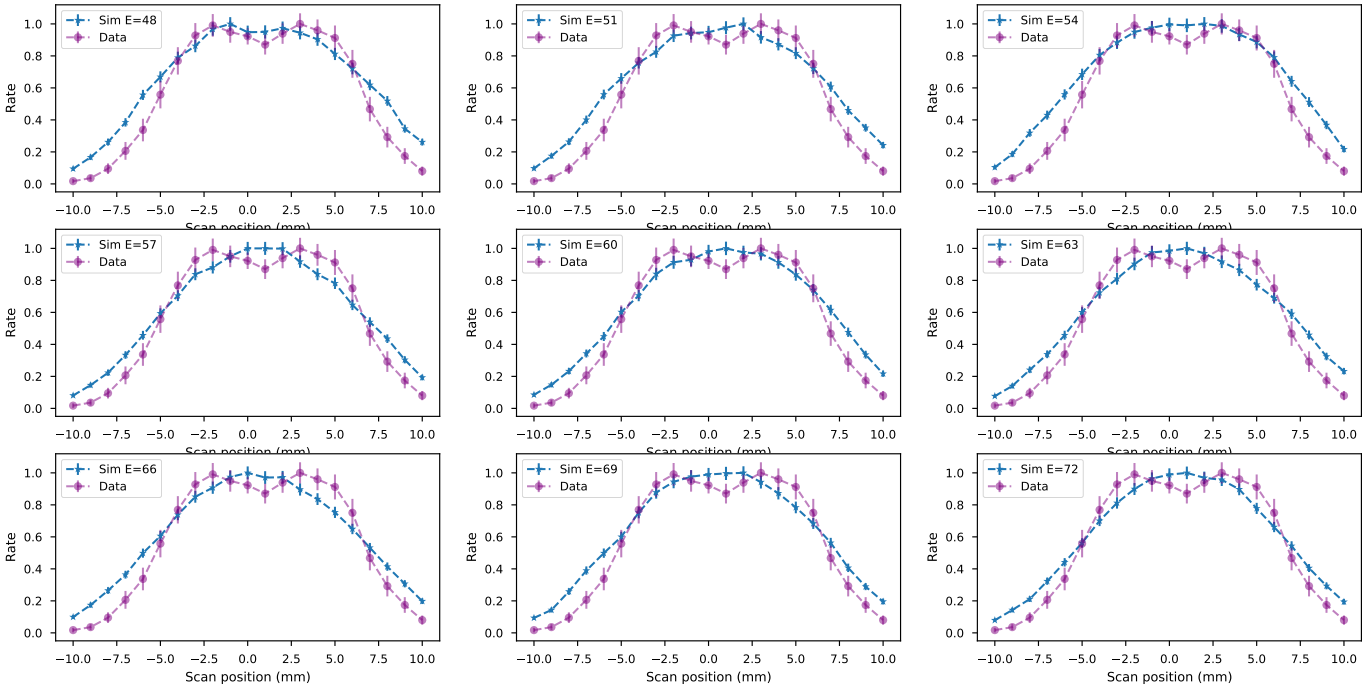

(b)

Figure 3.11: Simulation and data of the RCF of the proton detection bands $(H^+)He^+$ with one and two detected electrons. In the simulation data, the energy stated in the label refers to the H^+ ion in units of eV, and specifies the center of the 3 eV wide energy bin. The errors on the simulation are $\sqrt{N_i}$, where N_i is the rate at the scan position i. The data points are from Fig. 3.9.

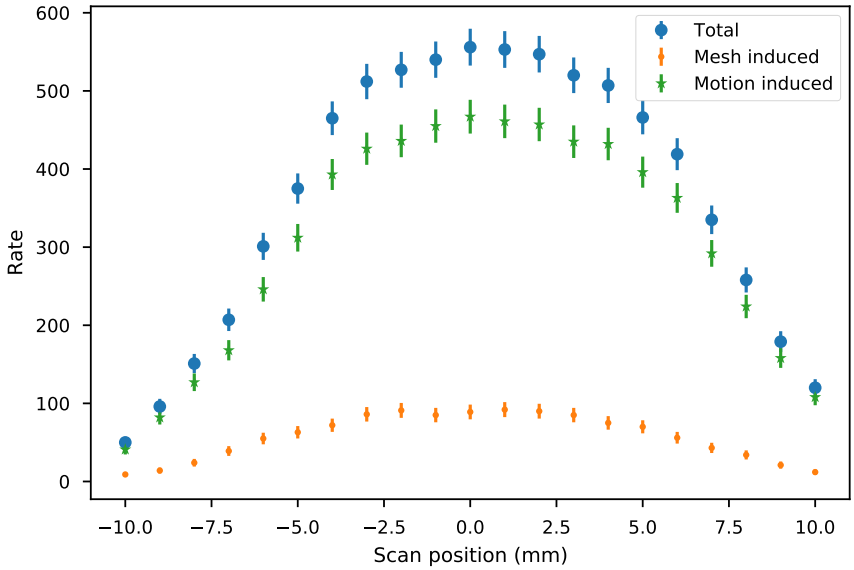

Figure 3.12: Simulation of the RCF to get the proton energy where the data is separated according to the mechanism in which the helium is lost: total data (blue circles), motion induced (green stars), and mesh induced (orange points). The errors on the simulation are $\sqrt{N_i}$, where N_i is the rate at the scan position i.

decay chamber exit; we observe a circular structure on the decay position when the He^+ misses the ion-detector due to its cyclotron motion, because of momentum conservation by the two ions. The detection position, on the bottom row, shows how the proton is detected (fig. 3.10a) and how the He^+ is not detected (Fig. 3.10b) in the ion detector.

The comparison of the RCF of the proton detection channels $(H^+)He^+$ between simulations and data can be seen in Fig. 3.11. Each plot contains the RCF with the proton energy stated in the label, and an energy bin of 3 eV. The double structure was not observed in the shown plots nor in the plots of other energy bins.

The next step consisted of investigating the simulation data. The RCF proton data was separated according to the mechanism in which the He^+ is lost, either by hitting the ion mesh or because of its cyclotron motion. This was done for all energies. Figure 3.12 shows the RCF where the data is segregated in the aforementioned way, for the case of H^+ energy of [31, 33] eV. Again, no double structure was found in any of the plots, for any proton-energy bin size.

Then, we segregated the RCF proton simulation data according to the number of detected electrons, either one or two. Figure 3.13 is an example plot, where the proton energy is in the range (31, 33) eV. Different energy bins were investigated but no double structure

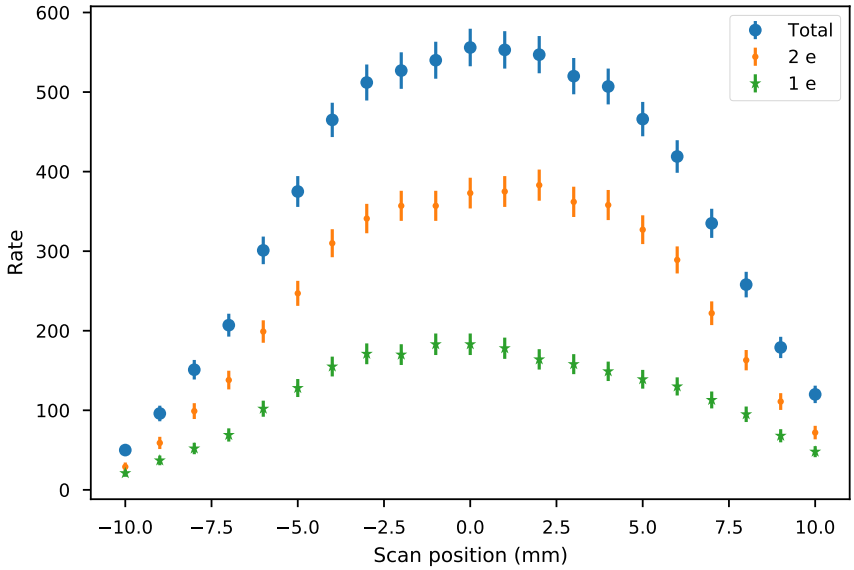

Figure 3.13: Simulation of the RCF to get the proton energy where the data is separated according to the number of detected electrons: total data (blue circles), two electrons (orange dots), and 1 electron (green stars). The errors on the simulation are $\sqrt{N_i}$, where N_i is the rate at the scan position i.

was found.

Finally, the shakeoff energy spectrum (Fig. 3.8) was used to weight the RCF proton data in the following manner. The proton starting energy was calculated in equation 3.16. Starting at that energy, the RCF was weighted with the shakeoff spectrum data, where the probability of the zero energy shakeoff electron was associated to the proton with energy $E_H = 32.45$ eV, and so on. Figure 3.14 shows the RCF of the proton detection channel weighted by the shakeoff energy spectrum. Again, we were unable to reproduce the data double structure.

3.3.5 Conclusion

A lower limit of the proton energy of the HT β-decay branch $\mathrm{H}^+ + \mathrm{He}^+ + \beta^- + e^-_{so}$ was calculated (Sec. 3.3.2).

We tried to extract the proton energy by comparing the RCF of the proton detection branch to simulations. The following things were tried: binning the data in different proton energy sizes; dividing the simulation data in accordance to the mechanism by which the helium ion is lost; separating the simulation data according to the number of detected electrons; and weighting the proton energy bins with the shakeoff energy spectrum.

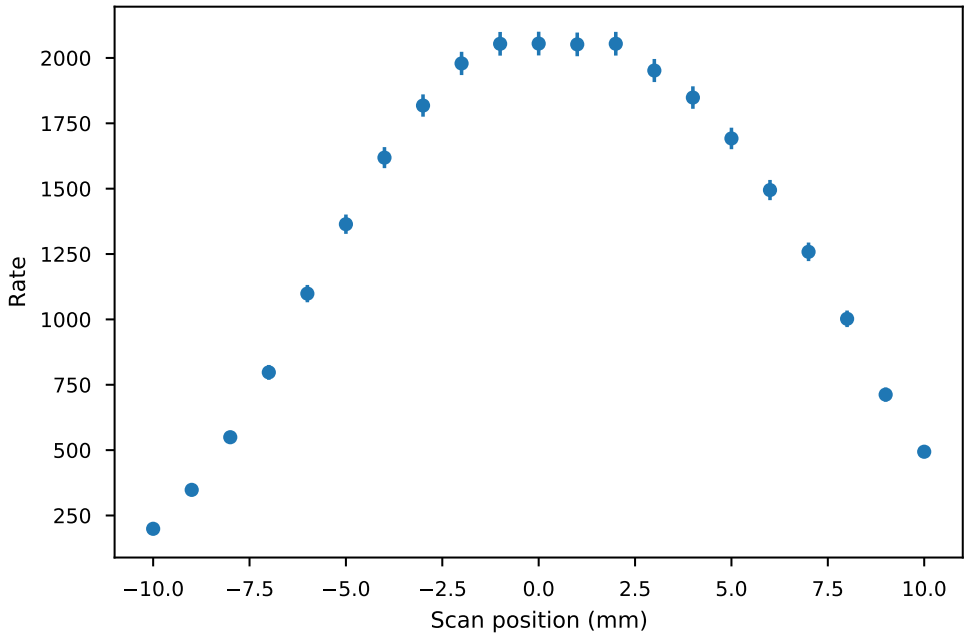

Figure 3.14: Simulation of the RCF of detection bands $(H^+)He^+$ weighted by the shakeoff energy spectrum (Fig. 3.8). The errors on the simulation are $\sqrt{N_i}$, where N_i is the rate at the scan position i.

The double structure, observed in the data, could not be reproduced with the simulations. The proton energy of the charge-2 branch could not be obtained via this method.

CHAPTER 4
THE KATRIN EXPERIMENT

The KArlsruhe TRItium Neutrino experiment (KATRIN) is designed to study the effective $\overline{\nu}_e$ mass (m_ν) by measuring the energy spectrum of the β-electron after tritium β-decay. The goal sensitivity on m_ν is 0.2 eV at the 90% confidence level. The measurement principle used to measure the β-energy spectrum is the MAC-E filter (Sec. 4.1).

The KATRIN experiment is located at the Karlsruhe Institute of Technology (KIT) Campus North, Karlsruhe, Germany. It is approximately 70 meters long and it consists of five main systems as shown in Fig. 4.1. The Rear System (Sec. 4.2.1), the Source System (Sec. 4.2.2), and the Transport System (Sec. 4.2.3) are located in the Source and Transport Section. The Spectrometer System (Sec. 4.3.1), and the Detector System (Sec. 4.3.2) are located in the Spectrometer and Detector Section. A more in depth description of the experimental set-up can be found in [86], along with additional references.

Besides the measurement principle and the experimental set-up, in this chapter I will give a brief overview of the analysis method used to extract m_ν. The data is analysed by comparing it with a spectrum model (Sec. 4.4.1). Then m_ν is extracted from the fit (Sec. 4.4.2). My analysis contributions on the study of the ions as a background source will be discussed with more detail in the next chapters (Chapters 7 and 8). Finally, the newest published results will be mentioned (Sec. 4.4.2).

4.1 Measurement principle, the MAC-E filter

The purpose of this section is to explain the measurement principle of the Magnetic Adiabatic Collimation with Electrostatic (MAC-E) filter used to measure the integrated β-energy spectrum in the KATRIN experiment.

The main goal of a MAC-E filter is to filter charged particles that have energies above a predefined energy threshold from particles that are not energetic enough. It does so by applying a magnetic adiabatic momentum collimator with an electrostatic energy filter.

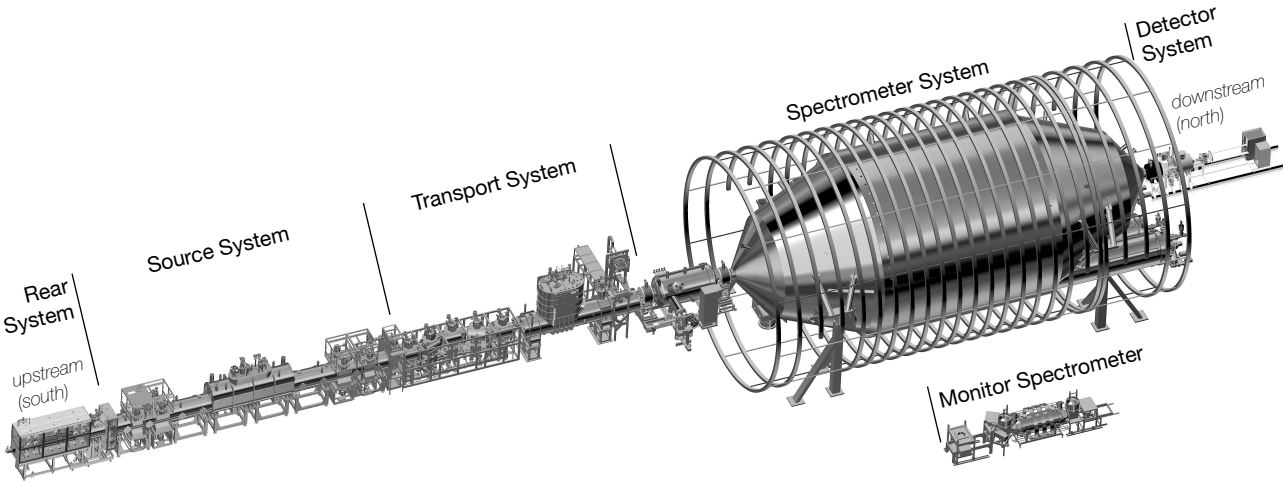

Figure 4.1: Experimental setup of KATRIN. The total length is about 70 m. The main five systems are identified together with the monitor spectrometer that, as the name suggests, monitors the main spectrometer. The β-electrons from β-decay are created in the source and are guided by magnetic fields towards the detector system (downstream) and the rear system (upstream). Figure taken from [86].

In the KATRIN experiment, the spectrometers have a retarding potential (U) that sets a threshold on the electron's kinetic energy (E). The electron will get to the Focal Plane Detector (FPD) if its momentum ($p_\parallel$) parallel to the magnetic field (B) is always greater than zero [87], or in other words, if the corresponding kinetic energy fraction ($E_\parallel$) is always greater than zero. The kinetic energy from motion parallel to the magnetic field is defined as:

$$E_\parallel = E \sin^2 \theta, \tag{4.1}$$

where θ is the pitch angle, relative to the magnetic field.

In a MAC-E filter, the transverse momentum of the electron is transformed to parallel momentum due to the following adiabatic invariant:

$$\frac{p_\perp^2}{B} = \text{const.} \tag{4.2}$$

This equation corresponds to the conservation of orbital momentum in the non-relativistic limit ($\mu = E_\perp / B = \text{const}$), where the relation between the electron's transverse momen-

tum and energy is:

$$p_{\perp}^2 = E_{\perp}(\gamma + 1) \cdot m_e, \tag{4.3}$$

and where m_e is the electrons mass, and the relativistic gamma factor is $\gamma = \frac{E}{m_e} + 1$. Using it we can define the adiabatic transmission condition [87] for all positions z:

$$0 \leq E_{\parallel}(z) = E + qU_s - E \sin^2 \theta \cdot \frac{B(z)}{B_s} \frac{\gamma + 1}{\gamma(z) + 1} - qU(z) \tag{4.4}$$

where U_s and B_s correspond to the electric and magnetic fields at the electron's creation position $z = s$ in the source.

A sketch of the MAC-E principle in the KATRIN main spectrometer is shown in Fig. 4.2.

The filter width of the MAC-E filter (ΔE), or the maximum residual transverse energy that is not analyzed by the filter, depends on the ratio of the Main Spectrometer (MS) maximum magnetic field, at its exit, and the minimum magnetic field (at the analysing plane), usually in its middle [87]:

$$\Delta E = \frac{B_{\min}}{B_{\max}} \cdot E \frac{\gamma + 1}{2}. \tag{4.5}$$

The filter width achieved by KATRIN during nominal neutrino mass measurements is $\Delta E = 2.8$ eV [77].

The maximum acceptance angle, or the maximum pitch angle that the βs can have where enough of their perpendicular momentum is transformed to parallel momentum to overcome the retarding potential, can be calculated by:

$$\theta_{\max} = \arcsin \sqrt{\frac{B_s}{B_{\max}}}, \tag{4.6}$$

where B_s is the magnetic field at the source where the β-electrons were created. The maximum acceptance angle for nominal KATRIN conditions is $\theta_{\max} = 50.4°$ [86].

The β-electrons that are not energetic enough are reflected and end up hitting the Rear Wall (RW) where they are neutralized. The integral β-energy spectrum is measured by varying the MS retarding potential. Since there is less data in the background region ($qU > 18.6$ keV) more measurement time is needed to record a good count-rate in this region, and less time at higher count-rate regimes. The KATRIN measurement time distribution will be shown in the next section.

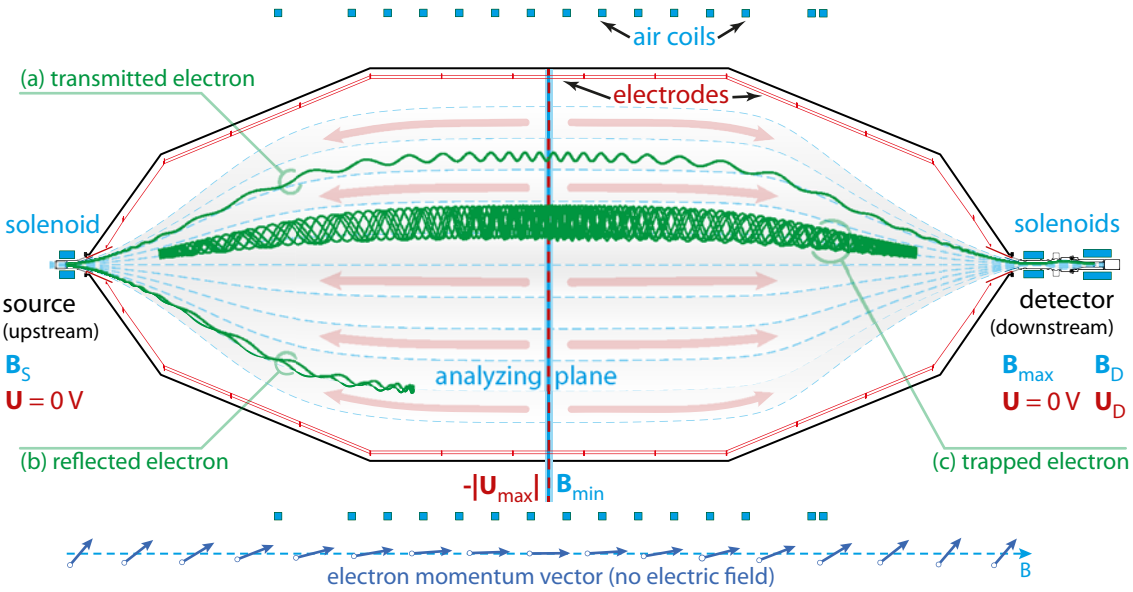

Figure 4.2: MAC-E filter principle. The trajectories of a transmitted, a reflected, and a trapped electron are represented with green lines. The rotation of electron momentum is depicted at the bottom in blue. The magnets, magnetic field lines, and the analysing plane are represented in light blue. Figure taken from [86].

4.2 Source and Transport Section

The Source and Transport Section (STS) is located inside the Tritium Laboratory Karlsruhe (TLK) which is a laboratory with all the safety requirements to work with large quantities of tritium. The main purposes of the STS are: to calibrate and monitor the tritium gas in the beamline (Sec. 4.2.1); to circulate pure tritium gas in the source section (Sec. 4.2.2); to produce β-electrons from β-decay and adiabatically guide them towards the spectrometer section (Sec. 4.2.2 and 4.2.3); and to pump out ions and neutral tritium gas (Sec. 4.2.3).

4.2.1 Rear system

The rear system is the only system located upstream from the source. It consists of: an e-gun, used to calibrate and monitor the total amount of gas in the beam-line; superconducting magnets that guide the electrons from the e-gun towards the source; and a rear wall which is used, among other things, to study and to influence the source plasma.

The RW is a gold-coated stainless-steel disk with a diameter of 145 mm. It has a 5 mm hole in the center through which the e-gun electrons go. Fig. 4.3 gives a cross-section view of the RW unit. Some of its main features are the following:

- A bias voltage can be applied to it, and it is connected to a picoammeter to measure the current flowing from the disk to the ground. The plasma and the RW have good

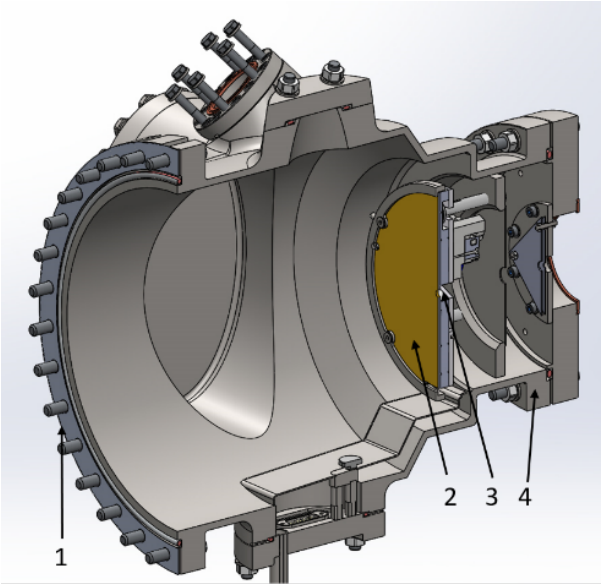

Figure 4.3: Cross section view of the rear wall unit. 1) and 4) are flanges connecting the unit with the Rear System and the source magnet respectively. 2) points to the RW and 3) to the hole in its center. Figure taken from [86].

conductance so changes in the RW voltage affect the plasma.

- The flux tube of β-electrons, secondary electrons, and ions, is completely mapped by the magnetic fields onto the RW. Some of these charged particles end up hitting the RW surface where they are absorbed and neutralized. The neutralized particles include: the ones created at the source with upstream momentum, and the reflected particles with insufficient energy to overcome the retarding potential of the spectrometers.

- A Cermax xenon lamp (type PE1000DUV) can be turned on to illuminate the RW with ultraviolet (UV) light, with the objective of producing photoelectrons.

4.2.2 Source system

The source system is also known as the Windowless Gaseous Tritium Source (WGTS). The WGTS tube is 10 m long and has a diameter of 90 mm. Tritium gas is injected in the central region of the tube, the tritium β-decays, and then the charged particles are guided with magnetic fields towards the spectrometer section and the rear section. The tritium molecules diffuse from the middle of the tube toward its ends where they are pumped out. The density profile within the WGTS can be seen in Fig. 4.4. A continuous tritium flow is maintained to achieve a quasi constant β-electron rate of around 10^{11} β per second. A

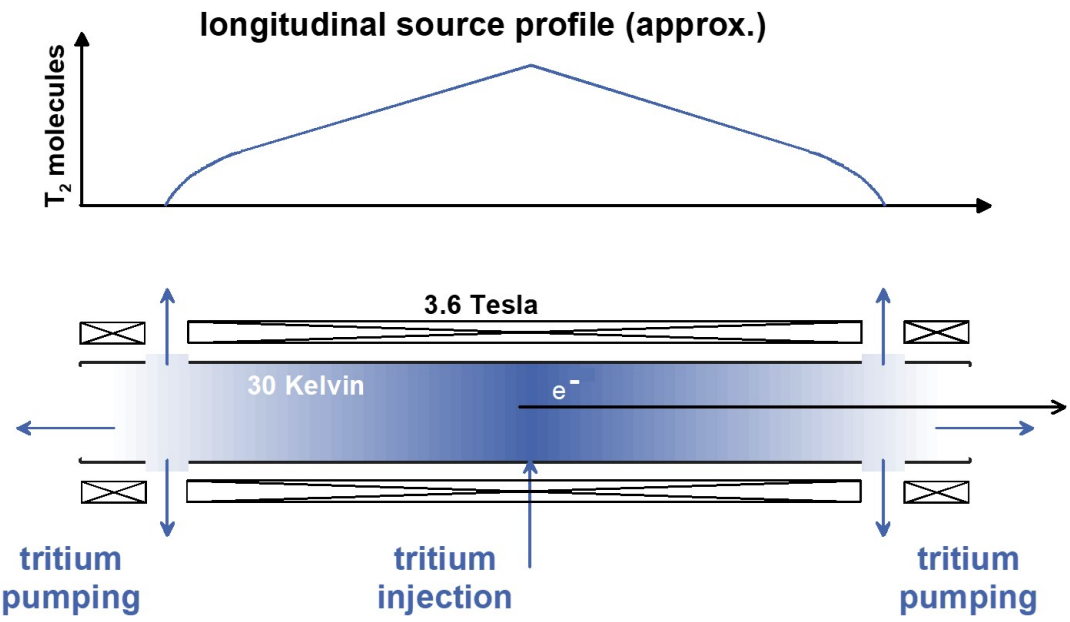

Figure 4.4: Tritium gas injection and pumping principle in the WGTS. The density profile is kept constant by the continuous injection and pumping of the tritium gas. Figure taken from [86].

nominal low temperature of 30 K is maintained to reduce the conductance of the tube.

There are some parameters of the WGTS that directly impact the measurement of the β-energy spectrum, and their exact values and stability are vital for the m_ν measurements. A complete list of the WGTS parameters and their impact on the systematic uncertainties of the m_ν measurements can be found in [88]. The most important parameters include:

- The tritium gas isotopic composition, or the tritium-purity, which refers to the fraction of tritium atoms within the inserted gas. The KATRIN tritium-purity requirement during neutrino mass measurements is 95% or more.
- The column density, which is the density of tritium molecules that are inside the flux tube[1] at a given time. It is expressed in units of molecules/cm^2.

A high stability of the tritium isotopic composition and of the column density is desirable to combine data from different m_ν measurement campaigns.

4.2.3 Transport system

As its name suggests, the transport system guides β-electrons adiabatically from the WGTS towards the spectrometer section using superconducting magnets. Besides that, it reduces

[1]The flux tube refers to the envelope in which beta electrons travel through the beamline.

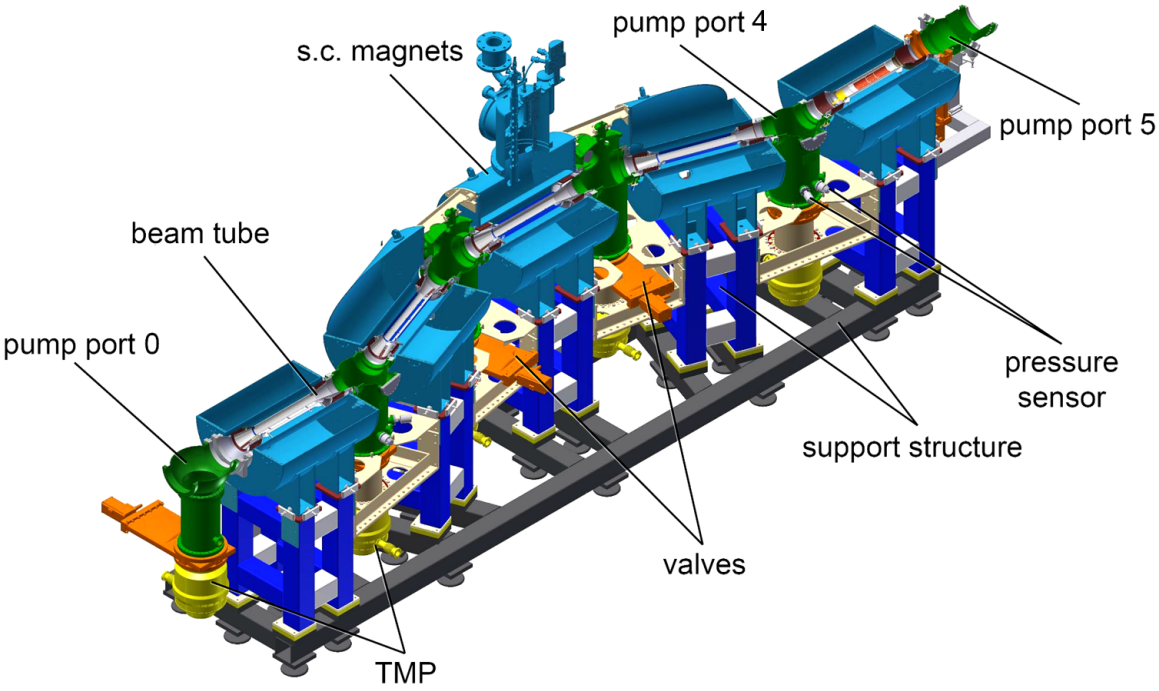

Figure 4.5: Drawing of the differential pumping section. The five superconducting (s.c.) magnets are represented in light blue, the six pump ports are represented in green, and the four dipole electrodes are grey. Figure taken from [86].

the tritium gas and ion flow by more than 12 orders of magnitude. This is necessary to comply with the background limit of 1 mcps coming from ion interactions or tritium β-decay in the spectrometer section. The flow reduction goal is achieved by a combination of differential and cryogenic pumping.

Differential Pumping Section

The Differential Pumping Section (DPS) is part of the transport system and it is located downstream of the WGTS and upstream of the cryogenic pumping section. It consists of a beam tube at room temperature that is surrounded by five adjacent superconducting magnets. Between each pair of magnets there is a pump port, and inside each of the first four magnets there is a dipole electrode (Fig. 4.5).

The main objectives of the DPS are:

- Guide the β-electrons adiabatically from the WGTS to the cryogenic pumping section.
- Reduce, together with the first pumping stage (located in the WGTS), the neutral tritium flow rate by seven orders of magnitude.

- Block and remove the tritium ions coming from the source.

The charged particles are guided adiabatically with 5 superconducting magnets. The magnets are cooled down with liquid helium and they are operated in persistent current mode. The neutral tritium flow is reduced by differential pumping. Two Turbo Molecular Pump (TMP), type Turbovac MAG W 2800, are attached to pump port 0, while the rest of the pump ports have a single TMP attached to each [86]. The tritium ions cannot be removed with the pumps because they follow the magnetic field lines and the pump ports are positioned outside of the ion flux tube. Instead the ions are blocked with ring electrodes and are removed with the dipole electrodes, as will be explained in Sec. 5.3.

Cryogenic Pumping Section

The Cryogenic Pumping Section (CPS) is a part of the transport system located downstream of the DPS and upstream of the pre-spectrometer. The CPS beam tube is partitioned into 7 regions, each of which is surrounded by a superconducting magnet cooled down by liquid helium. A cryo-sorption pump with a condensed argon layer is positioned in sections 2-5 of the beam tube and is cooled to 3 K. A drawing of the CPS is shown in Fig. 4.6. The sorption pump is located on the inner surface of the gold-plated beam-tube wall. The residual tritium contamination is minimized by the easy removal and generation of the condensed argon layer as opposed to a solid adsorbent layer.

The main objectives of the CPS are to guide the β-electrons towards the Pre-Spectrometer (PS) and to reduce the neutral tritium gas flow by seven orders of magnitude.

The argon pump has three operational modes: **preparation of argon pump**, in which the beam tube is set to 6 K to provide optimal conditions for porosity which leads to optimal adsorption capacity; **standard operation** in which the beam tube is set to 3 K to minimize thermal desorption of tritium molecules; **regeneration of argon pump** in which the argon is purged by setting the beam tube to 80 K and circulating helium gas. A new argon frost layer is generated after setting the beam tube to preparation-of-argon conditions. A purge is done once a year.

4.3 Spectrometer and Detector Section

The Spectrometers and Detector Section (SDS) is located downstream of the transport section. It consists of: three spectrometers, two of which are used to filter the β-electrons while the third one is used to monitor the main spectrometer (Sec. 4.3.1), and the main electron detector system (Sec. 4.3.2).

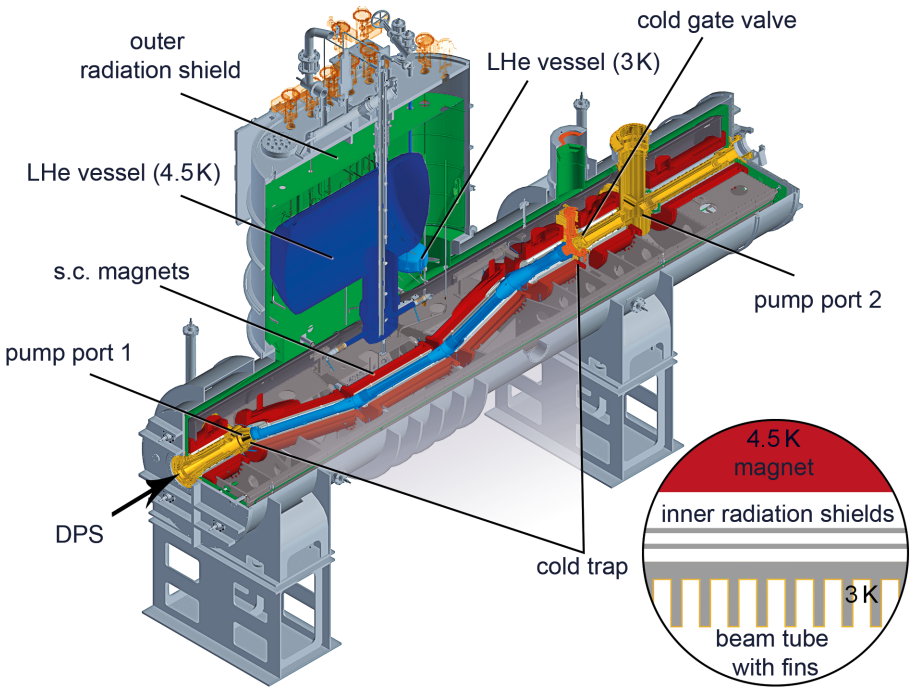

Figure 4.6: Drawing of the Cryogenic Pumping Section. The superconducting magnets are depicted in red, the cold trap is light blue, and the liquid helium tank is dark blue. Figure taken from [86].

4.3.1 Spectrometer system

The spectrometer system encompasses three different MAC-E filters: the PS which was used to filter most of the β electrons during KATRIN Neutrino Mass measurement 1 (KNM1) and KATRIN Neutrino Mass measurement 2 (KNM2), the MS which is used as a high- precision filter of the β-electrons near the tritium end point, and the Monitor Spectrometer (MoS) that is connected in parallel to the KATRIN beam line and used to monitor the MS. The MAC-E filter principle is explained in Sec. 4.1.

The three key subsystems of each spectrometer are: vacuum, high voltage system and magnetic fields.

Pre-Spectrometer

The Pre-Spectrometer is located between the CPS and the Main Spectrometer. Its main function is to filter the low-energy β-electrons, which are the great majority, to prevent them from reaching the MS where they can interact with residual gas and increase the background. It is also used to monitor the ion flux into the SDS (Sec. 5.4.2).

The PS consists of a stainless steel vessel which is 3.4 m long, has a diameter of 1.7 m and a total volume of 8.5 m^3 [89]. It is set to ultra-high vacuum, reaching a pressure on

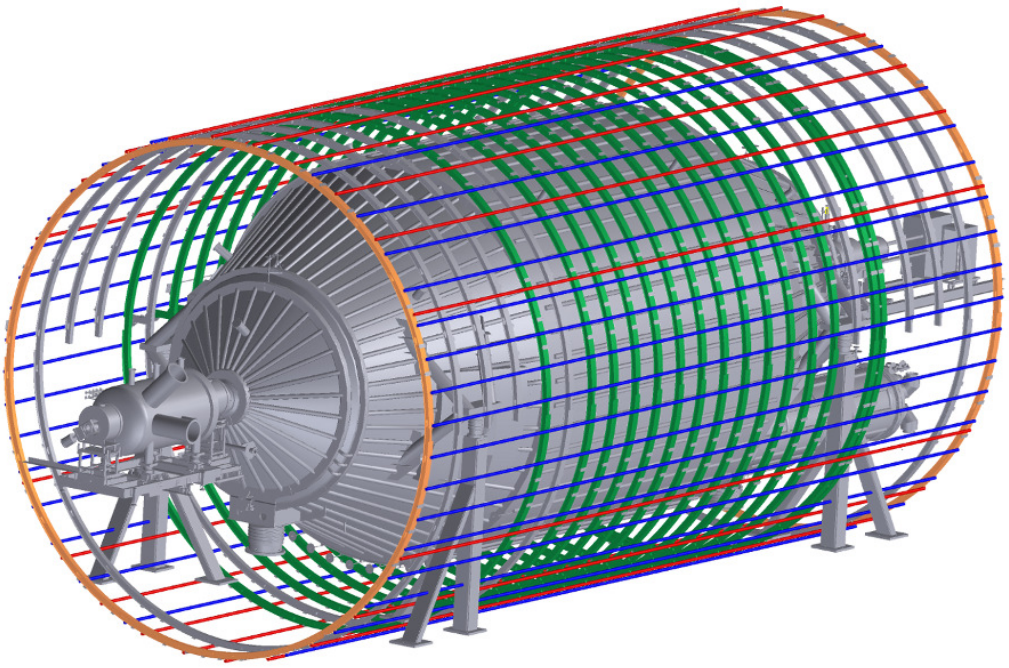

Figure 4.7: View of the SDS with the air coils. The green coils are used to shape the magnetic field inside the MS and the rest to correct for the earth magnetic field. One pump port can be seen on the lower right behind the air coils. Figure taken from [86].

the order of 10^{-11} mbar by way of two TMPs and by baking the PS to high temperatures, up to 350° C. It is mantained at that pressure via a getter pump [90]. Two superconducting solenoid magnets are located at the entrance and exit of the PS. They are set to $B = 3.15$ T and they create the magnetic field lines that charged particles follow.

Inside each magnet a ring electrode is set to a positive potential to block positive ions from flowing into the PS and the MS. There are three inner electrodes (two cone electrodes and a wire electrode) inside the vessel, and together with the vessel they can be set to high voltage. The downstream cone electrode measures a current that is used to monitor the flux of ions into the PS. A more extensive explanation can be found in Sec. 5.4.

Main Spectrometer

The Main Spectrometer is located downstream of the PS and upstream of the detector system. Its main function is to filter, with high resolution, β-electrons with energies above an adjustable potential threshold.

The MS consists of a stainless steel vessel in ultra-high vacuum. It is 23.2 meters long, it has a diameter of 9.8 m, it weighs over 200 t and its volume is around 1240 m^3 [91]. It has 11 ports with flanges on the upper part that provide high voltage feedthroughs, gas

inlets, pressure gauges, and a sapphire window through which UV light can shine into the vessel and produce photoelectrons in the process.

The magnetic field is shaped by two superconducting magnets located at the entrance and exit (the pinch magnet), set to $B = 3.15$ T and $B = 4.2$ T respectively. An air coil system surrounds the vessel with the purpose of compensating for the earth's magnetic field, and compensate for the fringe fields of the superconducting solenoids. A drawing of the SDS is shown in Fig. 4.7.

The pressure inside the vessel is on the order of 10^{-11} mbar. It is achieved by baking the vessel to 200° C and using getter pumps. Three TMPs located in horizontal pump ports are used to pump the vacuum system during bakeout.

The high voltage applied to the vessel (around -18.6 V) produces the retarding potential. It is fine-tuned with a two-layer inner wire electrode system. The wire electrodes also serve the purpose of reducing background. Particles hitting the vessel produce secondary electrons which are reflected back to the vessel by the negative potential of the wires before they can enter the flux tube.

4.3.2 Detector system

The detector system is the farthest downstream component of the experimental setup. It encompasses: the main detector also known as the FPD, calibration and monitoring devices, a scintillating veto device, two superconducting magnets, a Faraday Cup, and a data-acquisition system. It has ultra-high vacuum and high vacuum regions. An overview of the whole system is shown in figure 4.8.

The Focal Plane Detector

The main objective of the FPD is to detect the β-electrons that are transmitted through the MS inside the flux tube. The β-electrons are guided adiabatically towards the detector wafer by two superconducting magnets, the pinch magnet and the detector magnet. They are accelerated with the Post Acceleration Electrode (PAE), which is typically set to 10 kV, to move the signal peak into a region with less intrinsic background.

The FPD is a monolithic pin-diode array with 148 pixels on a silicon wafer with a diameter of 125 mm, a thickness of 503 μm, and a dead layer thickness of approximately 100 nm. The active area is 90 mm in diameter.

A Faraday cup, read out by Precision Ultra-Low Current Integrating Normalization Electrometer for Low-Level Analysis (PULCINELLA), is stored outside of the flux tube between the pinch and the detector magnets. It can be inserted into the beam tube, upstream

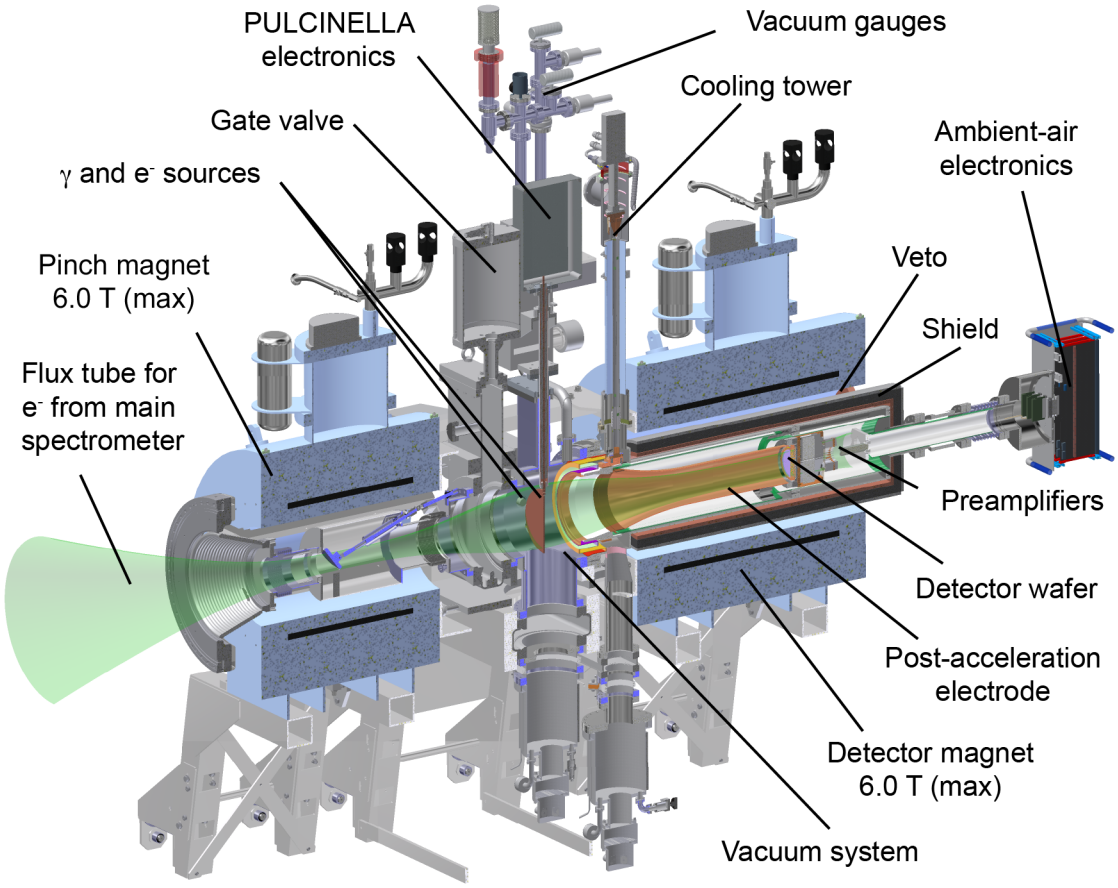

Figure 4.8: Overview of the detector system. The flux tube for the β-electrons (green shaded region) is inside the magnets (light blue). The γ calibration source, and the e^- calibration source can be moved to the center of the flux tube. PULCINELLA is the pico-ammeter that reads the currents on the Faraday cup. The detector wafer sits in the middle of the detector magnet. Figure taken from [92].

of the detector wafer.

Data Acquisition and Readout Electronics

Each pixel of the detector triggers and records data independently of the others. The signal coming from the detector wafer is amplified and shaped by pre-amplifier cards. Signals travel across the PAE potential on fiber optics. The signal is processed to determine the energy and timing of the signal; the energy and timing are reconstructed with a double trapezoidal filter.

From the data acquisition (DAQ) computer it is possible to choose different data taking settings. The **trace mode** records the waveform for each event; the **energy mode** saves the energy and timing information for each event, and is the normal operational mode; and the **histogram mode** is used for high-rate data where the recorded information is a histogram of all the event energies in a given time interval.

4.4 Neutrino mass analysis method

The KATRIN experiment measures the effective $\overline{\nu}_e$ mass m_ν (Eq. 1.26) by measuring the energy spectrum of the β-electron. The purpose of this section is: to give a quick overview of how m_ν is extracted from the β-energy spectrum (Sec. 4.4.1); and to present the current best-fit results of KATRIN m_ν value (Sec. 4.4.2).

4.4.1 KATRIN analysis method

The purpose of the KATRIN main analysis is to extract m_ν from the measured β-energy spectrum by fitting the data with a model of the spectrum with just four free parameters. The spectrum model is constructed using two main components: the theoretical tritium β-energy spectrum and the response function of the β-electrons while travelling in the KATRIN experiment.

Source spectrum modelling

There are two primary source modes in the KATRIN source section: krypton mode (used to calibrate), and tritium mode. Here, we focus on tritium mode. The first component of the spectrum model, constructed to fit KATRIN data, is the theoretical calculation of the source decay. The theory and the method used to do this calculation were covered in chapter 1.5, where equation 1.23 gives the differential β-energy spectrum. An integrated spectrum can be constructed by summing over the desired energy values weighted by their probabilities.

Response function

Before the β-electron is detected with the FPD, it travels throughout the KATRIN experiment. Since the experiment is not under perfect vacuum and the β-electron is not completely isolated, there will be some interactions that need to be accounted for.

The response function ($R(E, U_{\rm ret})$) covers the β-electron interactions within the KATRIN experiment. It depends on the electron energy (E) and the retarding potential ($U_{\rm ret}$). Some of the minimum ingredients that the response function needs to incorporate are: the transmission function, which incorporates the filter width (Eq. 4.5) and the maximum acceptance angle (Eq. 4.6) to calculate the transmission of β-electrons through the MAC-E filter; radial inhomogeneities of the electromagnetic field; source volume segmentation and effects; scattering probabilities; Doppler effect; cyclotron radiation, and other energy loss processes [87].

Figure 4.9 shows the response function with longitudinal source segmentation. The response function used for the m_ν analysis is the average function, the solid green line in Fig. 4.9. It is constructed by weighting the "location" response functions by the tritium density inside the WGTS. A detailed construction of the response function can be found in [87].

Finally the model used to fit the data is constructed by a convolution of the theoretical tritium β-energy spectrum and the response function.

Fit of the measured β-energy spectrum

The total rate measured by the FPD for a specific retarding potential ($U_{\rm ret}$) is then theoretically predicted with: the theoretical β-energy spectrum ($\frac{dN}{dE}(E, E_0, m_\nu^2)$) from equation 1.23 and the response function ($R(E, U_{\rm ret})$):

$$\frac{dN^{\rm pre}}{dt}(U_{\rm ret}, E_0, m_\nu^2, A_{\rm sig}, A_{\rm bg}) = \frac{1}{2} A_{\rm sig} \int_{qU_{\rm ret}}^{E_0} \frac{d^2N}{dtdE}(E, E_0, m_\nu^2) \cdot R(E, U_{\rm ret}) dE + A_{\rm bg}, \tag{4.7}$$

where the parameters are [87]:

- The $\overline{\nu}_e$ **effective mass squared** (m_ν^2) is our main parameter of interest. It distorts the spectrum especially near the end point and so it is in this region where the experimental data is gathered.

- The **tritium end point** (E_0), is the maximum kinetic energy that the electron can have after β-decay assuming a vanishing neutrino mass, and it depends on the KATRIN experimental energy scale.

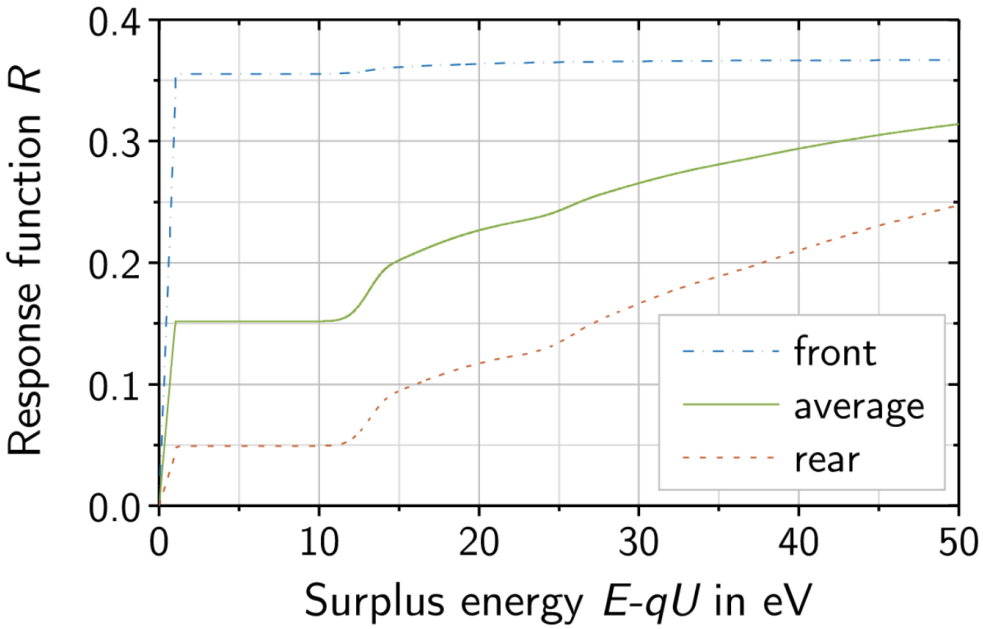

Figure 4.9: Response function (R) of the KATRIN experiment close to the front (dash-dotted blue line) and to the rear (dashed red line) of the WGTS. The average, weighted by the tritium density inside the WGTS, is also shown (solid green line). The retarding energy used is $qU = 18.545$ keV. Figure taken from [87].

- The **signal amplitude** (A_{sig}) is a factor close to 1 used to multiply the predicted signal rate that corrects for energy-independent model uncertainties.
- The **background rate amplitude** (A_{bg}) is the factor used to account for the background, which is assumed to be energy independent.

The effect, or the shift, that the previously described parameters induce on the β-spectrum is seen in the top plot of Fig. 4.10 using simulation data. The region of the spectrum where $m_\nu > 0$ makes the biggest distortion is seen in the middle plot of Fig. 4.10. Finally the measurement-time distribution is depicted on the bottom plot.

Having the complete spectrum model, it is possible to compare it with the measured data. The statistical analysis technique used is the following: compare the observed number of counts N_k^{obs} for a set of experimental retarding potentials U_k with the predicted counts $N^{\text{pre}}(U_k, m_\nu^2, E_0, ..)$ (Eq. 4.7) and infer the parameter m_ν^2 together with the nuisance parameters. The KATRIN experiment fits the model to the whole spectral shape and gets one set of parameters.

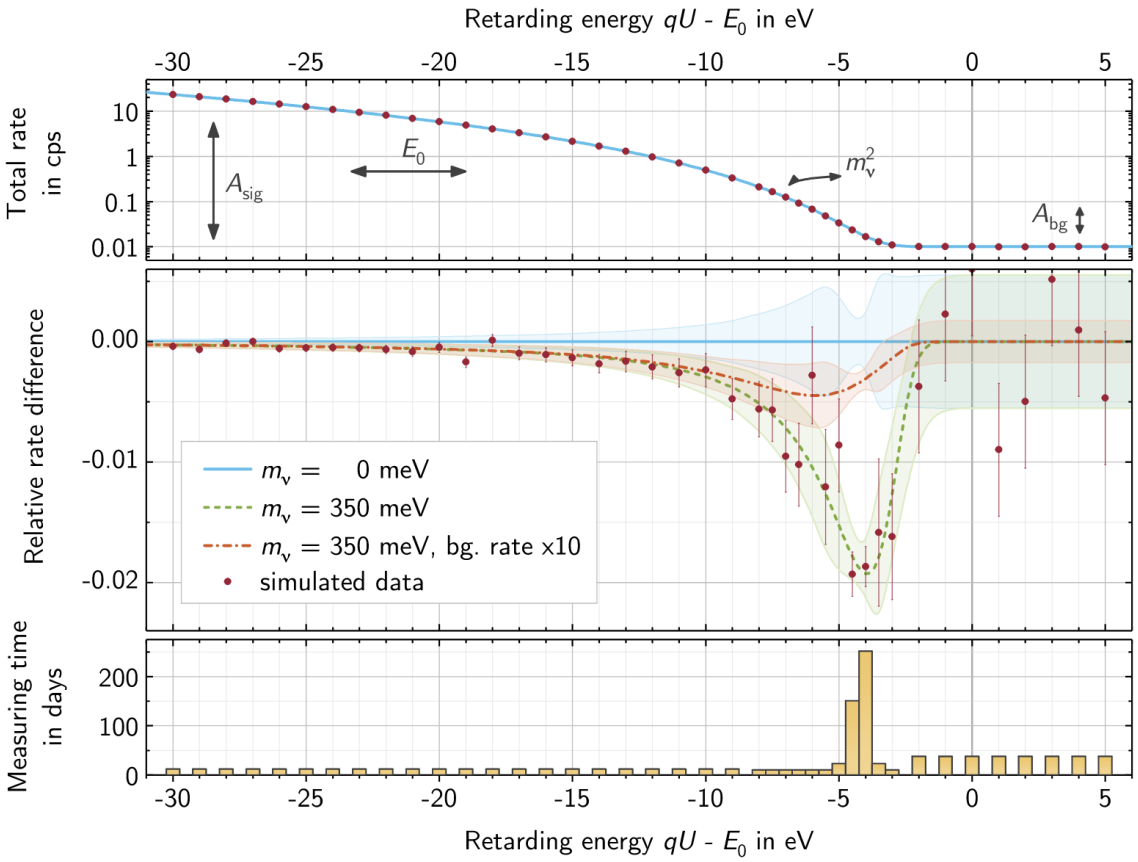

Figure 4.10: Simulation toy data of a β-spectrum for $m_\nu = 350$ meV with statistical uncertainties (red points), compared against the theoretical model with $m_\nu = 0$ (light blue). Top plot: sketch of how the free parameters can affect the β-energy spectrum. Middle plot: relative difference between theoretical models with $m_\nu = 0$ and $m_\nu = 350$ meV (green dashed line) or $m_\nu = 350$ meV with bg. rate $\times 10$ (red dotted dashed line); for a normal background the maximum distortion due to m_ν is around 4 eV below the endpoint, but the distortion is shifted towards lower energies for increased background. Bottom plot: Measurement time distribution attributed to each retarding potential. Figure taken from [87].

Effect	68.2 % CL uncertainty on m_ν^2 (eV^2)
Statistical	0.29
Non-Poissonian background	0.11
Source-potential variations	0.09
Scan-step-duration-dependent background	0.07
qU-dependent background	0.06
Magnetic fields	0.04
Molecular final-state distribution	0.02
Sum of smaller additional uncertainties	≈ 0.02
Total uncertainty	0.34

Table 4.1: Main systematic uncertainties on m_ν for the KNM2 measurement campaign in the KATRIN experiment. Table modified from [77].

Uncertainties

The data and the theoretical model of the spectrum contain experimental and theoretical parameters that have associated uncertainties. The uncertainties are propagated to the final result via statistical methods such as: covariance matrices, Monte-Carlo propagation, or Bayesian prior.

Up until now the uncertainties of the m_ν results presented by the KATRIN experiment are statistically dominated. This will change as more data is collected. Table 4.1 contains a current list of the main systematic uncertainties; the largest ones are related to background properties and source electric potential. That is why it is important to study the background in the KATRIN experiment.

4.4.2 Neutrino mass results

The current best limit on the m_ν comes from early runs of the KATRIN experiment. The figure 4.11 upper plot shows a fit to data from the KNM1 campaign with the error bars multiplied by 50 to make them visible. The normalized residuals are plotted in the middle plot and finally the measurement-time distribution used to get the data is displayed in the bottom plot.

The current m_ν best result was obtained by jointly fitting the data from the first two KATRIN neutrino mass campaigns (KNM1 and KNM2). The best fit to the squared neutrino mass obtained from KNM2 is $m_\nu^2 = 0.26^{+0.34}_{-0.34}$ eV^2; the upper limit was found to be $m_\nu < 0.9$ eV at 90 % CL [77] using the Lokhov-Tkachov method for the confidence interval [93]. By combining the results from the two campaigns the upper limit is found to be $m_\nu < 0.8$ eV at 90 % CL [77] again using the Lokhov-Tkachov method.

KATRIN continues to acquire and analyze data; the goal sensitivity on m_ν is 0.2 eV at

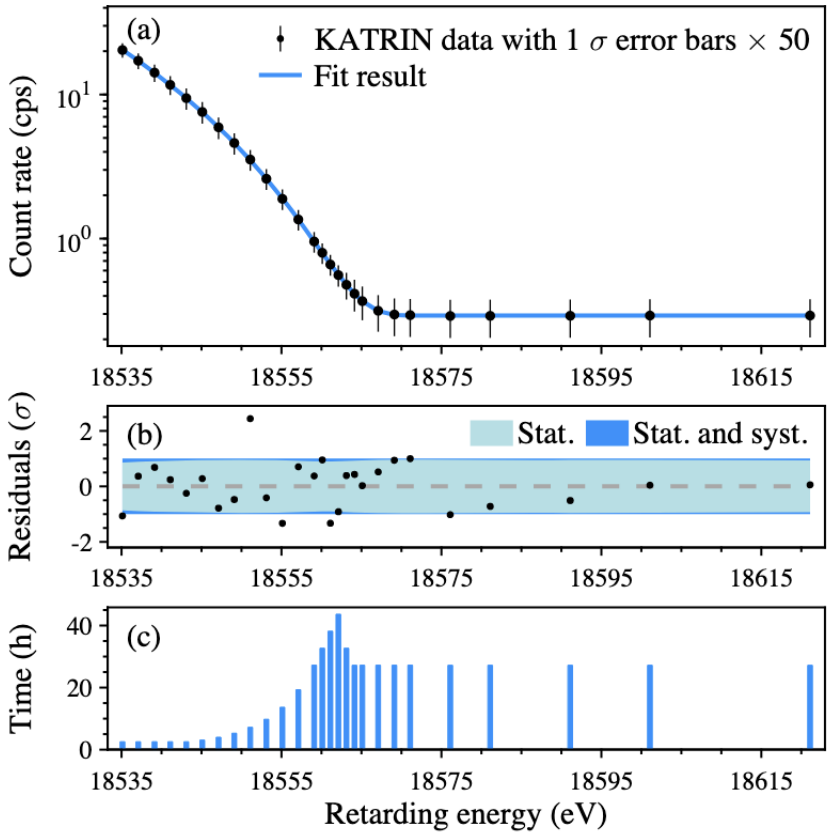

Figure 4.11: Upper plot: KATRIN KNM1 β-spectrum data (black dots) with error bars multiplied by 50 to make them visible, show with the fit result (blue line). Middle plot: Normalized residuals. The statistical uncertainties dominate (light blue) while the systematics are small in comparison (dark blue). Bottom plot: Measurement time distribution at each retarding potential. Figure taken from [47].

the 90% confidence level.

CHAPTER 5
INFLUENCE OF IONS IN THE KATRIN EXPERIMENT AND THEIR IMPACT ON NEUTRINO MASS MEASUREMENTS

Every time a β-electron is created in the source section, so is an ion. β-decay and scattering interactions are the main mechanisms by which ions are created in KArlsruhe TRItium Neutrino experiment (KATRIN) (Sec. 5.2). As discussed in Chapter 4, to measure the β-energy spectrum in KATRIN, β-electrons are guided toward the Focal Plane Detector (FPD) using superconducting magnets to create magnetic fields. But all charged particles follow the magnetic field lines, including ions (Sec. 5.3). If an ion flux gets to the Spectrometers and Detector Section (SDS) it contaminates the experiment and it can increase the FPD background to alarming rates, even above the design limit [86] (Sec. 5.1). That is why there are mechanisms in the transport section to stop the ion flux (Sec. 5.3.2), and to remove it from the flux tube (Sec. 5.3.4). The KATRIN experiment has four different ion monitoring mechanisms, located throughout the beam tube, to make sure there is no ion flux into the SDS (Sec. 5.4). To prevent tritium contamination in the SDS, a safety mechanism is triggered if an ion flux is detected in the Pre-Spectrometer (PS). This mechanism consists of closing the valve between the Cryogenic Pumping Section (CPS) and the PS.

5.1 Ion impact on neutrino mass measurements

Ions throughout the KATRIN experiment have an influence on the neutrino mass measurements, either directly or indirectly.

Ions in the Main Spectrometer (MS) can indirectly influence the measured FPD rate. They can create electrons in the MS that follow the flux tube all the way to the FPD, elevating the background rate (A_{bg} from equation 4.7) (Sec. 5.1.1). It was shown, by dedicated simulations, that an increase in background worsens the neutrino mass sensitivity.

Ions in the Windowless Gaseous Tritium Source (WGTS) can create plasma, which affects the kinetic energy of the β-electrons created around it (Sec. 5.1.2). And the electrodes used to remove and reflect the ions can shift the β-spectrum of the electrons created inside their potentials (Sec. 5.1.3).

5.1.1 Impact of ions in the main spectrometer (MS)

Since the ions are charged particles, if not blocked, they follow the magnetic field lines all the way to the PS. There, most of the ions leave the flux tube by being accelerated towards the PS vessel where they are neutralized. The probability of an ion reaching the MS is thus less than 1×10^{-4}, as shown by dedicated simulations [94]. Ions colliding with the inner PS vessel are neutralized and are either reflected (around 5%) or implanted into the surface. Neutralized T_3 molecules diffuse back to the PS after some time. The reflected and desorbed molecules are either diffused towards the MS or are pumped out. Around 1% of the tritium ions that enter the PS end up in the MS in the long run, either neutralized or still ionized [94].

Tritium atoms inside the MS mainly increase the FPD background rate via two direct and one indirect mechanisms [94]:

- By the creation of β-electrons via tritium β-decay. Most of the β-electrons created in the MS have kinetic energies in the keV scale. Consequently, they have different kinetic energies from the WGTS-β-electrons at the MS. If their energies are very different they can be distinguished by the intrinsic FPD energy resolution. But if low-energy electrons are created downstream of the analyzing plane[1] they will be accelerated by the post-acceleration electrode and end up hitting the FPD with energies similar to the WGTS-β-electrons.

- By the creation of secondary electrons via ionization of residual gas. Although the MS is in ultra-high vacuum, there is still residual gas inside the vessel. Ions entering the MS can ionize residual gas and create secondary electrons.

- By an indirect mechanism that is a consequence of the high-energy β-electrons created with the two previous mechanisms. The high-magnetic fields in the MS entrance and exit create a magnetic bottle. If the electrons are created with substantial transverse momentum relative to the magnetic field lines, they get trapped inside the magnetic bottle. These trapped electrons will ionize residual gas. And, as in the previous case, if the secondary electron is created after the analyzing plane, it will be detected by the FPD.

To minimize the ion contribution to the FPD background to 1 mcps or less, a T_2^+ and HT^+ ion flux upper limit of 2.5×10^5 molecules/s into the SDS is required [86]. Since the

[1] A β-electron has its minimum kinetic energy at the point where it passes the analyzing plane. This plane is transverse to the spectrometer axis. If an electron passes that plane, it means that it had enough energy to overcome the MS retarding potential and it will be guided towards the FPD.

most abundant ion species is the T_3^+ molecule, which has a higher activity than T_2^+ or HT^+, a conservative upper limit of ion flux ($\Phi_{\text{ion}}^{\text{SDS}}$) into the SDS was calculated [94]:

$$\Phi_{\text{ion}}^{\text{SDS}} < 1 \times 10^4 \text{ ions/s}. \tag{5.1}$$

5.1.2 Impact of ions in the tritium source section

Most of the ions are created in the Windowless Gaseous Tritium Source (WGTS), as will be explained in the next section. The bast majority of the ions get thermalized and removed in the WGTS. Some ions leave the source section and are removed from the flux tube. Nevertheless the creation of charged particles can lead to the creation of space charges, or plasma, in the WGTS.

The WGTS-plasma influences the β-electron kinetic energy which can lead to shifts in the β-energy spectrum. There are dedicated measurements to study plasma effects, instabilities, and their influence on neutrino mass measurements. More information can be found in [95].

5.1.3 Impact of tritium gas in the dipole section

There is another method by which ions indirectly affect the neutrino mass measurements in an energy-dependent way. As will be explained in section 5.3.4, there are three dipole electrodes set to high negative voltages, and one to a positive voltage, in the Differential Pumping Section (DPS); they are used to remove and to reflect the ion flux, respectively. Since they are located downstream from the source, next to the WGTS, their neutral tritium gas content is non-negligible.

If tritium β-decays inside a potential, the created β-electron will be affected by the potential. In case of a negative starting potential, the electron will lose energy in the process of travelling to a region at ground. In the case of a positive one, the electron will gain energy. This effect shifts the β-electron energy compared to the energies of the electrons created in the WGTS, which were all created in the same experimental settings. Since it is not possible to distinguish between electrons created in the WGTS or in the dipoles, they will introduce a distortion in the spectrum.

A dedicated measurement (Sec. 8.6.2) took place to: calculate the tritium gas density inside the dipoles; calculate the error induced on m_ν^2 by the β-spectrum distortion; and quantify if it was necessary to change the dipole set voltages, to minimize the spectrum distortion while still removing ions.

5.2 Ion creation mechanisms

There are different mechanisms in the KATRIN experiment that create ions. During nominal tritium conditions around 4×10^{12} ions/s are created in the source section via: β-decay (Sec. 5.2.1), scattering interactions (Sec. 5.2.2), and in smaller quantities via molecular dissociation (Sec. 5.2.3).

Other methods that don't depend on the circulation of tritium gas in the WGTS are Penning discharges (Sec. 5.2.4), and residual gas ionization (Sec. 5.2.4). These methods occur naturally during neutrino mass measurements, but they were also used during a non-tritium commissioning campaign to produce deuterium ions. The objective of the campaign was to study the ion systematic effects on the experiment without contaminating it with tritium ions. The results from said campaign can be found in chapter 7.

5.2.1 Tritium activity

A large portion of the ions in KATRIN are directly created in tritium β-decay, while the other most significant part comes from the resulting β-electrons scattering with tritium gas. As such, the tritium activity (A) plays a big role in the ion creation rate.

The tritium activity depends on the number of tritium ions (n_{T}) in the experiment, which can be calculated as follows [94]:

$$n_{\mathrm{T}} = 2 \cdot \sigma_{\mathrm{WGTS}} \cdot \epsilon_{\mathrm{T}} \cdot \rho d, \tag{5.2}$$

where the parameters are defined as follows:

- The column density (ρd) is the number of gas molecules within a unit area integrated along the beam tube (molecules/cm^2). The nominal column density is 5×10^{17} molecules/cm^2 [86].
- The tritium purity (ϵ_{T}) is the ratio of tritium atoms versus the total amount of atoms of the injected gas. The minimum required tritium purity during neutrino mass measurements is 95%.
- The cross-section area of the WGTS (σ_{WGTS}) is 63.6 cm^2 [42]. It is used to account for all the gas inside the experiment. It is a good approximation since more than 96% of the tritium-gas is inside the WGTS.
- The factor 2 accounts for the average number of tritium atoms per molecule since most of the molecules are T_2.

And so the tritium activity in KATRIN is calculated as:

$$A(\epsilon_{\mathrm{T}}, \rho d) = \lambda_{\mathrm{T}} \cdot n_{\mathrm{T}}(\epsilon_{\mathrm{T}}, \rho d) = 2\lambda_{\mathrm{T}} \cdot \sigma_{\mathrm{WGTS}} \cdot \epsilon_{\mathrm{T}} \cdot \rho d, \tag{5.3}$$

where the decay rate $\lambda_{\mathrm{T}} = \ln(2)/T_{1/2} = 1.78 \times 10^{-9}$/s is calculated from the tritium half-life $T_{1/2} = 4500 \pm 8$ d [96]. Using equation 5.3 with a tritium purity of $\epsilon_{\mathrm{T}} = 1$ we get an activity of around 1.13×10^{11} β-decays/s with nominal tritium column density.

The most probable tritium decay channel is:

$$\mathrm{T}_2 \rightarrow \mathrm{HeT}^+ + e^-_\beta + \overline{\nu}_e, \tag{5.4}$$

with a decay probability of $50.3 \pm 1.5\%$ [69]. Most of the tritium β-decay branches have one positive ion in their final state, but there is a very unlikely branch where no ions are produced, and other branches with two ions (see table 1.2). Using the β-decay branching ratio results from the Tritium Recoil Ion Mass Spectrometer (TRIMS) experiment [69], we estimate that the ion creation rate due to tritium β-decay is around 1.3×10^{11} ions/s.

One decay channel leads to a negative tritium ion (T^-):

$$\mathrm{T}_2 \rightarrow \mathrm{He}^{++} + \mathrm{T}^- + e^-_\beta + \overline{\nu}_e, \tag{5.5}$$

but it is a rare branch, with a probability of less than 0.018% [69]. These negative ions interact with the positive particles as will be explained in the following section.

5.2.2 Scattering in gas

Almost all tritium β-decays in the WGTS, where there is a high tritium gas density (the density profile is shown in Fig. 4.4). The β-electrons (e^-_β) follow magnetic field lines, and in doing so, they collide with T_2 molecules. On average each e^-_β undergoes 36 inelastic scattering processes at a nominal column density [98]. These interactions ionize the gas and create secondary electrons (e^-_{sec}), and ions. Most of the created ions are T_2^+ but T^+ ions are also created at a smaller rate [42]:

$$e^-_\beta + \mathrm{T}_2 \rightarrow e^-_\beta + e^-_{\mathrm{sec}} + \mathrm{T}_2^+ \qquad (\approx 96\%) \tag{5.6}$$

$$e^-_\beta + \mathrm{T}_2 \rightarrow e^-_\beta + e^-_{\mathrm{sec}} + \mathrm{T}^+ + \mathrm{T} \quad (\approx 4\%) \tag{5.7}$$

These ions can cluster into molecules of higher masses (T_3^+, T_5^+, T_7^+, ...) by colliding

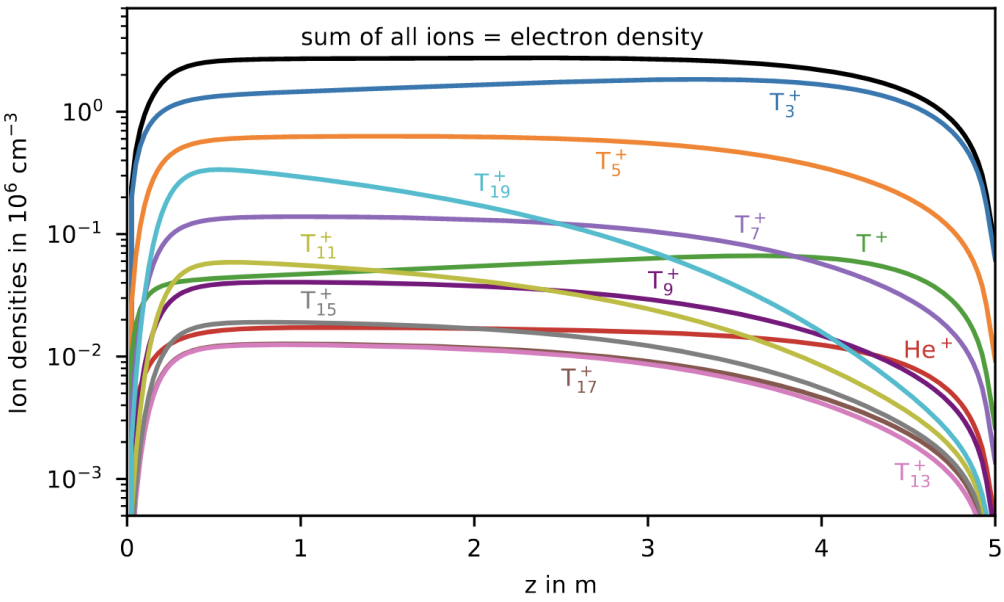

Figure 5.1: Simulation of the longitudinal ion density profile inside one half of the WGTS, from its center (z = 0 m) to the downstream exit (z = 5 m). The neutral tritium gas inlet is located at z = 0 m and the molecular tritium is created by recombination of T particles. The density of the other half should be the mirrored distribution. The sum of the ion densities is the electron density assuming quasi-neutrality. The simulation was done by F. Glück with a custom simulation software [97].

with neutral gas. Some of these processes include:

$$\begin{aligned} {}^3\mathrm{HeT}^+ + \mathrm{T}_2 &\rightarrow \mathrm{T}_3^+ + {}^3\mathrm{He}, \\ \mathrm{T}_2^+ + \mathrm{T}_2 &\rightarrow \mathrm{T}_3^+ + \mathrm{T}, \\ \mathrm{T}_3^+ + 2\mathrm{T}_2 &\rightarrow \mathrm{T}_5^+ + \mathrm{T}_2. \end{aligned} \tag{5.8}$$

Negative ions are created via dissociative attachment of electrons. Their creation rate, compared to positive ions, is small, around 1.0% [42, 86]:

$$e^- + \mathrm{T}_2 \rightarrow \mathrm{T}^- + \mathrm{T}. \tag{5.9}$$

The negative ions are spatially constrained to the WGTS because of negative potentials created by dipole electrodes in the DPS. So the negative ions end up recombining with positive ions [94]:

$$\begin{aligned} \mathrm{T}^+ + \mathrm{T}^- &\rightarrow \mathrm{T}_2, \\ \mathrm{T}_3^+ + \mathrm{T}^- &\rightarrow 2\mathrm{T}_2. \end{aligned} \tag{5.10}$$

And finally, positive ions can also recombine with thermalized[2] secondary electrons by binding the electron and releasing energy via a photon, or via dissociative recombination [94]. The following are examples of each case:

$$\begin{aligned} \mathrm{T}_2^+ + e^- &\rightarrow \mathrm{T}_2 + \gamma, \\ \mathrm{T}_3^+ + e^- &\rightarrow \mathrm{T}_2 + \mathrm{T}. \end{aligned} \tag{5.11}$$

The ion density profiles in the WGTS, or the densities of each type of ion, were simulated by F. Glück and are shown in Figure 5.1. The sum of the ion densities is the same as the electron density assuming quasi-neutrality of the plasma.

Most of the ions have thermal energies, a few meV, because of constant scattering interactions with the neutral gas. Only the ions created at the WGTS entrance are likely to retain their original energy profile after leaving the source section, but they are a minority [94].

5.2.3 High energy ions created by molecular dissociation

Most of the ions are thermalized when they leave the WGTS. Nevertheless during the First Tritium (FT), KATRIN Neutrino Mass measurement 1 (KNM1), and KATRIN Neutrino Mass measurement 2 (KNM2) campaigns ions with energies above 10 eV were observed. In this section we will describe how high energy ions are created.

Franck-Condon principle

As explained in section 1.5.2, a molecular state is defined by electronic, rotational, vibrational, and azimuthal quantum numbers.

The Franck-Condon principle describes a molecular transition from an initial electronic and vibrational state to another. When a molecule with a low energy (E'') transitions to a higher energy state (E'), the electronic transition is instantaneous compared to the nuclear motion, so the internuclear distance (R'') should be instantaneously compatible to the vibrational level (v′) of the new state.

When the internuclear distance (R_e) at the minimal potential energy is the same for both electronic states, then the vibrational states are the same (v″ = v′). But in some cases, $R'_e > R''_e$ and so the maximal transition probability goes to different vibrational states. It can happen that the transition leads to final vibrational states in the dissociation continuum. This process is illustrated in Fig. 5.2.

[2]Thermalized electrons are low-energy electrons that either lost their energy in scattering interactions, or were created at low energy.

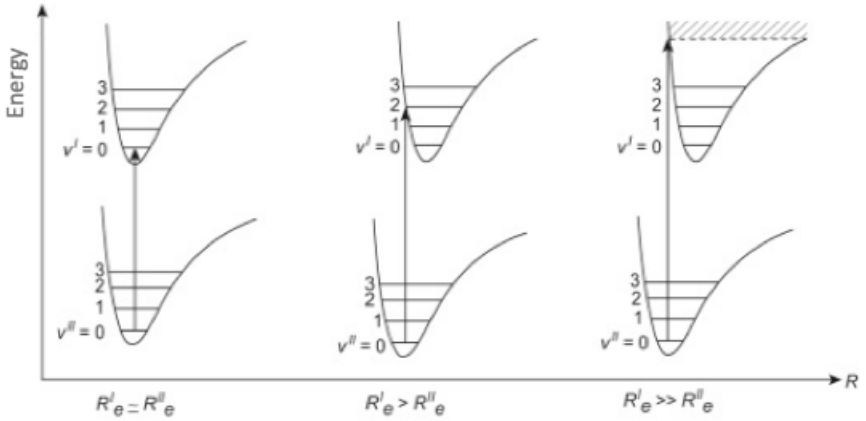

Figure 5.2: Illustration of the Franck-Condon principle in which a molecular electronic and vibrational transition occurs and the internuclear distance is conserved. This is the case because electrons transition much faster than nuclear transitions. Three cases are illustrated, when the internuclear distance at the minimal potential energy (R'_e) is: similar (left), slightly greater than (middle) and much greater (right) than R''_e. In the latter case, there are several compatible final states that can be populated, and they are part of the dissociation continuum. Figure from [99]

Molecular dissociation

When a molecule transitions to the dissociation continuum then, the molecule will eventually dissociate, or the internuclear distance of the atoms will increase, becoming very large. In KATRIN there are two main types of molecular dissociation, namely from electron scattering on molecules, and from the daughter molecules of β-decay.

Dissociative ionization by electron scattering

There is a high probability that the β-electrons will scatter with the tritium gas in the WGTS. The gas molecule can be left in an excited state after the energy transfer of an inelastic scattering. If the energy is high enough, dissociative ionization can occur, where one or more of the final state particles is ionized.

Figure 5.3 shows the potential-energy diagram of the ground state of H_2, some states of H_2^+, and H_2^{++}. Although it is not the same gas that we have in KATRIN, the plot helps us illustrate some concepts. Electrons colliding with H_2 may ionize it to the bound state $^2\Sigma_g^+$, the dissociative state $^2\Sigma_u^+$, or higher dissociative states. A double ionized state is possible, but unlikely. The proton energy after the dissociative ionization of H_2 is shown on the left of Fig. 5.3 for $^2\Sigma_g^+$, and $^2\Sigma_u^+$. The heights of the two curves are scaled and should not be compared.

The energy peak of the dissociative ionization protons is around 8 eV, but higher-energy

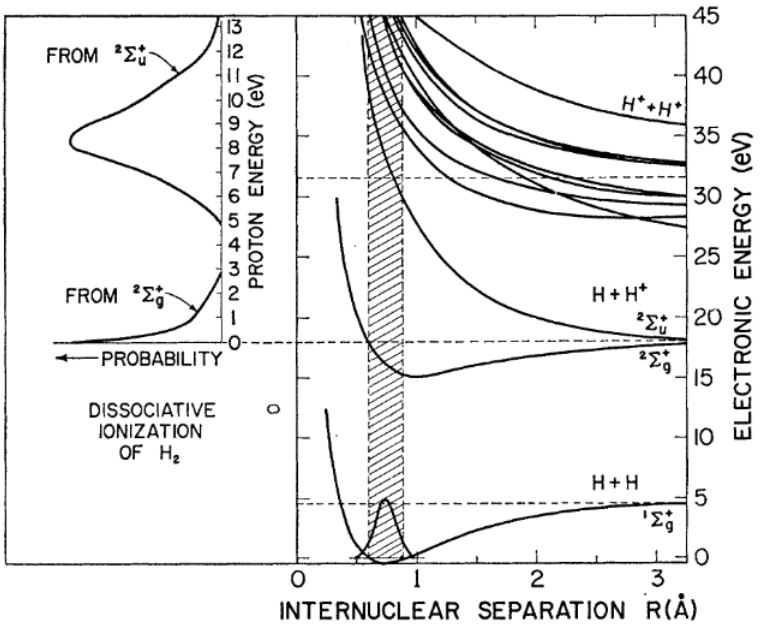

Figure 5.3: Potential-energy diagram of the ground state of H_2, some states of H_2^+, and H_2^{++}. The proton energy of dissociative ionization of H_2 is shown on the left. The two curves are scaled and should not be compared. Figure from [100]

protons are also created.

Dissociation of tritium β-decay daughter molecule

The probability of transitioning to the different final states of TT β-decay is shown in table 2.5. The daughter ends up in the bound-molecular final state with a probability of $50.3 \pm 1.5\%$, where the molecule dissociates depending on its energy (the quasibound state).

The potential energy curves of the first six electronic excited states of $^3HeT^+$ are shown in Fig. 5.4. The first state is the only one where the molecule can remain bound; the molecule will dissociate if found in any other state.

The energy spectrum of the excited states starts around 20 eV and has a peak around 28 eV, as shown in Fig. 5.5 . The double ionization threshold starts around 43 eV. After molecular dissociation of $^3HeT^+$, from momentum conservation, the ions have an energy peak around 13 eV. Higher energy ions are also possible, albeit less probable.

5.2.4 Non-tritium-induced ions

The following two ion-creation mechanisms were used to produce ions in a non-tritium measurement campaign. The data gathered in this campaign were used to calibrate the

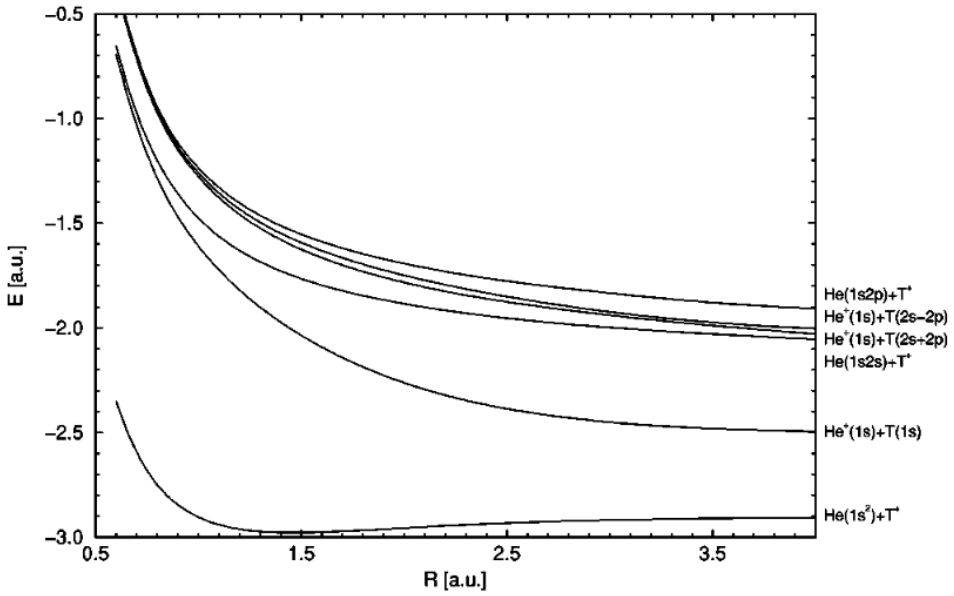

Figure 5.4: Potential curves for the first six electronic states of $^3HeT^+$. E is the electronic binding energy (in atomic units) relative to the total break-up threshold, and R is the internuclear separation. Figure from [68]

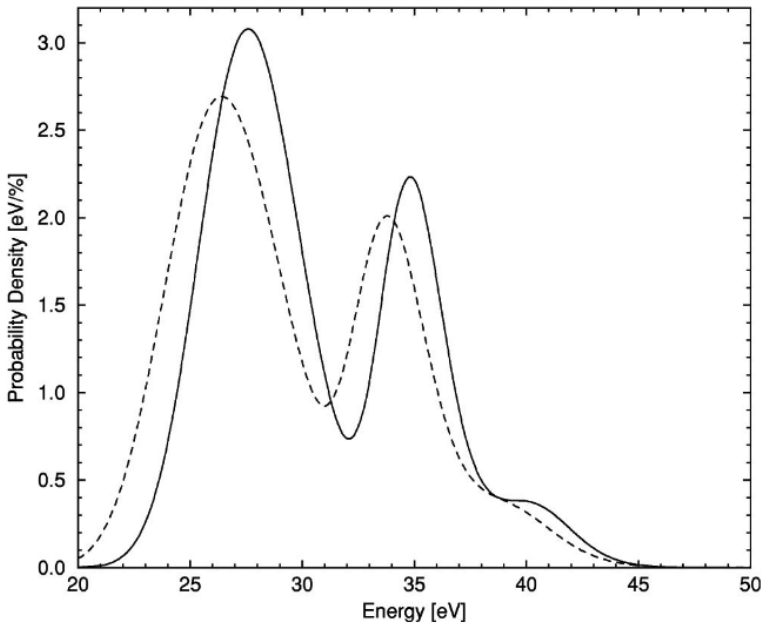

Figure 5.5: The probability density for transitioning to the excited states 2-6 below the doubly ionized state for $^3HeT^+$ (solid curve) and $^3HeH^+$ (dashed curve). Figure from [68]

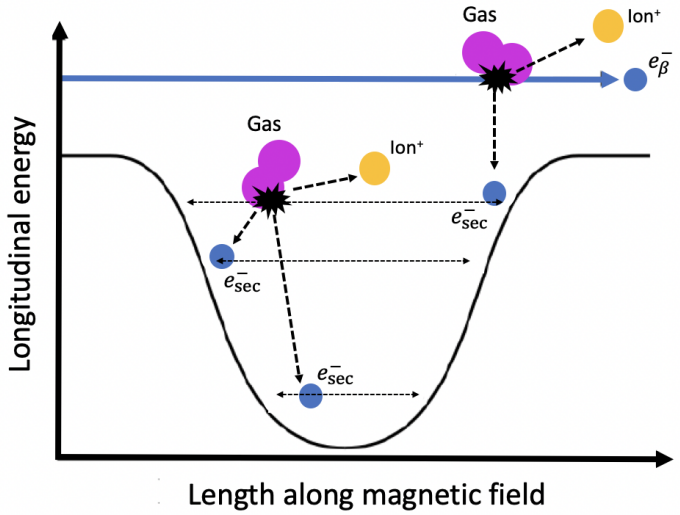

Figure 5.6: Sketch of the creation of ions by Penning discharge. Where residual gas (pink big circle) is ionized by e_β^- (blue small circle), an ion (orange medium circle) and a secondary electron e_{sec}^- (small blue circle) are created. The low-energy secondary electrons are trapped in the potential well and in turn ionize more residual gas molecules. The ions are accelerated away from the potential, gaining kinetic energy that corresponds to the electric potential at their creation location. The longitudinal energy refers to the energy due to longitudinal motion.

ion hardware as explained in section 7.3. Although tritium circulation is not necessary for these creation mechanisms, they can still produce tritium ions if tritium is present in the experiment. This means that during neutrino mass measurement campaigns these two ion creation mechanisms also create ions, although at a much smaller scale than the previous mechanisms.

Penning discharge ions

A Penning discharge can ignite when a Penning trap is formed in the experiment. A Penning trap occurs in a low gas-density volume, when electrostatic potentials constrain the movement of charged particles to follow magnetic field lines between them. If the charged particles are energetic enough, they will ionize the gas and produce an ion and a secondary electron. Depending on the electrostatic potential sign, the positive or the negative particle will leave the potential gaining the energy of the potential at their creation location, while the other particle will get trapped. There is a Penning discharge when an ionization cascade occurs, in other words, when the created secondary electron has enough energy to ionize and produce another secondary electron, which in turn can produce another, and so on. This process is illustrated in Fig. 5.6.

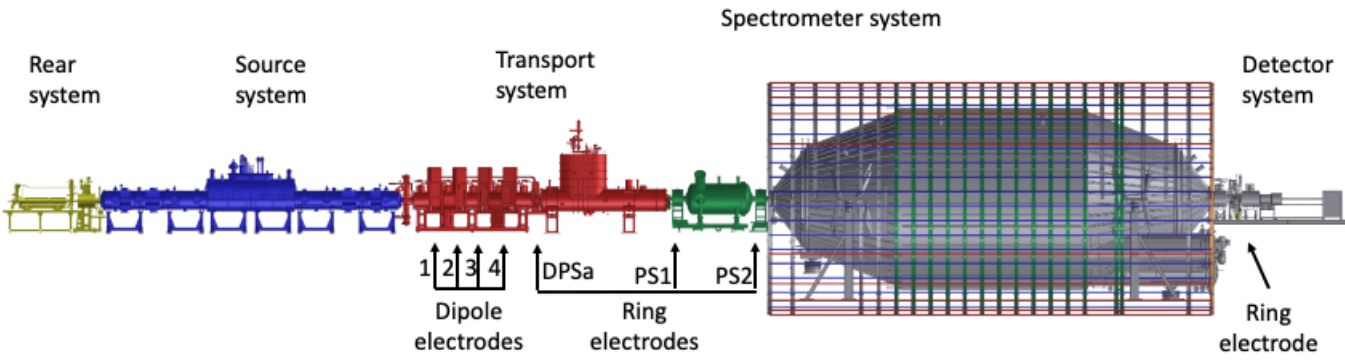

Figure 5.7: Locations of the dipole and the ring electrodes in KATRIN where Penning ions can be created.

The Penning discharge can be self-sustained if it does not need an external flux of charged particles to continue, and self-ignited if it does not need an input of charged particles to start the Penning discharge.

In KATRIN, magnetic fields guide charged particles throughout the beam line. There are several places where dipole or ring electrodes create electric potentials that trap secondary electrons and can produce Penning discharges. Figure 5.7 shows the location of the dipoles and electrodes in the KATRIN experiment that favour the creation of Penning discharges. The closer the electrodes are to the WGTS, the more residual gas there is in the beam tube, and so the Penning ion creation rate increases as shown in section 7.2. The Penning discharges at KATRIN are neither self-sustained nor self-ignited.

Eventually the trapped electrons run out of energy to ionize residual gas and they drop further into the potential well. They accumulate in the well and create space charges which can lead to neutralization of the electrodes (Sec. 5.3.3).

One advantage of creating ions by Penning discharges in the KATRIN experiment is that the ion energies and creation rate can be tuned by changing the electrode voltage setting.

Although this mechanism is used to create ions in a non-tritium environment, it also creates ions with neutrino mass experimental settings. That is why dedicated measurements were done to find optimal set voltages, by minimizing the Penning ion creation rate and maximizing ion blocking (Sec. 8.4).

Residual gas ionization

The final method used to create ions, when there was no tritium in the WGTS, consisted of ionizing residual gas with photoelectrons.

It is possible to create photoelectrons in different regions of KATRIN. They can be produced in the rear section by illuminating the Rear Wall (RW) with a UV-Cermax lamp (Sec. 4.2.1), and they can be produced in the MS by illuminating the vessel with a UV light (Sec. 4.3.1). The produced photoelectrons interact with residual gas in the WGTS, or in the MS, and ionize it. The residual gas density in the WGTS has to be small enough that the created ions can leave the WGTS but large enough that the photoelectrons can ionize the gas.

During the non-tritium ion-measurement campaign deuterium gas was injected in the WGTS and then pumped out. The residual deuterium gas was used to produce ions.

5.3 Propagation of ions in the beamline

In this section we will talk about what happens to the ions after they are created in the KATRIN experiment. As soon as they are created they propagate in the beamline following magnetic fields. Their direction (upstream or downstream) depends on their initial momentum direction (Sec. 5.3.1). Half of them go towards the RW where they are neutralized and removed. The other half travel all the way to the DPS, where they are blocked and reflected by ring electrodes (Sec. 5.3.2). The ring electrodes' blocking can deteriorate over time (Sec. 5.3.3), and studies were carried out to quantify this effect (Sec. 8.5). Finally, most of these ions are removed in the DPS with dipole electrodes (Sec. 5.3.4).

5.3.1 Gyromotion around magnetic fields

Starting in the rear section, all the way to the detector section, magnetic fields guide charged particles along the beam line towards both ends of the experiment. The particle's initial momentum direction will dictate if it moves towards the FPD or the RW. Meanwhile electric fields accelerate or decelerate them.

The charged particle momentum ($\vec{p}$) is influenced by the electric ($\vec{E}$) and the magnetic ($\vec{B}$) fields, as described by the Lorentz equation [101]:

$$\frac{d\vec{p}}{dt} = q(\vec{E} + \frac{\vec{p} \times \vec{B}}{\gamma m}), \tag{5.12}$$

where m is the particle's mass, q its charge, and γ is the relativistic Lorentz factor. The charged particles in KATRIN follow the magnetic field lines in cyclotron motion.

Electrons travelling upstream with enough energy will overcome the MS retarding potential and will reach the FPD. Ions moving towards the FPD should be blocked and reflected by ring electrodes before they can reach the SDS.

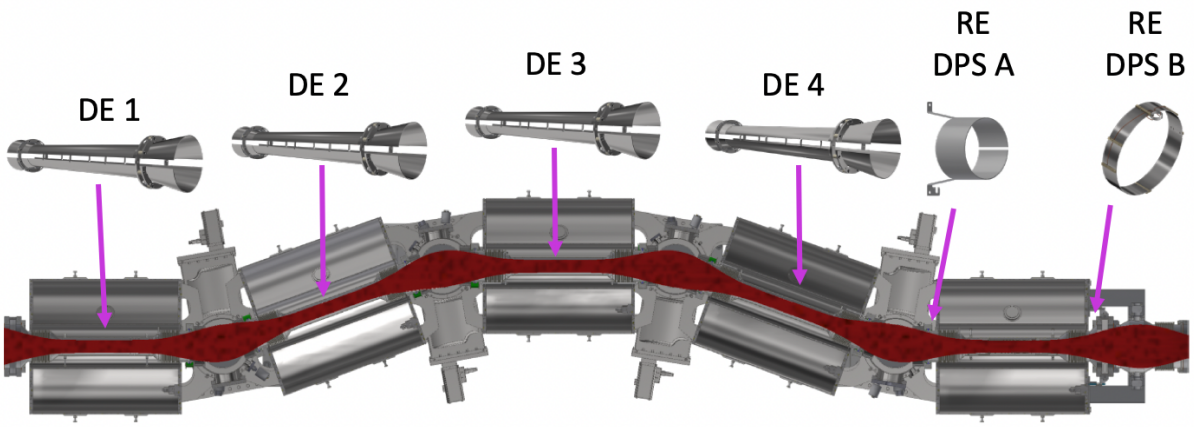

Figure 5.8: Dipole electrodes (DE) and ring electrodes (RE) inside the DPS. The WGTS is to the left and the CPS to the right in this image.

5.3.2 Blocking ions with electrodes

While one half of the ions travel towards the rear section, the other half of the ions travel towards the main detector. These ions must be blocked before reaching the SDS. This is achieved by a combination of ring and dipole electrodes. A sketch of the KATRIN experiment is shown in Fig. 5.7 with locations for the ring and dipole electrodes. The electrodes whose main purpose is to block and reflect the ions are: Dipole Electrode 4 (DE4), Ring Electrode DPS a (RE-DPSa) and PreSpectrometer magnet 1 (RE-PS1).

The electrode potentials are set to voltages ranging from 5 V to 200 V. The ions are not energetic enough to overcome the positive electrostatic potential and they are reflected towards the rear section. As explained in section 7.4 an optimal voltage setting was found for DE4, RE-DPSa and RE-PS1. Figure 5.8 shows the locations and forms of the dipole and ring electrodes inside the DPS. The dipole electrodes require two set-voltage values, for the upper and lower electrodes. Throughout this thesis we will write the set voltages as: $V_{\mathrm{upp}}/V_{\mathrm{down}}$ V where V_{upp} refers to the upper electrode and V_{down} to the lower electrode. The ring electrodes have just one set voltage on each entire ring.

The potential at the center of the ring electrodes is not the set voltage because of the potential grip of the surrounding beamtube, which is on ground potential, and because of the $1/r^2$ factor. This was simulated by R. Sack [102]. The nominal voltage, measured in Sec. 8.4, and the potentials at the electrode centers are shown in table 5.1.

DE4 is used for reflecting and blocking ions instead of removing ions, its original purpose, because of the neutralization of the ring electrode potentials with trapped secondary electrons, as will be further explained in the next section.

Blocking electrode	Nominal voltage (V)	Potential at center (%)
DE4	25/20	-
RE-DPSa	40	81.1
RE-PS1	200	46.5

Table 5.1: Nominal voltages of the ion-blocking electrodes. The potential at the center of the ring electrodes was simulated by Sack [102]. No simulations, of this kind, were carried out for DE4.

5.3.3 Neutralization of ring electrodes

The ring electrodes create positive potential wells where negative particles can be trapped, as shown in Fig. 5.6. Space charges are formed when several particles are trapped in the potential well. The effective potential that other particles see is affected by the space charge; for example, an ion with less energy than should be necessary to overcome the positive potential can see an effective potential lower than the set voltage, and so it can now overcome the potential. This effect is what we call, throughout this thesis, neutralization of the ring electrode.

An electron must have low energy, less than the ring-electrode set voltage, to be trapped in the positive potential. There are different mechanisms by which low-energy electrons can be created in KATRIN and be trapped in the positive potentials, including:

- Creation of β-electrons, with energies below 100 eV, by tritium β-decay. The decay must occur downstream of Dipole Electrode 3 (DE3), since otherwise the electrons would be reflected by the negative dipole potentials.
- Creation of secondary electrons via β-electron scattering with residual gas downstream of DE3.
- Creation of secondary electrons by Penning discharges inside the positive ring-electrode potential, as seen in Fig. 5.6.
- Trapping of secondary electrons by elastic or inelastic scattering with residual gas inside the positive ring-electrode potential.

The dangerous consequence of neutralization is that some ions are no longer blocked and reflected by the ring electrodes. Instead, they travel through the beamline all the way to the SDS where they create background. Measurements were carried out during KNM2 to measure how quickly neutralization took place in two ring electrodes at 90% column density (Sec. 8.5).

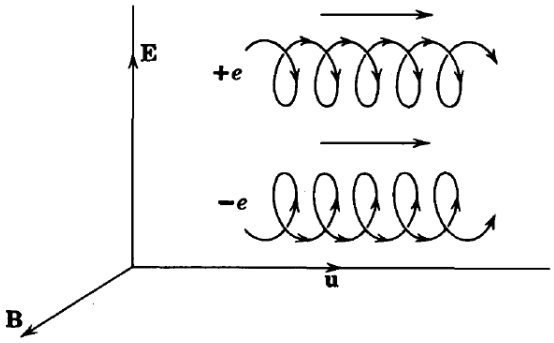

Figure 5.9: $E \times B$ drift of a charged particle when it is moving in an electric and a magnetic field with perpendicular components. Figure from [101]

5.3.4 Ion removal

One half of the ions travel towards the rear section, where they hit the RW and are neutralized in the process. The neutral particles are removed and pumped out together with the neutral gas coming from the WGTS. As for the other half, it is not enough to block and reflect them before they reach the SDS to comply with the background and experimental stability requirements. It is necessary to remove the ions from the flux tube to avoid the creation of space charges, and avoid the creation of plasma inside the beam line. Most of these ions are removed by the dipole electrodes, in the DPS, in the following manner.

Besides the cyclotron motion (Eq. 5.12), if there is a component of the electric field perpendicular to the magnetic field, the particle will drift perpendicularly to both fields. We can approximate the electric and magnetic fields in KATRIN to be uniform and static in a small region. And when such fields have a perpendicular component to each other, they will induce a drift velocity $\vec{u}$ on the particle, known as the $E \times B$ drift [101]:

$$\vec{u} = \frac{\vec{E} \times \vec{B}}{B^2}. \tag{5.13}$$

It is possible to understand this drift by noting that the particle starts its gyration motion around $\vec{B}$ and is accelerated by $\vec{E}$, gaining energy and moving to a path with larger radius, for half its cycle. On the other half it loses energy from the electric field and so its radius decreases. This shift in radius moves the particle perpendicularly to $\vec{E}$ and $\vec{B}$. A sketch of the $E \times B$ drift is shown in Fig. 5.9.

The dipole electrodes provide an electric field, which is perpendicular to the magnetic field that the charged particles follow. The nominal set voltages of the dipoles are shown in table 5.2. The particles drift out of the flux tube via the $E \times B$ drift, and in doing so, some

Dipole	Nominal set voltage (V/V)
1	-15/-5
2	-35/-5
3	-85/-5
4	+25/+5

Table 5.2: Nominal set voltages of the dipole electrodes in the DPS. The first three dipoles are used to remove ions while dipole 4 is used to block ions. Voltages are given for the upper and lower electrodes of each dipole as explained in Sec. 5.3.2.

of them hit the lobes of the dipoles. Even if the ions don't hit the lobes, they are removed from the flux tube and end up hitting the DPS vessel or other surfaces. The dipole lobes can be seen in figure 5.10. The lobes are connected to ammeters, so it is possible to measure the current that the ions induce when they hit the lobes and are neutralized. This way, it is possible to monitor the ion flux, as will be explained in the following sections.

As shown in equation 5.13, the drift is independent of the charge and mass of the particle, so all charged particles are affected. This means that β-electrons are also drifted by this mechanism. The slower the particle moves, the longer it will be exposed to the drift and the more it will be affected. This is why the fast electrons are not drifted away from the beam tube while slow ions are. The β-spectrum data analysis however, does need a correction for this effect.

5.4 Detection and monitoring of ions in the beam line

It is critical for the KATRIN experiment to prevent the ion flux from reaching the SDS (Sec. 5.1). There are different ion monitoring systems, throughout the beam line, that help us assess how well we are blocking and removing the ion flux. This section will cover the ion monitoring mechanisms. The first method, in the DPS, measures the current created by the removal of ions with the dipole electrodes (Sec. 5.4.1). The second method, in the PS, looks for a change in the Pre Spectrometer Downstream-Cone Electrode (PS-DCE) current that would indicate an ion flux inside the PS (Sec. 5.4.2). The third method uses a Faraday cup, which can be inserted in front of the FPD, to directly measure the ion flux (Sec. 5.4.3). Finally, the Ion Conversion to Electron (ICE) detection method relates the FPD counts to an ion flux (Sec. 5.4.4).

5.4.1 Dipole currents

The ions are removed from the flux tube, with the dipole electrodes, via the $E \times B$ drift as explained in section 5.3.4. The dipole lobes, seen in Fig. 5.10, are electrodes. The

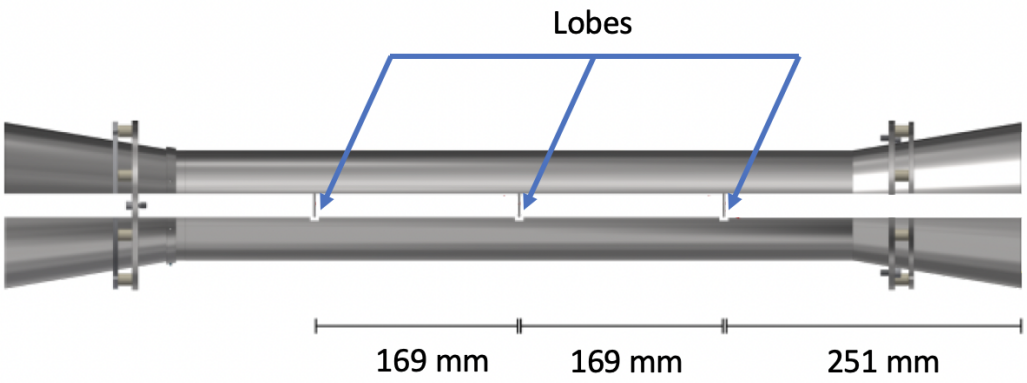

Figure 5.10: Dipole electrode with its dimensions, the length of the right side is mirrored on the left side. The lobe locations are shown with the arrows.

ions that hit the lobes while being drifted are neutralized in the electrodes. The electrodes are connected to a voltage supply, and because of charge compensation, a current is drawn from the voltage supply. This current is measured by an ammeter between the voltage supply and the electrode.

The current (I) measured by the ammeter tells us information about the ion flux ($\Phi_{\text{ion}}^{\text{DPS}}$) in the DPS. There are three dipole electrodes removing ions in the DPS so the total ion flux is:

$$\Phi_{\text{ion}}^{\text{DPS}} = \frac{I_1 \cdot \alpha_1}{q_e} + \frac{I_2 \cdot \alpha_2}{q_e} + \frac{I_3 \cdot \alpha_3}{q_e}, \tag{5.14}$$

where $q_e = 1.602 \times 10^{-19}$ C is the elementary charge, the subscript $\{1, 2, 3\}$ indicates the dipole electrode, and α_i is the detection efficiency of each dipole.

The detection efficiency is calculated in the following manner. The ions are drifted from the flux tube via the $E \times B$ drift. Some of the ions are neutralized by hitting a lobe, although ions can also be removed without hitting a lobe. The probability of detection depends on the probability of the ion hitting a lobe before being removed from the flux tube and being neutralized on the beam pipe. There are three lobes per dipole as can be seen in figure 5.10. A drift velocity is calculated for each dipole using Eq. 5.13. Then the probability of the ion hitting one of the lobes is calculated with the displaced distance (z-direction), the drift distance and the lobe area. A complete calculation of the probability of detection can be found in [94] giving the results shown in table 5.3. The removal probability was adapted from [94], for the case of three dipole electrodes with negative potentials instead of the four dipoles shown in the cited thesis. It refers to the percentage of ions that are removed in each of the dipoles based on the drift velocity, which depends on the set voltage (table 5.2).

	Dipole electrode		
	1	2	3
Set voltage (V/V)	-15/-5	-35/-5	-85/-5
Drift distance (mm)	8.53	18.09	32.15
Detection efficiency (α_i)	1	0.74	0.56
Removal probability (%)	14	32	54

Table 5.3: Detection efficiency of the dipole electrodes, and the drift distance of the ions which is influenced by the dipoles set voltage [94]. The removal probability, or the percentage of ions that are removed in each of the dipoles, was adapted for the 3 negative dipole case from [94].

5.4.2 Cone electrode in Pre-Spectrometer

The next ion monitoring mechanism in the beam-line is the PS downstream-cone (PS-DCE) current. It is located in the SDS and it serves the purpose of monitoring any ion flux that enters the spectrometers. It is the first monitoring mechanism in the section where we don't expect an ion flux. Its main advantage is that it does not require a special experimental setting. So the current is sampled every second, including during neutrino mass measurements.

If a positive ion entered the PS, the negative potentials of the vessel and wire electrodes would accelerate it towards the vessel. The paths that the ion can take are shown with simulations, for different experimental configurations, in section 6.3. The ion ends up colliding with the vessel, the cone electrodes, or the wires. With a small probability it could be trapped, although simulations (Sec. 6.3) show that after a sufficiently long time it ends up hitting one of the surfaces. The ion impact location depends, among other things, on its energy and on its radial position when entering the PS.

The PS-DCE is connected to a voltage supply, and an ammeter is connected in between the PS-DCE and the voltage supply. It is possible to measure the ion neutralization current with the ammeter. Figure 5.11 shows the location of the PS-DCE and the rest of the electrodes inside the PS. Also depicted are the magnets that guide the particles in the PS.

The PS-DCE current ($I_{\mathrm{ion}}^{\mathrm{DCE}}$) is affected by both the neutralization of ions and the sputtered electrons caused by the ion impact. Dedicated simulations were done to find the probability (P) of an ion hitting the PS-DCE for specific PS configurations (Chapter 6). Measurements and analysis were carried out to calibrate the current (Sec. 7.3.1) and to calculate an efficiency factor ($\varepsilon_{\mathrm{DCE}}$) that takes into account, amongst other things, the sputtered electrons and the probabilities. In other words, a change in the current was correlated

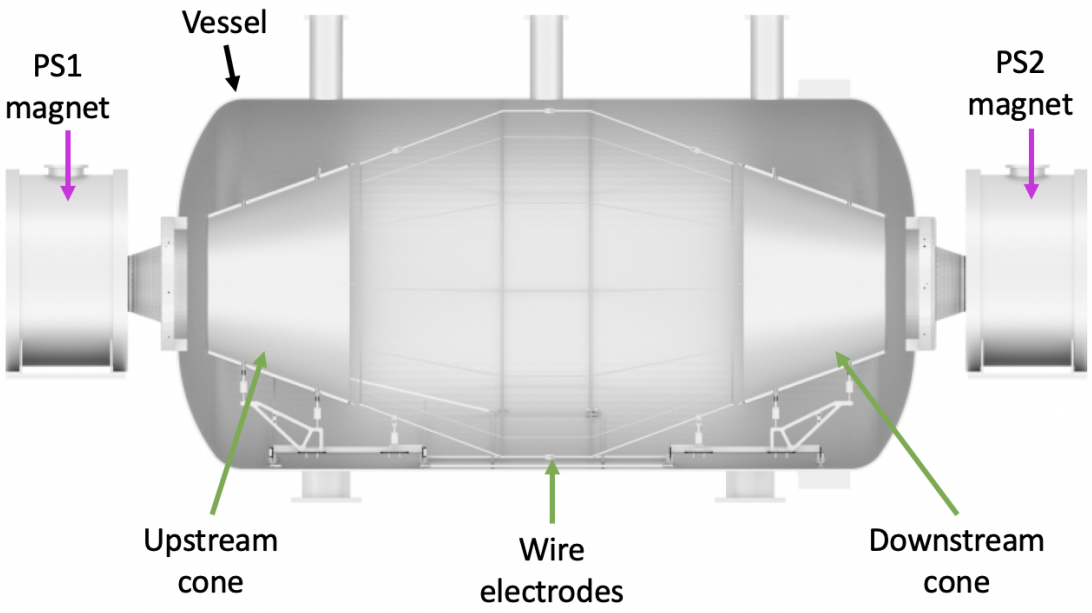

Figure 5.11: Pre-spectrometer experimental set up. The downstream-cone electrode is used to monitor the ion flux ($\Phi_{\text{ion}}^{\text{SDS}}$) into the SDS. It is connected to a voltage supply, which measured the current if the ion neutralization.

to an ion flux entering the SDS:

$$\Phi_{\text{ion}}^{\text{SDS}} = \frac{\Delta I_{\text{ion}}^{\text{DCE}}}{\varepsilon_{\text{DCE}}}. \tag{5.15}$$

A trigger was designed so that if there is a current measurement of 5 pA for more than 3 consecutive measurements (to prevent triggering on a spike) then the valve between the CPS and the PS is closed [94] .

5.4.3 PULCINELLA current

There is a Faraday cup that can be inserted in front of the FPD, between the pinch magnet and the detector magnet. It is attached to a sensitive ammeter known as PULCINELLA (Precision Ultra-Low Current Integrating Normalization Electrometer for Low-Level Analysis). Once inserted, the Faraday cup covers the entire flux tube. It can be used to directly measure an ion flux, but it requires a special experimental configuration.

PULCINELLA was used to calibrate the ICE ion monitoring mechanism, measuring a deuterium ion flux instead of a tritium ion flux so as not to contaminate the spectrometer section. For the ions to reach the Faraday cup it was necessary to change the electric fields in the SDS, otherwise the ions ended up hitting the PS vessel. The required experimental

settings can be found in Sec. 6.3.2. Also, dedicated simulations were used to show the percentage of ions that reach the Faraday cup if they started at the entrance of the PS (Sec. 6.3.2).

5.4.4 Ion Conversion to Electrons method (ICE)

The Ion Conversion to Electron (ICE) monitoring method is also used to measure the ion flux entering the SDS ($\Phi_{\rm ion}^{\rm SDS}$). While it achieves a higher sensitivity than the PS-DCE current it needs a special experimental configuration. For these reasons, the ICE monitoring method is mostly used during ion commissioning measurements and during dedicated background measurements, and it cannot be used in parallel with neutrino mass measurements.

The basic working principle is that ions that enter the PS will create secondary electrons via residual gas ionization or via surface-driven mechanisms. These electrons are detected with the FPD and the ion flux is inferred from the count rate.

For ICE monitoring, the PS vessel is set to -18.6 kV to block all the electrons coming from the source section. Before the measurements are carried out, the PS vessel has to be set to -25 kV for a few minutes to condition the experiment, otherwise discharges can be seen in the FPD. The PS upstream-cone, wire, and downstream-cone electrodes are set to -19.1 kV, -19.05 kV, and -19.0 kV respectively. The MS retarding potential is set to -10 kV and the magnetic fields are set to 1.1 mT so that the electrons created in the PS can travel adiabatically to the FPD.

This method was calibrated by comparing the FPD rate from ICE to the ion current measured by PULCINELLA (Sec. 7.3.2). The ion flux is related to the FPD rate ($R_{\rm FPD}$) as follows:

$$\Phi_{\rm ion}^{\rm PS} = \frac{R_{\rm FPD}}{\varepsilon_{\rm ICE}}, \tag{5.16}$$

where $\varepsilon_{\rm ICE}$ is an efficiency factor calculated as explained in section 7.3.2.

The primary advantages of the ICE monitoring method are: it achieves greater sensitivity than the PS-DCE current method; and the statistics are high, so a few minutes of data are enough to achieve the best sensitivity, limited by systematics, while the PS-DCE current needs a few hours to achieve the best sensitivity. The main drawback is that it needs a special setting, so it is not possible to make neutrino mass measurements at the same time as ICE measurements.

CHAPTER 6
SIMULATION OF IONS IN THE SPECTROMETER SECTION

As discussed in chapter 5, around 10^{12} ions/s are created in the KArlsruhe TRItium Neutrino experiment (KATRIN) source section [94]. These ions influence the experiment and among other things, they can ionize residual gas and create more background. Most of the ions are removed before they reach the spectrometer section and contaminate it, but it is important to monitor the ion flux in case they do reach the Spectrometers and Detector Section (SDS) so that we can trigger safety protocols.

There are different paths to study the behaviour of the ions in the experiment: they can be studied theoretically, with measurements and with simulations. In some cases all methods are necessary to characterize the effects and impacts that the ions have in the experiment.

In this chapter we present simulations of ions in the SDS and their results. The simulations were done with the Kassiopeia simulation package; a detailed description of how the software works can be found in a dedicated paper [103]. Here just a brief description of the software structure is given (Sec. 6.1) as well as an explanation of an extension to this package that was programmed to facilitate the simulations (Sec. 6.2).

Two different simulations were carried out to calibrate ion monitoring devices in the spectrometer section (Sec. 6.3). The first one was done to calibrate the current measured in the Pre-Spectrometer (PS) Downstream-Cone Electrode (PS-DCE) (Sec. 6.3.1). And the second one calibrated the Ion Conversion to Electron (ICE) monitoring method (Sec. 6.3.2). In this chapter we talk about the simulations, and in a later section we describe how the calibration is done combining data from measurements and from the simulations (7.3.1).

6.1 Kassiopeia package

Kassiopeia [103] is an object-oriented software that was explicitly designed to do particle tracking simulations for the KATRIN and Project 8 experiments. Its main purpose is to do high precision tracking simulations taking into account complex geometries and the magnetic and electric fields of the experiment. The code is mostly written in the C++ lan-

guage and the specific details of the simulations can be set by the user with a configuration file in Extensible Markup Language (XML). The underlying design of Kassiopeia will be explained below.

Simulation structure

The simulation starts by reading an XML file with the main configurations. Then the previously defined objects of the XML file are built and initialized. These objects include: the initial particle where it is possible to specify the initial conditions; the geometric shapes that represent surfaces and spaces; the magnetic and electric fields; and the terminators to end the simulation. Then the event loop is carried out as many times as specified by the user. There are three loops in the simulation: over the events, the tracks, and the steps. The **step** represents the evolution of a particle over a small distance of space and time; the **track** is a collection of steps representing the total evolution of a particle from the starting position to the final position; and the **event** is a collection of tracks that are related by a primary particle. In each space and surface interactions are calculated. Finally, the output is written in a root [104] file given in four intuitive levels: step, track, event, and run.

Particle propagation

The propagation of the particles is a key part of the simulation. It refers to the calculation of the trajectories that the particles take. In each step, the equations of motion are calculated to give the position for the next step. All the continuous physical processes that the particle undergoes are represented in the equation of motion, from the electric and magnetic fields forces to synchrotron losses. There are different types of trajectory calculators that depend on the terms used in the equation of motion. The full list can be found in the Kassiopeia paper [103] while here we will just list the ones that were used in the scope of this thesis.

- **Exact trajectory**; the position vector **r** and the momentum vector **p** of the particle trajectory over time t are calculated using the Lorentz equation:

$$\frac{\mathrm{d}\mathbf{r}}{\mathrm{d}t} = \frac{\mathbf{p}}{\gamma m}, \tag{6.1}$$

$$\frac{\mathrm{d}\mathbf{p}}{\mathrm{d}t} = q(\mathbf{E} + \frac{\mathbf{p} \times \mathbf{B}}{\gamma m}), \tag{6.2}$$

  where γ is the Lorentz factor, m is the rest mass of the particle, q is its charge, **E** is the electric field and **B** is the magnetic field.

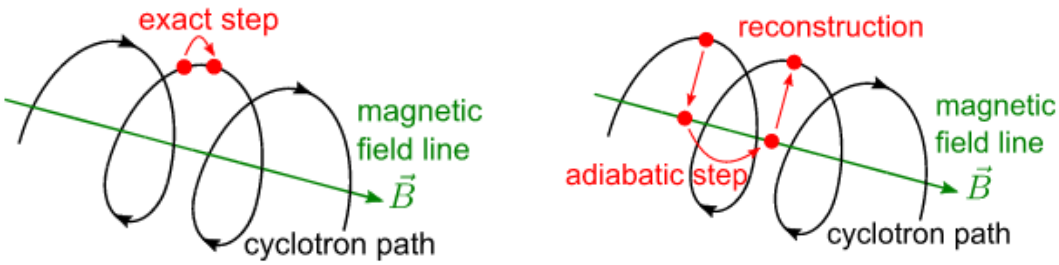

(a) Exact trajectory

(b) Adiabatic trajectory

Figure 6.1: Sketch of the particle propagation exact trajectory (a) and adiabatic trajectory (b). This figure comes from [103].

- **Adiabatic trajectory**; this trajectory works under the assumption that the electric and magnetic field are almost constant within a cyclotron radius of the particle movement. In this case, the quantity $\gamma\mu$, where μ is the magnetic moment, is conserved. The position is described with the center of motion vector $\mathbf{r}_c$ and the momentum is separated into its components parallel and perpendicular to the magnetic field $p_\parallel$ and $p_\perp$. After each step the exact position can be reconstructed. The equations of motion are the following:

$$\frac{\mathrm{d}\mathbf{r}_c}{\mathrm{d}t} = \frac{p_\parallel}{\gamma m}\frac{\mathbf{B}_c}{B_c}, \tag{6.3}$$

$$\frac{\mathrm{d}\mathbf{p}_\parallel}{\mathrm{d}t} = -\frac{p_\perp^2}{2\gamma m B_c}\nabla B_c + q\mathbf{E}_c \cdot \frac{\mathbf{B}_c}{B_c}, \tag{6.4}$$

$$\frac{\mathrm{d}\mathbf{p}_\perp}{\mathrm{d}t} = \frac{p_\perp p_\parallel}{2\gamma m B_c}\nabla B_c \cdot \frac{\mathbf{B}_c}{B_c}, \tag{6.5}$$

  Two additional equations are added to account for the gyration and drift caused by the magnetron motion. The complete equations and treatment can be found in [103].

An illustration of both trajectories can be seen in figure 6.1. The adiabatic trajectory has the advantage that it is faster to compute than the exact trajectory since its steps are larger.

Interactions

The particles can interact with surfaces or with other particles as they advance in their paths throughout the simulation. The probability that the particle interacts within a medium with a set density is calculated at each step. Scattering interactions are also implemented in the simulations. Surface interactions occur when a particle reaches a surface, then the

particle can be reflected back or terminated and the properties of the particle are modified accordingly.

6.2 Kassiopeia extension

The Kassiopeia software has a *modifier* class. The purpose of this class is to implement features or interactions that occur after a condition is satisfied. For example, a modifier might split a particle into two sub-particles (dissociation in flight) after the original particle has travelled a certain path length.

A new modifier was created for this work with the purpose of reflecting a particle after it reached a certain position. This was desired for simulations of ions in the SDS. In these simulations, the ions are created at the start of the PS, and they travel throughout the SDS where they interact with the electric and magnetic fields of the spectrometers. Some ions are reflected towards the Differential Pumping Section (DPS). In the real experimental settings, these ions would then be reflected back towards the spectrometer section by the electric fields created by positive voltages of the dipole electrodes. In the simulation, it was desired to reflect the ions at the start of the SDS so as to avoid the DPS part of the simulation.

The *reflection modifier* inverts the z component of the particle momentum p_z when it reaches a pre-specified position. The reflecting position can be specified by the user and the default value is set to the entrance of the PS.

The reflection modifier can be implemented in the simulations by including the following line in the general section of the XML file,

```
<ksmod_reflect_on_z name="mod_reflect_on_z"/>
```

and the following command in the navigation section,

```
<command parent="root_step_modifier" field="add_modifier" child="mod_reflect_on_z"/>
```

This modifier was used in some of the ion simulations that will be discussed in the following sections.

6.3 Simulations to calibrate ion monitoring devices

There are some mechanisms throughout the experiment used to monitor the ion flux (Sec. 5.4). Monitoring the spectrometer section is especially important because if the ions get there they can contaminate the experiment. An ion flux limit into the SDS was theoretically calculated [94] so as to keep the background contamination below the experimentally allowed limit.

The monitoring mechanisms needed to be calibrated so that we could infer the ion flux into the spectrometer section from the measurements. In this section we talk about two simulations that were carried out using the Kassiopeia software to calibrate the ion monitoring mechanisms.

6.3.1 Simulation to calibrate the PS cone current

As will be explained with more detail in Sec. 7.3.1, it is possible to know the ion flux into the PS by calibrating the current of the Pre Spectrometer Downstream-Cone Electrode (PS-DCE). And although ions are blocked by the ring electrodes before they reach the PS, it is useful to have a mechanism in place to monitor the ion flux in case of contamination.

When ions enter the PS they are accelerated towards the vessel wall by the high electric fields. Some of the ions hit the PS-DCE, sputter electrons and are neutralized in the process. The percentage, or the efficiency in which ions reach the PS-DCE depends on: the ion type, initial energy, initial position, and the PS electric and magnetic fields. Fortunately, the efficiency can be obtained from simulations. In order to calculate the ion flux from the measured PS-DCE current, simulations of ion inside the PS with different experimental conditions were done to obtain the ion efficiency.

Three different experimental settings were simulated and used to calculate the percentage of ions that reach the PS-DCE.

1. **Original;** System close to the original nominal setting where ions leave the flux tube and are neutralized in the vessel. Used prior to KATRIN Neutrino Mass measurement 1 (KNM1).

2. **Neutrino mass;** Settings used for neutrino mass measurement runs during both KNM1, and KATRIN Neutrino Mass measurement 2 (KNM2) that reduced the total background.

3. **Special;** System with modified electric fields with the purpose of getting all the sputtered electrons back to their starting point, namely the downstream cone electrode, so that the measured current does not depend on sputtered electrons. Used for the calibration of ion monitoring devices.

The decision to use the **neutrino mass** setting for the KATRIN Neutrino Mass measurements (KNM) measurement campaigns was taken after the calibration measurements took place. This measurement was not planned to be used in the calibration of the PS-DCE current, but it was used as a correction factor as will be explained in 7.3.1.

Configuration	Vessel (V)	Upstream Cone (V)	Wire (V)	Downstream Cone (V)
Original	-18600	-19100	-19050	-19000
Special	-450	+30	+30	-400
Neutrino mass	-10000	-10500	-10500	-10500

Table 6.1: The main configuration settings of the PS used to calibrate the PS-DCE current (Original and Special) and the settings used for neutrino mass measurements (neutrino mass).

Parameter	Initial value/range
Ion type	D_2^+ and T_3^+
Axial position, z	-2.18 m
Radial position, r	[0, 3.6] cm
Azimuthal angle, α	0° to 360°
Polar angle of momentum vector, θ	0° to 45°
Azimuthal angle of momentum vector, Φ	0° to 360°
Kinetic energy, E	40 eV

Table 6.2: The main configuration initial parameters of the simulations used to calibrate the PS cone current.

The parameters of these configurations are shown in Table 6.1. These parameters were used as inputs in the simulations. The rest of the simulation inputs are shown in table 6.2. Ions were initialized in the middle of the PreSpectrometer magnet 1 (PS1) with an initial energy of 40 eV since experimentally ions were created in the Dipole Electrode 4 (DE4) Penning trap with a voltage of 40V. The particle propagation was calculated with the exact trajectory.

Some examples of the paths that the ions can take in the three different configurations can be seen in Fig. 6.2. We say that an ion reaches the PS-DCE when its path ends by hitting the rightmost shaded region. In the case of the special setting (6.2c) the ions take more time to hit a surface but most of them get to the PS-DCE.

The objective of the simulations was to calculate the percentage of ions that hit the PS-DCE from the total ion flux into the PS, or the efficiency (ε). In other words, for a sample of N simulated ions, the efficiency is:

$$\varepsilon = \frac{k}{N} \tag{6.6}$$

where k ions got to the PS-DCE. Table 6.3 contains the results for each configuration. There are two different ion types in the simulation because deuterium ions were used in the

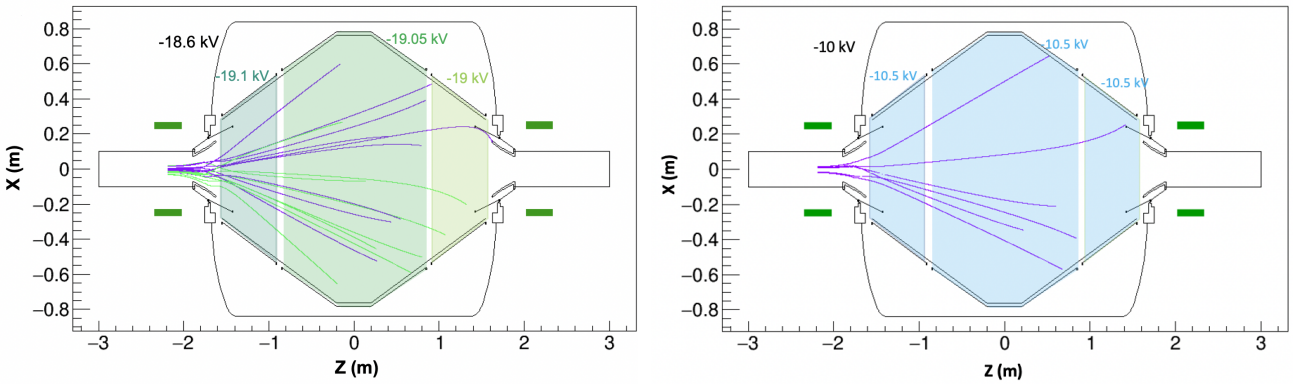

(a) Original setting

(b) Neutrino mass setting

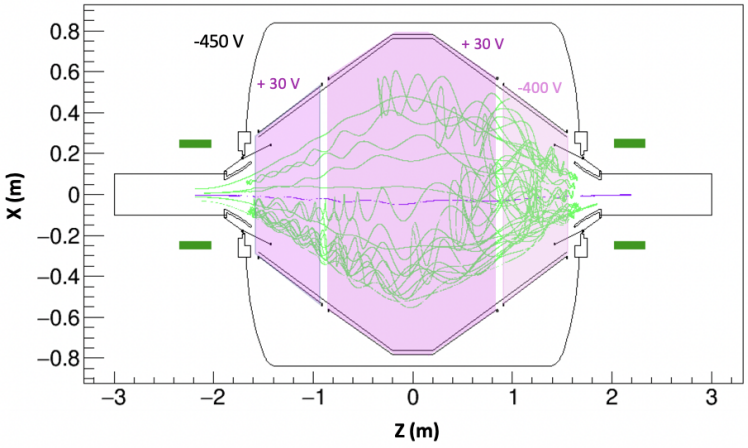

(c) Special setting

Figure 6.2: Simulations of ions inside the PS for three different configuration settings. The color of the ion track represents the ion initial energy and the shaded regions represent the surface areas of the upstream cone electrode, wire electrodes and downstream cone electrode (from left to right).

Configuration	Ion type	Efficiency (%)	Error (%)
Original	D_2^+	15.86	0.01
Original	T_3^+	21.11	0.01
Special	D_2^+	70.04	0.01
Special	T_3^+	64.34	8.25
Neutrino mass	D_2^+	12.50	0.02
Neutrino mass	T_3^+	15.30	0.02

Table 6.3: Simulated efficiency, or percentage of ions that reach the PS-DCE when starting at the PS entrance. Different configurations with two ion-types, namely D_2^+ and T_3^+, were simulated.

calibration measurements and tritium ions were used in the neutrino mass measurements.

The errors of the efficiencies in Table 6.3 come from the variance of the efficiency of a binomial distribution [105]:

$$\sigma^2 = \frac{k(N-k)}{N^3}. \tag{6.7}$$

The errors are small due to the large number of simulated events, which was between 5,000 and 10,000. The error of the simulation with **Special** configuration and tritium ions is bigger than the rest because it has a larger amount of trapped ions. With a dedicated simulation, they were shown to eventually hit the downstream cone if they were not terminated after a specific travelled length. In other words, for this simulation, the trajectories of some ions were terminated after they travelled a maximum path length, getting trapped in the spectrometers, instead of letting them being terminated because of hitting the vessel or exiting the flux tube. Simulations with a longer maximum path length were not done for the **Special** setting with tritium because of time constraints and because it was shown that the "trapped ions" would ultimately get to the PS-DCE.

The results shown in this section are used in Sec. 7.3.1 to calibrate the current measured at the PS-DCE. More details about how the calibration is done can also be found there.

6.3.2 Simulation to calibrate the ICE ion monitoring method

In Sec. 5.4.4 we talked about an ion monitoring method where, by reading the Focal Plane Detector (FPD) counts, it is possible to infer the ion flux into the spectrometer section (the ICE method). In order to calibrate this method and to be able to extract the ion flux, we simulated ions travelling from PS1, the entrance of the spectrometer section, to the Faraday Cup we used to measure the ions located in front of the FPD. Here we will briefly explain

DE1 (V/V)	DE4 (V/V)	PS vessel (kV)	PS U/W/D (V)	MS vessel (V)
200/200	-350/-350	0	185/185/185	200, 198, 195, 190, 180

Table 6.4: Experimental and simulation settings of the dipole section (DE2 and DE3 were set to zero) and spectrometer sections for the calibration of the ICE ion detection method. The PS values correspond to the upstream cone, wire and downstream cone electrodes in that order. The MS has four values that correspond to four different simulations.

Parameter	Initial value/range
Ion type	D_2^+
Axial position, z	-2.18 m
Radial position, r	[0, 3.6] cm
Azimuthal angle, α	0° to 360°
Polar angle of momentum vector, θ	0° to 45°
Azimuthal angle of momentum vector, Φ	0° to 360°
Kinetic energy, E	200 eV

Table 6.5: The main configuration initial parameters of the simulations used to calibrate the ICE method.

how this method is calibrated. A more detailed explanation can be found in Sec. 7.3.2, and in this section we will talk about the simulations carried out for this purpose.

The calibration basically consisted of reading the current created by the ions with a Faraday Cup and then comparing it to the electron counts on the FPD, with the Faraday cup removed. Normally, the ions don't reach the SDS, and if they did, they would be accelerated towards the vessel because of its negative potential. That is why a special measurement setting was used on the spectrometers so that the ions could reach the detector section. The simulation settings can be seen in Table 6.4, and are the same settings as the ones used during the calibration measurements. The rest of the parameters of the simulation can be seen in Table 6.5.

The current in the Faraday cup was measured for different Main Spectrometer (MS) settings. The first goal of the ion simulations was to get the efficiency with which the ions reached the Faraday cup in each setting. This efficiency can be seen in Fig. 6.3. The starting energy of the ions was always 200 eV, and the MS voltage was lowered to the values stated in Table 6.4 in order to let ions through. The ions with zero surplus energy (energy above the MS voltage setting) have low efficiency because their energy is not always enough to overcome the MS potential, depending on their starting angle. Ions with too much surplus energy lose efficiency due to their non-adiabatic motion.

The second goal of the simulations consisted of investigating the efficiency dependence

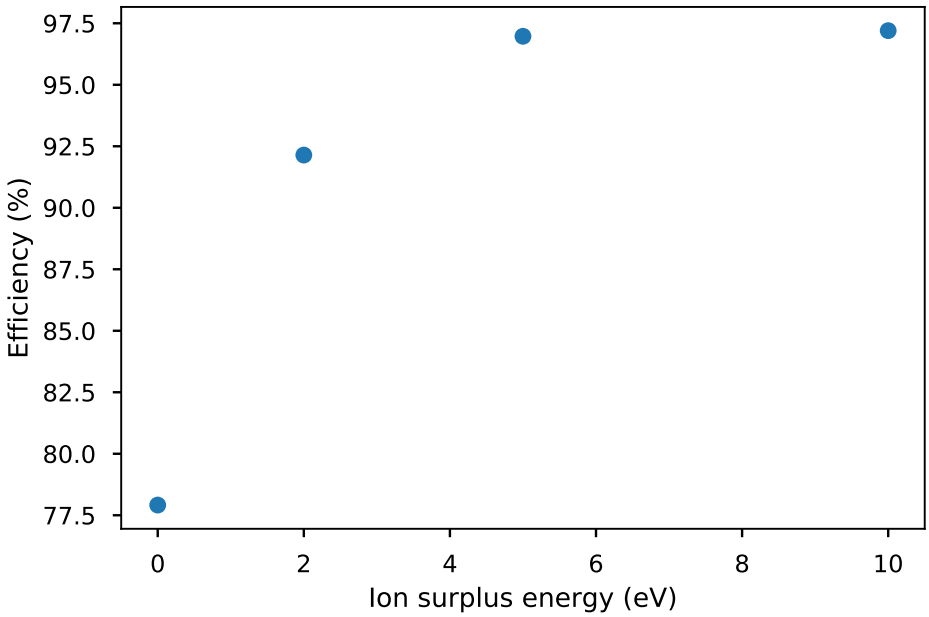

Figure 6.3: Efficiency of Penning ions to traverse the spectrometers and get to the Faraday cup. The binomial error was calculated according to Eq. 6.7 and is too small to see.

on the initial radial position of the ions. The results are shown in Fig. 6.4. If the ion starts in the center of the flux tube, it is highly probable it will reach the Faraday cup, and although most of the ions start there, not all ions do. Our flux tube has a radius of about 3.5 cm for this type of ion. As the ion moves away from the center, the efficiency decreases, and they don't reach the Faraday cup as often. The curve for the ions with surplus energy of 10 eV is slightly different to the rest because more of the ions don't follow the magnetic field lines and are trapped in the MS.

These results were compared to and agree with the simulation done by Emmanuel Weiss in [106], which were done using a different software programmed by Gluck. In the previously mentioned thesis and in Sec. 7.3.2 we talk about how to incorporate the simulation results into the analysis of the calibration of the ICE monitoring method.

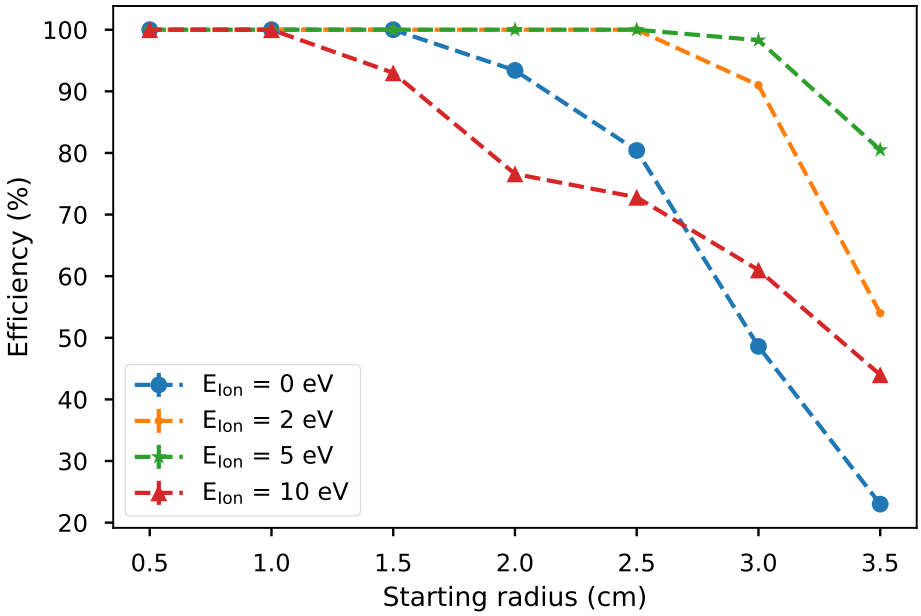

Figure 6.4: Dependence on the radial start position of the efficiency of Penning ions to get to the Faraday cup. The energy of the ions is their surplus energy. The binomial error was calculated according to Eq. 6.7 and is too small to see.

CHAPTER 7
ION INSIGHTS FROM COMMISSIONING STS-IIIA CAMPAIGN

The ion measurements, analysis and results of the KATRIN measurement campaign STS Commissioning Phase IIIa (STS-IIIa) are described in detail in this chapter. STS-IIIa was a commissioning measurement campaign, so we start by explaining the details and goals of this campaign (Sec. 7.1).

During neutrino mass measurements most of the ions come from tritium beta decay. But, since there was no tritium gas circulation during the STS-IIIa campaign, other non-tritium ion sources were explored (Sec. 7.2). Using these non-contaminating ions, the ion monitoring mechanisms were calibrated (Sec 7.3), and the ion blocking mechanisms were characterized (Sec. 7.4).

The results shown in this chapter are a collaborative work amongst the KATRIN Ion Lion Team: Fabian Friedel, Ferenc Glück, Magnus Schlösser, Manuel Klein and myself. In this chapter, it will be mentioned when there is an explicit contribution from one of my collaborators.

7.1 Commissioning phase STS-IIIa

The measurement campaign STS-IIIa was carried out in October 2018. It consisted of measurements, without tritium, with the goal of characterising different components of the KArlsruhe TRItium Neutrino experiment (KATRIN) experiment. The main tasks included: measuring the column density inside the beamline; calibration of the e-gun; and characterising the ion monitoring, blocking and removing mechanisms with inactive gas.

The main goals of the Ion Team in this campaign were the following:

1. Study ion sources with inactive gas (helium and deuterium) so as not to contaminate the spectrometer section
2. Verify that the ion blocking and removal mechanisms work
3. Corroborate optimal settings of the ion blocking and removal electrodes
4. Measure and identify different ion species

5. Calibrate the ion monitoring systems

As a safety measure, tritium was not used as a source. The ion blocking and removal mechanisms needed to be tested with a high, non-radioactive, ion column density before the experiment was deemed safe to insert significant amounts of tritium. This was necessary because, as explained in section 5.1, there is a flux limit of tritium ions that can enter the spectrometer section so as to maintain a low background in the Focal Plane Detector (FPD).

In the following sections, the measurements and results from this campaign are described in detail. All measurements were performed successfully, with the exception of measuring different ion species. That could not be done because the measuring unit Fourier Transform Ion Cyclotron Resonance (FT-ICR) did not work. It was believed to be erroneously connected, a problem that was impossible to fix during this campaign due to the apparatus location, inside the Differential Pumping Section (DPS), which cannot be opened in the middle of a measurement campaign. Nevertheless, after the campaign, more problematic hardware malfunctions were found and the unit could not be fixed.

7.2 Non-tritium ion sources

The ion flux, under KATRIN nominal conditions, comes mostly from tritium beta decay and from beta electrons scattering and ionizing tritium gas. In this campaign tritium was not used, so a new source of ions was needed.

Three different ion creation mechanisms were explored, since each one had unique advantages and drawbacks. In this section we will describe them, starting with the creation of helium ions in the main spectrometer (Sec. 7.2.1). Then we will describe two deuterium ion creation mechanisms, namely, the creation of deuterium ions from ionization of deuterium gas injected in the Windowless Gaseous Tritium Source (WGTS) (Sec. 7.2.2), and the creation of deuterium ions from Penning traps (Sec. 7.2.2).

7.2.1 Helium ion creation inside the Main Spectrometer

The first method investigated consisted of the creation of ions by photoelectrons ionizing helium gas inside the Main Spectrometer (MS). The advantages of using helium ions were the following:

- They did not contaminate the Spectrometers and Detector Section (SDS) because they are stable.
- The equipment necessary to insert helium gas and to produce photoelectrons in the MS was already installed.

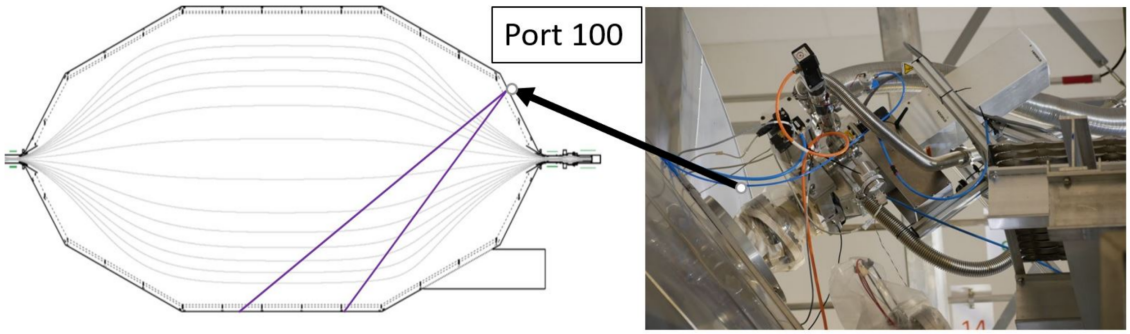

Figure 7.1: Left: sketch of the Main Spectrometer with the Light Hammer at pump port 100. The illumination envelope is shown by the purple lines. Right: picture of the LightHammer installation at pump port 100 [107].

- Dipole Electrode 4 (DE4) was the first dipole in the ions' path, since they propagated from the MS towards adjacent sections. This was important because during the Very First Tritium (VFT) campaign ions were only detected with Dipole Electrode 1 (DE1), even though all dipoles were expected to detect a small ion flux. This was attributed to inadvertent blocking of ions by work-function differences along the beamline [94]. No work-function differences were expected to block MS helium ions from reaching DE4.

The disadvantages, compared to deuterium ions, came from where and how they were created: their energy was not tunable; and half of them propagated upstream from the MS, which was the opposite direction from tritium ions. The direction of motion was also a disadvantage because the blocking and removing electrodes are located upstream of the MS, and although ions reached them and qualitative studies could be made, quantitative measurements were not possible.

Creation method

To create helium ions, a high-intensity Ultra-Violet Irradiator (Light Hammer), manufactured by Heraeus Noblelight, was used to illuminate the inside of the MS vessel. The Light Hammer is installed in the MS in pump port 100 and it created photoelectrons by illuminating the inner wall of the main spectrometer vessel. A sketch of the main spectrometer and a picture of the Light Hammer are shown in figure 7.1. Also depicted is the surface area of the main spectrometer which was illuminated and where photoelectrons were created. The helium gas was injected through pump port 100 into the main spectrometer where it was ionized by the photoelectrons. Around 10^9 He^+ ions/s were created using this method [107].

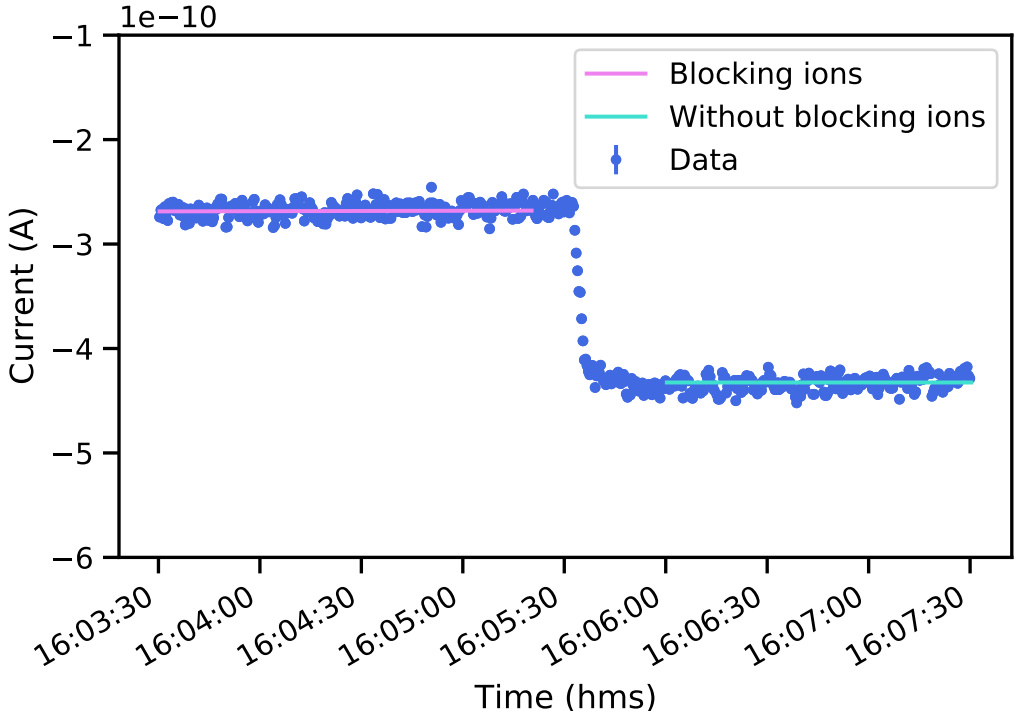

Figure 7.2: Current measured in DPS Dipole Electrode 3 (DE3) with (pink line) and without (light blue line) blocking ions with Ring Electrode DPS a (RE-DPSa). The current measured while RE-DPSa is blocking the ions is the offset current of the dipole when it is set to a negative potential.

Qualitative measurements

It was possible to measure the helium ion flux into the DPS with all the dipole electrodes. As a case study, consider measuring the helium ion flux in dipole electrode 3 (DE3). Figure 7.2 shows the current measured by DE3 before ($I^{\mathrm{DE3}}_{\mathrm{ions}}$) and after ($I^{\mathrm{DE3}}_{\mathrm{blocked}}$) blocking ions with RE-DPSa set to a positive potential of 200 V. The potentials of the dipole electrodes 2, 3 and 4 were +200/+200V, -350/-5V and 0/0V respectively to block the ions from reaching the WGTS (Dipole Electrode 2 (DE2)), remove ions (DE3) and let ions through (DE4).

The current created by the ions depositing their charge in DE3 was: $I^{\mathrm{DE3}}_{\mathrm{ions}} - I^{\mathrm{DE3}}_{\mathrm{blocked}} = (1.628 \pm 0.009) \times 10^{-10}$A. Using the elementary charge ($q_e = 1.602 \times 10^{-19}$ C) the detected ion flux ($\Phi^{\mathrm{DE3}}_{\mathrm{ion}}$) was:

$$\Phi^{\mathrm{DE3}}_{\mathrm{ion}} = (I^{\mathrm{DE3}}_{\mathrm{ions}} - I^{\mathrm{DE3}}_{\mathrm{blocked}})/q_e = (1.02 \pm 0.05) \times 10^9 \text{ ions/s} \tag{7.1}$$

Similar measurements were carried out with dipole electrodes 1, 2 and 4 giving the results shown in table 7.1. The flux measured by DE4 (setting 1) is significantly smaller

Setting	DE1 (V/V)	DE2 (V/V)	DE3 (V/V)	DE4 (V/V)	Φ_{ion} (ions/s)
1	0/0	0/0	+200/+200	-5/-350	$(5.2 \pm 2.3) \times 10^6$
2	0/0	+200/+200	-350/-5	0/0	$(1.02 \pm 0.05) \times 10^9$
3	+200/+200	-350/-5	0/0	0/0	$(1.72 \pm 0.12) \times 10^9$
4	-350/-5	0/0	0/0	0/0	$(1.20 \pm 0.38) \times 10^9$

Table 7.1: DPS dipole electrode configurations and helium ion fluxes measured by the dipole electrode 1, 2, 3 and 4 (settings 4, 3, 2 and 1 respectively) during the Light Hammer ion creation measurement.

than the one measured by the rest of the dipoles, possibly because there was not enough time to stabilize $I_{\text{ions}}^{\text{DE4}}$, so the current was still drifting when the measurement took place. The percentage of ions that reached the DPS compared to the created ion flux is not known since no simulations were done. No further investigations or simulations were pursued since this method of ion creation was just used to qualitatively check that the dipoles were working correctly.

Conclusion

With this measurement, the creation of helium ions inside the main spectrometer using the Light Hammer was confirmed. It was observed, for the first time, that each of the four DPS dipoles could remove ions from the flux tube. Furthermore, ions were effectively blocked with RE-DPSa.

7.2.2 Deuterium ion creation

The creation of deuterium ions was investigated because of their following advantages:

- They don't contaminate the SDS as tritium ions do because they are stable and do not decay
- They travel downstream from the Source and Transport Section (STS), the same direction as tritium ions do with nominal neutrino mass settings
- Their energy and flux can be tuned, depending on their creation location

To create these ions, deuterium gas was injected in the WGTS. This gas expanded throughout the source section into adjacent sections, namely the DPS, where it was mostly pumped out. Once deuterium injection was stopped, the main contributor of the residual

gas inside the beamline was thus deuterium. This is worth mentioning because some measurements were carried out with "residual gas" meaning deuterium gas but with no constant injection of this gas in the WGTS.

In order to ionize the gas, photoelectrons were created by illuminating the gold-plated rear wall with two mini Z UV lamps. Around 10^{11} photoelectrons/s were created by this method. These charged particles travelled through the beamline and ionized deuterium gas.

There are two different regions where most of the ions were created, the WGTS and the DPS. Their creation location depended on the deuterium column density, as will be explained.

WGTS deuterium ions

With high deuterium column density, the photoelectrons coming from the Rear Wall (RW) interacted with the gas in the WGTS. They ionized the gas and created deuterium ions in the WGTS. These ions left the WGTS only when the column density was sufficiently low; otherwise the ions scattered with the deuterium gas, losing energy and thermalizing, and did not make it to the spectrometer section.

These ions were observed during STS-IIIa. Figure 7.3 shows the mean rate measured at the FPD. The rate did not come directly from the ions; instead it came from electrons created by the ions ionizing residual gas in the spectrometer section (Ion Conversion to Electron (ICE) method). The rate increased when more ions reached the SDS. This effect will be further discussed and calibrated in section 7.3.2. The rate observed at zero volts came from all the ions that left the WGTS and got to the spectrometer section. As the RE-DPSa voltage was increased, fewer ions got to the spectrometer section because they were blocked by the positive electric field, as was explained in section 5.3.2, and so the rate decreased.

Deuterium WGTS ions were successfully created and observed. Nevertheless it was not possible to tune their energy or to increase the ion flux beyond the amount observed without RE-DPSa blocking. So a new source of ions was investigated.

DPS Penning ions

With low column density, the photoelectrons mostly travelled from the RW all the way to the DPS without ionizing the gas in the WGTS. They interacted with the residual gas near the dipole Penning traps due to the higher gas density inside. They ionized the residual gas and thus created Penning ions with specific kinetic energy corresponding to the dipole potential at their creation location, as was explained in chapter 5.2.4.

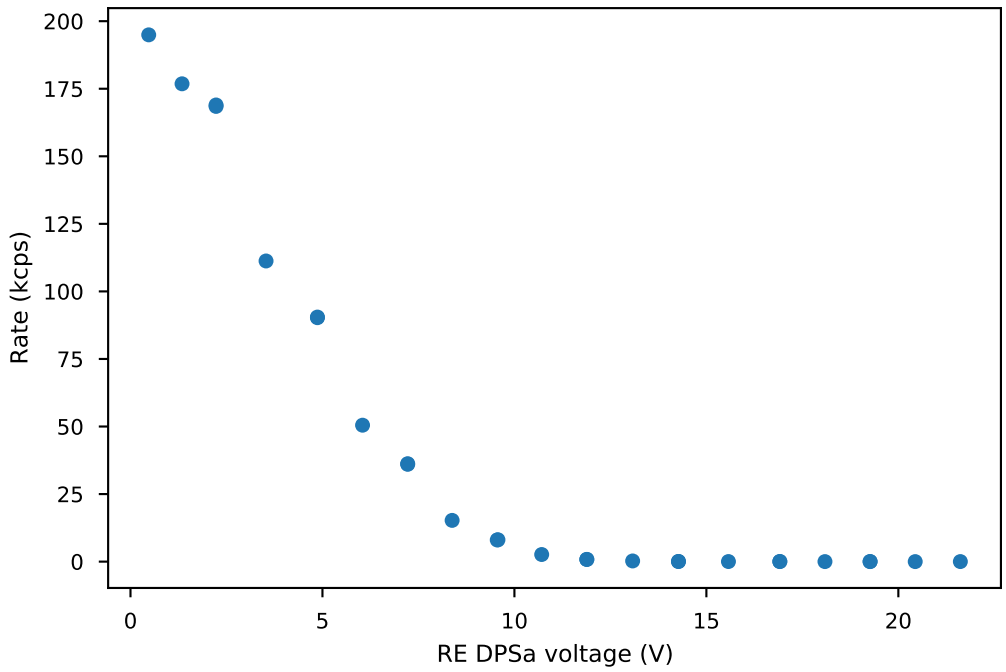

Figure 7.3: Mean rate measured in the FPD produced by deuterium ions created in the WGTS. The one σ errorbars are too small to be noticeable.

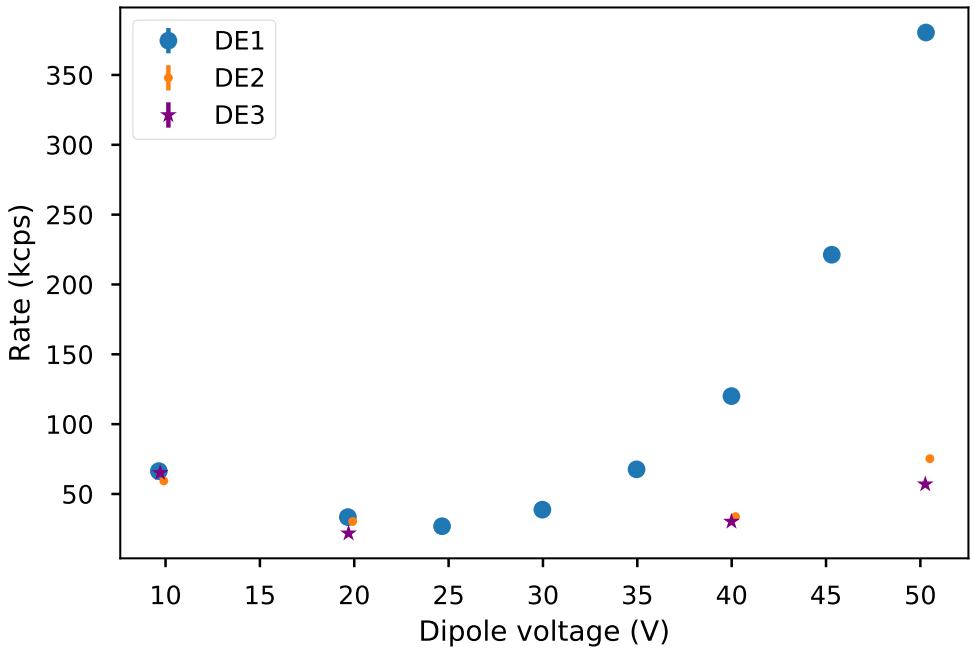

Figure 7.4: Mean rate measured in the FPD produced by Penning ions created in DE1 (blue circles), DE2 (orange dots), and DE3 (purple stars). The one σ errorbars are too small to be noticeable. There is no data for dipole 2 and 3 at 25, 30, 35 and 45 volts due to time constraints.

The creation of Penning ions with dipole electrodes 1, 2 and 3 was investigated. The measurement data can be seen in figure 7.4. For each measurement, the chosen dipole was set to the desired voltage, and the other two dipoles were set to zero volts. Penning ions were observed starting at 25 volts. The rate observed at 10 V and 20 V came from WGTS ionization and dissociative ions created in the WGTS, as discussed in the previous section and in section 5.2.3.

Deuterium gas density decreased further down the beam line; and so fewer ions were created when dipole electrodes 2 or 3 were used to produce the potential well instead of DE1. This can be seen by comparing the FPD rates created by the dipole Penning traps at set voltages of 40 V and 50 V. The Penning trap of DE3 created the lowest ion flux.

In conclusion, deuterium Penning ions were successfully created in dipole electrodes 1, 2 and 3. And it was found to be more convenient to use DE1 to create deuterium Penning ions because of the higher ion rate.

Some of the measurements that are discussed later in this chapter used this ion creation mechanism. A few examples are: the calibration of the ion monitoring devices (7.3.1, 7.3.2), and studies of the blocking mechanisms (7.4.1).

7.3 Ion monitoring devices

As mentioned in section 5.4, there are different ion monitoring systems along the beamline. The ones in the SDS had to be calibrated with non-contaminating ions in order to get a quantitative efficiency factor to convert measurement data into an ion flux flowing to the spectrometer section. They were calibrated during STS-IIIa because the ion sources were non-radioactive. The tritium flux limit of 1×10^4 ions/s [94] into the spectrometers was then monitored with the calibrated mechanisms.

The calibrations required: special settings of the hardware, deuterium ions created by Penning discharges in the dipole electrodes (Sec. 7.2.2), and dedicated simulations (Chapter 6). The calibration of two different ion-monitoring methods will be detailed below. Section 7.3.1 describes how the Pre Spectrometer Downstream-Cone Electrode (PS-DCE) current was calibrated. In section 7.3.2 the calibration of the ICE method is detailed. And finally, we discuss the argon pressure dependence of the ionization inside of the Pre-Spectrometer (PS) (Sec. 7.3.3), which is the underlying mechanism of the ICE method.

7.3.1 Calibration of the Pre-Spectrometer current

Ions are blocked by ring electrodes located at the DPS and at the entrance of the PS. Nevertheless, if a small ion flux escapes into the SDS, then it can be measured. Upon entering the

PS, the ions are accelerated by the negative potentials of the vessel and the wire electrodes and most leave the magnetic flux tube. These ions hit the vessel and the cone electrodes where they are neutralized. It is possible to measure the current created by the ions that reach the PS-DCE using an ammeter connected to the PS-DCE (Sec. 5.4.2). This current is created by the neutralization of ions reaching the PS-DCE but it is also affected by secondary electrons emitted on ion impact.

The objective of this measurement was to calibrate the current measured in the PS-DCE, thereby obtaining an efficiency factor to convert a PS-DCE current into an ion flux flowing to the SDS. The experimental settings used for this purpose were already defined in Sec 6.3.1 and they are the following:

1. **Original;** System close to the original nominal setting where ions leave the flux tube and are neutralized in the vessel. Nevertheless, after these measurements were carried out, it was decided to change the settings of the PS wires and vessel during the neutrino mass measurement campaigns.

2. **Special;** System with modified electric fields with the purpose of returning all the sputtered electrons back to their starting point, namely the downstream cone electrode (PS-DCE), so that the measured current does not depend on sputtered electrons. Special simulations were carried out by Ferenc Glück to map the sputtered electrons' paths to confirm that they would come back to the downstream cone electrode.

3. **Neutrino mass;** Experimental settings that reduced the total background. Used during the neutrino mass measurement campaigns KATRIN Neutrino Mass measurement 1 (KNM1) and KATRIN Neutrino Mass measurement 2 (KNM2).

The parameters of these configurations can be found in Table 6.1 and a sketch of the parameters is shown in Fig. 6.2. Fig. 6.2a shows the PS with the original setting, in which case the ions left the flux tube and were neutralized in the vessel. Fig. 6.2b shows the neutrino mass setting. Fig. 6.2c shows the PS with the special setting, in which case most of the ions were neutralized in the PS-DCE.

The calibration of the PS-DCE current was done for the PS in the original setting, because that was the setting originally planned to be used in the neutrino mass measurements. Fortunately, using data from other measurements, it was possible to relate the calibration to the neutrino mass setting. We will start by explain how the original setting was calibrated and then we will show how it can be related to the neutrino mass setting.

Configuration	Ion transport probability (%) P	Ion current (A) $I_{\text{ion}}^{\text{DCE}}$
Original	20 ± 3	$(76.0 \pm 0.3) \times 10^{-12}$
Special	60 ± 3	$(7.7 \pm 0.1) \times 10^{-12}$

Table 7.2: Measured PS-DCE current when deuterium Penning ions were created in DE1 and the electrode had a set voltage of 40 V, along with the probability (from simulations) of an ion reaching the PS-DCE for the calibration configurations.

Calibration of the PS-DCE current for the PS in the original setting

The calibration consisted of:

1. Making 40 eV deuterium Penning ions with DE1 set to 40 V to create a constant ion flux ($\Phi_{\text{ion}}^{\text{SDS}}$) into the SDS

2. Measuring the PS-DCE current with the PS in two different settings: the original and the special. The current was measured and averaged for an hour

3. Inferring the ion flux into the SDS from the measured PS-DCE current in the special setting, taking into account the ion transport probability of this setting (table 7.2)

4. Calculating the conversion factor $S(\text{original})$ of the special setting to the original setting

5. Calculating the efficiency factor ($\varepsilon_{\text{DCE}}^{\text{original}}$) that translates the PS-DCE current in the original setting to an ion flux into the SDS, taking into account the ion transport probability of this setting (table 7.2)

The probability of the ions reaching the PS-DCE is different for each configuration and it was calculated with the simulations discussed in chapter 6. These simulations were compared with results from Ferenc Glück's simulations, which were done with his own code, and not with the Kassiopeia software. Table 7.2 shows the mentioned probabilities as well as the measured ion currents ($I_{\text{ion}}^{\text{DCE}}$) for each setting; the error in the probabilities comes from the comparison between the two simulations. The ion current is calculated for each configuration by subtracting the background current, with no deuterium Penning ions, from the measured current.

By assuming that the special setting current measurement is unaffected by sputtered electrons, we can calculate the ion flux to the PS-DCE:

$$\Phi_{\text{ion}}^{\text{DCE}}(\text{special}) = I_{\text{ion}}^{\text{DCE}}(\text{special})/q_e = \Phi_{\text{ion}}^{\text{SDS}} \cdot \frac{P(\text{special})}{100} \tag{7.2}$$

where $I_{\text{ion}}^{\text{DCE}}(\text{special})$ is the current measured in the PS-DCE with the PS at the special setting, $\Phi_{\text{ion}}^{\text{SDS}}$ is the total flux of deuterium ions that enters the SDS, and $P(\text{special})$ is the probability of the ions reaching the cone electrode in the special configuration. Similarly, for the original setting,

$$\Phi_{\text{ion}}^{\text{DCE}}(\text{original}) = I_{\text{ion}}^{\text{DCE}}(\text{original})/(q_e \cdot S(\text{original})) = \Phi_{\text{ion}}^{\text{SDS}} \cdot \frac{P(\text{original})}{100}, \tag{7.3}$$

where $S(\text{original})$ is the conversion factor of the special setting to the original setting and the rest of the variables are analogous to those of the special configuration. From these equations and using the data from table 7.2 we obtain the conversion factor:

$$S(\text{original}) = \frac{I_{\text{ion}}^{\text{DCE}}(\text{original}) \cdot P(\text{special})}{I_{\text{ion}}^{\text{DCE}}(\text{special}) \cdot P(\text{original})} = 29 \pm 1. \tag{7.4}$$

And, from equation 7.3, we get the efficiency factor:

$$\varepsilon_{\text{DCE}}^{\text{original}} = \frac{I_{\text{ion}}^{\text{DCE}}(\text{original})}{\Phi_{\text{ion}}^{\text{SDS}}} = (9.2 \pm 1.4) \times 10^{-19}\text{C}, \tag{7.5}$$

with which it is possible to calculate the ion flux entering the SDS for a given PS-DCE current.

Unfortunately this calibration is only valid for the PS set to the original configuration and does not apply to the PS in the neutrino mass configuration. And no PS-DCE current measurement was taken with that configuration and with 40 eV DE1 ions. Since tritium campaigns began after those measurements, it was no longer possible to repeat the calibration due to possible contamination of the SDS with residual tritium ions. Using this same method to calibrate the new setting was no longer possible.

Calibration of the PS-DCE current for the PS in the neutrino mass setting

Although no direct calibration measurement was taken for the neutrino mass setting, data from other measurements was used to infer an efficiency factor ($\varepsilon_{\text{DCE}}^{\nu-\text{mass}}$). During the STS-IIIa campaign the PS was set to voltages quite similar to the ones used in the neutrino mass setting. No Penning ions were created at that time, but WGTS-deuterium ions were. Residual gas ions were created by photoelectrons, coming from the RW, ionizing the residual gas.

In an analogous manner to the conversion factor of the original setting, using the data

Configuration	Ion transport prob (%) P	Ion current (A) $I_{\text{ion}}^{\text{DCE}}$	PS U/W/D (V)
Neutrino mass	12.5 ± 3	-	-10500/-10500/-10500
Quasi-Neutrino mass	16 ± 3	$(0.79 \pm 0.01) \times 10^{-12}$	-10500/-10450/-10400
Original	20 ± 3	$(4.13 \pm 0.01) \times 10^{-12}$	-19100/-19050/-19000

Table 7.3: Measured PS-DCE current when WGTS-deuterium residual gas ions were created with photoelectrons from the RW, along with the probability (from simulations) of an ion reaching the PS-DCE for the calibration configurations. The Quasi-Neutrino mass configuration has PS settings close, although not the same, to the neutrino mass configuration.

from table 7.3 we obtain the conversion factor of the neutrino mass setting:

$$S(\nu\text{-mass}) = \frac{I_{\text{ion}}^{\text{DCE}}(\nu\text{-mass}) \cdot P(\text{original}) \cdot S(\text{original})}{I_{\text{ion}}^{\text{DCE}}(\text{original}) \cdot P(\nu\text{-mass})} = 7.9 \pm 2.3, \tag{7.6}$$

where the error due to not having the exact neutrino mass setting was estimated by calculating the difference between the conversion factors determined by using each one of the simulated ion transport probabilities for the different settings.

Finally, the efficiency factor was calculated to be:

$$\varepsilon_{\text{DCE}}^{\nu\text{-mass}} = \frac{I_{\text{ion}}^{\text{DCE}}(\nu\text{-mass})}{\Phi_{\text{ion}}^{\text{SDS}}} = (1.77 \pm 0.67) \times 10^{-19}\text{C}. \tag{7.7}$$

This efficiency factor was used for measurements during the tritium column density ramp up of KNM1 campaign (Sec. 8.2.2). And as will be explained, the uncertainty on the PS-DCE measured current was too large to give us information on the minimum allowed ion flux into the SDS (1×10^4 ions/s) during neutrino mass measurements, but we can still get information of bigger ion currents into the SDS.

7.3.2 Calibration of the ICE detection method

As seen in Sec. 5.4.4, there is a second method with which it is possible to measure the ion current into the SDS, namely the ICE method. The advantages of this method are: the ion flux is calculated directly from the FPD rate, and it is quite sensitive. The disadvantage is that the spectrometers need a special high-voltage setting, different from the neutrino-mass setting, so that the FPD can measure the appropriate electrons. As a consequence, ICE measurements cannot be done simultaneously with neutrino mass measurements, but they are done for commissioning measurements.

A description of the calibration method will be given. The complete analysis method

can be found in the bachelors thesis of Weiss [106], and a summary will be presented in this section.

Method

The calibration was carried out as follows:

1. Deuterium gas was injected in the WGTS to achieve a column density of around 1% of the nominal value.

2. Penning ions were created with DE1 at a voltage of 200 V to create a constant ion flux ($\Phi_{\mathrm{ion}}^{\mathrm{DSD}}$) into the SDS.

3. The photoelectrons and negative ions were stopped by the negative potential created by setting DE4 at -350 V.

4. The FPD rate ($\mathrm{R_{FPD}}$) was measured with the experiment at the ICE settings (found in table 7.4). The goal of the ICE setting was to measure the FPD electron rate created by the ion flux entering the SDS ($\Phi_{\mathrm{ion}}^{\mathrm{SDS}}$), but the RW was set to an incorrect value, changing the ion flux in this setting:

$$\Phi_{\mathrm{ion,ICE}}^{\mathrm{SDS}} = \frac{\Phi_{\mathrm{ion}}^{\mathrm{SDS}}}{C_{\mathrm{RW}}} \tag{7.8}$$

   where C_{RW} is a correction factor to take into account the different settings of the RW.

5. A Faraday Cup, read out by Pulcinella, was inserted in front of the FPD and the experiment was set-up using the Pulcinella settings (found in table 7.4). This allowed the ions to travel adiabatically from the SDS entrance to the Faraday cup.

6. The main spectrometer was used as an ion filter by setting the main spectrometer inner electrodes (IE) to five different positive potentials (U_{ret}). The current was measured each time by Pulcinella ($I_{\mathrm{Pulcinella}}(U_{\mathrm{ret}})$). Then it was compared with the simulations shown in Sec. 6.3.2. This current is related to the total ion flux entering the SDS as:

$$\Phi_{\mathrm{ion}}^{\mathrm{SDS}} = \frac{I_{\mathrm{Pulcinella}}(U_{\mathrm{ret}}) - I_{\mathrm{Pulcinella,back}}}{q_e C(U_{\mathrm{ret}})} \tag{7.9}$$

   where $I_{\mathrm{Pulcinella,back}}$ is the background current, and $C(U_{\mathrm{ret}})$ is a correction factor that depends on the retarding potential and accounts, amongst other things, for the transport probability calculated with the simulations.

Setting	RW (V)	DE1 (V/V)	DE4 (V/V)	PS vessel (kV)	PS U/W/D (V)	MS vessel (V)
ICE	-200	200/200	-350/-350	-18.460	-500/-450/-400	0
Pulcinella	-100	200/200	-350/-350	0	185/185/185	0

Table 7.4: Experimental settings for the calibration of the ICE ion detection method. The ICE setting is used to measure the FPD rate while the Pulcinella setting is used to directly measure the the ion current at the Faraday cup with Pulcinella.

U_{ret} (V)	Background	200	198	195	190	180
$I_{Pulcinella}$ (pA)	15.44	26.68	33.45	53.67	74.81	80.37
σ_I (pA)	0.11	0.21	0.43	0.86	1.24	0.20

Table 7.5: Experimental settings and measurements for the calibration of the ICE detection method, where U_{ret} is the setting of the MS IE common.

7. An efficiency factor ($\varepsilon_{\mathrm{ICE}}$) was calculated to translate the FPD rate into an ion flux into the SDS:

$$\varepsilon_{\mathrm{ICE}} = \frac{R_{\mathrm{FPD}}}{\Phi_{\mathrm{ion}}^{\mathrm{SDS}}}. \tag{7.10}$$

Results

The measured FPD electron rate created by ions entering the SDS in the ICE setting was:

$$R_{\mathrm{FPD}} = 2.230 \pm 0.003\,\mathrm{Mcps}. \tag{7.11}$$

Figure 7.5 shows the current measured with Pulcinella during the five MS retarding voltage settings of the Pulcinella configuration. The value of the constant fit to the data is shown in table 7.5. The different settings were done so as to have better statistics of the ion flux entering the SDS.

The correction factors were calculated as follows. The C_{RW} correction arose because the RW was mistakenly set to different voltages during the ICE setting and the Pulcinella setting. This changed the photoelectron energy and the total ion flux. The correction factor was calculated with simulation, giving a result of $C_{\mathrm{RW}} = 0.954 \pm 0.008$ [106].

The correction factor $C(U_{\mathrm{ret}})$ took into account: the broad range of ion energies, and their transport probabilities thorough the SDS. It was calculated using three different simulations:

- The starting energy distribution of the ions was calculated by simulating the electric and the magnetic field inside the DE1. The simulations were done by F. Friedel using

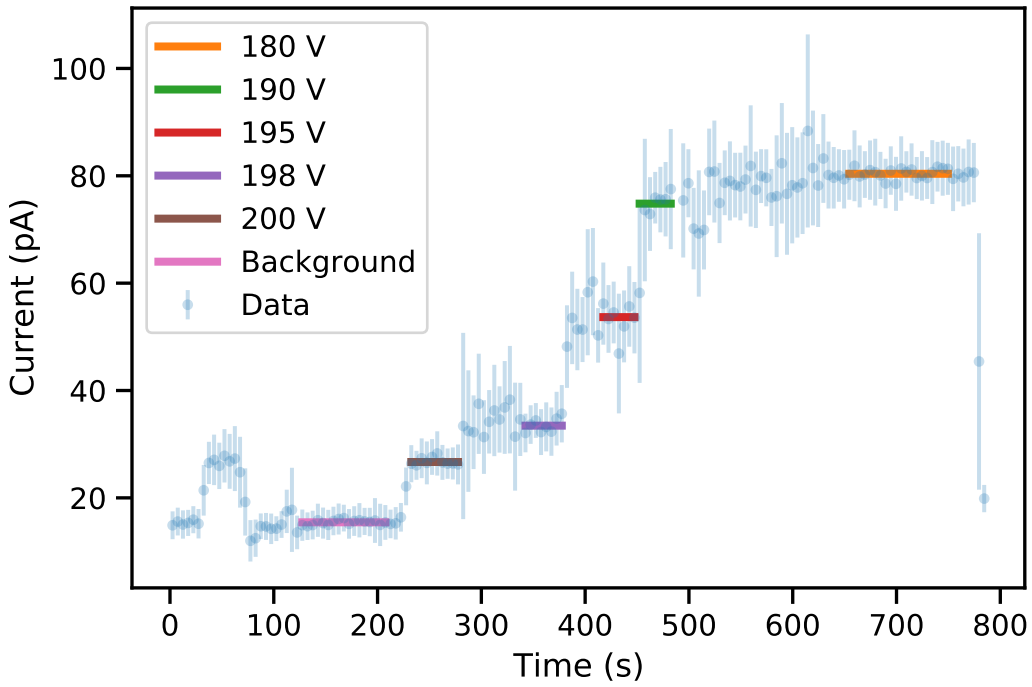

Figure 7.5: Current on the Faraday cup, measured by Pulcinella, during the ICE calibration measurements with the SDS on Pulcinella settings. The lines represent constant fits of the data during specific MS IE settings. The voltage in the legend refers to the U_{ret} of the MS. The settings where the U_{ret} was set to 198 V, 195 V, and 190 V are measuring the ion flux coming from DE1. While in the settings U_{ret} = 200 V and 180 V we are measuring ions from RE-DPSa. The changes in the experimental configuration are reflected in the data between these steps.

the software KEMField and KASSIOPEIA to simulate the electric and magnetic field respectively [95].

- The pressure profile along DE1 was calculated using MolFlow+ [108], which is a software package to simulate free molecular flow in vacuum. The simulations were carried out by F. Friedel [95].

- The ion adiabatic transport probability to Pulcinella was simulated with KASSIOPEIA and the results are shown in Sec. 6.3.2. The simulations consisted of ions moving downstream from the SDS entrance to the detector section. The simulations were carried out for different starting radii and different starting energies.

The total ion flux into SDS was calculated using Eq. 7.9 for each retarding potential shown in table 7.5. Since this flux should not depend on the retarding potential, a weighted mean of the ion flux at each setting was used:

$$\Phi_{\text{ion}}^{\text{SDS}} = (630 \pm 5) \times 10^6 \,\text{ion/s}. \tag{7.12}$$

Finally, the ICE efficiency was calculated using equation 7.14:

$$\varepsilon_{\text{ICE}} = (3.54 \pm 0.18) \cdot 10^{-3} \,\text{counts/ion}. \tag{7.13}$$

Using the ICE efficiency and equation 7.14 we get that 1 FPD count corresponds to an ion flux of around 282 ions/s. In conclusion, with this method it is possible to detect small changes of the ion flux into the SDS. This calibration was used during KNM1 and KNM2 campaigns. However, the PS and MS were baked after those campaigns. Hence, some of the ion transmission properties changed, as well as the residual gas properties. Since the ICE method relies on ions interacting with residual gas and with the vessel, the ICE calibration is no longer expected to be valid. Nevertheless, an ICE rate increase still indicates an SDS ion flux increase, so it can still be used to qualitatively monitor the ion flux.

7.3.3 Pressure dependence of argon ionization inside the PS

As stated above, the underlying mechanism of how ions create electrons inside the PS is not well understood. The ions, upon entering the PS, are accelerated towards the spectrometer walls and electrodes, where they are neutralized. Along their paths, they ionize residual gas and create secondary electrons. Some of these electrons can be detected with the FPD (R_{FPD}), giving us a hint of the ion flux ($\Phi_{\text{ion}}^{\text{SDS}}$) into the SDS.

During the VFT[1] campaign it was thought that the ion detection efficiency of the ICE rate ($\varepsilon_{\mathrm{ICE}}$) scaled linearly with gas density [94] or pressure inside the PS:

$$\varepsilon_{\mathrm{ICE}} = \frac{R_{\mathrm{FPD}}}{\Phi_{\mathrm{ion}}^{\mathrm{SDS}}} \approx s \cdot n \cdot \sigma, \tag{7.14}$$

where s is the ion path length inside the spectrometer, σ is the inelastic scattering cross section and n is the argon gas number density in the PS. The density follows the ideal gas law $n = pM/RT$ where p is the pressure, M is the molar mass, R is the gas constant and T the temperature. From equation 7.14 it follows that the ionizing efficiency depends linearly on the pressure of the gas inside the PS.

During the VFT campaign the primary ion source consisted of tritium beta decay in the WGTS. As a result, one of the backgrounds of the PS pressure-dependence measurement came from the beta electrons produced in the decay. This background was produced by the electrons travelling to the PS entrance and ionizing argon gas. Further measurements were planned for the STS-IIIa campaign to characterize the ionization pressure dependence without these backgrounds. The main advantage of deuterium ions, used in STS-IIIa, was that there were no electrons contaminating the measurements, since the photoelectrons were stopped in the DPS with the dipoles at negative potential.

The following subsections describe the measurements done to characterize the ionization of argon gas in the PS depending on the pressure. Results will be shown for different measurement settings, one with deuterium ions as a source and the other with "background ions" encountered in the VFT campaign. The data will be analysed and compared with results from previous campaigns.

Measurements

Two separate measurements were planned in order to characterize the ionization inside the PS: one for deuterium ions and the other for the background argon ions.

1. **Deuterium ions**. Deuterium Penning ions were created by setting DE1 to a positive potential. Photoelectrons coming from the RW were blocked by RE-DPSa at negative potential. There was no constant deuterium injection into the WGTS because there was enough residual deuterium gas in the DPS Penning traps for the photoelectrons to scatter and ionize. The expectation was that this configuration would depend linearly on pressure, as shown in equation 7.14.

[1]VFT campaign was the first campaign where tritium gas was injected into the WGTS. Also, all the beamline was used during this campaign. However the tritium concentration was extremely low 0.5% instead of the design concentration of 95%. The rest of the gas consisted of inactive deuterium gas.

Configuration	DE1 (V)	RE DPSa (V)	PS (V)
Deuterium Ions	+350/+350	-290	-500/-450/-400
Ar^+ ions	0	0	-500/-450/-400

Table 7.6: Experimental setting of the measurements of ionization inside the PS with deuterium and Ar^+ ions, the rest of the dipole electrodes were at zero volts.

2. **Ar^+ ions** . In this setting, all dipoles and RE-DPSa were turned off, so no Penning ions were created. Instead, the ions were created by electron-induced background. The photoelectrons travelled all the way to the PS but could not enter due to the high negative voltages. They scattered with argon gas between the PS and the Cryogenic Pumping Section (CPS), ionizing it and creating Ar^+ ions, which in turn entered the PS. This setting was thought to depend quadratically on the argon pressure, because the amount of argon gas that escapes to the CPS also depends on the argon pressure.

Table 7.6 shows the settings of the previously mentioned measurements and figure 7.6 is a sketch of the particle paths that played an important role in each of the measurements. Some of the final electrons created in the PS, in both configurations, travelled from the PS to the FPD where they were detected. It is important to note that not all photoelectrons ionized argon or deuterium and that not all ions ionized gas in the PS.

Results

There are two different methods to indirectly measure how many ions were created in the PS: the rate at the FPD and the current in the PS-DCE.

The FPD rate and the current in the PS-DCE, for both measurement configurations, are shown in Fig. 7.7. They follow the same trend because they are both measuring ions, although the FPD rate does so indirectly. Fig. 7.7a shows the results for the deuterium ion configuration where we see there is no argon-pressure dependence, although a linear dependence was expected. Figure 7.7b shows the results for the argon ion configuration, that is to say the "background" configuration. In this case there is a linear argon pressure dependence although a quadratic dependence was expected.

The pressure dependence of the argon ionization in the PS results obtained in the VFT campaign seems to come from the background of the measurement, that is from the β-electrons that ionize argon gas in the CPS since they show a linear dependence on argon pressure. This indicates that there is no need for high argon pressure inside the PS when doing ICE measurements. We conclude this since there is no argon pressure dependence

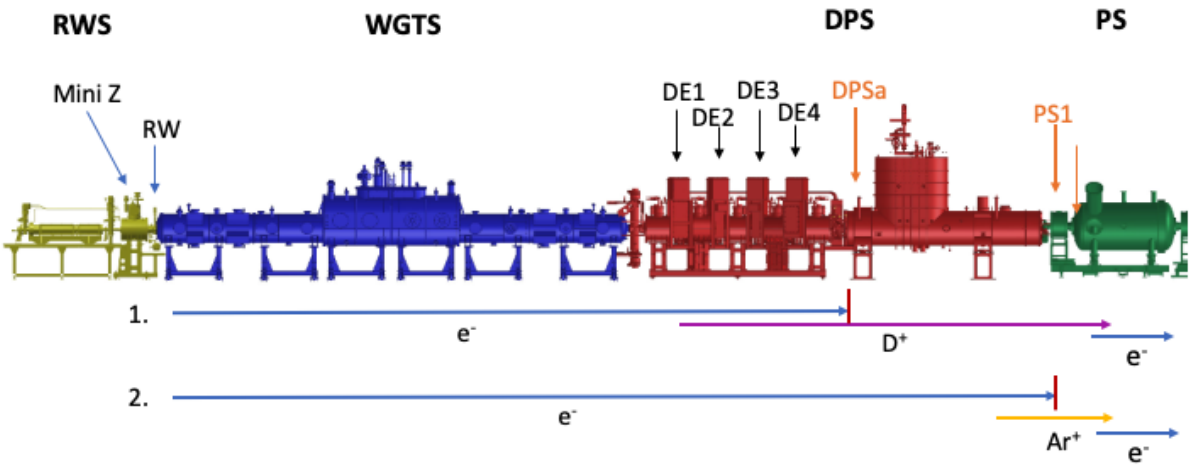

Figure 7.6: Sketch of the paths travelled by the relevant particles in both configurations of the PS pressure-dependence measurements. 1) The deuterium ion configuration where photoelectrons are created at the RW and travel all the way to RE-DPSa where they are blocked by the negative potential. Dipole electrode 1 is set to positive potential and so deuterium Penning ions are created there. These ions travel to the PS where they ionize argon gas and finally some of the emitted electrons are detected by the FPD. 2) The Ar^+ ion configuration: photoelectrons travel all the way to the PS where they are stopped by the negative potential of the spectrometer. They ionize argon gas in the downstream part of the DPS. The Ar^+ ions enter the PS and ionize argon gas, creating electrons in the process. Some of the emitted electrons are detected by the FPD.

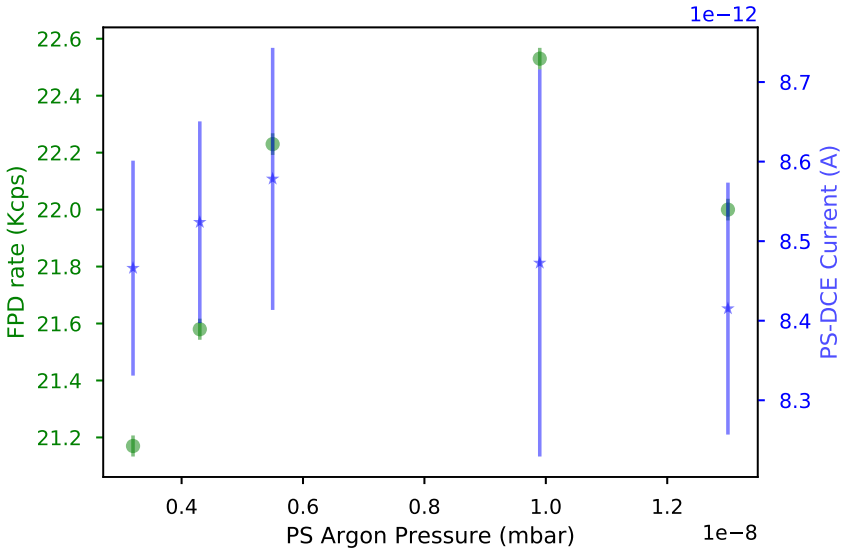

(a) Deuterium ions

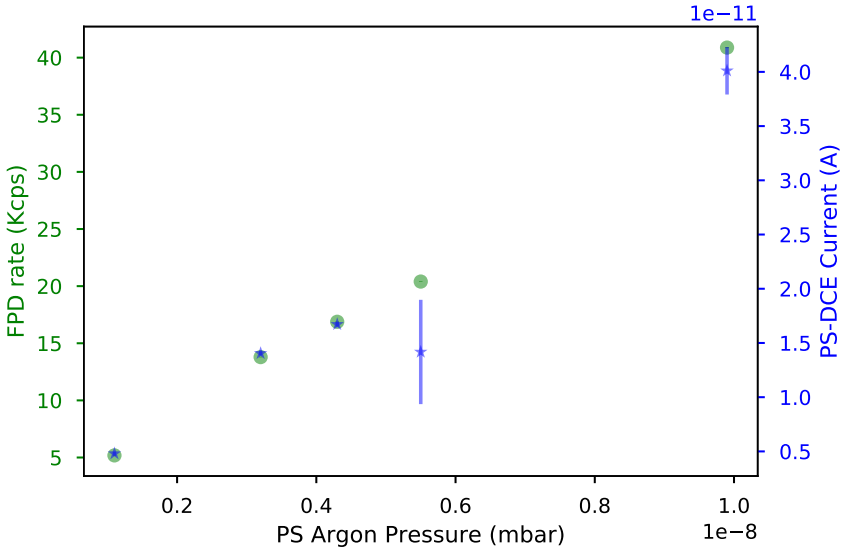

(b) Ar^+ ions

Figure 7.7: Rate measured in the FPD and current in PS downstream cone electrode PS-DCE for deuterium (a) and argon (b) configurations. The rate and the current are measuring (indirectly and directly) the ion flux into the SDS.

for deuterium ions ionizing the gas, which is the main ion creation method during ICE measurements. For this reason it is not recommended to use argon in future ICE measurements. Although the underlying mechanism of how ions create electrons inside the PS is still not well understood, ICE could be used to monitor the ion flux into the SDS as explained in 7.3.2.

7.4 Blocking ions with ring and dipole electrodes

Ring electrodes, located at strategic places in the flux tube as shown in Fig. 5.7, and dipole electrode 4, in the DPS, block the ion flux coming from the WGTS with their positive voltage settings as was explained in section 5.3.2. During the STS-IIIa campaign the blocking factor of RE-DPSa and PreSpectrometer magnet 1 (RE-PS1) was measured (Sec. 7.4.1). Also, during this campaign, it was qualitatively observed that all the dipoles could block ions if set at positive potentials. Finally the impact of changes of the column density on the blocking devices is discussed (Sec. 7.4.2).

7.4.1 Blocking factors of ring electrodes

The goal of this measurement was to measure how effectively the ring electrodes could block ions coming from the DPS. Deuterium Penning ions were used, and the ion flux was measured with the ICE method.

Method

For this purpose, the following procedure was carried out:

1. 40 eV deuterium Penning ions were created in DE1 and photoelectrons were blocked with DE4.
2. Argon gas was injected in the PS to increase the rate of the ICE measurement because this measurement was done before it was established that there was no need for argon gas (section 7.3.3).
3. All the blocking devices were set to zero.
4. Each ring electrode, in turn, was set to increasing positive potential until its maximum potential setting was reached.
5. At each set potential, a run was started to measure the FPD rate, and hence the ion flux via the ICE method.

The settings used are shown in table 7.7.

Blocking ring	DE1 (V/V)	DE4 (V/V)	RE-DPSa (V)	RE-PS1 (V)	PS (V)
RE-DPSa	+40/+40	-350/-350	$<$350	0	-500/-450/-400
RE-PS1	+40/+40	-350/-350	0	$<$ 300	-500/-450/-400

Table 7.7: Settings of the dipole electrodes for the ring electrode blocking factor measurement. The rest of the dipole electrodes were at zero volts. The PS set voltages correspond to the ICE settings.

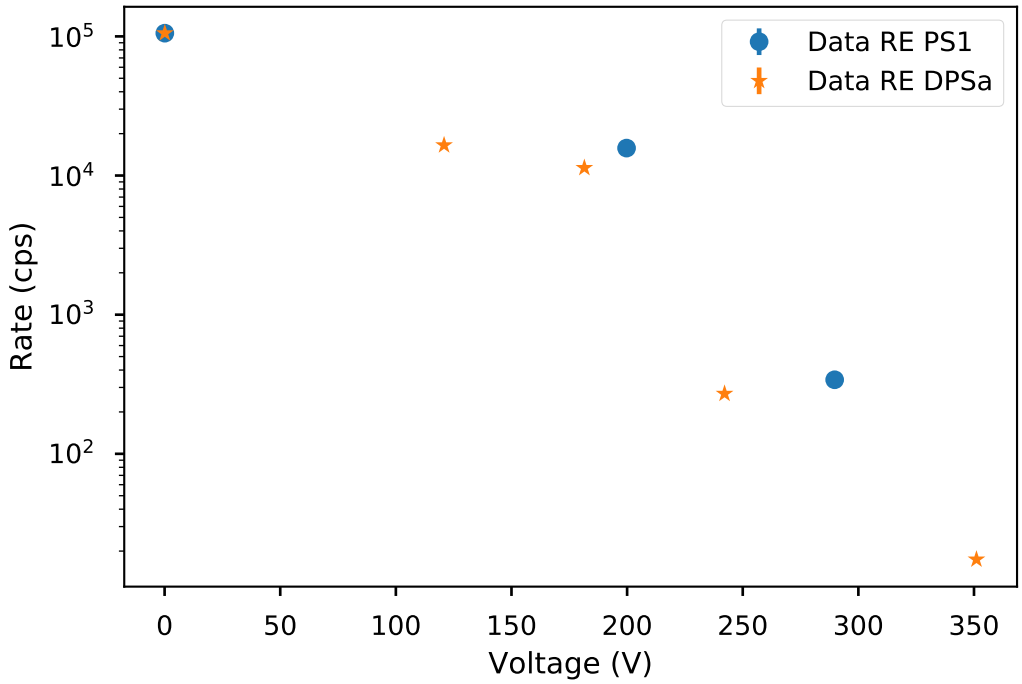

Figure 7.8: Rate measured in the FPD for different blocking voltages of the ring electrodes DPSa (orange stars) and PS1 (blue dots). The data shows that the best blocking factor is at the maximum voltage. The one σ errorbars are too small to be noticeable.

Ring electrode	Unblocked rate (kcps) $r_{\text{unblocked}}(U_0)$	Blocked rate (cps) $r_{\text{block}}(U_{\max})$	Blocking factor B
DPSa	105.45 ± 0.06	17.0 ± 0.2	0.9998 ± 0.0003
PS1	105.45 ± 0.06	340 ± 1	0.9967 ± 0.0001

Table 7.8: Blocking factors for ring electrodes RE-DPSa and RE-PS1 for 40 eV electrons, along with the unblocked and blocked FPD rates measured in ICE setting.

Results

Figure 7.8 shows the rate in the FPD for different blocking-potential settings. The rate ($r_{\text{unblocked}}(U_0)$) at 0 V is the total rate produced by the Penning ions with no blocking. Although most of the ions have energies around 40 eV, there is still a detectable rate above the set voltage of 40 V in the ring electrodes because the potential in the center of the ring electrodes is not the set voltage. It is the effective potential subject to the $1/r^2$ factor that was mentioned in section 5.3.2.

The blocking factor (B) is:

$$B \geq \frac{r_{\text{unblocked}}(U_0) - r_{\text{block}}(U_{\max})}{r_{\text{unblocked}}(U_0)}, \tag{7.15}$$

where $r_{\text{block}}(U_{\max})$ is the rate measured using the maximum potential setting of each ring electrode. The blocking factor calculated is a lower bound since the background, measured by determining the rate at the FPD with the valve between the STS and SDS closed, was not measured because the valves cannot be closed too often; they have a finite mechanical lifetime. But the background of this measurement is thought to have a very small impact.

The blocking factors for 40 eV ions coming from the DPS are shown in table 7.8, and are close to 1 in both cases. When both ring electrodes are set to positive voltages the first blocking device (RE-DPSa) does most of the blocking. The importance of this measurement was to quantitatively confirm that it is possible to stop ions before they reach the SDS, and to do so before using tritium ions with the danger of contaminating the spectrometers.

7.4.2 Impact of column density changes on blocking devices

The dependence of the blocking factors on the column density was first measured with deuterium ions as shown in this section. For safety reasons, a low tritium column density was used in the first measurement campaigns where tritium was injected in the WGTS. The amount of tritium was increased step by step. One of the key points necessary to increase the tritium injection was to know that the ion blocking would not deteriorate with

Mini Z	Column density (%)	DE4 (V)	PS electrodes (V)
On	$\leq$4	-350/-350	-500/-450/-400

Table 7.9: Settings for the measurement of the ion-blocking dependence on column density. The PS cone settings correspond to the ICE settings. The rest of the dipoles were set to zero volts.

the increase in column density.

Methodology

This measurement was carried out as follows:

1. Deuterium ions were created by ionizing deuterium gas injected in the WGTS with RW photoelectrons
2. At the start of the measurement the column density was $\approx 4\%$ of the nominal column density
3. The voltage of RE-DPSa was decreased from -35 V to 0 V, to perform a scan. At each voltage, a run was taken to record the FPD rate. Each run was around 1 minute long
4. The column density was gradually decreased for the rest of the measurement, until it reached $\approx 0\%$, by pumping out the deuterium gas
5. A RE-DPSa voltage scan with its corresponding FPD runs was performed every few minutes

The settings used in this measurement can be found in table 7.9.

Results

The rate measured by the FPD at each scan set point can be found in figure 7.9. The column density started at 4% of the nominal value and the rest of the scans were done at lower column densities. The exact value of the column density is not given because there was no good way to calculate the column density at these low values. But the gas was constantly pumped out in the WGTS and the DPS, and is therefore known to have decreased during the measurement. The black dotted line corresponds to the RE-DPSa optimal voltage setting (20 V) found in the VFT campaign [94].

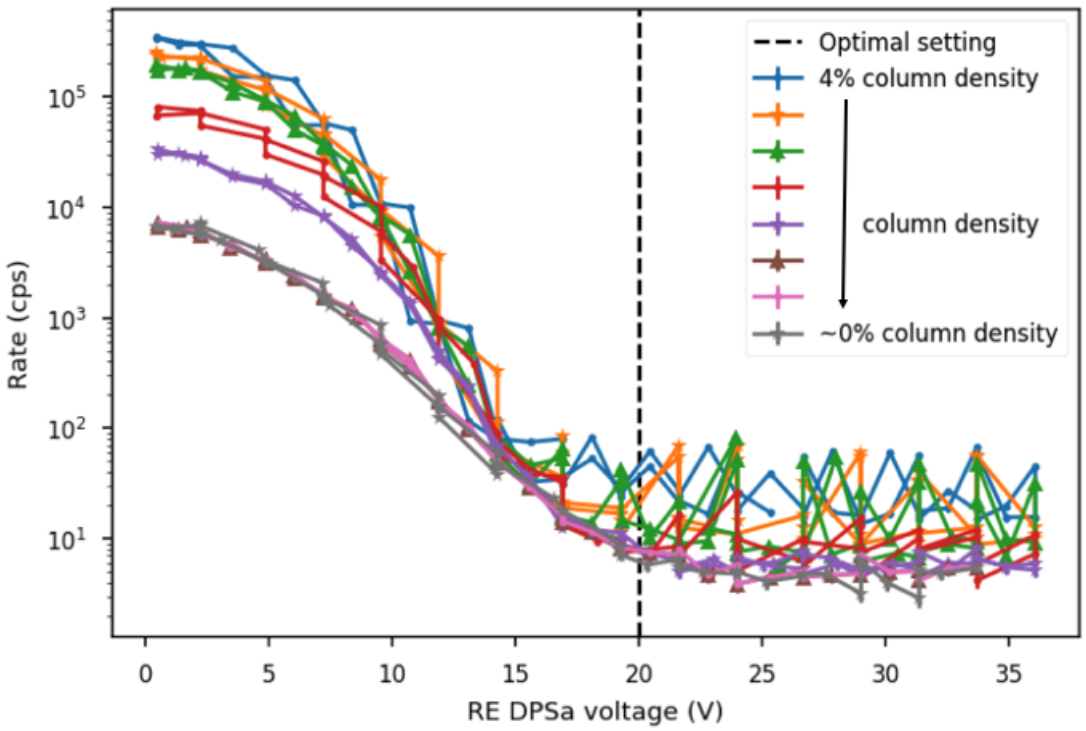

Figure 7.9: Rate measured in the FPD while doing voltage scans with the RE-DPSa, as the deuterium column density was gradually decreased from 4% to zero. The arrow in the labels means that the rest of the scans had a lower column density. The FPD rate measured at 0% column density is the electron background in the ICE setting.

It was found that the blocking of deuterium ions with RE-DPSa has no dependence on column density in this regime. The background-rate region is reached at 20 V in all scans. In subsequent campaigns the optimal set voltage of RE-DPSa was increased a few volts, as will be explained in the tritium campaign chapter (Sec. 8.4). The increment of the set voltage is not a problem from the perspective of this measurement since all the ions are already blocked at around 20 V, although it is important to take into account the creation of Penning ions when increasing the voltage settings. The penning ion creation rate was investigated and the results will be shown in the next section. This measurement was not carried out with RE-PS1 since it does not have a large penning ion creation rate and so it can be set to higher voltages.

In conclusion, a lower limit of the possible set voltage of RE-DPSa, for neutrino mass campaigns, was found to be 20 V.

CHAPTER 8
ION INSIGHTS FROM TRITIUM NEUTRINO-MASS CAMPAIGNS

In this chapter I will present the results from the ion measurements carried out during the tritium campaigns KATRIN Neutrino Mass measurement 1 (KNM1) and KATRIN Neutrino Mass measurement 2 (KNM2). A brief description and a time-line of each campaign is provided (Sec. 8.1).

As a safety measure, the tritium column density was first ramped up via a series of steps, and ion safety procedures were carried out at each step (Sec. 8.2). The ion energy spectrum of two ring electrodes was investigated (Sec 8.3) and the optimum voltage of the blocking devices was calculated (Sec. 8.4) taking into account the neutralization measurements (Sec. 8.5). Measurements were carried out to calculate the tritium density inside the dipoles (Sec. 8.6). And the ion flux into the Spectrometers and Detector Section (SDS) was monitored (Sec. 8.7).

The results shown in this chapter are a collaborative work among the KATRIN Ion Lion Team: Fabian Friedel, Ferenc Glück, Magnus Schlösser, Manuel Klein and myself. In this chapter, it will be mentioned when there is an explicit contribution from one of my collaborators.

8.1 KATRIN neutrino mass campaigns

The data analysed in this section was mostly collected during two neutrino mass campaigns: KNM1 measurement campaign which took place from March to May 2019; and KNM2 measurement campaign which took place from September to November 2019.

The goal of the KNM1 campaign was to obtain KATRIN's first result for the effective $\overline{\nu}_e$ mass (m_ν), with unprecedented sensitivity. During this campaign the column density was supposed to be set at 100% ($\rho d = 5 \times 10^{17}$ molecules/cm^2). Nevertheless it was set to 22% of its nominal value, $\rho d = 1.1 \times 10^{17}$ molecules/cm^2, as will be explained in the next section.

After tritium injection, but before the β-spectrum scan measurements, ion and plasma measurements took place. This presented the first opportunity to measure some systematics with a considerable tritium column density in the experiment. Also, the effect of the ion

blocking and removal mechanisms was monitored during the 5 weeks when β-spectrum data was taken. The ion results will be discussed with more detail in the following sections.

All the β-spectrum data taken during this campaign is equivalent to nine days' worth of data taken at KArlsruhe TRItium Neutrino experiment (KATRIN) nominal conditions [47]. A fit to the integrated β-spectrum gave $m_\nu^2 = -1.0^{+0.9}_{-1.1}$ eV^2. And using the Lokhov and Tkachov confidence interval method [93], this translated to an upper limit of $m_\nu < 1.1$ eV/c^2 at 90% CL [109]. The error was dominated by statistics.

The KNM2 campaign took place after the 2019 summer maintenance break. Its main goal was to accumulate more β-spectrum data to increase the statistics. This time, a column density of $\rho d = 4.2 \times 10^{17}$ molecules/cm^2 was achieved, which corresponded to 84% of the nominal value.

Ion and plasma measurements were also carried out at the beginning of this campaign. Special measurements were done during the column-density ramp up to ensure that the ion blocking and removal mechanisms worked correctly.

In this campaign, the best fit to the squared neutrino mass obtained was $m_\nu^2 = 0.26^{+0.34}_{-0.34}$ eV^2. The upper limit was found to be $m_\nu < 0.9$ eV/c^2 at 90% CL [77], again using the Lokhov-Tkachov method for the confidence interval [93].

By combining the data of both campaigns (KNM1 and KNM2), an upper limit of $m_\nu < 0.8$ eV/c^2 at 90% CL was found [77].

8.2 Column density ramp-up

The KNM1 and KNM2 campaigns presented the first opportunity to run the experiment with high column densities of tritium. Since new settings were tried out, protocols were designed to ensure the safety of the experiment. As explained in Sec. 5.1, there is a limit on the ion flux that can reach the SDS in order to comply with the Focal Plane Detector (FPD) background experimental limit. The bigger the column density, the more ions that can reach the SDS and contaminate the experiment, if our countermeasures don't work correctly.

One of the safety procedures consisted of gradually ramping up the column density, instead of setting it directly to its nominal set value. At each step, measurements were carried out to verify the blocking or reflection (Sec. 8.2.2 and Sec 8.2.3), and removal (Sec. 8.2.1) of the ions.

The timelines of the column density ramp-ups during KNM1 and KNM2 campaigns can be seen in table 8.1. Each column density step for KNM1 was set for a few days, and was reached with 20-min sub-steps (not shown in the table). A drift in the column density

Campaign name	Column density (ρd) (%)	(molecules/cm^2)	Date set (month day)	Comments
	5	0.3×10^{17}	March 4	-
	15	0.7×10^{17}	March 7	-
	50	2.4×10^{17}	March 10	ρd drift
KNM1	85	4.1×10^{17}	March 13	More pronounced ρd drift
	-	-	March 14	Experimental shut down
	5	0.3×10^{17}	March 26	-
	22	1.1×10^{17}	March 28	-
	27	1.2×10^{17}	Sept 18	Spikes in FPD rate
	34	1.8×10^{17}	Sept 18	Spikes in FPD rate
KNM2	55	2.7×10^{17}	Sept 18	Spikes in FPD rate
	69	3.5×10^{17}	Sept 18	-
	90	4.4×10^{17}	Sept 18	-

Table 8.1: Column density timeline during KNM1 and KNM2. Not depicted are the sub-steps taken for each large ρd step in KNM1. Each sub-step took around 20 min. The KNM2 steps took around 15 min each.

was observed above 50% nominal ρd [110]. The drift was provoked by a reduction of the inlet capillary diameter due to the adsorption of radiochemical reaction products of the tritium gas with the inner metal walls of the loop system [110]. The experiment was shut down briefly and the measurements restarted with a lower, more stable column density. This issue was a burn-in problem on the first exposure of the surfaces to significant tritium, and did not recur in KNM2.

In the case of KNM2 the whole ramp-up was done in one day. Spikes were observed in the Ion Conversion to Electron (ICE) monitoring data because the Pre-Spectrometer (PS) was not appropriately conditioned, as explained in Sec. 5.4.4.

8.2.1 Ion flux into the DPS

As explained in Sec. 5.4.1 it is possible to monitor the ion flux ($\Phi_{\rm ion}^{\rm DPS}$) entering the Differential Pumping Section (DPS) by reading the currents of the dipoles. These currents are created by the ions that hit the dipole lobes after being removed from the flux tube.

The goal of this measurement was to observe a linear increase on the dipole currents during the column-density ramp-up. Although the ion creation rate in the Windowless Gaseous Tritium Source (WGTS) depends quadratically on the column density (Sec. 5.2.1), a linear dependence was expected for the dipole currents. This is because with larger column densities, the T_3^+ ions would be transformed to T_5^+ ions by molecular recombination

processes as explained in Sec. 5.2.1. At 100% column density around 80% of the ions would be recombined and thus neutralized and wouldn't leave the WGTS [97]; at lower column densities, the recombination rate would be smaller and more ions would be able to leave the WGTS.

Measurement method during KNM1 and KNM2

The following measurement procedure was used during the KNM1 column-density ramp-up:

1. The dipoles Dipole Electrode 1 (DE1), Dipole Electrode 2 (DE2), and Dipole Electrode 3 (DE3) were set to nominal settings: -15V/-5V, -35V/-5V, -85V/-5V respectively
2. The column density was ramped up, and left at each sub-step around 20 min
3. The dipole current was monitored and at least two minutes' worth of stable data were taken at each sub-step, where no drift was observed in the currents
4. The column density was monitored for three days and then it was ramped up to the next step. The steps are shown in table 8.1

A different procedure was used during KNM2 ramp up. DE1 was the only dipole used to remove ions from the flux tube, hence the only one to detect an ion current. Then, the ions were reflected upstream with DE2. This setting was chosen because all ions removed with DE1 end up contributing to the current, unlike the rest of the dipoles where some of the removed ions don't end up hitting the lobes (Sec. 5.3.4).

The following procedure was used during KNM2 column-density ramp-up:

1. The dipoles DE1 and DE2 were set to -15V/-5V and +12V/+10V, to remove ions and to reflect them towards DE1 respectively
2. Valve 2 (V2)[1] was closed for five minutes to measure the background in the SDS
3. The column density was ramped up, and left at each step around 15 min. The steps are shown in table 8.1
4. The DE1 current was monitored. The currents of DE1 and of the Rear Wall (RW) were averaged over two minutes interval of stable current, at each step
5. V2 was closed a second time for five minutes to monitor the background

[1] V2 is located downstream of the dipoles, after the Cryogenic Pumping Section (CPS) and upstream of the PS.

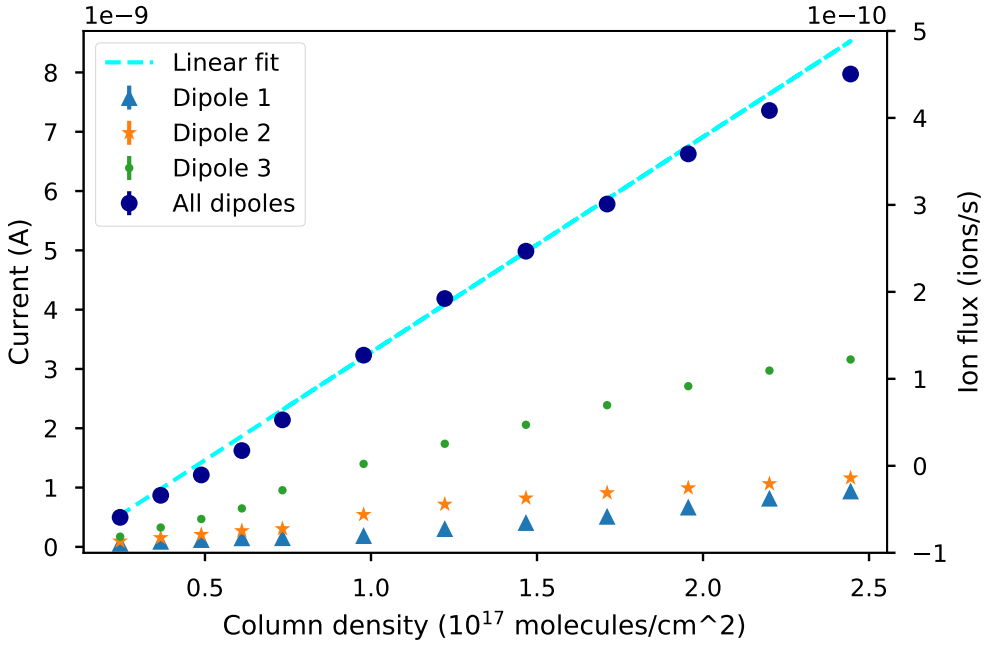

Figure 8.1: Currents during KNM1 column-density ramp-up: DE1 (blue triangles), DE2 (orange stars), DE3 (green dots), and the sum of all the dipole currents weighted by their detection efficiencies (blue circles). The corresponding ion flux is shown in the right y-axis. The errors are too small to be seen. A linear fit (cyan dashed line) was done to the current of all dipoles. The parameters can be seen in table 8.2.

Results

We observed, as expected, a linear increase in the current of the dipoles during the column density ramp-up of KNM1 and KNM2. This is shown in figures 8.1 and 8.2 respectively. The parameters of the linear fits are given in table 8.2.

In Fig. 8.1, the points shown as "all dipoles" are not just the sums of the three dipole currents. Instead we took into account the detection efficiency of each dipole (Sec. 5.4.1). The ion flux in the right y-axis was calculated using equation 5.14 for the "all dipoles" case. For the rest of the dipole currents, the flux was calculated by dividing the current by the electron charge (1.602×10^{-19} C).

Ramp-up	m (A cm^2/molecule)	b (A)
KNM1	$(3.63 \pm 0.08) \times 10^{-9}$	$(-3.5 \pm 1.2) \times 10^{-10}$
KNM2	$(2.683 \pm 0.001) \times 10^{-9}$	$(-1.10 \pm 0.04) \times 10^{-10}$

Table 8.2: Linear fit parameters to the dipole currents during KNM1 and KNM2 column density ramp ups.

During the KNM2 ramp up, the RW current was measured as well. Its magnitude is plotted in Fig. 8.2. This current measures mostly electrons, and the sign of the current is opposite from the dipole current; it is worth noting that the RW current shown in Fig. 8.2 is multiplied by -1. The charge flux, for either ions or electrons, is shown in the right y-axis.

The following results were obtained:

- A linear increase of the dipole currents was observed in each column density ramp up.
- The linear fit parameters found are not the same for the two measurement periods (table 8.2). This is likely due to the different measurement settings of the dipoles. During KNM2 all ions were removed with DE1 and they were reflected with DE2. Most of the ions need to go through DE1 more than once to be drifted enough to reach the lobes (Sec. 5.3.4). So, in this setting, the ions interact more with the WGTS gas where they can be neutralized or recombined. Meanwhile, during KNM1, all dipoles were at nominal settings and the ions were removed more quickly, resulting in a higher slope.
- During the KNM1 column-density ramp-up, most of the ions were removed with DE3 because it was the dipole with the highest negative potential, which meant that it was the dipole that drifted the ions the most. This was predicted in section 5.4.1.
- During the KNM2 ramp-up, a decrease in the DE1 current was observed when V2 was closed. This happened because the β-electrons were removed by hitting the valve when it was closed. Meanwhile, when V2 was open, the majority of the β-electrons were reflected in the spectrometer section by their retarding potentials. These reflected electrons ionized gas, making more ions in the process.
- The RW current was larger in magnitude than the dipole current because more charged particles reached it, since it is located at the upstream exit of the WGTS.

8.2.2 Monitoring with the PS downstream-cone current

During the KNM1 column-density ramp-up, the ion flux into the SDS was monitored with the Pre Spectrometer Downstream-Cone Electrode (PS-DCE) current. A calibration was done (Sec. 5.4.2) to get an efficiency factor ($\varepsilon_{\mathrm{DCE}}^{\nu\text{-mass}}$) that relates the current to the incoming ion flux ($\Phi_{\mathrm{ion}}^{\mathrm{SDS}}$) into the SDS.

The goal was to confirm that the ion flux in the SDS was below the limit after ramping up the column density.

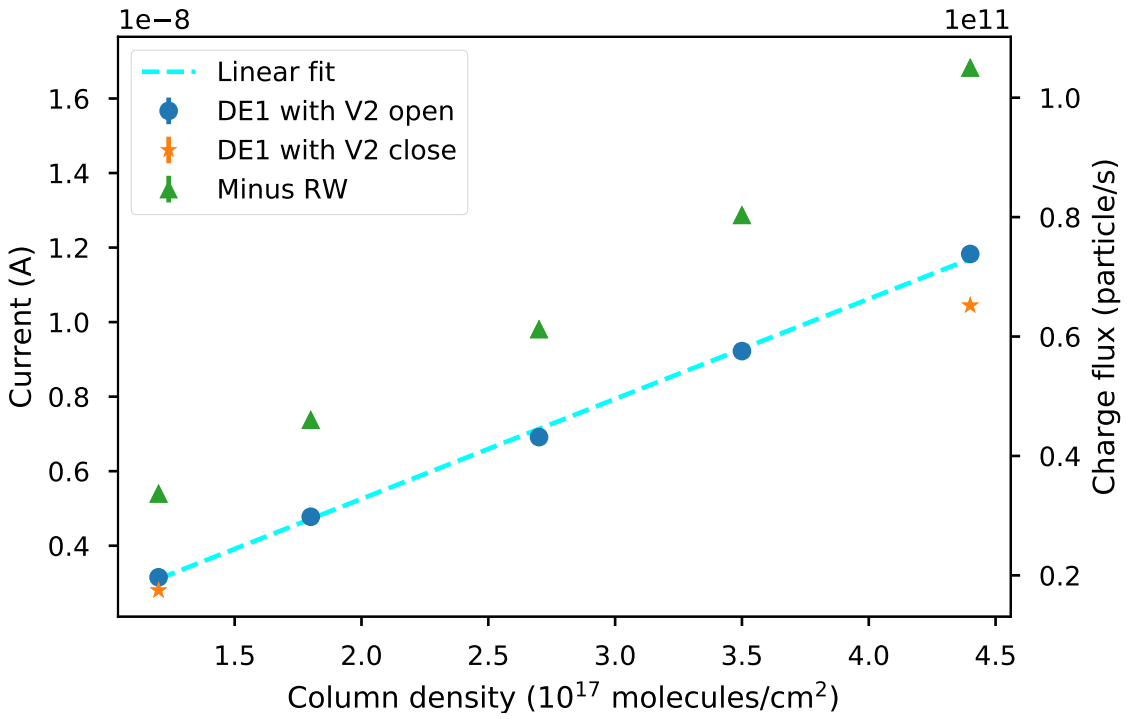

Figure 8.2: Currents during KNM2 column-density ramp-up: the RW (green triangles), DE1 with V2 open (blue dots), and with V2 closed (orange stars). The corresponding charge flux is shown in the right y-axis. The errors are too small to be seen. A linear fit (cyan dashed line) was done to the DE1 current. The parameters can be seen in table 8.2.

It was not possible to monitor the KNM2 column-density ramp-up with the PS-DCE current because the PS was set to ICE mode. This changed the adiabatic path of the ions and so the PS-DCE current calibration did not apply. Instead, the ion flux was monitored with the ICE method as will be explained in Sec. 8.2.3.

Measurement method

The measurement was carried out during the KNM1 column-density ramp-up as follows:

1. The PS was set to neutrino mass settings (Sec. 7.3.1).
2. The PS-DCE current ($I^{\mathrm{DCE}}_{\rho d_i}$) was measured and averaged over a one-hour interval to reach minimal systematic uncertainty [94]. The spikes in the current were studied and removed from the data.
3. The column density was ramped up to the next step, via sub-steps.
4. The PS-DCE current ($I^{\mathrm{DCE}}_{\rho d_f}$) was measured and averaged over an hour interval. The spikes were also removed.
5. The ion flux into the SDS was calculated with the difference between the currents at the two set points and the efficiency factor (Eq. 8.1).

Results

As an example, we show the data gathered from the column density ramp up from 15% to 50%. Figure 8.3 shows the PS-DCE current during the ramp up, as well as the throughput value which is related to the column density. The ramp up consisted of seven steps. The measured currents can be found in table 8.3.

The total ion flux into the SDS was calculated using the efficiency factor (Eq. 9.1):

$$\Phi^{\mathrm{SDS}}_{\mathrm{ion}} = \frac{I^{\mathrm{DCE}}_{50} - I^{\mathrm{DCE}}_{15}}{\varepsilon^{\nu\text{-mass}}_{\mathrm{DCE}}} = (9.5 \pm 82.2) \times 10^4 \ \ \mathrm{ion/s}. \tag{8.1}$$

The ion flux, and especially the error, are greater than the safety limit. But is worth noting that the systematic error of the PS-DCE currents is extremely large. In fact, the change in current is consistent with zero, as seen in Fig. 8.3. So, it was concluded that the systematic error on the current is too large for us to use the calculated efficiency factor reliably. That is why a new monitoring method was used during KNM2 column-density ramp-up, as will be shown.

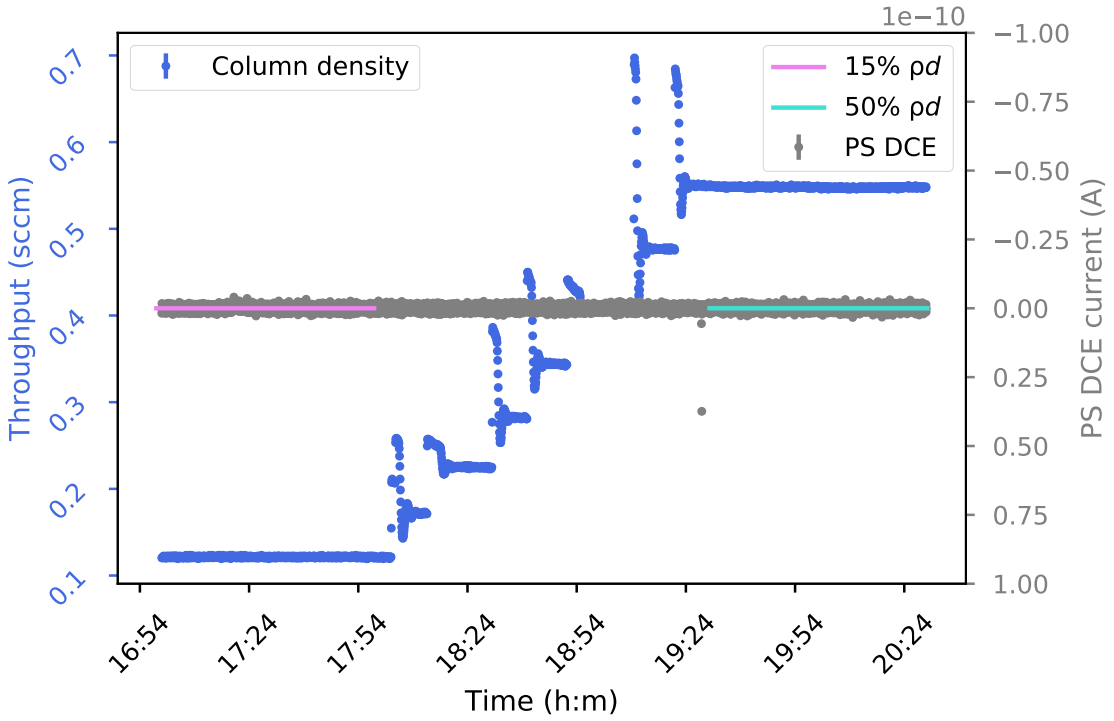

Figure 8.3: Current measured at the PS-DCE (gray points) during KNM1 column density ramp up from 15% to 50%. The pink and green lines represent the time periods over which the current was averaged to get the data in table 8.3. The spikes in the current were removed from the analysis. The y-scale of the PS current was chosen so that the spikes are shown. The throughput data shows of how the column density was ramped up in 7 steps.

Column density (%) ρd	DCE current (A) $I_{\rho d}^{\mathrm{DCE}}$	Error (A) σ_I
15	1.0×10^{-14}	8.2×10^{-14}
50	2.7×10^{-14}	8.3×10^{-14}

Table 8.3: Measured current with PS-DCE during KNM1 column density ramp up from 15% to 50% and its corresponding error.

8.2.3 Monitoring with ICE method

During the KNM2 column-density ramp-up the experiment was set for ICE. Hence, it was possible to monitor the ion blocking via the FPD rate. It was not possible to monitor ion blocking with the ICE method during the KNM1 column density ramp-up as the spectrometer section was kept in nominal neutrino mass settings.

The goal was to confirm that the ion flux into the SDS was below the limit at each column density step. We calibrated ICE (Sec. 7.3.2) to get an efficiency factor ($\varepsilon_{\mathrm{ICE}}$) that relates the FPD rate in ICE mode to the ion flux into the SDS. This factor was also used to get the maximum allowed FPD rate. This method is more sensitive than the PS-DCE current method and it can be done in real time.

Measurement method

The ion flux monitoring during the KNM2 ramp-up was done as follows:

1. The PS was set to ICE settings (Sec. 7.3.2)
2. A run was taken to record the FPD data
3. The column density was ramped up step by step, and at each step, a run was taken to record FPD data

Results

Fig. 8.4a shows the mean rate at each ρd step, averaged over a span of around 5 minutes (blue points). Also shown is the ICE rate limit that corresponds to the experimental ion flux limit of 10^4 ions/s into the spectrometer. At first glance, the FPD rate didn't seem to depend on column density. So the FPD rate was investigated. Fig. 8.4b shows that the rate has distinct spikes, which are not usually seen in the rate. The spikes gradually died down over time.

During KNM2, the special spectrometer ICE setting was reached without the proper conditioning of the PS so, as explained in 5.4.4, Penning discharges can occur. The spikes most probably originate from Penning discharges from the PreSpectrometer magnet 1 (PS1). If the spikes in the FPD rate are not removed, we don't observe an increase in rate with an increase in column density. But if we remove the spikes, by making a cut at 50 cps in the FPD rate, we observe the expected increase in FPD rate.

Nevertheless, by monitoring with the ICE method, the ion flux into the spectrometer section was found to be below the experimentally allowed limit during the ramp-up of column density in the KNM2 campaign.

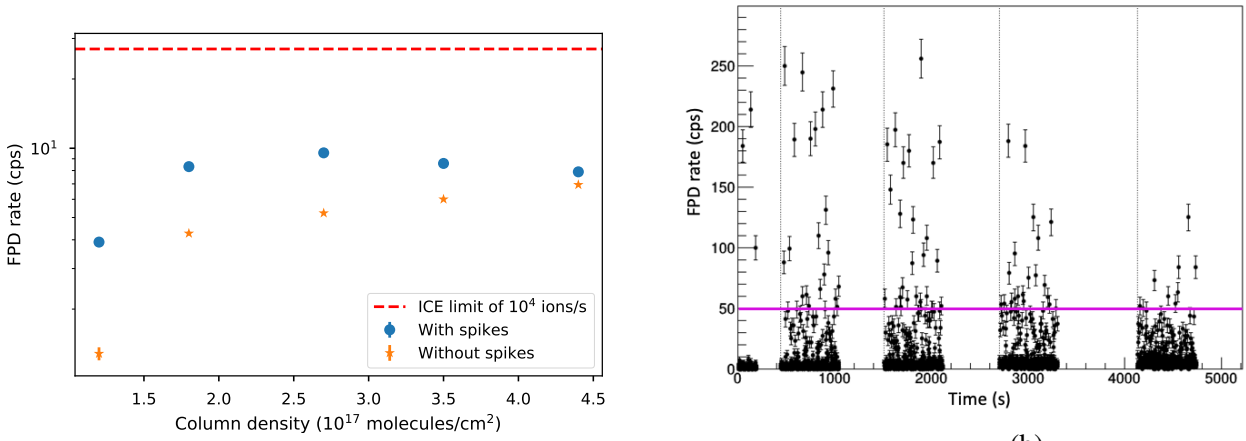

(a) (b)

Figure 8.4: ICE rate during KNM2 column density ramp-up. Plot (a) shows the mean rate, averaged over the entire run, with spikes (blue dots) and without spikes (orange stars). The error bars are too small to be seen. The ion flux limit into the SDS is depicted with a red line. The PS was not correctly acclimated to the ICE settings and spikes are seen in the rate (b). It can be observed how the spikes die down as the spectrometer gets acclimated to its new settings. The dotted black lines correspond to the start of a new run, or the stabilization of the column density step. The pink line represents the cut at 50 cps to get the data "without spikes".

8.2.4 Conclusions

During the KNM1 and KNM2 column density ramp-ups, the DPS ion flux was monitored with the dipole electrodes, and a linear dependence was found, as expected. The dipoles were found to effectively remove ions from the flux tube.

The ion flux into the SDS was monitored with the PS-DCE method and the ICE method in KNM1 and KNM2 respectively. During KNM1 ramp-up it was found that the systematic error on the PS-DCE current was too large to be used reliably to get the ion flux, nevertheless the change in current was consistent with zero. As a consequence, during KNM2 rapm-up we monitored with ICE. It was found that the ion flux into the SDS flux was always below the experimental limit of 1×10^4 ion/s. Hence, the blocking devices were found to work correctly at these column densities.

And so it was deemed safe to continue with the neutrino mass measurements at the newly attained column densities.

8.3 Ion energy spectrum

There are different ion creation mechanisms in KATRIN. Some of them depend on the tritium injection into the WGTS. During neutrino mass measurements, most of the ions were created in the source section. There, they scattered with tritium gas until they were thermalized (Sec. 5.2). The ions created near the WGTS downstream exit were the only ones that could leave that section without losing too much energy. In this thesis we call these ions the WGTS ions. Other type of ions, the Penning ions, are the ones created when gas is ionized in a Penning trap (Sec. 5.2.4); this mechanism depends on the electrode voltage.

The objective of this measurement was to study the ion energy spectrum, using the blocking ring electrodes Ring Electrode DPS a (RE-DPSa) and PreSpectrometer magnet 1 (RE-PS1) (location shown in figure 5.7). We divided the spectrum into two sections: one dominated by WGTS ions and the other dominated by Penning ions.

8.3.1 Measurement method

The following procedure was used to measure the ion energy spectrum.

1. Set the experiment to ICE mode to monitor the ion flux into the SDS
2. Change the voltage of all the ion blocking devices, except for the ring electrode chosen to do the scan, to zero volts
3. Perform a voltage scan of the chosen ring electrode and take a run at each step to record the FPD rate
4. Repeat the measurement with the other ring electrode
5. Repeat the measurement at different column densities

When doing the scans, an ion flux greater than the background limit was allowed into the SDS. This was deemed safe, for this measurement, because of two main reasons: the rate was monitored at all times with ICE; and the limit of 1×10^4 ions/s corresponds to a limit throughout all the neutrino mass measurements, so if the limit is not met for just a brief period of time, the background is not increased.

8.3.2 Results

Two ion-energy spectra were obtained for a 90% column density. The voltage scans were done with RE-DPSa (Fig. 8.5a) and with RE-PS1 (Fig. 8.5b).

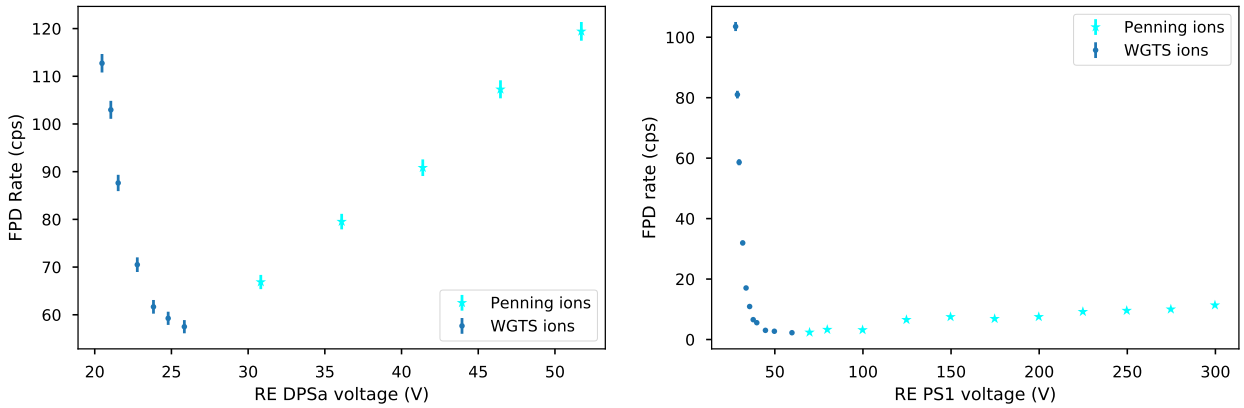

(a) (b)

Figure 8.5: Ion energy-spectrum from voltage scans with (a) RE-DPSa, and (b) RE-PS1. The WGTS ions (dark blue dots) were blocked as the voltage was increased while the Penning ion (light blue stars) creation increased.

The potential at the center of each ring electrode is lower than the set voltage (U_{RE}) (Sec. 5.3.2). To overcome the potential, the ion must have at all times a kinetic energy above the local potential. But, since the ion momentum was not collimated like in a MAC-E filter, the only energy that contributed to overcome the potential was the initial kinetic energy from motion parallel to the electric field. So, we could infer the minimum energy of the ions that made it through the ring electrode, for a chosen voltage:

$$KE_{\mathrm{ion}}^{\mathrm{min}}(U_{\mathrm{RE}}) = \Delta U_{\mathrm{RE}} \cdot \varepsilon_{\mathrm{center}}, \tag{8.2}$$

where $\varepsilon_{\mathrm{center}}$ is the efficiency at the center of the ring electrode from [102], and ΔU_{RE} is the change in the potential from the ion's creation location (assumed to be zero) to the ring electrode. This energy corresponded to ions travelling in the middle of the flux tube with momentum parallel to the axis.

This method was not sensitive enough to get the maximum energy of the WGTS ions, but we got the maximum detected ion energy from the minimum WGTS ion rate. However, the minimum WGTS ion rate was hidden by the Penning ions in the case of the RE-DPSa spectrum, so we used the minimum rate from the spectrum. The maximum detected WGTS ion energy is shown in table 8.4. These high energy ions mostly gain their energy via molecular dissociation (Sec. 5.2.3).

Finally, the WGTS ion spectrum was measured with three different column densities, as shown in Fig. 8.6. The background was higher in the scan performed with the highest column density because it was measured during the KNM2 campaign while the other two

Ring electrode	Efficiency at center $\varepsilon_{\text{center}}$	Voltage at min. rate (V) $U(r_{\min})$	Max. ion KE (eV) $KE(U(r_{\min}))$
DPSa	0.84	26 ± 1	21.9 ± 0.8
PS1	0.46	60 ± 1	27.6 ± 0.5

Table 8.4: Ring electrode efficiency at its center [102], voltage at minimum rate from Fig. 8.5, and the maximum detected ion kinetic energy calculated using equation 8.2 with the voltage at the minimum rate.

spectra were measured during the KNM1 campaign.

The following insights were obtained from this analysis:

- The closer the blocking device is to the WGTS, the more Penning ions it will create. This follows from the fact that closer to the WGTS there is more residual gas in the beam line. So it is more probable that the trapped electrons will ionize residual gas.
- In the RE-DPSa ion spectrum, WGTS ions with energies up to 22 eV were detected. Penning ions dominate the ion spectrum soon after, so it was not possible to detect higher-energy WGTS ions.
- In the RE-PS1 ion spectrum, WGTS ions with energies up to 27.6 eV were detected. At this point the FPD rate was very close to the background. So even if more energetic ions were created, the low density makes it hard to detect via this method.
- All WGTS ions are blocked with RE-PS1 at 60 V, regardless of the column density, to within our sensitivity limit.

8.4 Optimal voltage settings of ion-blocking devices

The three main ion-blocking or ion-reflecting devices are: Dipole Electrode 4 (DE4), RE-DPSa, and RE-PS1. They are located downstream of the WGTS, in the stated order, as shown in Fig 5.7. The optimal voltage settings of the ion-blocking devices depend on the blocking efficiency, on the Penning ion creation rate, and on neutralization times, as explained in section 5.3.2.

The objective of this measurement was to find a voltage setting that maximized the ion blocking and minimized the Penning-ion creation rate for each ion blocking device.

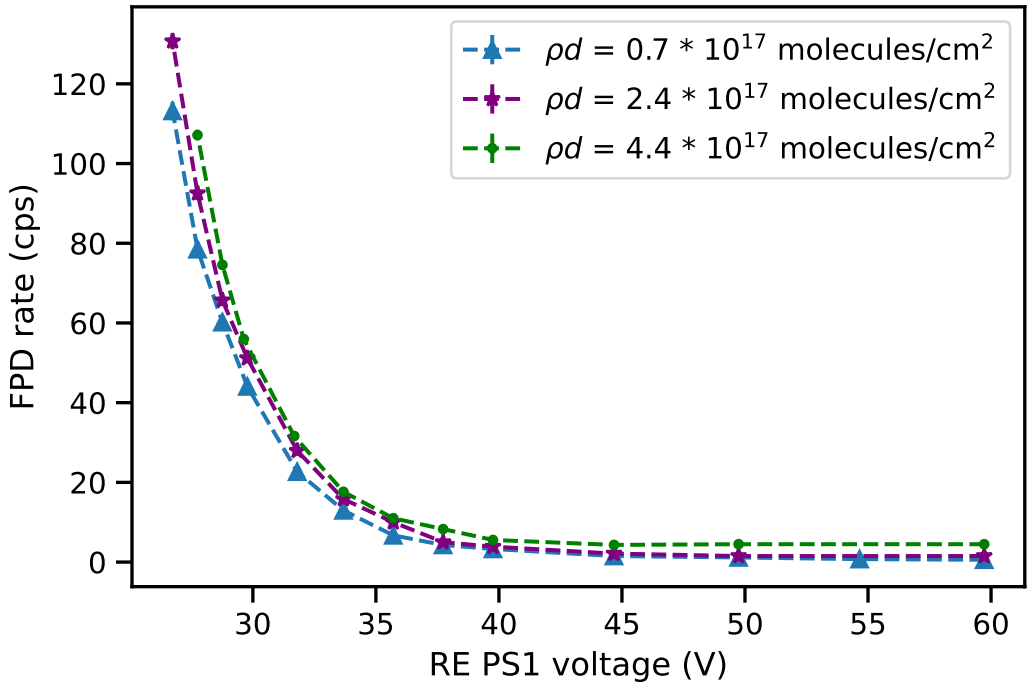

Figure 8.6: The WGTS-ion energy spectrum of RE-PS1. The scans were made with three different column densities. The scan performed with the highest column density was performed during the KNM2 campaign, the rest were performed during the KNM1 campaign. The one sigma errors are too small to be seen.

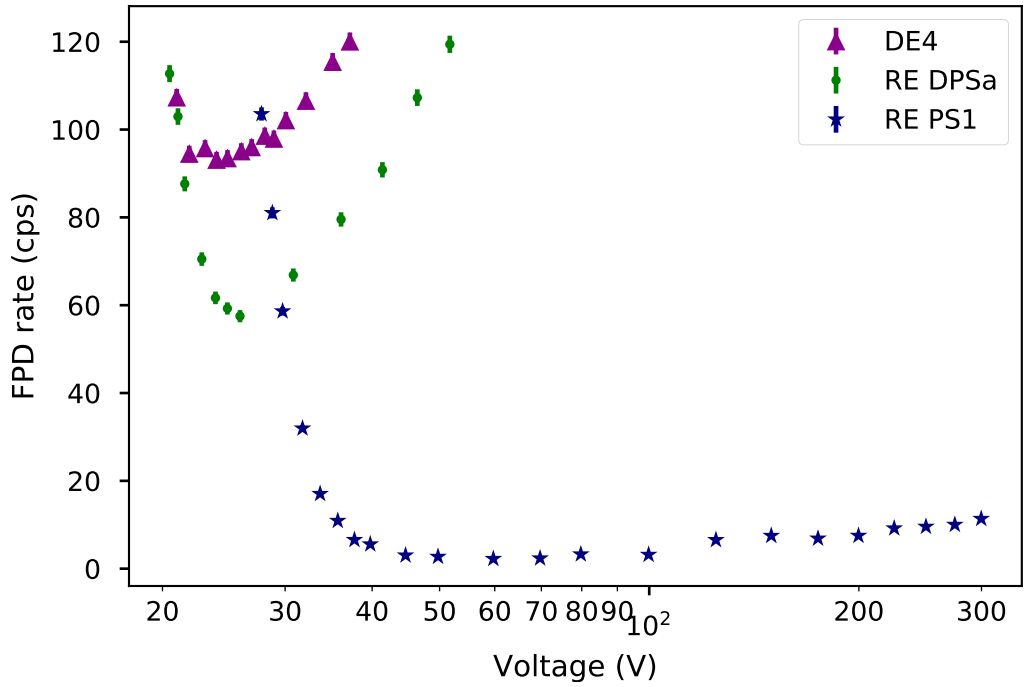

Figure 8.7: Voltage scan, at around 70% column density, of the blocking devices: dipole electrode 4 (violet triangles), ring electrode DPSa (green dots), and ring electrode PS1 (dark blue stars). The measurements were done to find the optimal voltage. The experiment was set to the ICE monitoring settings, so the rate is the ICE rate. The rate at low voltages corresponds to WGTS ions and the rate at higher voltages corresponds to Penning ions. The one sigma errors are too small to be seen.

8.4.1 Measurement method

The first optimization measurement was carried out at around 70% column density. The measurement method was the same as the one used to get the ion energy spectrum (Sec. 8.3.1), since it is from the ion energy spectrum that we find the minimum FPD rate:

1. Measure an ion energy spectrum with the chosen blocking device, following the procedure detailed in section 8.3.1. The rest of the blocking devices remain grounded throughout the scan.

2. Find the minimum FPD rate

3. Choose an optimal voltage. The method is complex and will be explained with more detail in the text

Device	Voltage at minimum rate	Optimal voltage
DE4 (V_{upp}/V_{down})	+25/+20	+25/+20
RE-DPSa (V)	+26	+40
RE-PS1 (V)	+55	+200

Table 8.5: Set voltages of the main blocking devices at the minimum FPD rate from Fig. 8.7, along with the chosen optimal voltages.

8.4.2 Results

The ion energy spectra for all three blocking devices can be seen in figure 8.7. The scans were performed at around 70% column density. While the voltage of the active blocking device was small, we observed WGTS ions. Then, as we raised the voltage, the WGTS ions were blocked and Penning ions were created.

A similar measurement was carried out at 90% column density giving very similar results. From these measurements we gained the following insights:

- The highest voltage is not necessarily the optimal blocking voltage due to Penning ion creation.
- The recommended optimal voltages are not necessarily the voltages of the minimum ICE rate for two reasons. First, WGTS ions should be blocked since they are tritium ions, while Penning ions aren't necessarily tritium ions. And it is good to have a high voltage in case of neutralization, as will be explained in the next section.
- It is recommended to set DE4 to its minimum ICE rate since the Penning ion rate is quite high, and RE-DPSa at a higher voltage than at its minimum ICE rate because of possible neutralization and to block more WGTS ions.
- RE-PS1 needs higher voltages to block the ions because its radius is larger, so the blocking potential at its center is smaller.
- The Penning ion creation rate in RE-PS1 was low. So, it could be set to a high voltage without creating more ions than the ion flux limit, which corresponds to an FPD rate of around 30 cps.
- RE-PS1 is ultimately the blocking device that maintains the rate below the flux limit, although DE4 and RE-DPSa also help to block low-energy WGTS ions.

The voltages at the minimum FPD rate and the recommended optimal blocking voltages are shown in table 8.5. As shown in Klein's thesis [94] the optimal setting of these blocking devices is not affected by setting the rest of the devices to its optimal setting.

8.5 Neutralization of the blocking electrodes

Neutralization of blocking potentials occurs when negative particles are trapped in the positive potentials created by the ring electrodes, neutralizing the effective blocking potential, as explained in section 5.3.3. The consequence of neutralization is that ions are no longer reflected. Instead, they travel through the beamline all the way to the SDS where they create background.

The goal of the neutralization measurements was to measure the time scale at which neutralization occurred in ring electrodes RE-DPSa and PS1 at different column densities. In this section we present the neutralization measurement method (Sec. 8.5.1), the main results (Sec. 8.5.2) and a proposal for how to minimize neutralization (Sec. 8.5.3).

8.5.1 Measurement method

Measurements of neutralization of a blocking potential were done by comparing the FPD rates, with the experiment in ICE mode, before and after the potential trap was neutralized. The measurements were carried out as follows:

1. Set the SDS in ICE monitoring mode
2. For a few minutes, set the blocking device, for which neutralization will be measured, to a negative potential so that electrons are repelled from it. This step is called "emptying the trap"
3. After some pre-specified time (neutralization time) in which all the dipoles are at their nominal settings, set the remaining blocking devices to zero volts
4. Perform a voltage scan of the WGTS ions with the chosen blocking device. This scan is called the "after neutralization" scan
5. Empty the trap of the chosen blocking device
6. Perform a second scan the "before neutralization" voltage scan with the chosen blocking device
7. Return the rest of the blocking devices to their nominal configuration
8. Fit the WGTS ion spectra and compare the parameters to find the neutralization or effective voltage shift, which depends on time and column density
9. If the neutralization was low, repeat with longer time periods and higher column densities

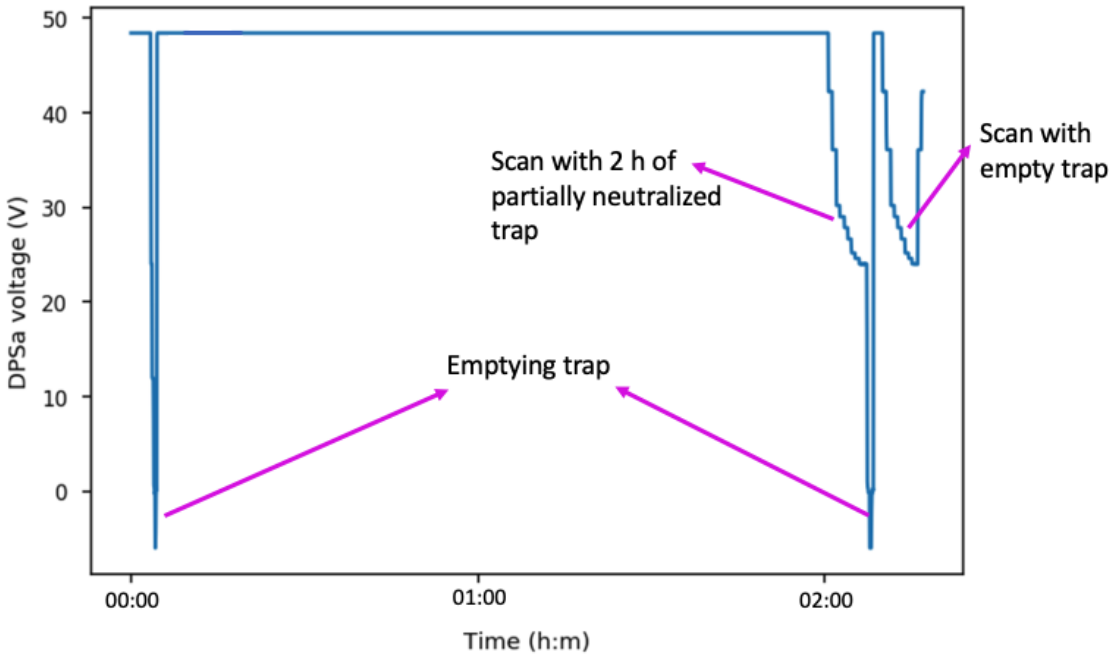

Figure 8.8: Voltage in ring electrode DPSa during a 2 hour neutralization measurement. The trap is emptied at the start of the measurement. After two hours a RE-DPSa voltage scan is performed, and after emptying the trap again, a second scan is performed.

As an example, a plot of the voltage of ring electrode DPSa during a neutralization measurement is shown in figure 8.8 for a time period of 2 hr.

The FPD rate ($R^{\mathrm{ICE}}_{\mathrm{FPD}}(u)$) collected at each voltage step (u) of the blocking-device scan, was fitted with the following function:

$$R^{\mathrm{ICE}}_{\mathrm{FPD}}(u) = a \cdot e^{-c\cdot(u-N)} + b, \tag{8.3}$$

where b is to account for the background and was fixed with data extracted from background runs; a and c are free parameters in the "before neutralization" scan and are fixed values in the "after neutralization" scan using the values from the "before" scan; and N, which tells us the shift in the x-axis, or the neutralization in volts, is left as a free parameter in both cases. The shift in the x-direction (voltage) will tell us how much neutralization per time we had. It is given by:

$$N_t = N_{\mathrm{after}} - N_{\mathrm{before}}, \tag{8.4}$$

where N_t is the net neutralization shift in voltage, N_{after} is the free parameter of the "after neutralization" scan and N_{before} of the "before neutralization" scan.

The quantity $u - N_t$ indicates the effective potential of the blocking device, in volts, that an ion interacts with.

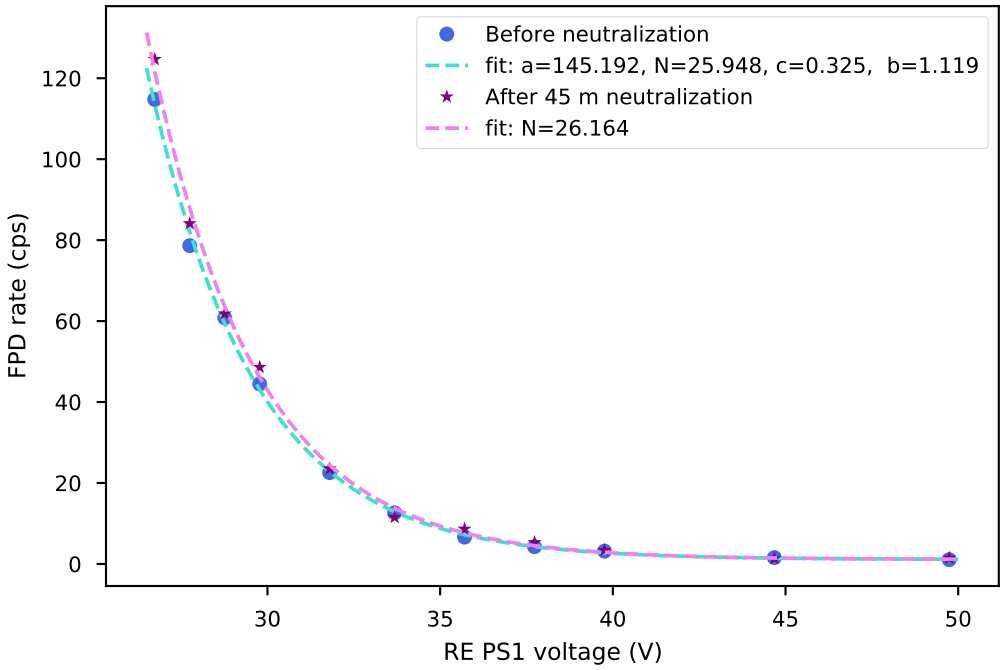

Figure 8.9: FPD rate of RE-PS1 voltage scan at 15% column density before neutralization (blue dots) and after neutralization (purple stars) with their corresponding fits to equation 8.3. The neutralization time period was 45 minutes. The errors on the fit parameters are not shown in the caption due to space, but they can be seen in table 8.6. The one sigma errors on the data points are too small to be seen.

As an example, Fig. 8.9 shows the data fitted by equation 8.3 of RE-PS1 neutralization measurement after approximately 45 minutes at a 15% column density. The results of the fit are shown in table 8.6. The total neutralization was obtained using equation 8.4 and the errors are summed in quadrature.

Since the neutralization dependence on column density was not known, we started the neutralization measurements with low column densities. We found small neutralization values so we gradually increased the column density and performed more neutralization measurements. The time period of the neutralization measurement was also increased gradually: we started with 10 min measurements and ended with measurements that lasted weeks.

Two other neutralization example plots are shown in Fig. 8.10. Both of them are with a 90% column density. Plot 8.10a is an example of RE-DPSa while plot 8.10b is another example of RE-PS1 neutralization. The ring electrode set voltages during the scan are different for each ring because they have different radii, so they require different voltage

Parameter	Value	Error
a (cps)	145.1915843	9.4×10^{-7}
c (V^{-1})	25.94797	0.00002
b (cps)	0.32	0.01
N_b (V)	1.12	0.83
N_a (V)	26.163	0.036
N_t (V)	0.215	0.036

Table 8.6: Fit parameters of the FPD rate of the RE-PS1 neutralization measurements at 15% column density. The parameters correspond to the fit of equation 8.3 to the data of Fig. 8.9.

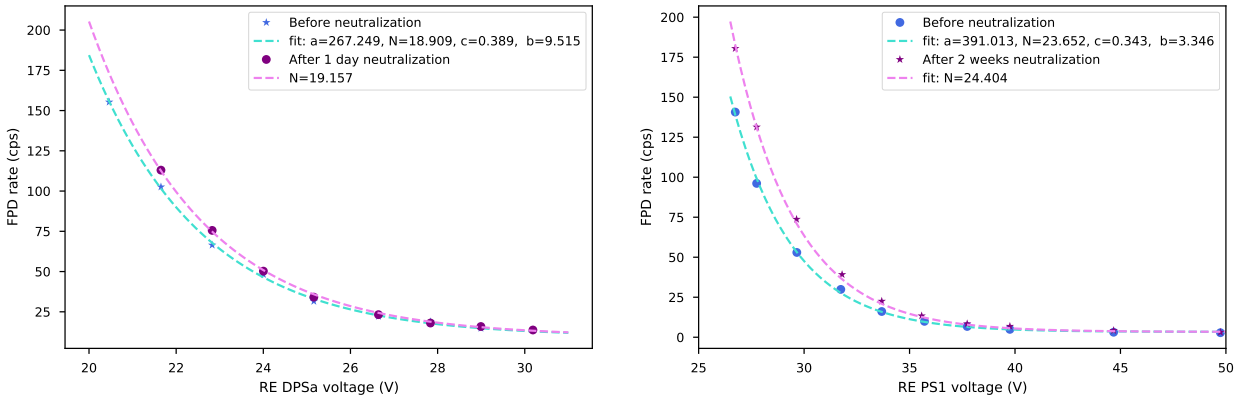

(a) (b)

Figure 8.10: Data and fits for the neutralization measurements of (a) RE-DPSa at 100% column density with a time period of one day, and (b) RE-PS1 at 100% column density with a time period of 2 weeks.

settings to block the ions.

8.5.2 Results

The results shown in table 8.7 were obtained with data taken during the KNM2 measurement campaign, following the aforementioned procedure. Table 8.7 shows the nominal voltage setting of each device, the minimum voltage, and the measured neutralization during the longest neutralization measurement time period at 84% column density. The minimum voltage of the blocking devices corresponds to the voltage setting at which the ring electrode blocks all ions coming from the WGTS section. This value was calculated in section 8.4.

After 14 days of trap-filling, RE-PS1 showed a neutralization of ~ 0.96 V and DPSa

Ring electrode	Nominal (V)	Minimum (V)	Neutralization (V)	Measurement time (days)
RE-DPSa	40	25	0.09 ± 0.24	8
RE-PS1	200	60	0.96 ± 0.28	14

Table 8.7: Neutralization results of RE-DPSa and RE-PS1 at nominal voltage and at 84% column density during the stated measurement time. Also shown are the minimum voltages needed to block all the WGTS ions.

~ 0.60 V. These shifts in voltage are very small compared with the nominal values of the ring electrodes. They present no danger of contamination of the SDS, since the final effective voltages (RE-PS1 = ~ 199V and RE-DPSa ~ 39 V) will be greater than the minimal voltages, to block all ions, of each device. Even thou neutralization is almost negligible, we still recommend to set RE-PS1 to 200 V (higher than the minimal FPD rate in ICE settings), to block all the WGTS ions. This is possible because the FPD background, in neutrino mass settings, does not increase by setting RE-PS1 to a high voltage.

8.5.3 Countermeasure

Based on the previous results, it is recommended that the ring electrodes RE-DPSa and RE-PS1 traps be emptied every two weeks. This is supported by the long neutralization time measured during KNM2.

8.6 Tritium density inside dipole electrodes

A small quantity of tritium gas propagates from the WGTS into the DPS. When tritium gas β-decays inside one of the dipole negative potentials, the created β-electron gains kinetic energy corresponding to the potential at its creation location. This introduces a distortion on the β-spectrum (Sec. 5.1). If the gas density inside the dipoles is small, the distortion is negligible.

The goal of this measurement was to calculate the tritium gas density inside the dipole electrodes, so that the induced error on m_ν^2 due to the β-decay could be calculated by the fitter teams.

In this section, we explain the measurement principle used to calculate the tritium gas density inside DE1 (Sec. 8.6.1) and we state the calculated gas density. Then the induced error on m_ν^2 is shown (8.6.2).

Setting	DE1 (V/V)	FPD rate (mcps)
Background	-2/-2	90 ± 14
DE1 gas	-350/-350	256 ± 7

Table 8.8: DE1 set voltages for the DE1 tritium gas density measurement. The mean rate at each setting was calculated with the values from Fig 8.11.

8.6.1 Measurement method

The measurement principle consisted of using the main spectrometer retarding potential to filter β-electrons coming from the dipoles, from those coming from the WGTS. This was done as follows:

1. The Main Spectrometer (MS) retarding potential was set to -18,577 V, a value beyond the tritium end point energy, to block all the β-electrons. DE1 was set to -2 V
2. A run was taken to record the FPD data at this "background" setting
3. DE1 was set to -350 V in monopole mode, its maximum allowed value. This allowed some of the β-electrons that were created in the potential to gain enough energy to overcome the MS retarding potential
4. A second run was taken to record the FPD rate at the "DE1 gas" setting
5. Steps 1-4 were repeated five times to get enough statistics

Fig 8.11 shows the FPD rate during a time span of two hours. The mean and standard deviation were calculated for each setting. The results are shown in table 8.8. The difference in rate is:

$$R_{\mathrm{FPD}} = R_{\mathrm{FPD}}^{\mathrm{DE1gas}} - R_{FPD}^{\mathrm{bg}} = 166 \pm 16 \text{ mcps}. \tag{8.5}$$

Using the measured rate, and dedicated simulations, Glück and Friedel calculated the tritium density inside DE1. The complete calculations can be found in [95]:

$$n_{\mathrm{TT}}^{\mathrm{DE1}} = 1.1 \times 10^{10} \text{ atoms/cm}^3. \tag{8.6}$$

This value is consistent with previous gas-flow simulations.

Due to the DPS pump-port location, in between the dipoles, the gas density in the next downstream dipole (DE2) was expected to be around one order of magnitude smaller than

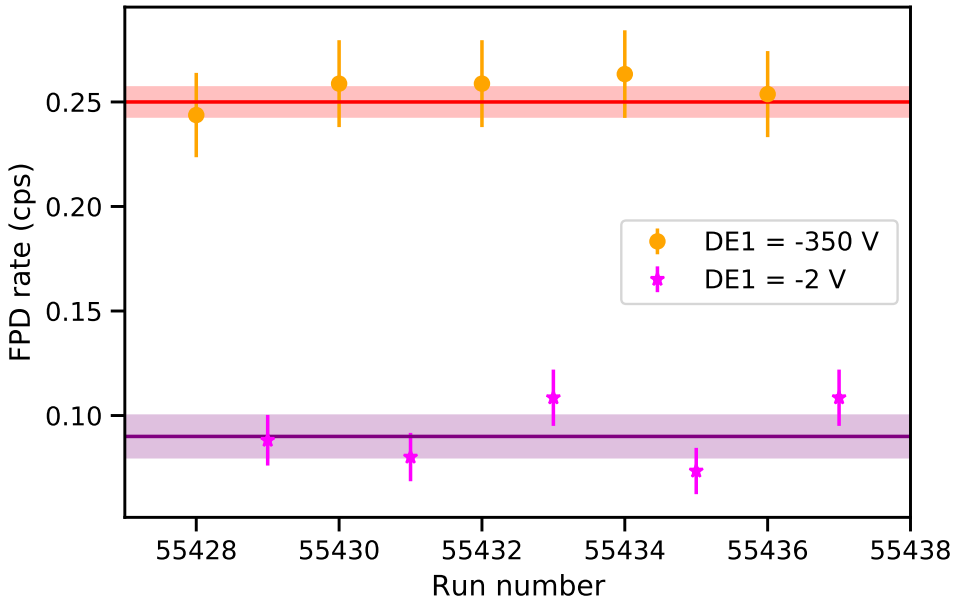

Figure 8.11: FPD rate during the DE1 tritium gas density measurement. There are two DE1 settings, -350 V for the DE1 gas setting and -2 V for the background setting. The mean rate and its standard deviation, of each setting, is represented with a solid line and a shaded region respectively.

that of DE1. The gas density measurement was not repeated with the rest of the dipoles, because the gas density there was not enough to affect the FPD rate at our resolution. So the density was assumed to be one order of magnitude smaller at each successive dipole, as predicted by simulations.

8.6.2 Impact on the neutrino mass squared

The KATRIN experiment measures a β-energy spectrum. The β-electrons originating at the WGTS have different initial conditions than the β-electrons originating at other locations. We can think of the measured spectrum as the sum of different spectra, each one originating at a specific location, weighted by their probabilities. This probability is given by the tritium density or the number of β-decays at each location.

The β-spectrum fitter teams investigated the impact of tritium decay in the DPS as follows. They generated Monte Carlo data for each β-spectrum, with the initial conditions of the WGTS and of each dipole. In all cases, the true Monte Carlo m_ν^2 value was set to zero. Then, they created a combined spectrum by summing the weighted spectra. And finally, the combined spectrum was fitted with m_ν^2 as a free parameter. A more detailed description of the analysis, using the KATRIN fitter CMKAT, can be found in [111].

The neutrino mass squared shift due to tritium decay in the dipoles was calculated to be [111] :

$$\Delta m_\nu^2 = m_{\nu,\,\mathrm{WGTS}}^2 - m_{\nu,\,\mathrm{combined}}^2 = 6.0 \times 10^{-4} \ \ \mathrm{eV}^2. \tag{8.7}$$

The shift due to background generated by tritium decay in the dipoles is very small when compared to the main systematic uncertainties of the experiment (Sec. 4.4.1). So this background was found to be negligible.

8.7 Monitoring residual tritium ion flux into the pre-spectrometer

During the neutrino mass measurements of KNM1 and KNM2 campaigns, the ion flux into the SDS was monitored. The PS-DCE current monitors all the time. As explained in section 5.4.2, if the current is measured to be above 5 pA for more than 3 consecutive signals (to prevent triggering on a spike) then the valve between the CPS and the PS (V2) is automatically closed. During the aforementioned campaigns, the safety mechanism was never triggered.

Monitoring with the ICE method is harder since the PS needs special settings. Nevertheless, the experiment was set to the ICE settings 5 times during KNM2. Plot 8.12 shows the FPD rate during the ICE measurements. The rate was found to be below the safety limit at all times.

Combining these monitoring results, the ion current ($\Phi_{\mathrm{ion}}^{\mathrm{SDS}}$) into the SDS was found to be below the safety limit during the KNM1 and KNM2 campaigns.

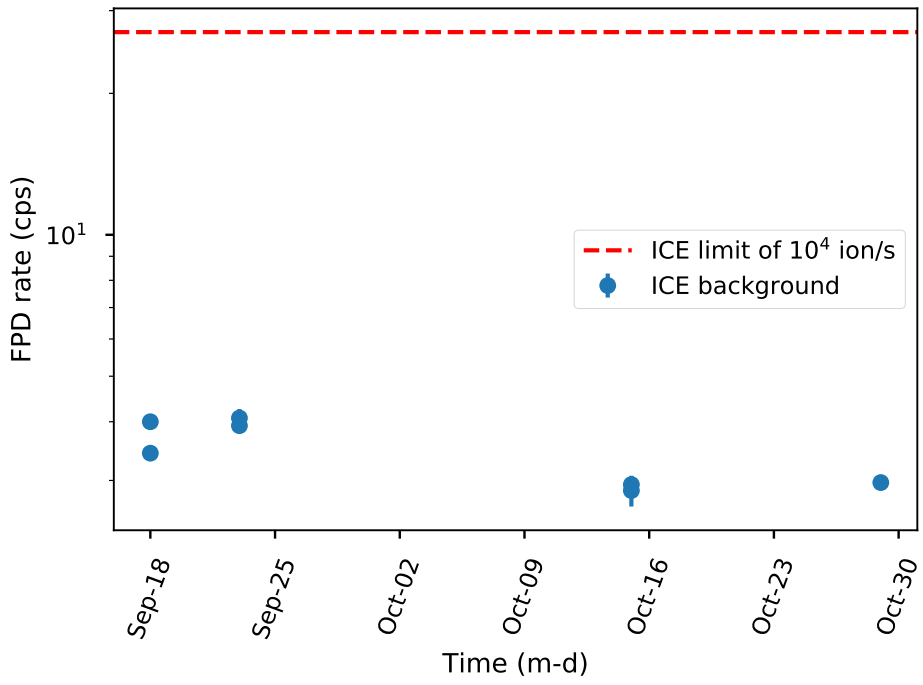

Figure 8.12: FPD rate during ICE measurements (blue dots). The red line represents the safety limit of the FPD rate corresponding to an ion flux into the SDS of 10^4 ion/s. The ICE rate is always below the limit.

CHAPTER 9
SUMMARY AND CONCLUSIONS

The absolute mass scale of the neutrino is one of the major open questions of neutrino physics. Different experiments have studied it throughout the years. The current best limit on the effective electron neutrino mass comes from the KATRIN experiment at $m_\nu < 0.8$ eV at the 90% confidence level, based on the first two measurement campaigns [77].

The KATRIN experiment is designed to study the effective $\overline{\nu}_e$ mass by measuring the energy spectrum of the β-electron after tritium β-decay and fitting it with a theoretical calculation. Final-state excitations modify the β-energy spectrum. The excitations cannot be measured but they can be calculated with theory. Hence, to test the validity of the theory, other predicted quantities are measured. One such quantity is the branching ratio of HT and TT β-decay to the bound molecular final states $^3HeH^+$ and $^3HeT^+$ respectively.

In the 1950s two experiments measured the branching ratio to the bound-state daughter molecule of HT and TT β-decay [66, 67]. And, theoretical calculations were carried out by Jonsell *et al.* [68], giving results that strongly disagree with the experimental results. The goal of the Tritium Recoil Ion Mass Spectrometer (TRIMS) experiment is to resolve this discrepancy by measuring these branching ratios to the bound molecular state utilizing a different method from the previous experiments.

The TRIMS experiment is a time-of-flight mass spectrometer that consists of a decay chamber where the source β-decays. Magnetic fields guide the charged particles towards the ion- and electron- detectors while electric fields accelerate them. The source has two main operational modes with sources consisting of different mixtures of HT and TT gas.

The selected TRIMS analysis projects mentioned in this thesis, and their outcomes, are the following:

- **Data quality check and treatment of defective runs**. Some of the defective runs were manually found and characterized in the TRIMS data base. An automatic method was programmed to find all the defective runs due to glitches in the digitizer. Around 8% of the runs were found to be defective. So as not to lose statistics, a method was designed to cut the data of the defective interval from the run, and still use the rest of the data in the analysis (Sec. 3.1).

- **Ion detector characterization**. Ion interactions with the silicon detector were modelled using the software Stopping and Range of Ions in Matter (SRIM) to better un-

derstand the TRIMS ion-energy reconstruction and compute correct branching ratios. The interactions that depend on the type of ion are of special importance because they can modify the branching ratios. The studied interactions included:

1. *Backscattered ions*. These ions lose energy in the process of backscattering. If the ion is backscattered it will return to the ion detector, due to the electric field, but it will have a smaller incident energy. It will fall out of the fiducial volume energy cut and so it will be lost. The percentage of backscattered ions was obtained with the SRIM simulations. This number depends on ion type and on ion energy. The correction for backscattered ions was done directly on the calculated branch intensities (Sec. 3.2.3).
2. *Dead layer effects*. A 100 nm half dead layer was simulated with SRIM to calculate the energy lost in the dead layer of the ion detector. The ion detected energy was reconstructed from the ion incident energy in the TRIMS Geant4 simulation (Sec. 3.2.4).
3. *Pulse-height-defect*. Only the electronic stopping power, in the active layer, contributes to the detected voltage signal. The nuclear stopping power, or the nuclear recoil energy, in the active layer is lost and causes the so-called pulse-height defect. Lists of the electronic and nuclear stopping powers per ion energy were obtained with SRIM (Sec. 3.2.5).

Using the results of the dead layer effect and the pulse height defect, a function was constructed to convert the ions' detected energy to incident energy in the TRIMS experiment.

- **Proton energy of the decay branch $\mathbf{He^+ + H^+ + \beta^- + e^-_{so}}$.** A theoretical calculation was done to obtain the minimum proton energy of $E_{\mathrm{H}} \geq 32.45\,\mathrm{eV}$. An empirical method was also investigated. In TRIMS there are two detection channels of the $\{\mathrm{He^+ + H^+ + \beta^- + e^-_{so}}\}$ decay branch that can give us information on the proton. They are the ones where the $\mathrm{He^+}$ ion is not detected in the ion detector while the $\mathrm{H^+}$ ion, or the proton, is detected. The proton energy was sought by comparing the experimental data of the proton detection branch to the simulation data. The following things were tried: binning the data in different proton energy sizes; dividing the simulation data in accordance to the mechanism in which the helium ion is lost; separating the simulation data according to the number of detected electrons; and weighting the proton energy bins with the shakeoff energy spectrum. The proton energy could not be obtained via this method because the structures observed in the data could not be

reproduced in the simulation (Sec. 3.3).

Now, we return to the KATRIN experiment. Its goal sensitivity on m_ν is 0.2 eV at the 90% confidence level. The measurement principle used to measure the β-energy spectrum is the Magnetic Adiabatic Collimation with Electrostatic (MAC-E) filter. Past experiments (Mainz [75] and Troitsk [76]) also used the MAC-E filter principle, but in the KATRIN experiment, the spectrometer has much finer filter width. Another novelty of the KATRIN experiment is its high density tritium source, where around 10^{11} β-decays per second occur. Every time a β-electron is created in the source section, so is an ion.

To measure the β-energy spectrum in KATRIN, β-electrons are guided toward the FPD using superconducting magnets to create magnetic fields. But all charged particles follow the magnetic field lines, including ions. If an ion flux gets to the SDS it contaminates the experiment and it can increase the FPD background to alarming rates, even above the design limit [86], which in turn worsens the neutrino mass sensitivity. That is why there is an ion flux limit into the SDS of 1×10^4 ions/s. There are mechanisms in the transport section to stop or reflect the ion flux, and to remove it from the flux tube.

The KATRIN experiment has four different ion monitoring mechanisms, located throughout the beam tube, to make sure there is no ion flux into the SDS. To prevent tritium contamination in the SDS, a safety mechanism is triggered if an ion flux is detected in the PS. This mechanism consists of closing the valve between the CPS and the PS.

During the STS Commissioning Phase IIIa (STS-IIIa) campaign, non-tritium ion sources were explored. Using these non-contaminating ions, two of the ion monitoring mechanisms were calibrated, and the ion blocking mechanisms were characterized. The calibration of the ion monitoring mechanisms required simulations, measurements, and analysis. It was a unique opportunity since the neutrino mass measurements were carried out right after this campaign, where tritium was injected in the source. These calibrations can't be repeated after the tritium injection because they would contaminate the experiment. The calibrations were carried out as follows.

- **Calibration of the current measured in the PS Downstream-Cone Electrode (PS-DCE)**. Upon entering the PS, the ions are accelerated by the negative potentials of the vessel and the wire electrodes. These ions hit the vessel and the cone electrodes where they are neutralized. It is possible to measure the current created by the ions that reach the PS-DCE. This current is created by the neutralization of ions reaching the PS-DCE but it is also affected by secondary electrons emitted on ion impact. The calibration consisted of comparing the PS-DCE current in two different settings, one with no secondary electron emission and one at neutrino mass settings. The ion

transport probability of the two settings was taken into account by using results from the simulations. Finally, the efficiency factor that translates the current to an ion flux was calculated to be (Sec. 7.3.1):

$$\varepsilon_{\mathrm{DCE}}^{\nu\text{-mass}} = \frac{I_{\mathrm{ion}}^{\mathrm{DCE}}(\nu\text{-mass})}{\Phi_{\mathrm{ion}}^{\mathrm{SDS}}} = (1.77 \pm 0.67) \times 10^{-19}\mathrm{C}. \tag{9.1}$$

- **Calibration of the ICE monitoring method**. In this method, the ion flux is calculated directly from the FPD rate. It is quite sensitive, but it needs a special experimental setting. The calibration consisted on measuring the ion flux in the detector section using a Faraday cup inserted in front of the FPD and comparing it with the measured rate. Simulations were also used to account for ion transport probability. The ICE efficiency, which translates the FPD rate to ion flux was calculated to be (Sec. 7.3.2):

$$\varepsilon_{\mathrm{ICE}} = (3.54 \pm 0.18) \cdot 10^{-3}\,\mathrm{counts/ion}. \tag{9.2}$$

The previously calibrated monitoring mechanisms were used during the KNM1 and KNM2 measuring campaigns, where they measured tritium ion fluxes, those results are shown in this thesis. Both mechanisms were also used in subsequent campaigns, although the ICE method less so since it requires special settings.

During the KNM1 and KNM2 campaigns the tritium column density was first ramped up via a series of steps, and ion safety procedures were carried out at each step. This was necessary because a high tritium column density was attained for the first time during these campaigns. During the ramp-ups, the dipoles were found to effectively remove ions from the flux tube (Sec. 8.2.1). The ion flux into the SDS was monitored with the PS-DCE method and the ICE method in KNM1 and KNM2 respectively. During KNM1 ramp-up it was found that the systematic error on the PS-DCE current was too large to be used reliably to get the ion flux, nevertheless the change in current was consistent with zero (Sec. 8.2.2). As a consequence, during KNM2 ramp-up we monitored with ICE (Sec. 8.2.3). It was found that the ion flux into the SDS flux was always below the experimental limit of 1×10^4 ion/s. Hence, the blocking devices were found to work correctly at these column densities. Following campaigns did not require the ion safety procedure during the ramp-up since it was already established that the ion blocking and monitoring devices were working correctly.

The ion energy spectrum of two ring electrodes was investigated (Sec. 8.3), and the optimum voltage of the blocking devices was calculated (Sec. 8.4) taking into account the neutralization measurements (Sec. 8.5). Due to the low neutralization of the blocking

devices, we recommended to clean the ring electrodes of stored electrons every two weeks.

Measurements were carried out to calculate the tritium density inside the dipole electrodes and their induced error on the neutrino mass squared was found to be negligible (Sec. 8.6). Finally, the ion flux into the SDS was monitored and found to be below the experimental limit at all times (Sec. 8.7). And so it was deemed safe to continue with the neutrino mass measurements at the newly attained high column densities.

BIBLIOGRAPHY

[1] Laurie M. Brown. "The idea of the neutrino". In: *Physics Today* 31,9,23 (1978). DOI: 10.1063/1.2995181.

[2] James Chadwick and Charles D. Ellis. "A Preliminary Investigation of the Intensity Distribution in the β-Ray Spectra of Radium B and C". In: *Proc. Camb. Philos. Soc.* 21 (1922), pp. 274–280. URL: https://www.biodiversitylibrary.org/item/88477#page/2/mode/1up.

[3] Fred L. Wilson. "Fermi's theory of Beta decay". In: *American Journal of Physics* 36,12 (1968). DOI: 10.1119/1.1974382.

[4] C. L. Cowan Jr. et al. "Detection of the Free Neutrino: a Confirmation". In: *Science* 124,3212 (1956), pp. 103–104. DOI: 10.1126/science.124.3212.103.

[5] Julian Schwinger. "A theory of the fundamental interactions". In: *Annals of Physics* 2(5) (1957), pp. 407–434. DOI: 10.1016/0003-4916(57)90015-5.

[6] Joshua P. Ellis. "Ti k Z-Feynman: Feynman diagrams with Ti k Z". In: *Comput. Phys. Commun* 210 (2017), 103123. ISSN: 0010-4655. DOI: 10.1016/j.cpc.2016.08.019.

[7] NobelPrize.org. Nobel Prize Outreach AB 2021. *Frederick Reines Facts*. Mon. 23 Aug 2021. URL: https://www.nobelprize.org/prizes/physics/1995/reines/facts/.

[8] G. Danby et al. "Observation of High-Energy Neutrino Reactions and the Existence of Two Kinds of Neutrinos". In: *Phys. Rev. Lett.* 9 (1 1962), pp. 36–44. DOI: 10.1103/PhysRevLett.9.36. URL: https://link.aps.org/doi/10.1103/PhysRevLett.9.36.

[9] NobelPrize.org. Nobel Prize Outreach AB 2021. *The Nobel Prize in Physics 1988*. Mon. 23 Aug 2021. URL: https://www.nobelprize.org/prizes/physics/1988/summary/.

[10] R. P. Feynman, R.B. Leighton, and M. Sands. *The Feynman lectures on physics*. Fondo Educativo Interamericano, 1963.

[11] DONUT Collaboration. "Observation of tau neutrino interactions". In: *Phys. Lett. B* 504,3 (2001), pp. 218–224. URL: http://dx.doi.org/10.1016/S0370-2693(01)00307-0.

[12] Hitoshi Murayama. “The origin of neutrino mass”. In: 15.5 (2002), pp. 35–39. DOI: 10.1088/2058-7058/15/5/36. URL: https://doi.org/10.1088/2058-7058/15/5/36.

[13] M. Goldhaber, L. Grodzins, and A. W. Sunyar. “HelicityofNeutrinos”. In: *Physical Review* 109, 1015 (1958). DOI: 10.1103/PhysRev.109.1015.

[14] Borexino Collaboration. “Neutrinos from the primary protonproton fusion process in the Sun”. In: *Nature* 512 (2014), 383386. DOI: 10.1038/nature13702.

[15] J. N. Bahcall et al. “Solar Neutrino Flux”. In: *Astrophysical Journal* 137 (1963), pp. 344–346. URL: http://adsabs.harvard.edu/pdf/1963ApJ...137..344B.

[16] Bruce T. Cleveland et al. “Measurement of the solar electron neutrino flux with the Homestake chlorine detector”. In: *The Astrophysical Journal* 496 (1998), 505526. URL: https://iopscience.iop.org/article/10.1086/305343.

[17] B. Pontecorvo and V. Gribov. “Neutrino astronomy and lepton charge”. In: *Physics Letters B* 28 (1969), pp. 493–496. DOI: 10.1016/0370-2693(69)90525-5.

[18] C.Giganti, S. Lavignac, and M. Zito. “Neutrino oscillations: The rise of the PMNS paradigm”. In: *Progress in Particle and Nuclear Physics* 98 (2018), pp. 1–54. DOI: 10.1016/j.ppnp.2017.10.001.

[19] Volodymyr Takhistov. “Review of Atmospheric Neutrino Results from Super-Kamiokande”. In: *PoS* ICHEP2020 (2021), p. 181. DOI: 10.22323/1.390.0181. arXiv: 2012.06864 [hep-ex].

[20] C. Patrignani. “Review of Particle Physics”. In: *Chinese Physics C* 40 (2016), pp. 248,249. URL: https://iopscience.iop.org/article/10.1088/1674-1137/40/10/100001/pdf.

[21] Koichiro Nishikawa et al. “Long-Baseline Neutrino Oscillation Experiments”. In: *Advances in High Energy Physics* 2013 (2013), p. 475749. DOI: 10.1155/2013/475749.

[22] Pablo F. de Salas et al. “Neutrino Mass Ordering from Oscillations and Beyond: 2018 Status and Future Prospects”. In: *Frontiers in Astronomy and Space Sciences* 5 (2018), p. 36. ISSN: 2296-987X. DOI: 10.3389/fspas.2018.00036. URL: https://www.frontiersin.org/article/10.3389/fspas.2018.00036.

[23] A. Nucciotti. “The Use of Low Temperature Detectors for Direct Measurements of the Mass of the Electron Neutrino”. In: *Advances in High Energy Physics* 2016 (2016), p. 9153024. DOI: 10.1155/2016/9153024.

[24] Joseph A. Formaggio, André Luiz C. de Gouvêa, and R. G. Hamish Robertson. “Direct measurements of neutrino mass”. In: *Phys. Rep.* 914 (2021), pp. 1–54. DOI: https://doi.org/10.1016/j.physrep.2021.02.002.

[25] Guido Drexlin. *KATRIN measuring sub-eV neutrino masses*. International Europhysics Conference on High Energy Physics EPS-HEP. July 27, 2003. URL: https://slideplayer.com/slide/7719684/.

[26] Julien Lesgourgues and Sergio Pastor. “Massive neutrinos and cosmology”. In: *Physics Reports* 429 (2006), 307379. URL: http://ific.uv.es/~pastor/RINO/PREP429.pdf.

[27] Cora Dvorkin et al. *Neutrino Mass from Cosmology: Probing Physics BSM*. 2019. arXiv: 1903.03689 [astro-ph.CO].

[28] Planck Collaboration. “Planck2018 results. VI. Cosmological parameters”. In: *A and A* 641 (2020), p. 67. URL: https://arxiv.org/pdf/1807.06209.pdf.

[29] Elliott H. Lieb and Horng-Tzer Yau. “A Rigorous Examination of the Chandrasekhar Theory of Stellar Collapse”. In: *Astrophys. J.* 323 (Dec. 1987), p. 140. DOI: 10.1086/165813.

[30] W. David Arnett and Jonathan L. Rosner. “Neutrino mass limits from SN1987A”. In: *Phys. Rev. Lett.* 58 (18 1987), pp. 1906–1909. DOI: 10.1103/PhysRevLett.58.1906. URL: https://link.aps.org/doi/10.1103/PhysRevLett.58.1906.

[31] Thomas J. Loredo and Donald Q. Lamb. “Bayesian analysis of neutrinos observed from supernova SN 1987A”. In: *Phys. Rev. D* 65 (6 2002), p. 063002. DOI: 10.1103/PhysRevD.65.063002.

[32] Fengpeng An et al. “Neutrino physics with JUNO”. In: *J. Phys. G* 43.3 (2016), p. 030401. ISSN: 1361-6471. DOI: 10.1088/0954-3899/43/3/030401. URL: http://dx.doi.org/10.1088/0954-3899/43/3/030401.

[33] B. Abi et al. *DUNE, Far Detector Technical Design Report, Volume II: DUNE Physics*. 2020. arXiv: 2002.03005 [hep-ex].

[34] A. S. Barabash. “Average and recommended half-life values for two-neutrino double beta decay: Upgrade-2019”. In: *Workshop on calculation of the $\beta\beta$-decay matrix elements* (2019). DOI: 10.1063/1.5130963.

[35] R. Arnold et al. “Measurement of the double-beta decay half-life and search for the neutrinoless double-beta decay of ^{48}Ca with the NEMO-3 detector”. In: *Phys. Rev. D* 93 (11 2016), p. 112008. DOI: 10.1103/PhysRevD.93.112008.

[36] M. Agostini et al. “Final Results of GERDA on the Search for Neutrinoless Double-Decay”. In: *Physical Review Letters* 125.25 (2020). ISSN: 1079-7114. DOI: 10.1103/physrevlett.125.252502. URL: http://dx.doi.org/10.1103/PhysRevLett.125.252502.

[37] G. Anton et al. “Search for Neutrinoless Double-β Decay with the Complete EXO-200 Dataset”. In: *Phys. Rev. Lett.* 123 (16 2019), p. 161802. DOI: 10.1103/PhysRevLett.123.161802. URL: https://link.aps.org/doi/10.1103/PhysRevLett.123.161802.

[38] LEGEND Collaboration et al. “LEGEND-1000 Preconceptual Design Report”. In: *arXiv e-prints*, arXiv:2107.11462 (July 2021), arXiv:2107.11462. arXiv: 2107.11462 [physics.ins-det].

[39] J. B. Albert et al. “Sensitivity and discovery potential of the proposed nEXO experiment to neutrinoless double-β decay”. In: *Phys. Rev. C* 97 (6 2018), p. 065503. DOI: 10.1103/PhysRevC.97.065503. URL: https://link.aps.org/doi/10.1103/PhysRevC.97.065503.

[40] A. Gando et al. “Search for Majorana Neutrinos Near the Inverted Mass Hierarchy Region with KamLAND-Zen”. In: *Phys. Rev. Lett.* 117 (8 2016), p. 082503. DOI: 10.1103/PhysRevLett.117.082503. URL: https://link.aps.org/doi/10.1103/PhysRevLett.117.082503.

[41] L. I. Bodine, D. S. Parno, and R. G. H. Robertson. “Assessment of molecular effects on neutrino mass measurements from tritium β decay”. In: *Phys. Rev.* C91.3 (2015), p. 035505. DOI: 10.1103/PhysRevC.91.035505. arXiv: 1502.03497 [nucl-ex].

[42] KATRIN collaboration. “KATRIN Design Repor”. In: *FZKA scientific report* (2005). DOI: 10.5445/IR/270060419.

[43] G. Drexlin et al. “Current Direct Neutrino Mass Experiments”. In: *Adv. High Energy Phys.* 2013 (2013). DOI: 10.1155/2013/293986.

[44] A. Ashtari Esfahani et al. “Electron radiated power in cyclotron radiation emission spectroscopy experiments”. In: *Phys. Rev. C* 99 (5 2019), p. 055501. DOI: 10.1103/PhysRevC.99.055501. URL: https://link.aps.org/doi/10.1103/PhysRevC.99.055501.

[45] C. Hassel et al. “Recent Results for the ECHo Experiment”. In: *J. Low Temp. Phys.* 184 (2016), 910921. DOI: 10.1007/s10909-016-1541-9.

[46] B. Alpert et al. “HOLMES”. In: *Eur. Phys. J. C* 75 (2015). DOI: 10.1140/epjc/s10052-015-3329-5.

[47] M. Aker et al. “Analysis methods for the first KATRIN neutrino-mass measurement”. In: *Physical review D* 104 (2021). DOI: 10.1103/PhysRevD.104.012005.

[48] R. G. H. Robertson and D. A. Knapp. “Direct Measurements of Neutrino Mass”. In: *Annual Review Nuclear Particle Science* 38 (1988), p. 185. DOI: 10.1146/annurev.ns.38.120188.001153.

[49] A. Saenz and P. Froelich. “Effect of final-state interactions in allowed β decays. II. Reliability of the β-decay spectrum for T_2”. In: *Phys. Rev. C* 56 (1997), p. 2162. DOI: 10.1103/PhysRevC.56.2162.

[50] D. H. Wilkinson. “Small terms in the beta-decay spectrum of tritium”. In: *Nucl. Phys. A* 526 (1991), pp. 131–140. DOI: 10.1016/0375-9474(91)90301-L.

[51] C.-E. Wu and W. W. Repko. “One-half-plus to one-half-plus beta decay with neutrino mass effects in the elementary particle treatment of weak interactions”. In: *Phys. Rev. C* 27 (4 1983), pp. 1754–1760. DOI: 10.1103/PhysRevC.27.1754. URL: http://link.aps.org/doi/10.1103/PhysRevC.27.1754.

[52] F. Simkovic, R. Dvornicky, and A. Faessler. “Exact relativistic tritium beta-decay endpoint spectrum in a hadron model”. In: *Phys. Rev. C* 77 (2008), p. 055502. DOI: 10.1103/PhysRevC.77.055502. arXiv: 0712.3926 [hep-ph].

[53] S.S. Masood et al. “Exact relativistic beta decay endpoint spectrum”. In: *Phys. Rev. C* 76 (2007), p. 045501. DOI: 10.1103/PhysRevC.76.045501. arXiv: 0706.0897 [hep-ph].

[54] W. Kolos and L. Wolniewicz. “Accurate Computation of Vibronic Energies and of Some Expectation Values for H_2, D_2, and T_2”. In: *J. Chem. Phys.* 41.12 (1964), pp. 3674–3678. DOI: 10.1063/1.1725797.

[55] J. A. Coxon and P. G. Hajigeorgiu. "Experimental Born–Oppenheimer Potential for the $X^1\Sigma^+$ Ground State of HeH^+: Comparison with the Ab Initio Potential". In: *J. Molec. Spectrosc.* 193 (1999), p. 306. DOI: 10.1006/jmsp.1998.7740.

[56] N. Doss et al. "Molecular effects in investigations of tritium molecule β decay endpoint experiments". In: *Phys. Rev. C* 73 (2006), p. 025502. DOI: 10.1103/PhysRevC.73.025502.

[57] A. Saenz, S. Jonsell, and P. Froelich. "Improved Molecular Final-State Distribution of HeT^+ for the β-Decay Process of T_2". In: *Phys. Rev. Lett.* 84 (2000), pp. 242–245. DOI: 10.1103/PhysRevLett.84.242.

[58] O. Fackler et al. "Accurate theoretical β-decay energy spectrum of the tritium molecule and its neutrino mass dependence". In: *Phys. Rev. Lett.* 55 (1985), p. 1388. DOI: 10.1103/PhysRevLett.55.1388.

[59] R. G. H. Robertson et al. "Limit on $\bar{\nu}_e$ Mass from Observation of the β Decay of Molecular Tritium". In: *Phys. Rev. Lett.* 67 (1991), p. 957. DOI: 10.1103/PhysRevLett.67.957.

[60] W. Stoeffl and D. J. Decman. "Anomalous Structure in the Beta Decay of Gaseous Molecular Tritium". In: *Phys. Rev. Lett.* 75 (1995), p. 3237. DOI: 10.1103/PhysRevLett.75.3237.

[61] J. F. Wilkerson and R. G. H. Robertson. "Direct Measurements of Neutrino Mass". In: *Neutrino Physics*. Ed. by David O. Caldwell. New York: Springer, 2001.

[62] D. K. Veirs and G. M. Rosenblatt. "Raman Line Positions in Molecular Hydrogen: H_2, HD, HT, D_2, DT, and T_2". In: *J. Molec. Spectrosc.* 121 (1987), p. 401. DOI: 10.1016/0022-2852(87)90058-0.

[63] M.-C. Chuang and R. N. Zare. "Rotation-Vibration Spectrum of HT: Line Position Measurements of the 1-0, 4-0, and 5-0 Bands". In: *J. Molec. Spectrosc.* 121 (1987), p. 380. DOI: 10.1016/0022-2852(87)90057-9.

[64] A. Carrington et al. "Infrared bound to quasibound vibration-rotation spectrum of HeH^+ and its isotopes". In: *Chem. Phys.* 81 (1983), p. 251. DOI: 10.1016/0301-0104(83)85319-1.

[65] M. W. Crofton et al. "Infrared spectra of $^4HeH^+$, $^4HeD^+$, $^3HeH^+$, and $^3HeD^+$". In: *J. Chem. Phys.* 91 (1989), p. 5882. DOI: 10.1063/1.457456.

[66] A. H. Snell, F. Pleasanton, and H. E. Leming. "Molecular Dissociation Following Radioactive Decay: Tritium Hydride". In: *J. Inorg. Nucl. Chem.* 5 (1957), pp. 112–117. DOI: 10.1016/0022-1902(57)80051-7.

[67] S. Wexler. "Dissociation of TH and T_2 by β-decay". In: *J. Inorg. Nucl. Chem.* 10 (1959), pp. 8–16. DOI: 10.1016/0022-1902(59)80180-9.

[68] S. Jonsell, A. Saenz, and P. Froelich. "Neutrino-mass determination from tritium β decay: Corrections to and prospects of experimental verification of the final-state spectrum". In: *Phys. Rev. C* 60 (1999), p. 034601. DOI: 10.1103/PhysRevC.60.034601.

[69] The TRIMS Collaboration. "TRIMS: Measurement of branching ratios to ionic final states in the beta decay of molecular tritium". Paper in preparation.

[70] F. Pleasanton and A. H. Snell. "Ionization following internal conversion in xenon". In: *Proc. R. Soc. London A* 241 (1957), pp. 141–152. DOI: 10.1098/rspa.1957.0119.

[71] K.-E. Bergkvist. "A high-luminosity, high-resolution study of the end-point behaviour of the tritium β-spectrum (I). basic experimental procedure and analysis with regard to neutrino mass and neutrino degeneracy". In: *Nucl. Phys. B* 39 (1972), pp. 317–370. DOI: 10.1016/0550-3213(72)90376-8.

[72] J. F. Wilkerson et al. "Limit on $\bar{\nu}_e$ Mass from Free-Molecular-Tritium Beta Decay". In: *Phys. Rev. Lett.* 58 (1987), p. 2023. DOI: 10.1103/PhysRevLett.58.2023.

[73] H. Sun et al. "An Upper Limit for the Electron Anti-Neutrino Mass". In: *Chin. J. Nucl. Phys.* 15 (3 1993), p. 261.

[74] H. Kawakami et al. "New upper bound on the electron anti-neutrino mass". In: *Phys. Lett. B* 256 (1991), p. 105. DOI: http://dx.doi.org/10.1016/0370-2693(91)90226-G.

[75] C. Kraus et al. "Final results from phase II of the Mainz neutrino mass search in tritium β decay". In: *Eur. Phys. J. C* 40 (2005), p. 447. DOI: 10.1140/epjc/s2005-02139-7.

[76] V. N. Aseev et al. "Upper limit on the electron antineutrino mass from the Troitsk experiment". In: *Phys. Rev. D* 84 (2011), p. 112003. DOI: 10.1103/PhysRevD.84.112003.

[77] M. Aker et al. "First direct neutrino-mass measurement with sub-eV sensitivity". arXiv:2105.08533 [hep-ex]. 2021.

[78] Ying-Ting Lin. "The Tritium Recoil-Ion Mass Spectrometer Experiment". PhD thesis. University of Washington, 2019.

[79] Y.-T. Lin et al. “Beta Decay of Molecular Tritium”. In: *Phys. Rev. Lett.* 124 (22 2020), p. 222502. DOI: 10.1103/PhysRevLett.124.222502.

[80] John N. Bahcall. “Theory of Bound-State Beta Decay”. In: *Phys. Rev.* 124 (2 1961), pp. 495–499. DOI: 10.1103/PhysRev.124.495.

[81] James F. Ziegler. “SRIM-2003”. In: *Nucl. Instr. Meth. B* 219-220 (2004), pp. 1027–1036. DOI: 10.1016/j.nimb.2004.01.208.

[82] James Ziegler, Jochen Biersack, and Matthias Ziegler. *SRIM, The Stopping and Range of Ions in Matter*. SRIM Company, 2008, 2010.

[83] B. L. Wall et al. “Dead layer on silicon p-i-n diode charged-particle detectors”. In: *Nucl. Inst. Meth. A* 744 (2014), pp. 73–79. DOI: 10.1016/j.nima.2013.12.048.

[84] W. Kołos et al. “Molecular effects in tritium β decay: Transitions to the discrete electronic states of the HeT^+ molecule”. In: *Phys. Rev. A* 31 (2 1985), pp. 551–555. DOI: 10.1103/PhysRevA.31.551. URL: http://link.aps.org/doi/10.1103/PhysRevA.31.551.

[85] Hamish Robertson. Internal comunication. 2021.

[86] M. Aker et al. “The design, construction, and commissioning of the KATRIN experiment”. In: *Journal of Instrumentation* 16.08 (2021), T08015. DOI: 10.1088/1748-0221/16/08/t08015. URL: https://doi.org/10.1088/1748-0221/16/08/t08015.

[87] M. Kleesiek et al. “β-Decay spectrum, response function and statistical model forneutrino mass measurements with the KATRIN experiment”. In: *Eur. Phys. J. C* 79 (2019). DOI: 10.1140/epjc/s10052-019-6686-7.

[88] M Babutzkar et al. “Monitoring of the operating parameters of the KATRIN Windowless Gaseous Tritium Source”. In: *New Journal of Physics* 14 (2012). URL: https://iopscience.iop.org/article/10.1088/1367-2630/14/10/103046.

[89] F. M. Frankle et al. “Radon induced background processes in the KATRIN prespectrometer”. In: *Astroparticle Physics* 35(3) (2011), pp. 128–134. DOI: 10.1016/j.astropartphys.2011.06.009.

[90] S. Gorhardt et al. “Impact of a cryogenic baffle system on the suppression of radon-induced background in the KATRIN Pre-Spectrometer”. In: *Journal of Instrumentation* 13 (2018). DOI: 10.1088/1748-0221/13/10/T10004.

[91] M. Arenz et al. “Commissioning of the vacuum system of the KATRIN Main Spectrometer”. In: *Journal of Instrumentation* 11 (2016). DOI: 10.1088/1748-0221/11/04/P04011.

[92] J.F.Amsbaugh et al. “Focal-plane detector system for the KATRIN experiment”. In: *Nucl. Instrum. Methods Phys. Res. Sec. A* 778 (2015), pp. 40–60. DOI: 10.1016/j.nima.2014.12.116.

[93] A. V. Lokhov and F. V. Tkachov. “Confidence intervals with a priori parameter bounds”. In: *Physics of Particles and Nuclei* 46 (2015), 347365. DOI: 10.1134/S1063779615030089.

[94] Manuel Klein. “Tritium ions in KATRIN: blocking removal and detection”. PhD thesis. Karlsruhe Institute of Technology, 2018.

[95] Fabian Friedel. “Tritium ions in KATRIN”. PhD thesis. Karlsruhe Institute of Technology, 2020.

[96] L. L. Lucas and M. P. Unterweger. “Comprehensive Review and Critical Evaluation of the Half-Life of Tritium”. In: *J. Res. Natl. Inst. Stand. Technol.* 105(4) (2000), 541549. DOI: 10.6028/jres.105.043.

[97] Ferenc Glck. Internal comunication. 2020.

[98] Ferenc Glck. *Longitudinal plasma simulations*. Talk at internal KATIRN meeting. 2020.

[99] JV.P. Gupta. *Principles and Applications of Quantum Chemistry*. Academic Press, 2016, pp. 291–337. DOI: https://doi.org/10.1016/B978-0-12-803478-1.00009-1.

[100] Gordon H. Dunn and L. J. Kieffer. “Dissociative Ionization of H_2: A Study of Angular Distributions and Energy Distributions of Resultant Fast Protons”. In: *Phys. Rev.* 132 (5 1963), pp. 2109–2117. DOI: 10.1103/PhysRev.132.2109. URL: https://link.aps.org/doi/10.1103/PhysRev.132.2109.

[101] John David Jackson. *Classical Electrodynamics*. John Wiley & Sons, 1962, pp. 412–419.

[102] Rudolf Sack. “Aufbau einer Ionenquelle und Simulation der Transporteigenschaften der DPS und CPS am KATRIN Experiment”. MA thesis. Karlsruhe Institute of Technology, 2015.

[103] Daniel Furse et al. “Kassiopeia: a modern, extensible C++ particle tracking package”. In: *New Journal of physics* 19:053012 (2017).

[104] R. Brun and F. Rademakers. “ROOT - An Object Oriented Data Analysis Framework”. In: *Nucl. Instr. & Meth. in Phys. Res. A* 389 (1997), pp. 81–86. DOI: 10.1016/S0168-9002(97)00048-X.

[105] Diego Casadei. “Estimating the selection efficiency”. In: *JINST* P08021 (2012).

[106] Emmanuel Weiss. “Determination of the Ion Conversion to Electron efficiency of the KATRIN Pre-Spectrometer”. Bachelor’s Thesis. Karlsruhe Institute of Technology, 2018.

[107] Woo-Jeong Baek. “Investigation of background processes of ions and Rydberg atoms in the KATRIN spectrometers”. MA thesis. Karlsruhe Institute of Technology, 2017.

[108] R. Kersevan and J.-L. Pons. “Introduction to MOLFLOW+: New graphical processing unit-based Monte Carlo code for simulating molecular flows and for calculating angular coefficients in the compute unified device architecture environment”. In: *Journal of Vacuum Science & Technology A* 27.4 (2009), pp. 1017–1023. DOI: 10.1116/1.3153280. eprint: https://doi.org/10.1116/1.3153280. URL: https://doi.org/10.1116/1.3153280.

[109] M. Aker et al. “Improved Upper Limit on the Neutrino Mass from a Direct Kinematic Method by KATRIN”. In: *Phys. Rev. Lett.* 123 (22 2019), p. 221802. DOI: 10.1103/PhysRevLett.123.221802.

[110] A. Marsteller. “Characterization and Optimization of the KATRIN Tritium Source”. PhD thesis. Karlsruhe Institute of Technology, 2020. DOI: 10.5445/IR/1000127553.

[111] Larisa Thorne. “Neutrino mass analysis and systematics of the KATRIN experiment, using CMKAT”. PhD thesis. Carnegie Mellon University, 2020.